UNIVERSIDADE DE BRASÍLIA – UNB
INSTITUTO DE GEOCIÊNCIAS - IG
PÓS-GRADUAÇÃO EM GEOLOGIA

Footprint geofísico e petrofísico do Depósito Salobo, Província Mineral de Carajás

Moriá Caroline de Araújo

Tese de Doutorado nº 217

31 de Março de 2025, Brasília – DF

UNIVERIDADE DE BRASÍLIA – UnB
INSTITUTO DE GEOCIÊNCIAS - IG
PÓS-GRADUAÇÃO EM GEOLOGIA

Footprint geofísico e petrofísico do Depósito Salobo, Província Mineral de Carajás

Geophysical and petrophysical footprint of Salobo Deposit, Carajás Mineral Province

Moriá Caroline de Araújo

Tese de Doutorado
Área de Concentração: Prospecção Mineral e Geologia Econômica

Orientadora
Profa. Dra. Adalene Moreira Silva (UnB)
Coorientadora
Profa. Dra. Catarina Labouré Bemfica Toledo (UnB)

Banca Examinadora
Presidente
Profa. Dra. Adalene Moreira Silva (UnB – Orientadora)
Membros Externos
Prof. Dr. Dionísio Uendro Carlos (UNESP)
Dr. Marco Antônio Couto Jr. (UBC – Pesquisador Associado)
Membro Interno
Prof. Dr. Marcelo Henrique Leão Santos (UnB)

31 de Março de 2025, Brasília – DF

Ficha catalográfica elaborada automaticamente,
com os dados fornecidos pelo(a) autor(a)

de Araújo, Moriá Caroline
dD278f Footprint geofísico e petrofísico do Depósito Salobo, Província Mineral de Carajás / Moriá Caroline de Araújo; orientador Adalene Moreira Silva; co-orientador Catarina Labouré Bemfica Toledo. Brasília, 2025.
135 p.

Tese(Doutorado em Geologia) Universidade de Brasília, 2025.

1. IOCG. 2. Salobo. 3. Provincia Mineral de Carajás. 4. Footprint Geofísico. 5. Footprint Petrofísico. I. Moreira Silva, Adalene, orient. II. Labouré Bemfica Toledo, Catarina, co-orient. III. Título.

AGRADECIMENTOS

A realização desta tese foi um percurso repleto de desafios, aprendizado e crescimento. A sua conclusão foi o segundo maior desafio da minha vida e veio acompanhado do maior de todos: a perda da minha mãe, meu porto seguro emocional e físico. Sua ausência tornou cada etapa mais difícil, mas também me fez encontrar apoio e força nas pessoas ao meu redor, que foram fundamentais para que eu conseguisse seguir em frente e concluir este trabalho. Expresso a minha profunda gratidão a todas as pessoas e instituições que apoiaram de alguma forma e me ajudaram na finalização dessa etapa da minha vida.

A minha família, minha base, sou imensamente grata. Ao meu pai, Márcio de Araújo, por sua força e amor incondicionais. Ao meu parceiro, André Walczuk, pelo apoio, paciência e compreensão imensuráveis. Ao meu irmão, Samuel de Araújo, por estar sempre ao meu lado, mesmo que a distância. Às minhas tias, que foram um refúgio de carinho e cuidado. Sem vocês, esta jornada não teria sido possível.

Um agradecimento especial a Daniel Shkromada, cuja generosidade em compartilhar conhecimento e disponibilidade fizeram toda a diferença. Seu suporte técnico foi essencial para o desenvolvimento desta tese e dos artigos. Sua contribuição foi mais do que acadêmica; foi um pilar fundamental para que eu pudesse chegar até aqui. Não existem palavras para descrever a quão grata eu sou a você.

Aos meus amigos, que, nos momentos de maior cansaço e dúvida, não me deixaram desistir e de alguma forma, seja emocional ou técnica me ajudaram: Maria Alagia, Luisa Barbosa, Lucas Teles, Luana Campos, Helena Nonato, Lorena Braga, Juliana Araújo e Raphael Prieto. Vocês foram fundamentais para manter minha motivação e meu equilíbrio emocional ao longo dessa jornada.

Agradeço também ao suporte técnico dos membros dos laboratórios que contribuíram significativamente para esta pesquisa. Meu reconhecimento a Érico Zacchi e Cintia Stumpf, do Instituto de Geociências da UnB; Edvaldo Faria, do Laboratório de Petrofísica da Vale S.A. em Carajás; e Victor Nogueira, do Laboratório AXT Pty Ltd, na Austrália. O conhecimento e a dedicação de vocês foram essenciais para a realização deste trabalho.

A todos que, de alguma forma, estiveram ao meu lado, meu mais sincero e profundo agradecimento. Sem vocês, esta conquista não seria possível.

O presente trabalho foi financiado em parte pela Coordenação de Aperfeiçoamento de Pessoal de Nível Superior - Brasil (CAPES), Código de Financiamento 001, e apoiada pelo Conselho Nacional de Desenvolvimento Científico e Tecnológico (CNPq) e pelo Programa CT-Universal (Projeto 408592/2021-4). Os autores expressam sua gratidão ao consórcio Vale-ADIMB-Universidades Brasileiras pelo apoio e permissão para a publicação deste trabalho, como parte do Projeto Geodinâmica e Metalogênese da Província Mineral de Carajás (PA) e do Quadrilátero Ferrífero (QF), financiado pela Vale S.A. Além disso, Adalene M. Silva e C. Toledo agradecem pelas bolsas de pesquisa concedidas pelo CNPq (Projetos 309846/2023-4 e 313807/2021-3).

“Descobrir consiste em olhar para o que todo mundo está vendo e pensar em uma abordagem diferente”

Roger Von Oec

RESUMO

Os depósitos de óxido de ferro-cobre-ouro (IOCG - *Iron oxide copper-gold*) representam um conjunto de mineralizações com características distintas, refletindo a diversidade das rochas hospedeiras e dando origem a assinaturas petrofísicas complexas e geofísicas variadas. Embora muitos desses depósitos tenham sido descobertos inicialmente por meio de modelos exploratórios tradicionais, a prospecção futura exigirá abordagens mais avançadas e robustas. Na Província Mineral de Carajás, a complexidade dos depósitos IOCG impõe um desafio adicional ao desenvolvimento de um modelo geofísico eficaz. Diante desse cenário, esta tese foca na caracterização do *footprint* geofísico e petrofísico do depósito IOCG Salobo, com ênfase em suas porções mais profundas, por meio da integração de dados geofísicos multifonte e multiescala com as propriedades físicas das rochas. Além disso, a pesquisa abrange a integração de dados geofísicos, petrofísicos, geológicos e geoquímicos proporcionando uma abordagem mais abrangente para a compreensão do depósito.

Para a caracterização do *footprint* geofísico foram identificadas assinaturas e anomalias distintas associadas ao ambiente mineralizado do depósito Salobo. Foram utilizados diversos conjuntos de dados geocientíficos, incluindo: 1) dados aeromagnéticos e gamaespectrométricos com espaçamento entre linhas de voo de 500 metros para mapear a assinatura regional do depósito; 2) dados aerogeofísicos de maior resolução, como gravimetria gradiométrica, eletromagnético, magnético e gamaespectrométricos, para o mapeamento em escala de distrito; e 3) dados geofísicos terrestres, incluindo magnetometria, gamaespectrometria, TDEM (eletromagnético no domínio do tempo) e DCIP (*Direct Current resistivity and Induced Polarization*), para o mapeamento em escala de depósito. O depósito Salobo apresenta contraste nos dados magnetométricos, gravimétricos gradiométricos, TDEM e DCIP. Em escalas regional e de distrito, a mineralização está associada a fortes anomalias magnéticas e gravimétricas, devido à alta suscetibilidade magnética da magnetita associada ao metassomatismo de ferro disseminado no granito que hospeda a mineralização, incluindo zonas de alteração hidrotermal ricas em magnetita. Modelos de condutividade recuperado pelo TDEM aéreo e terrestre mapearam zonas de alta concentração de calcocita-bornita. Além disso, anomalias proeminentes de urânio e U/Th foram observadas nos dados gamaespectrométricos de alta resolução. Levantamentos de DCIP indicam que a resistividade é mais eficaz para mapear o depósito do que a cargabilidade. Os modelos de cargabilidade mostram uma anomalia muito mais ampla, possivelmente influenciada por eventos tardios de alteração estéril associados ao evento de 1,88 Ga.

A assinatura petrofísica do depósito Salobo indica correlações entre as rochas hospedeiras, a alteração hidrotermal e a mineralização. A análise das propriedades físicas, como densidade, suscetibilidade magnética, resistividade e cargabilidade, permite diferenciar

zonas distintas alteradas hidrotermalmente. As rochas hospedeiras apresentam baixa densidade, alta resistividade e pouca variação nas demais propriedades. Em contraste, as zonas alteradas exibem mudanças significativas, com aumento de densidade, suscetibilidade magnética e cargabilidade, indicando um contraste dentro do ambiente mineralizado. As zonas enriquecidas em ferro e potassificadas apresentam alta suscetibilidade magnética e alta densidade devido à abundância de magnetita e sulfetos, respectivamente. O contraste de resistividade nessas áreas sugere a presença de minerais condutores, como bornita, calcocita e calcopirita. A cargabilidade também aumenta, refletindo os sulfetos disseminados e magnetita. No entanto, as anomalias magnéticas e de cargabilidade podem gerar interpretações errôneas, pois a magnetita também ocorre em zonas distais e estéreis. A resistividade se destaca como um vetor chave para mapear a mineralização e para a definição de alvos exploratórios, pois não apenas delineou diretamente o corpo mineralizado de Salobo, mas também permitiu a diferenciação dos tipos de minério. A resistividade galvânica (DCIP) marcou zonas de alto e baixo teor de minério, enquanto a resistividade indutiva (TDEM) realçou principalmente as áreas de alto teor. A análise detalhada das assinaturas geofísicas e petrofísicas permitem diferenciar a zonação do envelope de alteração e permitiu delinear as porções distais, proximais e a zona mineralizada.

A integração de dados geofísicos, petrofísicos e de mapeamento mineral aprimora a interpretação e pode ser aplicada tanto em escala regional quanto de depósito para identificar padrões estruturais e zonas de alteração hidrotermal, essenciais para o mapeamento de sistemas minerais do tipo IOCG no Cinturão Norte do Cobre. Este estudo propõe vetores exploratórios resumidos em dois guias. O primeiro destaca os principais vetores geofísicos, enquanto o segundo aborda os vetores petrofísicos. Esse resultado pode contribuir para aprimorar estratégias de exploração e reduzir riscos em contextos geológicos semelhantes.

Palavras Chaves: IOCG, Salobo, Provincia Mineral de Carajás, *Footprint* Geofísico e *Footprint* Petrofísico.

ABSTRACT

Iron oxide copper-gold (IOCG) deposits present significant challenges due to their complex petrophysical characteristics and geophysical signatures. While many of these deposits were initially discovered using traditional exploratory models, future exploration will require more advanced and robust approaches. In the Carajás Mineral Province, the complexity of IOCG deposits further challenges the development of an effective geophysical exploration model. To assist this challenge, this thesis focuses on characterizing the geophysical and petrophysical footprint of the Salobo IOCG deposit, with emphasis on its deeper sections, through the integration of multi-source and multi-scale geophysical data with the physical properties of rocks.

Additionally, the research encompasses the integration of geophysical, petrophysical, geological, and geochemical data, providing a more comprehensive approach to understanding the deposit.

To define the geophysical footprint, distinct geophysical signatures and anomalies associated with the mineralized zone of the Salobo deposit were identified and characterized. Various geoscientific datasets were used, including 1) 500-m flight line spacing airborne magnetic and gamma spectrometric data for mapping the regional signature of the deposit, 2) higher resolution airborne gravity gradiometry, time-domain electromagnetic (TDEM), magnetic, and gamma spectrometric data for district-scale mapping, and 3) ground magnetic, gamma spectrometric, fixed-loop time domain electromagnetic, and DCIP (Direct Current resistivity and Induced Polarization) data for deposit-scale mapping. Salobo shows significant magnetic, gravity gradiometry, TDEM, and DCIP signatures. At regional and district scales, the mineralization is associated with strong magnetic and gravity anomalies due to the high magnetic susceptibility of magnetite widespread Fe metasomatism in the granite host, which includes magnetite-rich alteration zones. Airborne and ground TDEM models detected the high-grade chalcocite-bornite zones. Prominent uranium and U/Th anomalies are observed in high-resolution gamma spectrometric data. DCIP surveys indicate that resistivity is more effective in mapping the deposit than chargeability. Chargeability models show a much larger anomaly and appear to be influenced by 1.88 late-stage and barren alteration events.

The petrophysical signature of the Salobo deposit reveals correlations between host rocks, hydrothermal alteration, and mineralization. Analyzing physical properties, such as density, magnetic susceptibility, resistivity, and chargeability, allows for the differentiation of distinct alteration zones. Host rocks exhibit low density, high resistivity, and minimal variation in other properties. In contrast, altered zones display significant changes, with increased density, magnetic susceptibility, and chargeability, indicating mineral enrichment. Iron-enriched and potassic-altered zones have high density and magnetic susceptibility due to the abundance of magnetite and sulphides. The contrast of resistivity in these areas suggests the presence of conductive minerals such as bornite, chalcocite, and chalcopyrite. Chargeability also increases, reflecting the dissemination of sulphides and magnetite. However, magnetic and chargeability anomalies can produce misinterpretations, as magnetite also occurs in distal and barren zones. Thus, resistivity stands out as a key vector for mapping mineralization and defining exploration targets, as it not only directly delineated the mineralized body of Salobo but also enabled the differentiation of ore types. Galvanic resistivity (DCIP) identified zones of both high and low ore grades, while inductive resistivity (TDEM) primarily highlighted high-grade areas. A detailed analysis of petrophysical signatures enables the distinction between mineralized zones and altered areas with no economic potential, optimizing mineral exploration efficiency.

The integration of geophysical, petrophysical, and mineral mapping data enhances interpretation and can be applied at both regional and deposit scales to identify structural patterns

and hydrothermal alteration zones, which are essential for mapping IOCG mineral systems in the Northern Copper Belt. This study proposes exploration vectors summarized in two guides. The first highlights the main geophysical vectors, while the second focuses on petrophysical vectors. These findings can contribute to improving exploration strategies and reducing risks in similar geological settings.

Keywords: IOCG, Salobo, Carajás Mineral Province, Geophysical Footprint and, Petrophysical Footprint

RESUMO ..... **V**

ABSTRACT ..... **VI**

LISTA DE FIGURAS ..... **XII**

LISTA DE TABELAS ..... **XIX**

1. INTRODUÇÃO **20**

1.1. Objetivos 22

1.2. Localização e Acessos 22

1.3. Materiais e Métodos 24

1.3.1. Trabalho de Campo e Amostragem 24

1.3.2. Geofísica Aérea 27

1.3.3. Geofísica Terrestre 29

1.3.4. Petrofísica 31

1.3.5. Litogeoquímica 32

1.3.6. Quantitative Evaluation of Minerals by Scanning Electron Microscopy (QEMSCAN) 33

1.3.7. TESCAN Integrated Mineral Analyzer (TIMA) e Laser-induced breakdown spectroscopy (LIBS) 33

2. GEOPHYSICAL SIGNATURE OF THE SALOBO IOCG DEPOSIT AND IMPLICATIONS FOR MINERAL EXPLORATION **36**

ABSTRACT 36

2.1. Introduction 36

2.2. Geological Context 37

2.2.1. Salobo Deposit 39

2.3. Materials and Methods 41

2.4. Results 45

2.4.1. Regional Scale Footprint 45

2.4.2. District Scale Footprint 47

2.4.3. Deposit Scale Footprint 50

2.5. Discussion 54
2.5.1. Magnetics 54
2.5.2. Gravity Gradiometry 55
2.5.3. Time Domain Electromagnetic – TDEM 56
2.5.4. Gamma Spectrometry 56
2.5.5. Induced Polarization 56
2.5.6. Multiscale and multisource Geophysical footprint of the Salobo Deposit 57
2.6. Conclusion 60
Acknowledgments 61
Appendix A 62
Appendix B 62
Appendix C 63
References 64
3. PETROPHYSICAL SIGNATURE OF THE SALOBO IOCG DEPOSIT: INSIGHTS INTO LITHOLOGY, HYDROTHERMAL ALTERATION, AND MINERALIZATION ... 69
ABSTRACT 69
3.1. Introduction 70
3.2. Geological Context 71
3.2.1. Salobo Deposit 73
3.3. Materials and Methods 74
3.3.1. Sampling 74
3.3.2. Petrophysics 75
3.3.3. Petrography and Scanning Electron Microscope (SEM) 75
3.3.4. Laser-induced breakdown spectroscopy (LIBS) 76
3.3.5. Integration of petrophysical data and mineral mapping 76
3.4. Results and Discussion 78
3.4.1. Host rocks 80
3.4.2. Calcic-Sodic alteration 81
3.4.3. Iron enrichment 84

3.4.4. Potassic alteration 90
3.4.5. Mineralisation and ore body 92
3.4.6. Later albitization alteration 97
3.4.7. Post-ore alteration 98
3.5. Evaluating the Petrophysical Footprint of Salobo 100
3.5.1. Geophysical Footprint 102
3.5.2. Implications for Mineral Exploration 104
3.6. Conclusion 106
Acknowledgments 107
Appendix A 108
Appendix B 115
Appendix C 116
References 117
4. INTEGRAÇÃO DE DADOS MULTIFONTES 120
5. CONCLUSÕES 129
REFERÊNCIAS BIBLIOGRÁFICAS 132
APPENDIX A 135

LISTA DE FIGURAS

Figura 1. 1 – A) Localização da Província Mineral de Carajás. B) Mapa da Província Mineral de Carajás e adjacências indicando as associações tectonoestratigráficas e mineralizações associadas. O polígono preto indica a localização da área de estudo (Modificado de Santos et al., 2000; Vasquez & Rosa-Costa, 2008; Tavares, 2015). 21

Figura 1. 2 - Localização da área de estudo no estado do Pará no Brasil, com a indicação dos principais municípios próximos e acessos da região (QGIS Development Team, 2015. QGIS Geographic Information System. Open Source Geospatial Foundation Project. Disponível em: http://qgis.osgeo.org)..... 23

Figura 1. 3 - Seção geológica do depósito Salobo destacando alterações geológicas, furos de sondagem profundos (SALO-DH00002, 2-1 e 2-2) e os intervalos amostrados em campo. Inclui foto de amostras representativas do ambiente mineralizado, com descrição e identificação mineralógica realizadas em escala macroscópica. Abreviações: Act – Actinolita, Bn – Bornita, Bt – Biotita, Chl – Clorita, Grt – Granada, Gru – Grunerita, Mag – Magnetita, Pl – Plagioclásio e Qz – Quartzo. 25

Figura 1. 4 - Seção geológica do depósito Salobo destacando alterações geológicas, furos de sondagem profundos (SALO-DH00003, 3-1 e 3-2) e os intervalos amostrados em campo. Inclui foto de amostras representativas das diferentes assembleias hidrotermais, com descrição e identificação mineralógica realizadas em escala macroscópica. Abreviações: Act – Actinolita, Bn – Bornita, Bt – Biotita, Chl – Clorita, Ccp – Calcopirita, Grt – Granada, Mag – Magnetita, Pl – Plagioclásio e Qz – Quartzo. 26

Figura 1. 5 – Equipamentos geofísicos utilizados para aquisição de dados terrestres magnetométricos, eletromagnéticos, gamaespectrométricos e de polarização induzida. Apresenta ainda os equipamentos utilizados para a aquisição de dados petrofísicos de susceptibilidade magnética, condutividade, gamaespectrometria, resistividade e cargabilidade. 31

Figure 2. 1 – A) Tectonic compartmentalization of the Amazonian Craton in Brazilian territory and the location of the Carajás Mineral Province (Modified from Santos et al., 2000). B) Geological map of the northern portion of the Carajás Mineral Province, known as the Northern Copper Belt, encompassing the Cinzento Lineament. The location of the Salobo Deposit is highlighted

(modified from Vasquez & Rosa-Costa, 2008). C) Geological map of the Salobo deposit showing the main geological units, alteration zones, and mineralized zone..... 40

Figure 2. 2 - Illustrative section of the alteration zoning and photos of samples collected along drill hole SALO-DH00002-2. Description and mineralogical identification performed at the macroscopic scale. Abbreviations: Act – Actinolite, Bn – Bornite, Bt – Biotite, Chl – Chlorite, Grt – Garnet, Gru – Grunerite, Mag – Magnetite, Pl – Plagioclase, and Qz – Quartz. 42

Figure 2. 3 – Databases used for the analysis and main acquisition parameters grouped by investigation scale. Each map shows the survey lines (black lines), a basic product of each survey, and the orebodies projected to surface (black polygon). 44

Figure 2. 4 – Regional scale geophysical footprint. All profiles and sections were made along the AB profile, which is shown in the maps. The regional Cinzento shear zone is shown in the maps. A) Location of the AB profile crossing the thickest portion of Salobo; B) Section through the alteration zones; C) Magnetic data reduced to Equator (RTE); D) Total Gradient (TG) magnetic data; E) Section through the magnetic inversion model; F) RTE and TG profiles; G) Potassium concentration; H) Uranium concentration; I) Thorium concentration; J) K, Th, and U profiles. XMT - Magnetite Schist. 46

Figure 2. 5 – Magnetic footprint at the district scale. The Cinzento Shear zone is shown in both maps. A) Reduce to Equator (RTE) map showing the three main anomalies along the magnetic trend. B) Total Gradient (TG) data. C) Section extracted from the inversion along AB profile. MVI model magnetization shown as vector cones coloured by susceptibility. D) 3D visualization of Salobo magnetic signature on surface, and a 0.09 SI amplitude isosurface extracted from the inversion model. XMT - Magnetite Schist. 47

Figure 2. 6 - Gravity footprint at a district scale. A) Vertical gravity (g_D) map. B) Vertical gravity (g_D) and vertical gravity gradient (G_{DD}) along the AB profile. C) Topography along the AB profile. D) Section extracted from the gravity inversion model along the AB profile. E) 3D visualization of Salobo's G_{DD} signature, and a 3D isosurface from the inversion model (0.5 g/cm³). XMT - Magnetite Schist and DTM- Digital Terrain Model. 48

Figure 2. 7 – EM footprint at the district scale. The regional Cinzento shear zone is shown in the maps. A) X component of channel 3. B) Profiles of X component data for channels 3 – 8. C) Channel 3, Z component data. D) Profiles of the Z component for channels 3 – 8. E) EM CDI on the AB profile. F) Time constant (Z component). G) Time constant (Z component) profile. XMT - Magnetite Schist, EM – Electromagnetic, CDI – Conductivity-Depth Image and TAU – Decay Time Constants. 49

Figure 2. 8 – District scale gamma-ray spectrometric footprint. Cinzento Shear Zone, Old Salobo Granite, Salobo-Pojuca domain and XMT are shown in maps. A) RGB ternary composition image (K, eTh, eU). B) 1D profiles of K, eTh, and eU along the AB profile. C) U/Th ratio. D) U/Th ratio along the AB profile. XMT - Magnetite Schist. 50

Figure 2. 9 - Magnetic footprint at the deposit scale. The regional Cinzento shear zone is shown in the maps. A) Reduce to Equator (RTE) data. B) Total Gradient (TG). C) RTE and TG signatures along the AB profile. D) Section extracted from the inversion along AB profile. MVI model magnetization shown as vector cones coloured by susceptibility. XMT - Magnetite Schist. 51

Figure 2. 10 – Deposit scale electromagnetic footprint. A) RDI slice of apparent resistivity from ground EM data at 300m depth and Cinzento shear zone. B) RDI section along the AB profile and isosurfaces of MVI susceptibility and density from inversions of magnetic and gravity data. RDI – Resistivity-Depth Image, EM – Electromagnetic, MVI - Magnetic Vector Inversion and XMT - Magnetite Schist. 52

Figure 2. 11 - Deposit scale gamma spectrometric footprint. Cinzento Shear Zone, Old Salobo Granite, Salobo-Pojuca domain and XMT are shown in all maps. A) Gamma spectrometric ternary map (K = Red, eTh = Green, and eU = Blue). B) Total count C) K concentration, D) K concentration, and total count signatures along the AB profile. E) U concentration. F) Th concentration. G) U/Th ratio. H) Th concentration, U concentration, and U/Th ratio signatures along the AB profile XMT - Magnetite Schist and TC - Total count. 53

Figure 2. 12 - Deposit scale DCIP footprint. A) Chargeability 2D models showing three anomalous trends and a possible extension of the mineralization to the west. B) Resistivity 2D models showing a strong anomaly associated with XMT. XMT - Magnetite Schist..... 54

Figure 2. 13 – Multiscale and multisource geophysical footprint of Salobo. A) Multiscale magnetic data. B) Multiscale gravity data. C) Multiscale gamma spectrometric data. D) District-scale airborne TDEM data. E) Multiscale TDEM data. F) Profile of modelled resistivity and chargeability at 150m depth. XMT - Magnetite Schist, RS – Regional Scale, DS – District Scale, DeS – Deposit Scale, g_D and G_{DD} Falcon component, EM – Electromagnetic, TDEM - Time-Domain Electromagnetic, TAU - Time Constant, DCIP – Direct Current resistivity and Induced Polarization and SGB - Geological Survey of Brazil 58

Figure 2. 14 - Priority guideline of the implemented geophysical methods at the Salobo Deposit. The low-priority methods are not related to its effectiveness in the mineral exploration of IOCG-type deposits. EM – Electromagnetic, DCIP – Direct Current resistivity and Induced Polarization and IOCG - Iron Oxide Copper-Gold. 60

Figure 3. 1 – A) Tectonic division of the Amazonian Craton, showing the location of the Carajás Mineral Province (Modified from Santos et al., 2000). B) Geological map of the northern part of the Carajás Mineral Province, also known as the Northern and Southern Copper Belt, including the Cinzento Lineament. The location of the main Cu-Au deposits, including Salobo, is shown (modified from Vasquez & Rosa-Costa, 2008 and Tavares, 2015). 72

Figure 3. 2 – A) Geological map of the Salobo deposit illustrating the main geological units, alteration halos, and the mineralized zones. B) Geological cross-section depicts the alteration types of the Salobo deposit, highlighting the deep drilling holes SALO-DH00002, 2-1, and 2-2, along with the location of all samples (red points along the holes). C) Geological cross-section depicts the alteration types of the Salobo deposit, highlighting the deep drilling holes SALO-DH00003, 3-1, and 3-2, along with the location of all samples (red points along the holes) (Modified from Araújo et al., submitted). 74

Figure 3. 3 - Flowchart detailing all workflow steps, from sampling to the integration of petrophysical data and, mineral mapping, for the characterization of the petrophysical footprint of the Salobo deposit. Abbreviations: MS – Magnetic Susceptibility, HA – Hydrothermal Alteration, Initial Alt – initially altered rock, Mod Alt - moderately altered rock, Adv Alt - advanced altered rock, Chl – Chloritized, Dia - Diabase (Dia), Ab – Albite, Act – Actinolite, Alm – Almandine, Bt – Biotite, Bn – Bornite, Ccp – Chalcopyrite, Gru – Grunerite, Kfs – K-feldspar, Mag – Magnetite, Pl – Plagioclase, and Qz – Quart. 77

Figure 3. 4 - Petrophysical boxplots of hydrothermal alteration zones of Salobo Deposit and statistical summary table. A) Density boxplot; B) Magnetic Susceptibility boxplot; C) Resistivity boxplot; D) Chargeability boxplot; E) Statistical summary table of petrophysical data for hydrothermal alteration zones, including minimum, average, maximum, median, and standard deviation. Abbreviations: MS – Magnetic Susceptibility 79

Figure 3. 5 - TIMA image of well-preserved host rock and petrophysical boxplots for the assigned classes. A) Sample 3A, representing the well-preserved host rock, is primarily composed of hornblende, plagioclase, quartz, and albite. B) Density boxplot. C) Magnetic susceptibility boxplot. D) Resistivity boxplot. E) Chargeability boxplot. Abbreviations: Ab – Albite, Chl – Chlorite, Hbl - Hornblende, Ilm – Ilmenite, Pl – Plagioclase, Qz – Quartz, Initial Alt – initially altered rock, Mod Alt - moderately altered rock, Adv Alt - advanced altered rock, Chl – Chloritized and Dia - Diabase (Dia). 81

Figure 3. 6 - TIMA image and petrophysical scatter chart of calcic-sodic alteration zone Salobo Deposit. A) Sample 2C, illustrating the initial calcic-sodic alteration zone, is mainly composed of Act, Bt, Ccp, and Py, with minor Ab. B) Sample 3-2A, representing the moderate calcic-sodic alteration zone, is predominantly composed of Qz, Ab, Ep, and Ttn. C) Sample 2P, illustrating the advanced calcic-sodic alteration zone, is predominantly composed of Ab and Qz, with minor amounts of Mag. D) Scatter plot of density vs. magnetic susceptibility, highlighting samples with Ab, Act, Bt, and ore (Py, Ccp, Cct, Bn and Mag). The circle/square size represents resistivity values, with larger circles indicating higher resistivity. The gray-shaded oval marks highlight the high densities in samples with high Act content associated with a higher ferromagnesian content in the protolith. Abbreviations: Ab – Albite, Act – Actinolite, Bt – Biotite, Bn – Bornite, Ccp - Chalcopyrite, Cct – Chalcocite, Ep – Epidote, Mag – Magnetite, Py – Pyrite, Qz – Quart and Ttn – Titanite. 83

Figure 3. 7 - TIMA image and petrophysical scatter plots of Salobo Deposit samples and subzones hydrothermal alteration. A) Sample 2-2B composed of Pl, Qz, and Bt. B) Density vs. magnetic susceptibility scatter plot. Samples size represents Pl+Bt>20%, with larger sizes indicating higher mineral content. Abbreviations: Ab – Albite, Ap – Apatite, Bt – Biotite, Cal – Calcite, Chl - Chlorite, Mag – Magnetite, Pl – Plagioclase, and Qz – Quartz. 85

Figure 3. 8 - TIMA image and petrophysical scatter plots of K-Fe subzone of Salobo Deposit. A) Sample 3-2G (Ca-Fe-K to K-Fe subzone transition), predominantly composed of Alm, Bt, Chl, Pl, and minor Qz. B) Gru+Alm+Srl-Drv content vs. density scatter plot. Symbol size scaled by Mag. C) Sample 3-1I (K-Fe subzone), predominantly composed of deformed Alm, Bt, and Chl. D) Density vs. resistivity scatter plot. Symbol size represents Mag>20%. The gray-shaded oval marks the negative correlation between density and resistivity. Abbreviations: Pl - Plagioclase, Bt - Biotite, Gru - Grunerite, Alm - Almandine, Chl - Chlorite, Qz - Quartz, Srl-Drv - Schorl-Dravite, and Mag – Magnetite..... 86

Figure 3. 9 - TIMA image and petrophysical plots of the iron enrichment of Salobo Deposit. A) Sample 2K is predominantly composed of Gru, Alm, Chl and Mag. B) Sample 2L is predominantly composed of minor Gru, Alm, Chl and major Mag. C) Iron enrichment zone vs. mineral content (volume %) and density (g/cm^3) vs. magnetic susceptibility (x10^{-3} SI), resistivity and chargeability (mV/V) plot of Salobo Deposit samples. Abbreviations: Gru - Grunerite, Alm - Almandine, Chl - Chlorite, and Mag – Magnetite. 89

Figure 3. 10 - TIMA image, petrophysical plots of potassic alteration and matrix correlation of Salobo Deposit samples. A) Sample 2N composed of Gru, Alm, Chl, Bt, Qtz, Mag, Cpy and Bn. B) Scatter plot of sample resistivity (Ω.m) vs. ore content (% volume), with subzone alteration

Salobo samples. Abbreviations: Gru - Grunerite, Alm - Almandine, Chl - Chlorite, Qtz – Quartz, Mag – Magnetite, Cpy -Chalcopyrite, Bn – Bornite, Bt – Biotite, and Cct – Chalcocite..... 91

Figure 3. 11 - TIMA image and Principal Component Plots of the mineralization zone of Salobo Deposit. A) Sample 3S is predominantly composed of Mag, Alm, Chl, Bt, and minor Bn, Ccp, Ttn and Ap. B) Sample 2-2J is predominantly composed Mag, Act and Chl, and minor Ap. C) Density vs. Magnetic susceptibility of Salobo samples. D) Principal Component Analysis plot of among minerals and physical properties within the Salobo IOCG system. The hatched oval marks highlight the six main clusters identified. Abbreviations: QFC – Qz-Ffs-Cal, FM - ferromagnesian silicates, Aln – Allanite, Ap – Apatite, Bn Bornite, Bt - Biotite, Cct - Chalcocite, Ccp - Chalcopyrite, Ep - Epidote, Flr - Fluorite, Gn - Galena, Gyp - Gypsum, Ilm - Ilmenite, Kfs - K-Feldspar, Mag - Magnetite, Mln - Millerite, Mol - Molybdenite, Mnz - Monazite, Ms - Muscovite, Pn - Pentlandite, Px - Pyroxene, Py - Pyrite, Sch-Drv - Schorl-Dravite, Sp - Sphalerite and Ttn - Titanite. 95

Figure 3. 12 - TIMA image and Principal Component Plots of the later albitization and post-ore alteration zone of Salobo Deposit. A) Sample 3-1L, representing the transition from high-grade mineralization to the later albitization alteration zone, includes Qz, Chl, Bt, Mag, Bn, Ab, and Kfs; B) Sample 2T, showing the transition from remnants of mineralization to the later albitization alteration zone, composed of remnant Mag, Chl, Qz, and Ab. C) Sample 3-1B, illustrating the post-ore alteration zone, is predominantly composed of Ab, Pl, Kfs, Ccp, and Py; D) Principal Component Analysis plot of among minerals and physical properties within the Salobo IOCG system. The gray-shaded oval marks highlight the four main clusters identified. Abbreviations: Ab -Albite, Alm – Almandine, Bn Bornite, Bt - Biotite, Cct - Chalcocite, Ccp - Chalcopyrite, Chl – Chlorite, Ep - Epidote, Flr - Fluorite, Ilm - Ilmenite, Kfs - K-Feldspar, Mag - Magnetite, Ms – Muscovite, Pl – Plagioclase, Px - Pyroxene, Py – Pyrite and Qz -Quartz..... 99

Figure 3. 13 - Petrophysical illustrative log of hydrothermal zone and subzone of Salobo deposit samples, main minerals, and physical properties average. Abbreviations: Ab -Albite, Act – Actinolite, Alm – Almandine, Ap – Apatite, Bn Bornite, Bt - Biotite, Cct - Chalcocite, Ccp - Chalcopyrite, Chl – Chlorite, Ep – Epidote, Gru -Grunerite, Ilm - Ilmenite, Kfs - K-Feldspar, Mag - Magnetite, No.S - Number of Samples, Pl – Plagioclase, Py – Pyrite and Qz -Quartz. 101

Figure 3. 14 - Influence of main minerals of Salobo IOCG Deposit and its impact on petrophysical and geophysical footprint. The size of columns in petrophysical footprint is correlated with mineral influence levels, where small columns are low influence, medium columns are moderate influence and large columns are high influence. 104

Figure 3. 15 - Conceptual framework illustrating the interconnections between mineralogical, petrophysical, geophysical, geological, and geochemical datasets used in this study. Mineralogy serves as the central axis, integrating analytical techniques such as LIBS, TIMA/QEMSCAN, and thin-section petrography to provide insights into mineral composition, texture, and alteration. Petrophysical and geophysical data contribute to characterizing ore-forming processes by defining variations in density, magnetic susceptibility, and chargeability. This integrated approach improves exploration targeting by refining the interpretation of alteration halos, mineralized zones, and structural controls..... 106

Figura 4. 1 – Strip Log ilustrativo das principais zonas e subzonas de alteração do Depósito Salobo, valores petrofísicos médios e valores litogeoquímicos médios dos principais elementos indicadores de mineralização. Abreviações: Au – Ouro, Ag – Prata, Bi – Bismuto, Cu – Cobre, Fe – Ferro, Mo – Molibdênio, No.S – Número de amostras e U – Urânio. 122

Figura 4. 2 - - Strip Log ilustrativo das principais zonas e subzonas de alteração do Depósito Salobo, valores petrofísicos médios e valores litogeoquímicos médios dos principais elementos indicadores de alteração. Abreviações: Ca - Cálcio, Hf – Háfnio, K – Potássio, Na – Sódio, No.S – Número de amostras e Zr - Zircônioi. 124

Figura 4. 3 – Gráfico de dispersão das amostras das principais subzonas de alteração hidrotermais do Salobo. A) Diagrama bivariante de Fe x (Ca + Mg) para amostras das principais subzonas de alteração hidrotermais do Salobo com indicação do enriquecimento de sódio no sistema) Diagrama bivariante de Zr x Hf para amostras das principais subzonas de alteração hidrotermais do Salobo com indicação do enriquecimento de sódio e decaimento de Fe, Ca, Mg e K no sistema. C) Diagrama bivariante Fe x Na para amostras das principais subzonas de alteração hidrotermais do Salobo. 127

LISTA DE TABELAS

Tabela 1. 1 - Parâmetros gerais da aquisição de dados dos aerolevantamentos realizados pelo Serviço Geológico do Brasil (SGB) que recobrem o depósito Salobo..... 27

Tabela 1. 2 - Parâmetros gerais da aquisição de dados dos aerolevantamentos cedidos pela Vale S.A. que recobrem o depósito do Salobo. TDEM - Transiente Eletromagnético no Domínio Tempo e AGG-Gradiometria da Gravidade (Airborne Gravity Gradiometer)..... 29

Tabela 1. 3 - Parâmetros gerais da aquisição de dados dos levantamentos terrestres cedidos pela Vale S.A. que recobrem o depósito do Salobo. DCIP - Direct Current resistivity and Induced Polarization; TDEM - Transiente Eletromagnético no Domínio Tempo. 30

Table 3.1 - Spearman correlation matrix showing the relationships between key minerals in the potassic alteration zone and their associated physical properties..... 92

1. Introdução

A Província Mineral de Carajás (PMC), localizada na região sudeste do estado do Pará, Brasil, é reconhecida internacionalmente como uma das principais províncias minerais do Brasil. Esta província abriga depósitos minerais de classe mundial que incluem *commodities* como manganês, platinóides, níquel, ferro, cobre e ouro. Dentre vários, se destacam os depósitos do tipo IOCG (*Iron Oxide-Copper-Gold*) (Hitzman et al., 1992; Santos et al., 2000; Skirrow, 2022) gerados ao longo de múltiplos eventos mineralizantes ocorridos no Neoarqueano (aproximadamente 2,7 e 2,5 Ga) e no Paleoproterozoico (cerca de 2,1 e 1,8 Ga). Esses depósitos são objeto de debates na literatura científica devido à diversidade de suas características, que variam em relação aos ambientes geotectônicos, idades, tipos de rochas hospedeiras e processos de alteração hidrotermais (Hitzman, 2000; Pollard, 2000, 2006; Barton & Johnson, 2004; Williams et al., 2005; Groves et al., 2009; Xavier et al., 2010).

Dentre os depósitos IOCG, mundialmente o que mais se destaca é o de *Olympic Dam*, Austrália, devido ao seu tamanho e teor 2660 Mt a 1.2% Cu, 1.4 kg/t U_3O_8 e 0.5 g/t Au (Esdale et al., 2003) e, também, pelo estilo e características geológicas. Em escala nacional, o maior depósito de cobre é o Salobo, localizado na Zona Cisalhamento Cinzento no Cinturão Norte do Cobre da PMC, com reservas estimadas em 1088,9 Mt a 0,62% Cu e 0,35 g/t Au (VALE, 2023) (Figura 1.1). Descoberto em 1977 e operado pela VALE S.A. desde 2011, a mineralização do depósito Salobo é composta predominantemente por bornita, calcocita, magnetita, quantidades menores de calcopirita e ouro, além de exibir significativos teores de Co, Ni, As, Ag, Mo e ETR (Lindenmayer, 2003; Melo, 2014; Melo et al., 2019).

O depósito está hospedado em rochas gnáissicas neoarqueanas da Suíte Igarapé Gelado (2.763 ± 4,4 Ma) (Figura 1.1) que estão fortemente modificadas por processos de alteração hidrotermal, com formação de rochas ricas em hastingsita-actinolita, grunerita-almadina-biotita-(turmalina) e magnetita com bornita e calcocita disseminadas (Lindenmayer, 2003; Requia et al., 2003; Melo et al, 2016; Melo et al., 2019). Assembleias hidrotermais tardias ricas em hematita foram reconhecidas dentro das zonas mineralizadas, que superpõem a alteração típica IOCG e revela evolução por múltiplos pulsos hidrotermais (Melo, 2014, 2018). O sistema hidrotermal evoluiu de alteração sódica-cálcica (hastingsita - actinolita) para um estágio de enriquecimento em ferro (grunerita-almandina) e formação de turmalina. A alteração potássica com biotita acompanha a formação de magnetita e é cogenética à formação do minério (Melo, 2014; Melo et al., 2019).

Estudos geofísicos desempenham um papel importante na compreensão da PMC e para o Salobo, com destaque para métodos magnetométricos, eletromagnetométricos e elétricos (Silva, 2012; Henrique et al., 2013; Leão-Santos, 2014; Leão-Santos et al., 2015, 2022; Aisengart et al., 2019). Parte destes trabalhos efetuaram a caracterização da assinatura geofisica e

petrofísica de depósitos IOCG como dos depósitos Furnas e o Cristalino (Melo et al., 2015, 2017; Leão-Santos et al., 2022). Contudo, a caracterização do *footprint* do depósito Salobo, bem como uma caracterização integrada das assinaturas geofísica e petrofísica com dados multifonte e multiescala na Província Mineral de Carajás permanece inexplorada. Esta pesquisa busca, de forma inovadora, empregar dados petrofísicos em escala de detalhe para compreender a assinatura do depósito Salobo e desenvolver modelos prospectivos para outros depósitos de classe mundial na PMC.

A utilização de propriedades físicas das rochas é fundamental para o avanço e o sucesso na interpretação e modelagem geofísica, especialmente em depósitos complexos. Essa abordagem é essencial não apenas para mapear a mineralização, alterações hidrotermais e as rochas hospedeiras, mas também para compreender a geometria em profundidade dos corpos mineralizados e a arquitetura dos sistemas mineralizantes. Assim, a meta principal desta pesquisa é caracterizar o *footprint* do depósito Salobo por meio da integração de dados geofísicos, petrofísicos e informações geológicas disponíveis, com o intuito de contribuir significativamente para o entendimento da PMC e seu *endowment*.

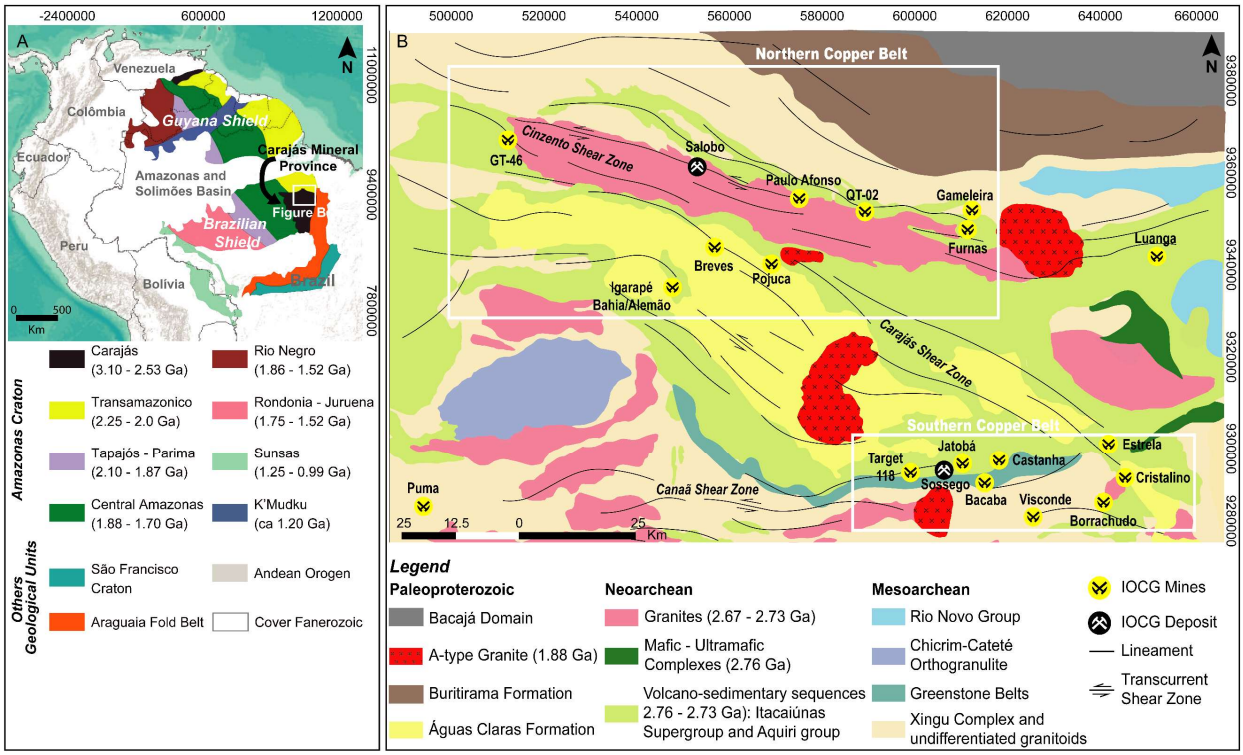


Figura 1. 1 – A) Localização da Província Mineral de Carajás. B) Mapa da Província Mineral de Carajás e adjacências indicando as associações tectonoestratigráficas e mineralizações associadas. O polígono preto indica a localização da área de estudo (Modificado de Santos et al., 2000; Vasquez & Rosa-Costa, 2008; Tavares, 2015).

1.1. Objetivos

O objetivo central dessa pesquisa é caracterizar o *footprint* geofísico e petrofísico das mineralizações e alterações hidrotermais tipo IOCG do depósito Salobo, especialmente com foco na porção mais profunda, a partir do estudo de dados geofísicos multifonte e em multiescala e de propriedades físicas das rochas.

Para tanto, os objetivos específicos são:

I. Processar e interpretar dados geofísicos aéreos e terrestres de magnetometria, gravimetria gradiométrica, gamaespectrometria, eletromagnetometria no domínio do tempo e polarização induzida;
II. Processar e interpretar dados petrofísicos tais como densidade, susceptibilidade magnética, condutividade, resistividade e cargabilidade para caracterização das assinaturas petrofísicas dos diferentes tipos de rochas;
III. Caracterizar a rocha hospedeira, as zonas de alteração e a mineralização por meio da integração de dados petrográficos e mineralógicos, utilizando amostragens detalhadas e técnicas avançadas de análise, como QEMSCAN (*Quantitative Evaluation of Minerals by Scanning Electron Microscopy*), TIMA (*TESCAN Integrated Mineral Analyzer*) e LIBS (*Laser-induced breakdown spectroscopy*), para identificação mineral, química e textural, contribuindo para a compreensão das variações de propriedades físicas da rocha dentro do ambiente mineralizado.
IV. Modelagem e integração dos dados geofísicos, petrofísicos, mineralógicos e litogeoquímicos para o mapeamento de padrões de alteração hidrotermal e sua influência na zonalidade do depósito Salobo.

1.2. Localização e Acessos

O depósito Salobo localiza-se na parte sudeste do estado do Pará, no norte do Brasil. Este pertence a microrregião de Parauapebas, no município de Marabá e faz parte da Província Mineral de Carajás. Grandes centros urbanos como Santarém e Belém estão a 1057 km e 555 km de distância de Marabá, respectivamente e, tem como principais acessos as BR 150 e BR 230. Parauapebas, cidade de maior atividade urbana próximo a Marabá, está a 170 km aproximadamente e, pode ser acessada pela BR 155 e PA-275. A partir de Parauapebas, o acesso ao depósito Salobo é realizado pela rodovia estadual PA-160, por um trajeto de aproximadamente 105 km (Figura 1.2).

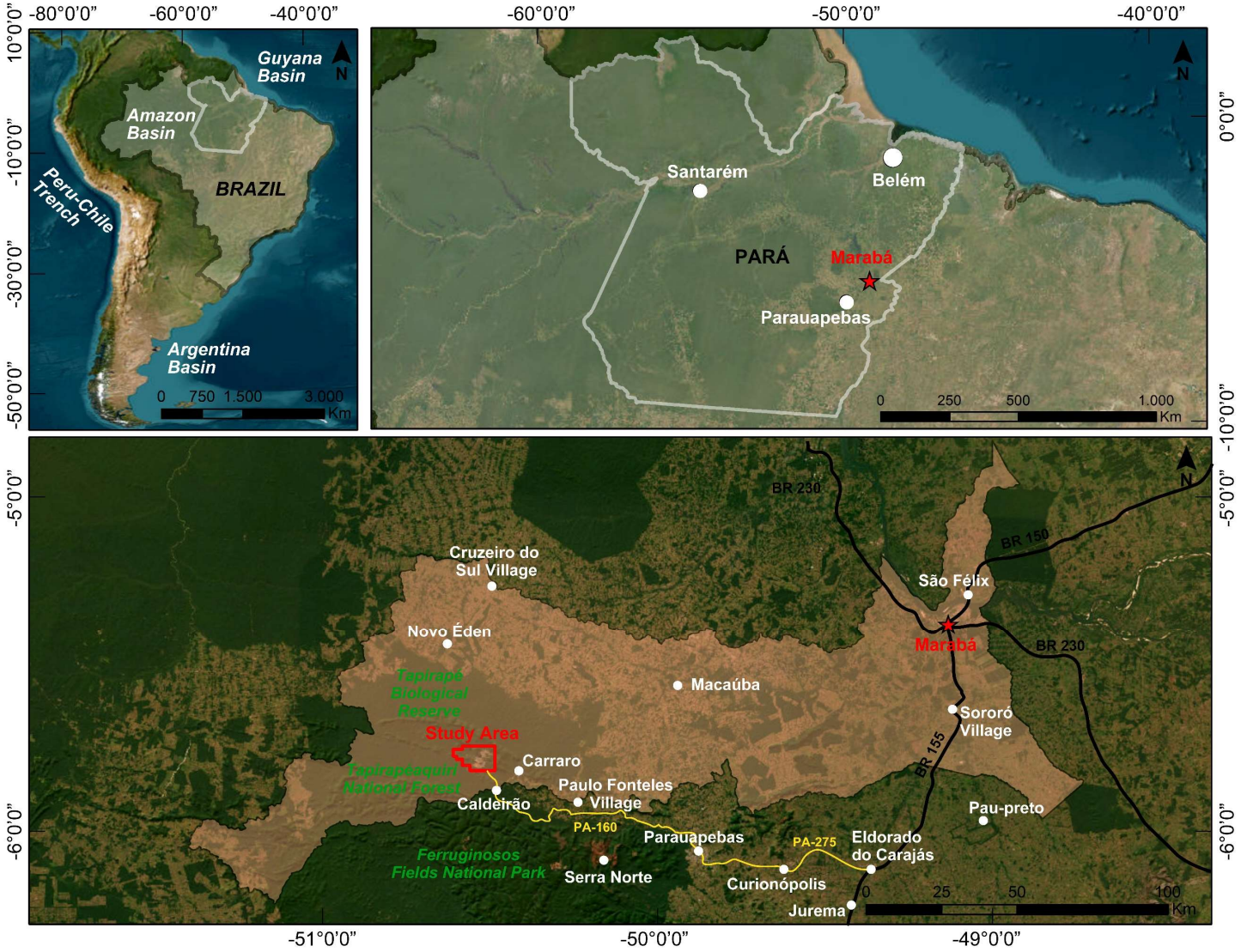


Figura 1. 2 - Localização da área de estudo no estado do Pará no Brasil, com a indicação dos principais municípios próximos e acessos da região (*QGIS Development Team, 2015. QGIS Geographic Information System. Open Source Geospatial Foundation Project. Disponível em: http://qgis.osgeo.org*).

1.3. Materiais e Métodos

Os dados utilizados dentro desta pesquisa fazem parte do acervo do Serviço Geológico do Brasil (SGB) e da Vale S.A. Dentre vários, incluem dados geofísicos aéreos e terrestres que recobrem o depósito Salobo, e dados de testemunhos de sondagem.

1.3.1. Trabalho de Campo e Amostragem

O trabalho de campo, com duração de 15 dias, envolveu a descrição de testemunhos de seis furos de sondagem com profundidade média de 1300 m do projeto Salobo Profundo (SALO-DH00002, 2-1, 2-2, 3, 3-1 e 3-2) para caracterizar rochas encaixantes, hospedeiras, zonas de alteração hidrotermal e minério. Foram coletadas 84 amostras para análises petrofísicas, litogeoquímicas e petrográficas da porção abaixo da cava planejada. Todas as amostras foram descritas e fotografadas para registro da textura e orientação espacial. Os furos interceptaram rochas encaixantes, zonas de alterações hidrotermais (proximal e distal) e a zona mineralizada. A amostragem incluiu granitos da Suíte Igarapé Gelado, zonas de alteração sódico-cálcica (hastingsita, actinolita, allanita, escapolita, calcopirita), zonas de enriquecimento em ferro (grunerita, almandina, turmalina, magnetita, entre outras) e alterações potássicas (biotita), além de zonas mineralizadas com bornita e calcocita (Melo et al., 2016) (Figuras 1.3 e 1.4).

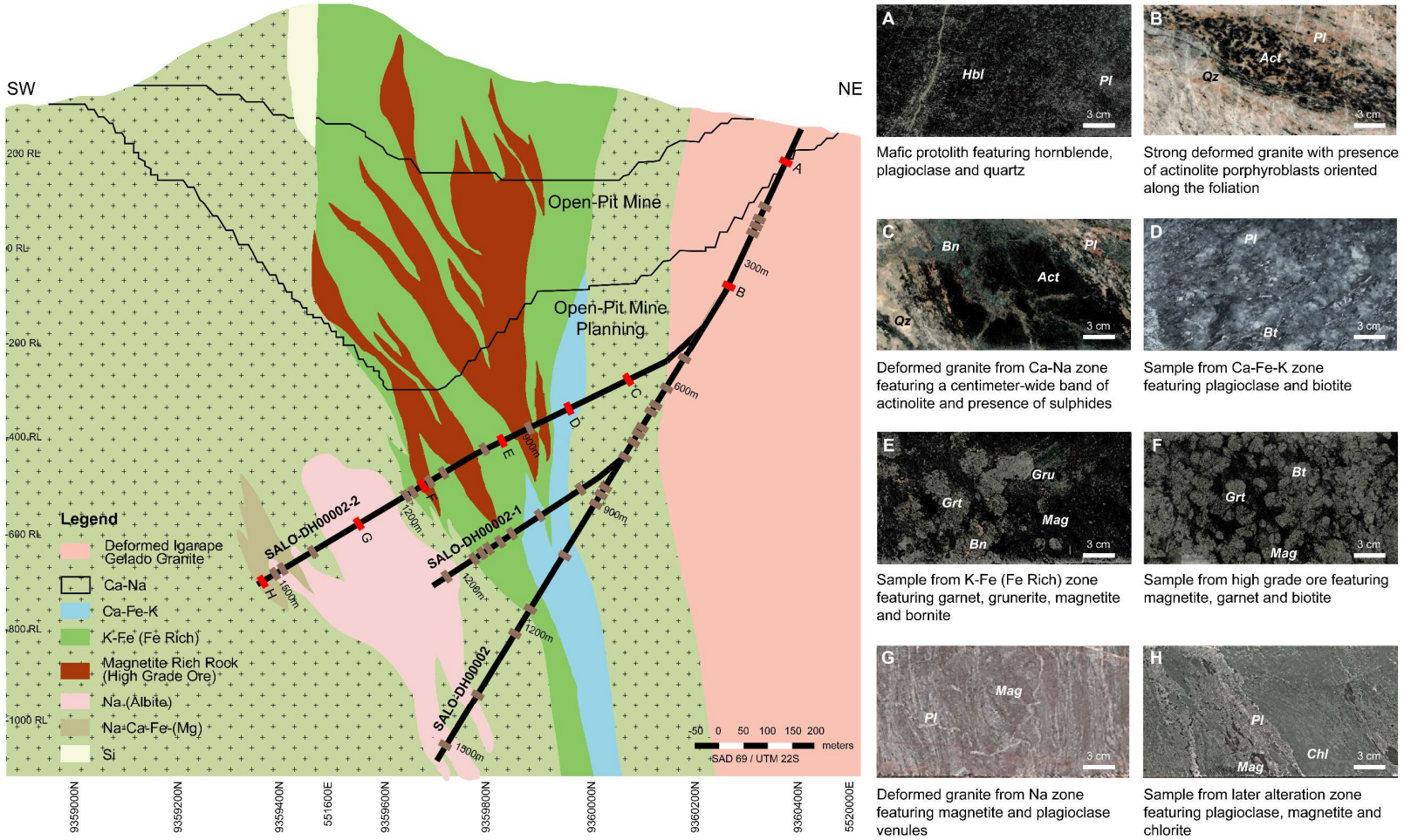


Figura 1. 3 - Seção geológica do depósito Salobo destacando alterações geológicas, furos de sondagem profundos (SALO-DH00002, 2-1 e 2-2) e os intervalos amostrados em campo. Inclui foto de amostras representativas do ambiente mineralizado, com descrição e identificação mineralógica realizadas em escala macroscópica. Abreviações: Act – Actinolita, Bn – Bornita, Bt – Biotita, Chl – Clorita, Grt – Granada, Gru – Grunerita, Mag – Magnetita, Pl – Plagioclásio e Qz – Quartzo.

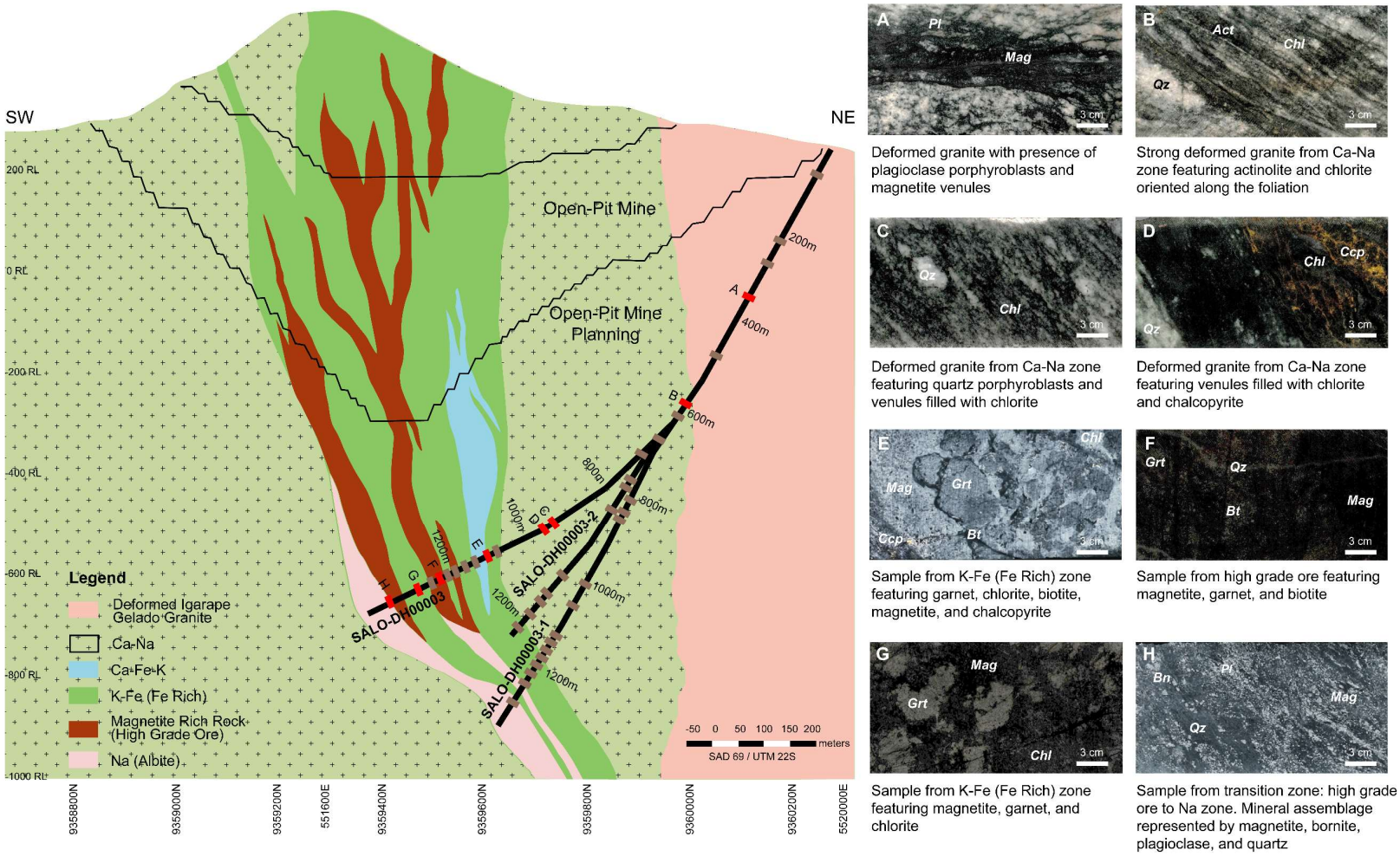


Figura 1. 4 - Seção geológica do depósito Salobo destacando alterações geológicas, furos de sondagem profundos (SALO-DH00003, 3-1 e 3-2) e os intervalos amostrados em campo. Inclui foto de amostras representativas das diferentes assembleias hidrotermais, com descrição e identificação mineralógica realizadas em escala macroscópica. Abreviações: Act – Actinolita, Bn – Bornita, Bt – Biotita, Chl – Clorita, Ccp – Calcopirita, Grt – Granada, Mag – Magnetita, Pl – Plagioclásio e Qz – Quartzo.

1.3.2. Geofísica Aérea

Como mencionado acima, a área de estudo é recoberta por diversos tipos de aerolevantamento da base pública do Serviço Geológico do Brasil (SGB), disponível no endereço: https://geosgb.sgb.gov.br/home.html. Além disso, dados de levantamentos aerogeofísicos de propriedade da Vale S.A, foram cedidos, e utilizados para o desenvolvimento desta tese. Os dados públicos do SGB integram o Projeto Rio Maria (código 1129), pertencente à série 1000 dos aerolevantamentos do Brasil, iniciativas conduzidas pelo antigo Departamento Nacional de Produção Mineral (DNPM) em parceria com o Serviço Geológico do Brasil. Esses levantamentos incluem dados magnetométricos e gamaespectrométricos. As informações referentes a cada aerolevantamento foram sumarizadas na Tabela 1.1.

Tabela 1. 1 - Parâmetros gerais da aquisição de dados dos aerolevantamentos realizados pelo Serviço Geológico do Brasil (SGB) que recobrem o depósito Salobo.

GEOLOGICAL SURVEY OF BRAZIL DATA (SGB)

Project Name and Number	***Rio Maria (1129)***	***Rio Maria (1129)***
Method	Magnetic	Gamma-Ray Spectrometric
Date	2015	2015
Line Direction	N-S	N-S
Spacing Line	500 m	500 m
Tie Line Direction	E-W	E-W
Tie Line Spacing	10 km	10 km
Sampling Rate	0.1 s	1 s
Nominal Terrain Clearance	100 m	100 m
Acquisition System	Aeromaster – VN2001	Aeromaster – VN2001
Equipment Model	Mobile: Scintrex CS-3 Base Station: GSM-19	Gamma: Pico Envirotec – GRS 410

Os dados cedidos pela Vale S.A. são magnetométricos, gradiometria gravimétrica, gamaespectrométricos e eletromagnéticos no domínio do tempo. As informações referentes a cada aerolevantamento estão sumarizadas na Tabela 1.2. Abaixo, destacam-se alguns detalhes dos sistemas eletromagnético no domínio do tempo (TDEM) e o de aerogradiometria da gravidade.

O QUESTEM 450 é um sistema eletromagnético no domínio do tempo (TDEM) e opera em uma frequência de 25 Hz. O transmissor tem forma de onda meio seno, uma largura de pulso "*on time*" de 4 ms e "*off time*" de 16 ms. As bobinas receptoras são triaxiais (3 bobinas ortogonais X, Y e Z), posicionadas em um "*bird*" deslocado a uma altura de 60 m sobre o terreno. Esta faz aquisição de 256 amostras dos canais EM por transiente, em um intervalo de 200 ms e registra 18 canais. A distância transmissor-receptor é de 90 m e todo o sistema ainda conta com um monitor de linhas de transmissão de 60 Hz.

Os dados de aerogradiometria da gravidade foram adquiridos com um HeliFALCON AGG (*Airborne Gravity Gradiometer*) e fazem parte da atual tecnologia de gradiometria de gravidade que difere dos dados convencionais de gravidade de alta resolução. Os levantamentos gravimétricos convencionais medem a componente vertical do campo da gravidade (g_D) e carregam um único sensor. Em levantamentos aéreos onde já existe a aceleração da aeronave é necessário a redução do erro a partir de filtragens, o que resulta na perda de informações de comprimento de onda mais curto. Se as filtragens forem feitas de maneira reduzida para preservar comprimentos de onda curtos, observa-se um erro maior. Em contrapartida a gradiometria gravimétrica usa uma medição diferencial para remover a aceleração da aeronave e fornece dados com resolução espacial e sensibilidade comparáveis aos dados gravimétricos terrestres (Dransfield, 2010; Carlos, 2013).

Uma das principais diferenças entre o método convencional e o gradiométrico está na largura do comprimento de onda, onde quanto menor a largura de comprimento de onda, menor será a probabilidade de retenção de sinais gerados por feições geológicas rasas a intermediárias. No caso o sistema gradiométrico possui menor largura do comprimento de onda do que o método convencional (Carlos, 2013). O sistema HeliFALCON é um sistema de alta precisão que opera em uma plataforma rotativa que mede o gradiente do campo gravitacional e apropriado para a aquisição em terrenos mais acidentados. Este sistema é composto por três *Gravity Gradient Instruments* (GGI's), cada um com dois pares de acelerômetros. O gradiômetro é instalado na cabine do helicóptero o mais próximo possível do avião e pode estar junto a demais equipamentos. Cada componente do gradiente de gravidade contém informações sobre a distribuição de densidade em subsuperfície (Carlos, 2013).

Tabela 1. 2 - Parâmetros gerais da aquisição de dados dos aerolevantamentos cedidos pela Vale S.A. que recobrem o depósito do Salobo. TDEM - Transiente Eletromagnético no Domínio Tempo e AGG-Gradiometria da Gravidade (*Airborne Gravity Gradiometer*).

AIRBORNE SURVEY VALE DATA			
Project Name	***FALCON***	***QUESTEM***	***Salobo-Jaca***
Method	Magnetic and AGG	TDEM	Gamma-Ray Spectrometric
Date	2012 and 2018, respectively	1997	1996
Line Direction	N 30º E	N 20º E	N 17º E
Spacing Line	200 m	250 m	250 m
Tie Line Direction	N 60º E	N 70º E	N 73º E
Tie Line Spacing	5 km	5 km	5 km
Sampling Rate	0.1 s	0.2 s	1 s
Nominal Terrain Clearance	60 m	110 m	60 m
Acquisition System	FADAS	GPS Picodas/NovAtel	RMS DGR-33
Equipment Model	Mobile: Scintrex CS-3 Base Station: Scintrex CS-3 Grav: HeliFALCON	QUESTEM 450	Exploranium GR-820

1.3.3. Geofísica Terrestre

Os levantamentos terrestres foram executados com objetivo de detalhar e auxiliar na interpretação da alteração hidrotermal e mineralizações. Os dados privados cedidos pela Vale S.A. são magnetométricos, gamaespectrométricos, TDEM e de DCIP, e foram executados sob a mesma malha de direção N 23º E. Todas as informações podem ser verificadas na Tabela 1.3. O levantamento magnético terrestre contou com dois GSM-19-*Overhauser da GEM System* (Figura 1.5), sendo um móvel para aquisição de dados e outro fixo para identificação de

possíveis tempestades magnéticas e determinar a variação diurna. O magnetômetro móvel realizou leituras a cada 20 m e o magnetômetro base realizou leituras a cada 5 s.

O levantamento eletromagnético terrestre (domínio do tempo) contou com *loop's* de 200 x 200 m, espaçamento entre linhas de 200 m e espaçamento de leituras de 100 m, configurando o arranjo *loop*-central (Dentith & Mudge, 2014). O transmissor utilizado foi um Geonics EM57 (Figura 1.5), com tensão de saída de 18 a 150 V, de ajuste contínuo, e corrente máxima de 25 Ampères. O receptor foi um Geonics PROTEM Receiver (Figura 1.5) com bobinas uniaxial para medidas sequenciais de três componentes – x, y, e z - ou triaxial para medidas simultâneas das três componentes, operando nas frequências base de 0.3, 0.75, 3, 7.5 e 30 Hz. No total foram feitas leituras em 750 loops para cobrir a área do Salobo.

Tabela 1. 3 - Parâmetros gerais da aquisição de dados dos levantamentos terrestres cedidos pela Vale S.A. que recobrem o depósito do Salobo. DCIP - Direct Current resistivity and Induced Polarization; TDEM - Transiente Eletromagnético no Domínio Tempo.

GROUND SURVEY VALE DATA

Method	Magnetic	Gamma-Ray Spectrometric	DCIP	TDEM
Date	2002	2002	2002	2003
Line Direction	N 23º E	N 23º E	N 23º E	N 23º E
Line Spacing	100 m	100 m	100 m	200 m
Station Spacing	20 m	20 m	80 m	100 m
Others Information	------	Integration Time: 60 s	Array DP-DP, n = 6	Loops 200 x 200 m
Total Kilometres	212 km	214 km	180 km	750 Loops

Para a aquisição dos dados gamaespectrométricos utilizou-se o equipamento modelo GR-320 enviSPEC da *Exploranium* (Figura 1.5), sempre posicionado a 50 centímetros de altura em relação à superfície do terreno, tempo de integração de 60s e leituras a cada 20 metros. Para o

levantamento de DCIP foi utilizado o arranjo dipolo-dipolo com espaçamento de eletrodos de 80 metros e 6 níveis de investigação, em uma configuração para o domínio do tempo, composto por um transmissor VIP 4000, alimentado por um grupo gerador Honda EP-6500S de 6,5 kVA e um receptor ELREC-6 (Figura 1.5) de 20 canais e fabricados pela IRIS Ltda.

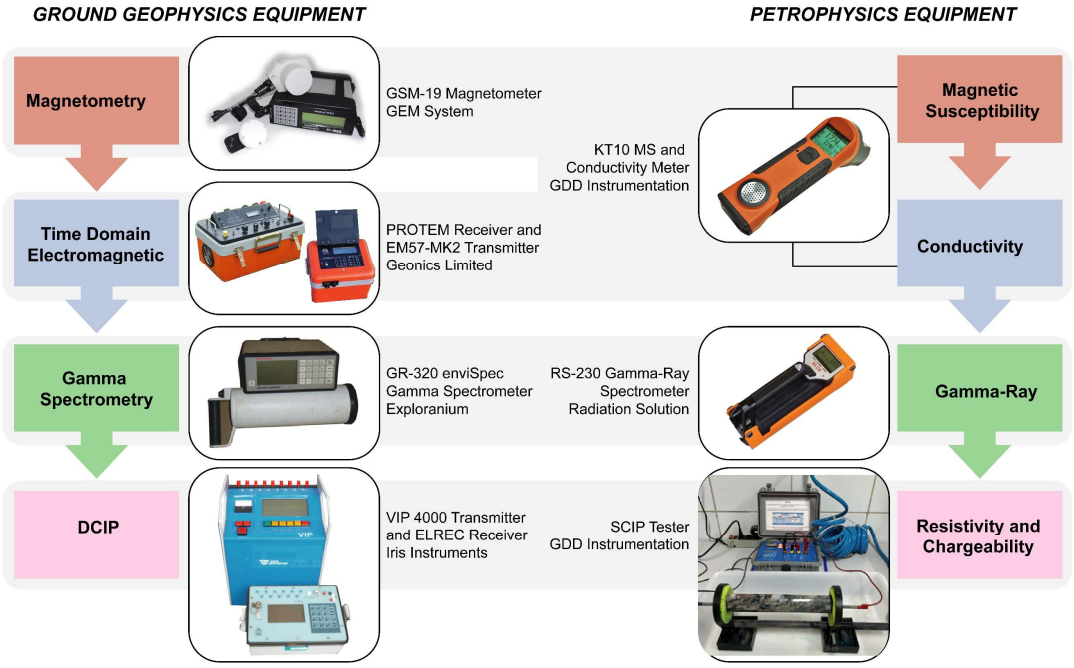


Figura 1. 5 – Equipamentos geofísicos utilizados para aquisição de dados terrestres magnetométricos, eletromagnéticos, gamaespectrométricos e de polarização induzida. Apresenta ainda os equipamentos utilizados para a aquisição de dados petrofísicos de susceptibilidade magnética, condutividade, gamaespectrometria, resistividade e cargabilidade.

1.3.4. Petrofísica

Foram selecionadas 84 amostras das zonas mineralizadas e suas encaixantes em furos de sondagem, do qual ¼ de alíquotas foram destinadas à coleta de dados petrofísicos, ½ destinado à obtenção de dados litogeoquímicos e o restante reservados para petrografia, mapeamento mineral (LIBS - *Laser-induced breakdown spectroscopy*, TIMA - *TESCAN Integrated Mineral Analyzer* e QEMSCAN - *Quantitative Evaluation of Minerals by Scanning Electron Microscopy*). Todas as amostras destinadas às análises petrofísicas foram fotografadas para registro tanto das orientações espaciais, quanto da eventual presença de mineralizações.

Para a aquisição de susceptibilidade magnética (SM) e condutividade foi utilizado um susceptibilímetro KT10 (Figura 1.5), sendo importante frisar que para os dados magnéticos o aparelho mede a SM da magnetização total. Cada amostra foi medida quatro vezes, onde a primeira medida não foi registrada e apenas utilizada como um valor de referência. Para maior acuracidade dos dados foi estabelecido que todas as medidas deveriam variar no máximo 10% do valor realizado na primeira leitura. Caso houvesse variação, o processo era reiniciado.

As medidas gamaespectrométricas representam a emissão de radiação gama natural dos principais radioelementos da natureza, sendo eles K, U e Th. Os dados foram coletados utilizando o gamaespectrômetro modelo RS-230 (Figura 1.5), da empresa *Radiation Solution*. Este equipamento é composto por um único módulo, com detector embutido, constituído por um cristal de iodeto de sódio ativado por tálio (NaI(Tl)), com volume de 124 cm³, acoplado a uma unidade fotomultiplicadora.

A aquisição foi realizada em local afastado de outros materiais radioativos pois estes podem afetar a medida feita pelo equipamento. Antes de iniciar a atividade o equipamento foi configurado para atuar em janelas de leituras próximas à 1,46 MeV, 1,76 MeV e 2,62 MeV para medição de K, U e Th, respectivamente. No início da aquisição, efetuou-se a estabilização automática do equipamento no período de cinco minutos até que as leituras dos elementos se apresentassem estáveis. O tempo de leitura escolhido foi de 120 s e em caso de valores muito anômalos e fora do background da área de estudo, este tempo foi aumentado para 180 s.

Os dados de resistividade e cargabilidade foram adquiridos com o uso do equipamento SCIP Tester (Figura 1.5), da empresa GDD Instrumentation Inc. Este é um instrumento portátil, amplamente utilizado na aquisição de dados de resistividade e polarização induzida (IP) no domínio do tempo, especialmente em testemunhos de sondagem. O equipamento realiza medições diretas desses parâmetros e exibe, em tempo real, as curvas de decaimento IP, sendo amplamente empregado em exploração mineral e pesquisas geofísicas, por contribuir significativamente no aprimoramento de modelos de inversão. Para garantir a confiabilidade das medições nesta pesquisa, as amostras tiveram suas laterais serradas para obtenção de extremidades planas e foram mantidas submersas em água por 20 dias antes da aquisição dos dados. Durante as medições, esponjas de celulose foram posicionadas nas extremidades das amostras, assegurando um melhor contato com os eletrodos do equipamento.

1.3.5. Litogeoquímica

Das 84 amostras coletadas, ½ de cada amostra foi enviada para a coleta de dados litogeoquímicos. As amostras foram preparadas no laboratório de preparação das amostras, controlado pela Gerência de Desenvolvimento de Projetos e Suporte Analítico da Vale S.A., localizado na infraestrutura de apoio à Mina N5, Carajás. As polpas foram posteriormente encaminhadas para o laboratório analítico comercial ALS *Chemex* (Canadá), onde as análises litogeoquímicas foram efetuadas seguindo os procedimentos analíticos do laboratório. A determinação dos elementos maiores foi realizada por Fluorescência de Raio-X (XRF) e a leitura de 48 elementos traço, incluindo os Elementos Terras Raras (ETR), elementos *High Field Strength* (HFSE) and *Large Ion Lithophile Elements* (LILE) foi realizada pelo método Espectrometria de Massas com Plasma Indutivamente Acoplado (ICP-MS). A descrição

completa dos métodos analíticos pode ser acessada ALS *Chemex Home Page* (www.alsglobal.com).

1.3.6. Quantitative Evaluation of Minerals by Scanning Electron Microscopy (QEMSCAN)

Foram selecionadas 56 amostras, das 84 amostras totais coletadas em campo, para a confecção de lâminas delgadas polidas. Foram selecionadas 20 lâminas, das 56 lâminas totais, para aquisição de dados QEMSCAN. A escolha dessas contra amostras foi feita com base nos valores petrofísicos anômalos. O QEMSCAN é um sistema automatizado de análise de imagem, composto por um microscópio eletrônico de varredura por emissão de campo, modelo FEI Quanta 650, que opera com fonte de tungstênio, modo alto vácuo, 25 kV de aceleração do feixe e 10 nA de corrente na amostra. Acoplado a esse equipamento, há ainda dois espectrômetros por dispersão de energia tipo SDD Bruker XFlash 5030 (Pirrie et al., 2004; Ayling et al., 2012).

O equipamento utiliza tanto a intensidade do sinal de elétrons retroespalhados quanto um sinal de raios X de dispersão de energia em cada ponto de medição. Os raios X são usados para atribuir identidades minerais a cada ponto de medição comparando o sinal de elétrons retroespalhados e os espectros de raios X com um programa de identificação de espécies minerais ou banco de dados (Ayling et al., 2012). O produto disponibilizado é um mapa mineral que permite o realce das mineralizações e alterações de uma determinada amostra. Integrou-se os resultados destes mapas minerais aos dados petrofísicos, com o objetivo de identificar o conduto (*footpath*) do sistema mineralizante do Salobo e assim ter suporte nas modelagens e vetorização.

1.3.7. TESCAN Integrated Mineral Analyzer (TIMA) e Laser-induced breakdown spectroscopy (LIBS)

Foram selecionadas 14 contra amostras, das 56 lâminas confeccionadas, para aquisição de dados TIMA e LIBS. Os estudos de caracterização mineralógica desempenham um papel importante na caracterização de depósitos minerais. Cada sistema mineral possui um conjunto único de minerais com diferentes composições químicas e propriedades físicas (Harmon et al., 2013; Mohamed et al., 2021). O TIMA é uma microscopia eletrônica de varredura (MEV) ou *Scanning Electron Microscopy* (SEM) utilizado para identificação de mineralogia mineral de forma automatizada e disponibiliza associações e análise de tamanho de grão (Paradis et al., 2021). A indústria mineral tem utilizado essa técnica para pesquisa geológica e otimização de processos de metalurgia devido ao mapeamento de alta velocidade; visualização e quantificação de propriedades petrológicas como alteração, zonas de contato, fraturas e estruturas de deformação, recristalização; análise de pesquisa modal; mapeamento mineral de alta resolução,

mapeamento de pontos, espectrometria de pontos e mapeamento de linhas; medições quantitativas de espectroscopia de energia dispersiva de raios X (EDS) (Rifai et al., 2020).

O instrumento TIMA utilizado para esta tese é composto por um canhão de emissão por campo (FEG - *Field Emission Gun*), quatro SDD da EDAX e um *autoloader* que comporta até 100 amostras. As análises foram realizadas pela empresa AXT na Austrália. Este equipamento exige que a superfície da amostra seja perfeitamente plana para a análise automatizada. A preparação da amostra envolve corte, polimento e revestimento em carbono. A superfície foi polida utilizando LaboForce-100, equipamento de polimento semiautomático da Struers. Uma fina camada (20 nm) de carbono foi aplicada na superfície da amostra usando o revestidor de carbono Q150T ES da Quorum, a fim de otimizar a precisão, durabilidade e qualidade da análise mineral, além de proteger a amostra e o instrumento de análise. O tempo total necessário para preparar uma amostra para a análise TIMA foi de cerca de 1 hora.

A tecnologia LIBS, desenvolvida pela ELEMISSION Inc, vem sendo implementada em diversas áreas da exploração mineral, desde área mais avançada de geometalurgia para otimização no processo de extração de elementos mais escassos do grupo da platina (Rifai et al., 2020) por exemplo, até estudos mais específicos de mapeamentos multielementares de alta resolução de estruturas geológicas que apresentaram altos níveis de detalhe e complexidade na distribuição dos elementos e revelaram correlações entre elementos que permitiram inferir o conteúdo mineralógico de amostras(Rifai et al., 2018).

Harmon et al. (2013) revisou a maior parte das publicações relacionadas à geoquímica, e mostrou que o LIBS já foi muito aplicado na análise de amostras de minério, com foco na análise quantitativa de elementos menores e maiores do minério. Em alguns casos era realizada a identificação e classificação para distinguir minerais valiosos de gangas.

A espectrometria de emissão óptica por plasma induzido por laser (LIBS), utiliza um pulso de curta duração de alta energia gerado por um laser focalizado na amostra, a fim de obter a excitação e vaporização da mesma em seus constituintes (átomos, íons e/ou moléculas) (Hahn and Omenetto, 2010). O laser incidente na amostra provoca a quebra da estrutura atômica ou molecular por aquecimento causando vaporização de uma pequena parte do material que pode conter átomos, íons e/ou moléculas constituintes da amostra. Tais espécies vaporizadas (excitadas), após certo tempo, retornam para seu estado de menor energia (estado fundamental), emitindo assim uma radiação eletromagnética característica da transição do nível de energia. Os comprimentos de onda característicos (λ's) da radiação emitida serão coletados, analisados e relacionados à presença de analitos na amostra. E a intensidade do sinal (altura ou área do pico) coletado é proporcional à concentração do analito (Hahn and Omenetto, 2011).

A análise LIBS realizada com o instrumento CORIOSITY-G3 não exigiu uma preparação avançada de amostra, apenas uma rápida limpeza para remover o revestimento de carbono aplicado para análise TIMA. Este revestimento de carbono deve ser removido pois pode induzir

um viés nas medições LIBS ao detectar estes vestígios e garantir que os espectros LIBS estejam relacionados apenas aos minerais naturalmente presentes nas rochas.

2. Geophysical Signature of the Salobo IOCG Deposit and Implications for Mineral Exploration

Moriá Caroline de Araújo[1], Adalene Moreira Silva[1], Catarina Labouré Bemfica Toledo[1] and Daniel Shkromada de Oliveira[1]

[1]University of Brasília, Geosciences Institute, Brasília, DF, Brazil
moria_araujo@hotmail.com, adalene@unb.br, catarinatoledo@unb.br, daniel.oliveira@fundamentogeofisica.com.br

Submission to ***Journal of Applied Geophysics*** date: 08/23/2024
Decision on submission date: 10/30/2024
Status of decision: ***Approved following minor revision***
Status: *Revisions Being Processed*

ABSTRACT

Geophysics is a prerequisite for effective mineral exploration projects. Its significance has increased recently with technological advancements, deeper exploration and geophysical data is now a crucial tool for reducing drilling risks. Salobo, a world-class IOCG (Iron Oxide Copper-Gold) deposit (1088.9 Mt at 0.62% Cu and 0.35 g/t Au) in the Carajás Mineral Province, is located in secondary structures associated with the first-order Cinzento shear zone. Due to their high sulphide and iron oxide content, IOCG deposits often make excellent geophysical targets. However, the IOCG classification is broad and encompasses deposits with significantly different characteristics. These differences include petrophysical characteristics which directly impact their geophysical signatures and require specific exploration models. Multiscale magnetic, gravity gradiometry, gamma spectrometric, TDEM (Time-Domain Electromagnetics), and DCIP (Direct Current resistivity and Induced Polarization) data collected at Salobo were used to investigate alteration zones and mineralization, highlighting the importance of an integrated approach in geophysical exploration. Priority guidelines for IOCG geophysical exploration were created considering Salobo's geophysical footprint. These can be used to optimize drilling campaigns in geological contexts similar to Salobo's.

Keywords: Inversion, Integration, Multisource, Multiscale and Mineral exploration

2.1. Introduction

Geophysics is widely used to assist exploration programs in identifying alteration zones and mapping the geometry of mineral deposits. Its importance in modern mineral exploration programs has risen, especially due to recent technological advances, a growing number of deeper targets, and the ever-increasing amount of geophysical data available to exploration teams worldwide. Reducing the risk of drilling using geophysical data is now often not an option, but a requirement.

Located in the Carajás Mineral Province, a globally renowned polymetallic province, Salobo is the second biggest IOCG deposit in the world. It contains reserves of 1088.9 Mt at 0.62% Cu and 0.35 g/t Au (VALE, 2023) and stands out as one of the few known Archean IOCG deposits (Hitzman, 2000; Groves et al., 2009; Xavier et al., 2010). Mineralization is found within secondary structures associated with the first-order Cinzento shear zone, formed around 2.55 Ga. The shear zone marks the contact between the Neoarchean volcano-sedimentary rocks of the Itacaiúnas Supergroup, and the Igarapé Gelado metagranite. The ore is primarily composed of bornite, chalcocite, magnetite, and smaller amounts of chalcopyrite and gold, with significant contents of Co, Ni, As, Ag, Mo, and REE (Rare Earth Elements) (Melo, 2014; Melo et al., 2019, Costa et al., 2016).

IOCG deposits are usually good geophysical targets given their high sulphide and iron oxide concentrations. Several authors have described the geophysical signatures of IOCG deposits: Olympic Dam (Esdale et al., 2003), Prominent Hill (Freeman and Hart, 2003), Carrapateena (Vella and Cawood, 2012), Candelaria (Austin et al., 2014), Santo Domingo (Moul & Witherly, 2017) amongst others. However, the IOCG definition is broad and encompasses many significantly different deposits. These differences often have a direct impact on their petrophysical characteristics and geophysical signature. Austin et al. (2017) shows how these changes can affect the geophysical signature of IOCG deposits in Australia. Leão-Santos (2015) and Melo et al. (2014, 2015, 2017) focused on the geophysics of Furnas and Cristalino, two IOCG deposits in the Carajás Mineral Province. Despite being in the same province and classified as IOCG, their geophysical signatures are clearly different. Therefore, geophysical exploration models to be used for each of those must be different. It is crucial to understand the signatures of mineral deposits and the processes that control them to properly design efficient exploration programs.

Geophysics has been systematically applied in the search for mineral deposits in the Carajás Mineral Province. Magnetics, electromagnetics, and induced polarization (IP) are the most commonly used geophysical methods (Melo et al., 2014, 2015, 2017; Aisengart et al., 2019; Melo & Li, 2019; Leão-Santos et al., 2022). This paper aims to describe Salobo's geophysical footprint by separately evaluating and integrating multisource and multiscale geophysical data to enhance the effectiveness of each method in identifying IOCG (Iron Oxide Copper-Gold). Thus, this paper provides an overview of key geophysical signatures and proposes a priority guideline to be followed in these target types.

2.2. Geological Context

Carajás Mineral Province is located in the southeastern portion of the Amazonian Craton, one of the main Precambrian geotectonic units in South America. This craton spans approximately 5,600,000 km², is comprised of the Guiana and Central Brazil shields, and is

overlain by the Amazonas and Solimões sedimentary basins (Santos et al., 2000; Teixeira et al., 2019; Quadros, 2020) (Figure 2.1A).

The evolution of the Amazonian Craton is marked by successive episodes of crustal accretion during the Paleoproterozoic and Mesoproterozoic, and subduction of Archean crustal blocks (Vasquez & Rosa-Costa, 2008; Duncan et al., 2010). Santos et al. (2000) divided the craton into seven tectonic or geochronological provinces: Carajás (3000 – 2500 Ma), Transamazonian (or Maroni-Itacaiunas) (2260 – 1990 Ma), Tapajós – Parima (2030 – 1860 Ma), Amazônia – Central (1900 – 1860 Ma), Rondônia – Juruena (1850 – 1540 Ma), Rio Negro (1820 – 1520 Ma), and Sunsás (1450 – 1000 Ma) (Figure 2.1A).

The Carajás Province was tectonically formed and stabilized during the Archean and represents the oldest crustal nucleus of the Amazonian Craton. It is divided into two distinct tectonic segments referred to as: the Rio Maria Domain to the south and the Carajás Domain to the north (Vasquez & Rosa-Costa, 2008). The frequently discussed yet relatively understudied zone known as the Transitional Domain separates the Rio Maria and Carajás domains (Dall'Agnol et al., 2006, 2013; Feio et al., 2013). The Rio Maria Domain is characterized by the amalgamation of granite-greenstone terrains in the Mesoarchean, between 3.05 Ga and 2.82 Ga (Dall'Agnol et al., 2006; Althoff et al., 2014).

The Carajás Domain is predominantly comprised of Neoarchean to Paleoproterozoic volcano-sedimentary sequences, deposited over the Mesoarchean Xingu Complex (3066 ± 6 Ma), comprised of TTG (Tonalite-Trondhjemite-Granodiorite) gneisses and migmatites (Delinardo da Silva, 2014), and mafic granulites. The Neoarchean volcano-sedimentary sequences are part of the Itacaiúnas Supergroup (2.76 - 2.74 Ga), subdivided into the Igarapé-Salobo, Igarapé Pojuca, Grão Pará, and Igarapé Bahia groups (Wirth et al., 1986; DOCEGEO, 1988; Machado et al., 1991). The Igarapé Salobo Group includes gneisses, amphibolites, quartzites, metagreywackes, and iron formations. The Igarapé Pojuca Group is composed of metabasalts, schists, and rocks with cordierite and anthophyllite. The Grão Pará Group (~2.76 Ga) (Gibbs et al., 1986; Machado et al., 1991; Trendall et al., 1998; Martins et al., 2017) consists of the Parauapebas Formation, strictly composed of mafic rocks, followed by a sequence of jaspilites from the Carajás Formation (Lindenmayer et al., 2001; Macambira, 2003) and the upper metavolcanic sequence of the Igarapé Bahia Group (Tallarico et al., 2005). These sequences are overlain by sedimentary rocks of the Serra Azul and Águas Claras Formations (2.68 - 2.06 Ga) (Araújo Filho et al., 2020; Rossignol et al., 2020).

Layered mafic-ultramafic complexes intrude rocks of the Xingu Complex and the Grão Pará Group (Ferreira Filho et al., 2007). These intrusions have Neoarchean ages (Machado et al., 1991; Lafon et al., 2000) and represent a significant coeval magmatic event along with the extensive basaltic volcanism of the Grão Pará Group (Machado et al., 1991; Ferreira Filho et al., 2007). Three episodes of granitic magmatism were identified within the Carajás Domain: 1)

Neoarchean magmatism (~2.76-2.73 Ga) marked by subalkaline type-A granitic bodies represented by the Plaquê and Planalto Suites, Estrela Complex, and Serra do Rabo granites, intruding into the Grão Pará Group (Dall'Agnol et al., 2013; Feio et al., 2013); 2) Younger intrusions (~2.56 Ga), such as the peralkaline to metaluminous Old Salobo and Itacaiúnas granites (Machado et al., 1991), present along the Northern Copper Belt; 3) Paleoproterozoic anorogenic granitic plutons (~1.88 Ga), representing the latest magmatic episode, including the Central Carajás Granite and the Young Salobo, which belong to an extensive anorogenic magmatic province spread throughout the Amazonian Craton (Dall'Agnol et al., 2006).

NE-SW shortening and progressive transtensional and transpressional deformation along E-W- and ESE-NNW-striking shear zones led to the inversion of the basin where the Itacaiúnas Supergroup was formed. These regional shear zones were reactivated several times since the Mesoarchean (Melo et al 2015; Pinheiro & Holdsworth, 1997; Tavares et al., 2017 and 2021). The Cinzento shear zone is the northernmost of the three main regional shear zones in the Carajás and controls the location and shape of most of the deposits in the northern part of the province, such as Paulo Afonso, Furnas, and Salobo.

2.2.1. Salobo Deposit

The deposit is primarily hosted in deformed granites of the Igarapé Gelado granite (2763 ± 4.4 Ma) (Melo, 2018) and in Mesoarchean gneisses of the Xingu Complex (2950±25 – 2857 ± 6.7 Ma) (Melo, 2018), occurring as imbricated slices within the granites (Melo, 2014; Melo et al., 2019) (Figure 2.1B). In the southern part of the deposit lie sheared quartzites, remnants of volcano-sedimentary sequences from the Itacaiúnas Supergroup. Detrital zircons suggest U-Pb ages of approximately 3.1-3.0, 2.95, 2.86, and 2.74 Ga (Melo, 2018) (Figure 2.1B). These rocks are highly deformed and hydrothermally altered, developing sub-vertical mylonitic foliation associated with the Itacaiúnas shear zone (ca. 2.7 Ga) and Cinzento shear zone (2.555 ± 4 Ma) (Machado et al., 1991).

The host rocks of the Salobo Deposit are intruded by the A-type Old Salobo Granite (Lindenmayer, 2003), with a crystallization age of 2573 ± 2 Ma (Machado et al., 1991), and the Paleoproterozoic anorogenic and alkaline to metaluminous Young Salobo Granite (1.880 ± 80 Ma) (Cordani, 1981; Lindenmayer, 1990). Diabase dikes cut across the mineralization and its host rocks (Lindenmayer, 1990; Machado et al., 1991) (Figure 2.1C).

Ductile deformation along the Itacaiúnas shear zone resulted in widespread, subvertical NW-SE foliation. Transtensive deformation along the Cinzento shear zone system also reactivated pre-existing structures, forming a subparallel brittle-ductile shear zone in the NNE portion and a brittle shear zone in the south. The brittle-ductile shear zone deformation resulted in lenticular-shaped ore shoots, with a correlation between copper mineralization and magnetite content (Burns et al., 2019; Melo et al., 2019).

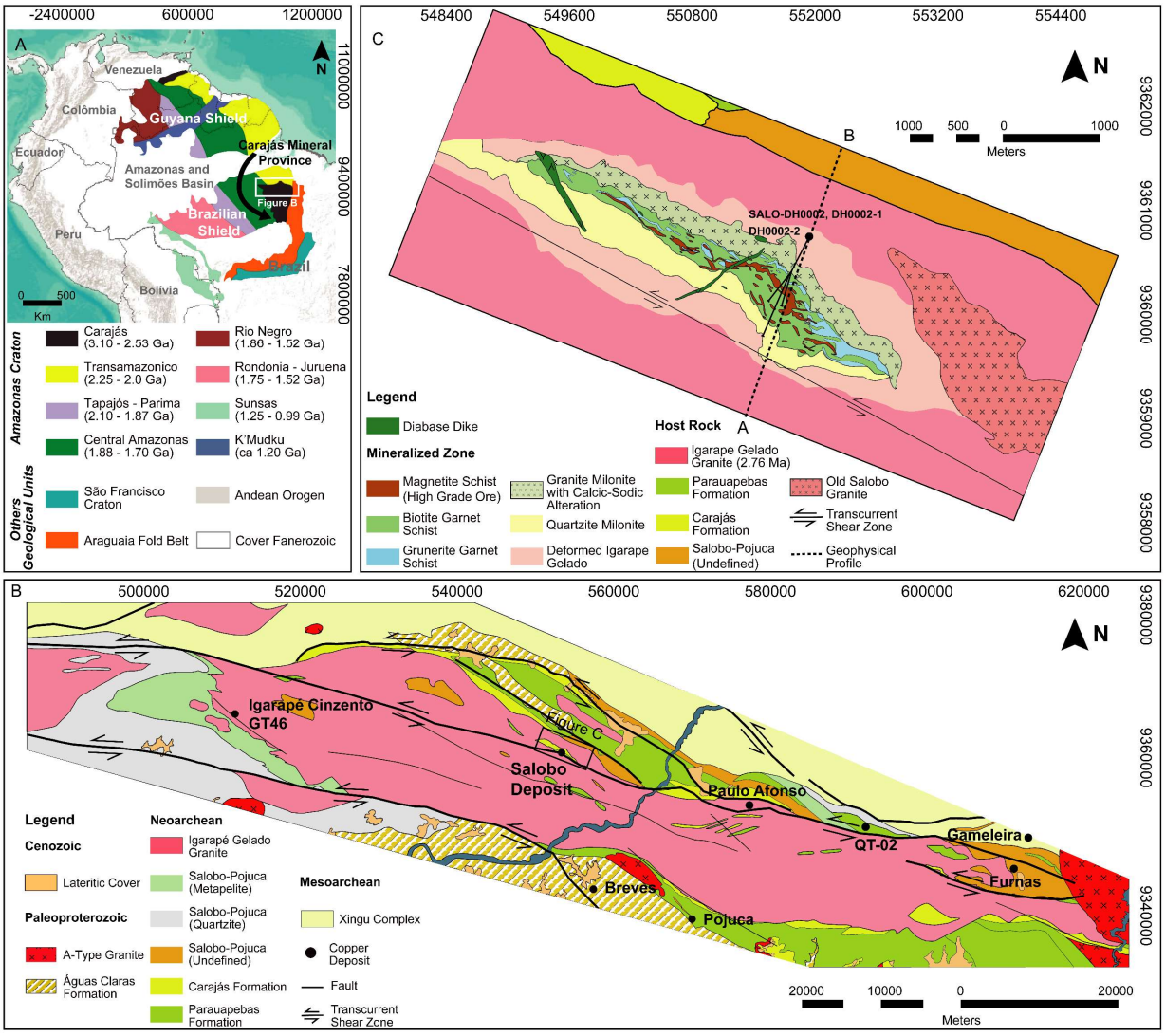


Figure 2. 1 – A) Tectonic compartmentalization of the Amazonian Craton in Brazilian territory and the location of the Carajás Mineral Province (Modified from Santos et al., 2000). B) Geological map of the northern portion of the Carajás Mineral Province, known as the Northern Copper Belt, encompassing the Cinzento Lineament. The location of the Salobo Deposit is highlighted (modified from Vasquez & Rosa-Costa, 2008). C) Geological map of the Salobo deposit showing the main geological units, alteration zones, and mineralized zone.

The distal parts of the deposit are dominated by high-temperature calcic-sodic alteration, with hastingsite and actinolite as main minerals, and silicification (Figures 2.1C and 2.2). The primary hydrothermal alteration phase involves a significant iron enrichment, with almandine-grunerite-magnetite as main minerals, and the formation of tourmaline. The proximal alteration zone of the deposit is characterized by intense potassic-ferric alteration, with the development of biotite and the deposition of Cu sulphides and Au (Melo, 2014, 2018) (Figures 2.1C and 2.2). A low-temperature hydrothermal assemblage, composed of stilpnomelane-greenalite-chamosite and Fe-pyrosmalite, overprints the higher-temperature assemblage (Melo et al, 2016). The

deposit also exhibits late-stage potassic and propylitic hydrothermal alteration, rich in hematite, overlaying the typical IOCG hydrothermal assemblage (Melo et al, 2016) (Figures 2.1C and 2.2).

The orebodies exhibit elongated and lenticular shapes in the NW-SE direction, parallel to the sub-vertical mylonitic foliation. The high-grade ore is primarily comprised of intergrown bornite (≤60%) and chalcocite (≤40%) (Requia et al., 2003). Chalcopyrite occurs in smaller proportions, usually intergrown with other ore minerals or associated with late massive sulphide veins that intersect bornite and chalcocite-rich zones (Lindenmayer & Teixeira, 1999; Melo et al, 2016). Covellite, digenite, and native copper also occur in fractures, grain boundaries, or as inclusions in other ore minerals. Molybdenite, uraninite, ilmenite, and apatite are frequently observed in the mineralized zones (Requia et al., 2003; Melo et al, 2016). The gold appears as inclusions in bornite, chalcocite, chalcopyrite, and magnetite, and is strongly associated with arsenic-rich minerals such as safflorite and cobaltite (Melo et al, 2016; Melo et al., 2019). Re-Os ages in molybdenite from rocks in the mineralized zones indicate an age of 2576 ± 8 Ma (Requia et al., 2003).

2.3. Materials and Methods

The mineral systems approach emphasizes understanding the large-scale geological processes that lead to mineral deposit formation, as well as the overall geological system. Geophysics and petrophysics have made mineral exploration more targeted and efficient, considering the broader geological context, allowing the prioritization of areas with higher potential and better target generation. Geophysics at different scales is required to properly understand a mineral deposit in terms of its mineral system. The regional scale provides a broad understanding of large and deep geological features such as first-order structures and intrusives, while deposit scale provides insights into the controls of mineralization. Multisource and multiscale analyses can significantly improve the efficiency, cost-effectiveness, and success rate of exploration mineral projects.

Salobo's geophysical footprint was analyzed on various scales to provide a more detailed and comprehensive understanding of its signature. At the regional scale, magnetic and radiometric data collected and made available by the Geological Survey of Brazil (SGB) were used at a 1:50,000 scale (Figure 2.3). The district scale analysis was conducted using higher resolution airborne gravity gradiometry, EM (electromagnetic), magnetic, and radiometric data provided by Vale S.A. at a 1:25,000 scale (Figure 2.3). The deposit scale analysis was conducted at 1:10,000 scale using ground magnetic, gamma-ray spectrometric, fixed-loop time domain EM (FLEM), and DCIP data, also provided by Vale S.A. (Figure 2.3). All survey parameters and other information at investigation scales are detailed in Appendix A, B, and C. All the analyses were limited to Salobo's tenement as part of the agreement to use confidential data.

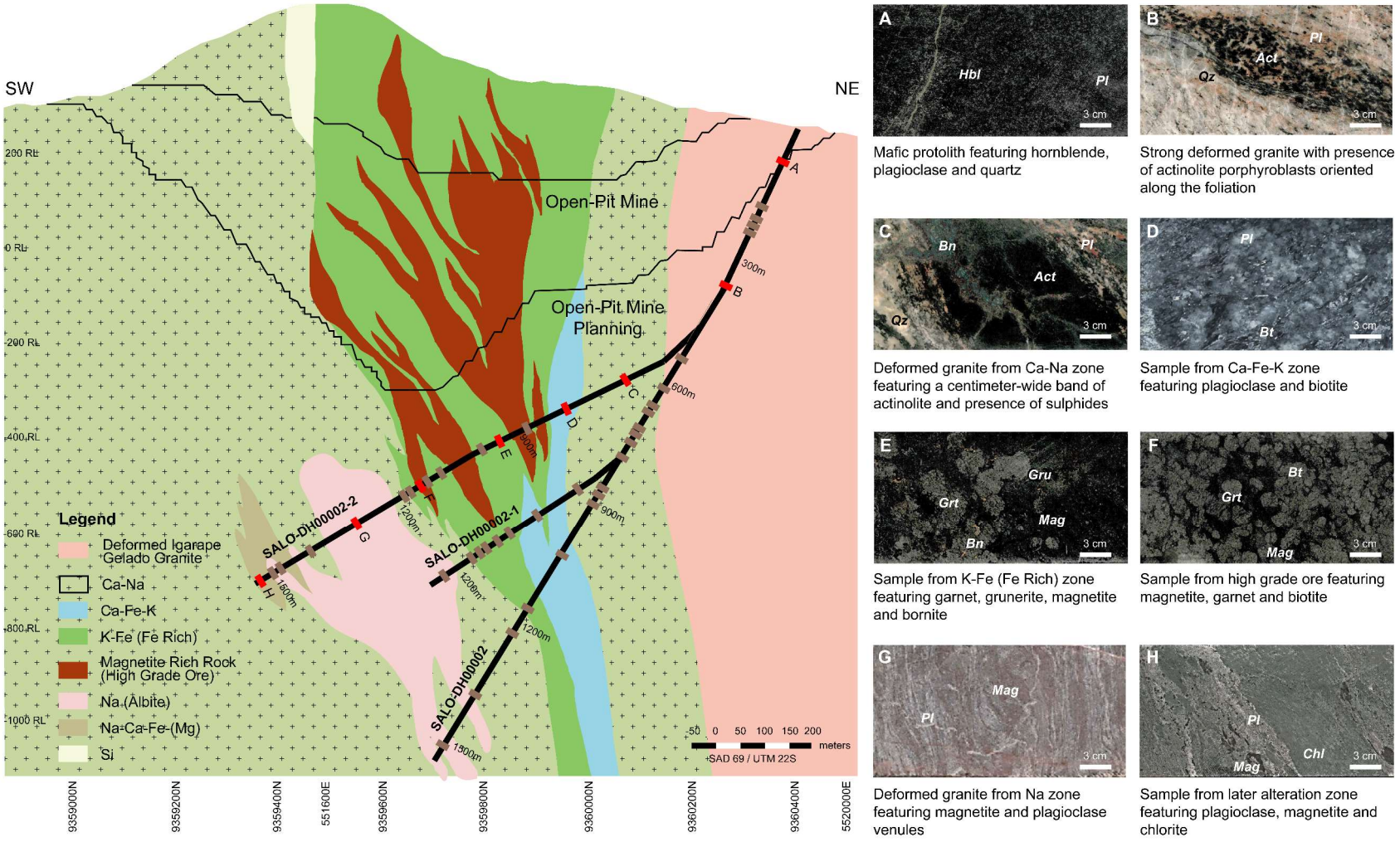


Figure 2. 2 - Illustrative section of the alteration zoning and photos of samples collected along drill hole SALO-DH00002-2. Description and mineralogical identification performed at the macroscopic scale. *Abbreviations: Act – Actinolite, Bn – Bornite, Bt – Biotite, Chl – Chlorite, Grt – Garnet, Gru – Grunerite, Mag – Magnetite, Pl – Plagioclase, and Qz – Quartz*.

The geophysical data processing was divided into four stages: preprocessing (e.g., diurnal correction and noise filtering), processing (e.g., generation of transformed maps, such as Reduction to the Pole), and inversion. The processing was done in Oasis Montaj version 2022.2 and integration was done in Geoscience Analyst Pro Geophysics 4.0. All historical data was re-processed using industry standards to ensure that only good-quality products were used to characterize the deposit. Oasis Montaj's VOXI Earth Modelling was used to invert magnetic, gravity gradiometry, and DCIP data. Magnetic Vector Inversion (MVI) was used for magnetic data.

In the time-domain electromagnetic data analysis, the SPIKER algorithm was employed (Smith and Buselli, 1991; Smith et al., 1994; Asten, M. W.; 1998; Macnae, J. et. al., 1998). This algorithm is a processing technique that links each apparent conductivity measurement with a specific depth. In cases where actual conductivity changes rapidly with depth, the apparent conductivity curves tend to vary more gradually, producing a smoothed version. To counteract this smoothing effect, the SPIKER algorithm applies an approximate inverse operator to the apparent conductivity curves, resulting in a sharper and more accurate representation of subsurface conductivity. The enhanced products of this algorithm are presented as conductivity sections or resistivity sections recovered by the algorithm, providing improved resolution for subsurface analysis.

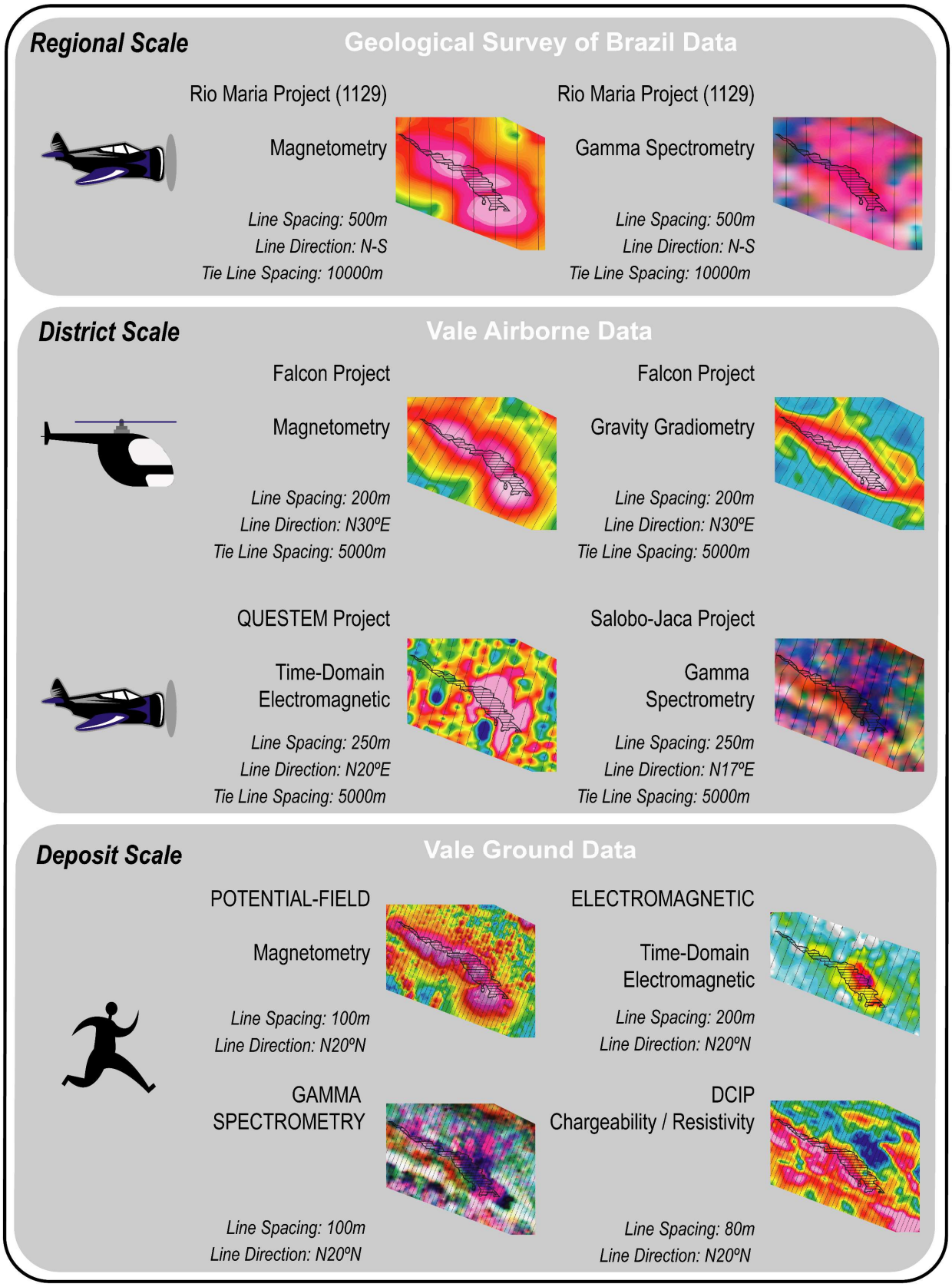


Figure 2. 3 – Databases used for the analysis and main acquisition parameters grouped by investigation scale. Each map shows the survey lines (black lines), a basic product of each survey, and the orebodies projected to surface (black polygon).

2.4. Results

Data from every geophysical survey done in the area shows an anomalous zone consistent with the projection of the orebodies to the surface (Figure 2.3). A NE-SW-oriented profile (AB profile), that cuts through the thicker, central part of the mineralized zone, was used to compare the deposit's signatures in various geophysical datasets and for the characterization of the geophysical footprint at regional, district, and deposit scales. A slice of a 3D model for the magnetite schist (XMT) unit is presented in the results as a reference (Figure 2.4A). XMT represents the magnetite alteration zone at Salobo, which hosts the best Cu-Au grades and can be used as a proxy for mineralization. The available data and models are presented first, followed by an interpretation and integration of the results.

2.4.1. Regional Scale Footprint

Magnetic data reduced to the Equator (RTE) shows a 2600 nT anomaly throughout the entire extension of the deposit (Figure 2.4C). The dipolar nature of the Salobo's RTE anomaly and the fact that the deposit is nearly vertical indicates that a significant remanent magnetization component is present (Figure 2.4F). Total gradient data (TG; analytical signal amplitude) shows that it is approximately 1800 meters long with a gradient value of 1.53 nT/m (Figures 2.4D and 2.4F). A section through the MVI model highlights two laterally constrained and seemingly homogeneous magnetic zones and a less magnetic zone to the North (Figure 2.4E).

K concentration data exhibits anomalies of up to 0.69% near the mineralized body and minimal values at the border of the deposit (Figure 2.4G). The eU channel, ranging between 0.7 and 7 ppm, does not show an obvious anomaly (Figure 2.4H). The eTh channel (Figure 2.4I) shows an opposite signature to %K, with negative anomalies over the mineralized body and positive anomalies at XMT body border. The eU and %K profiles (Figure 2.4J) indicate small lateral variation. However, the eTh profile displays a noticeable decrease in values when entering the mineralized zone marked as XMT.

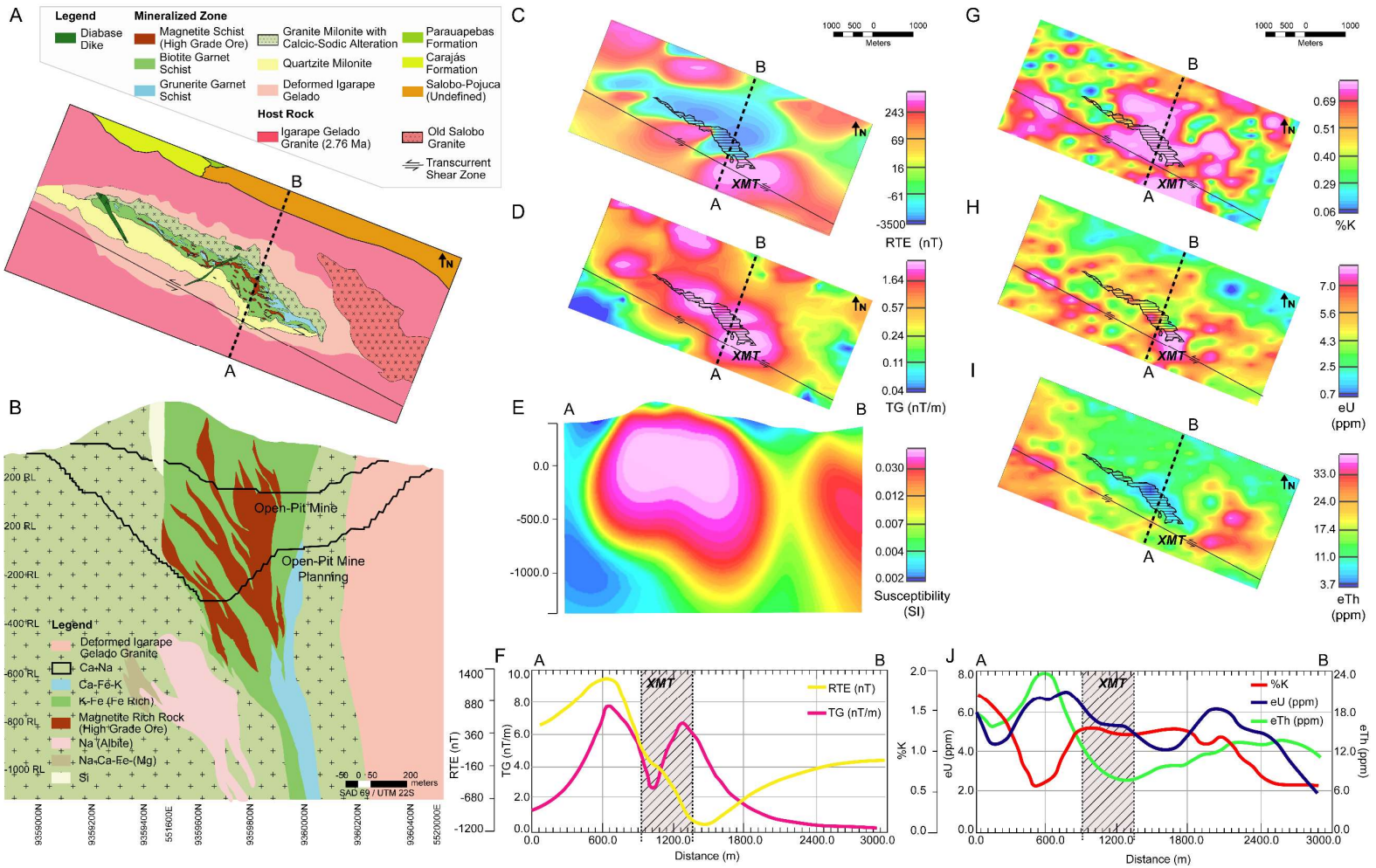


Figure 2. 4 – Regional scale geophysical footprint. All profiles and sections were made along the AB profile, which is shown in the maps. The regional Cinzento shear zone is shown in the maps. A) Location of the AB profile crossing the thickest portion of Salobo; B) Section through the alteration zones; C) Magnetic data reduced to Equator (RTE); D) Total Gradient (TG) magnetic data; E) Section through the magnetic inversion model; F) RTE and TG profiles; G) Potassium concentration; H) Uranium concentration; I) Thorium concentration; J) K, Th, and U profiles. XMT - Magnetite Schist.

2.4.2. District Scale Footprint

Higher- resolution airborne magnetic data also shows anomalies directly associated with the deposit with amplitudes of up to 2100 nT. Three main anomalies stand out along the magnetic trend (Figure 2.5A). TG (Total Gradient) data (Figure 2.5B) shows a more intense, narrow, and discrete anomaly when compared to the regional data (Figure 2.4D), with a gradient value of 7.2 nT/m and an extension of approximately 1300 meters. The MVI model for the area shows three main magnetic zones that relate to more structurally complex zones within the deposit where Fe alteration is strongest (Figure 2.5C). Figure 2.5C also presents the MVI susceptibility model results as vector cones, which provide a visual indication of the modelled direction of magnetization. The size and color of each cone are determined by the scale colour of MVI susceptibility. The 0.09 SI isosurface matches the extent and geometry of the deposit (Figure 2.5D).

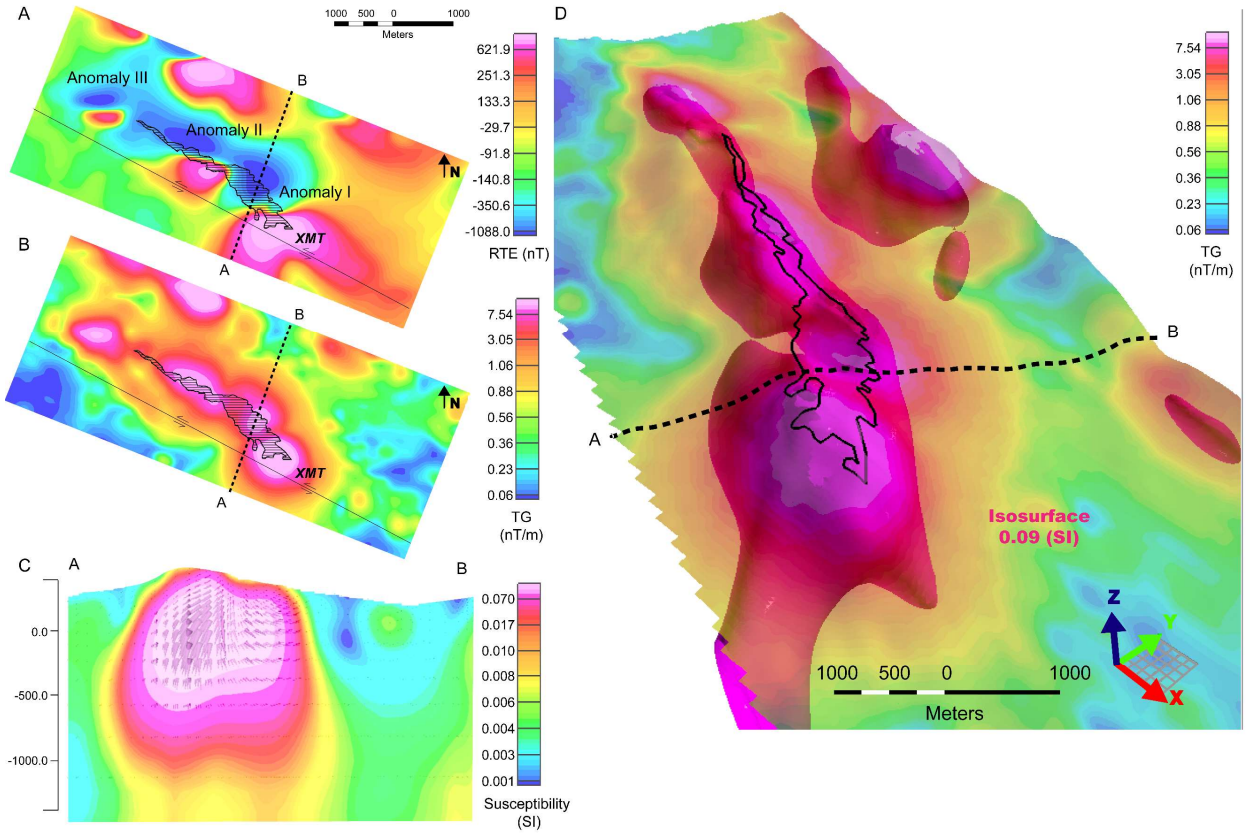


Figure 2. 5 – Magnetic footprint at the district scale. The Cinzento Shear zone is shown in both maps. A) Reduce to Equator (RTE) map showing the three main anomalies along the magnetic trend. B) Total Gradient (TG) data. C) Section extracted from the inversion along AB profile. MVI model magnetization shown as vector cones coloured by susceptibility. D) 3D visualization of Salobo magnetic signature on surface, and a 0.09 SI amplitude isosurface extracted from the inversion model. XMT - Magnetite Schist.

Salobo is associated with a discrete and strong vertical gravity and vertical gravity gradient anomaly (Falcon g_D and G_{DD} component) with an amplitude of 6.5 mGal and 180 E, respectively (Figures 2.6A and 2.6B). The anomaly strikes NW-SE, which has about 3.7 km strike length and

1 km width (Figure 2.6E). It clearly shows the shape of the mineralization and is directly associated with the deposit's magnetic anomaly (Figures 2.4D, 2.5B, and 2.9B). A section extracted from the inversion model along the AB profile (Figure 2.6D) shows a clear discrete North-dipping high-density zone (Figure 2.6E).

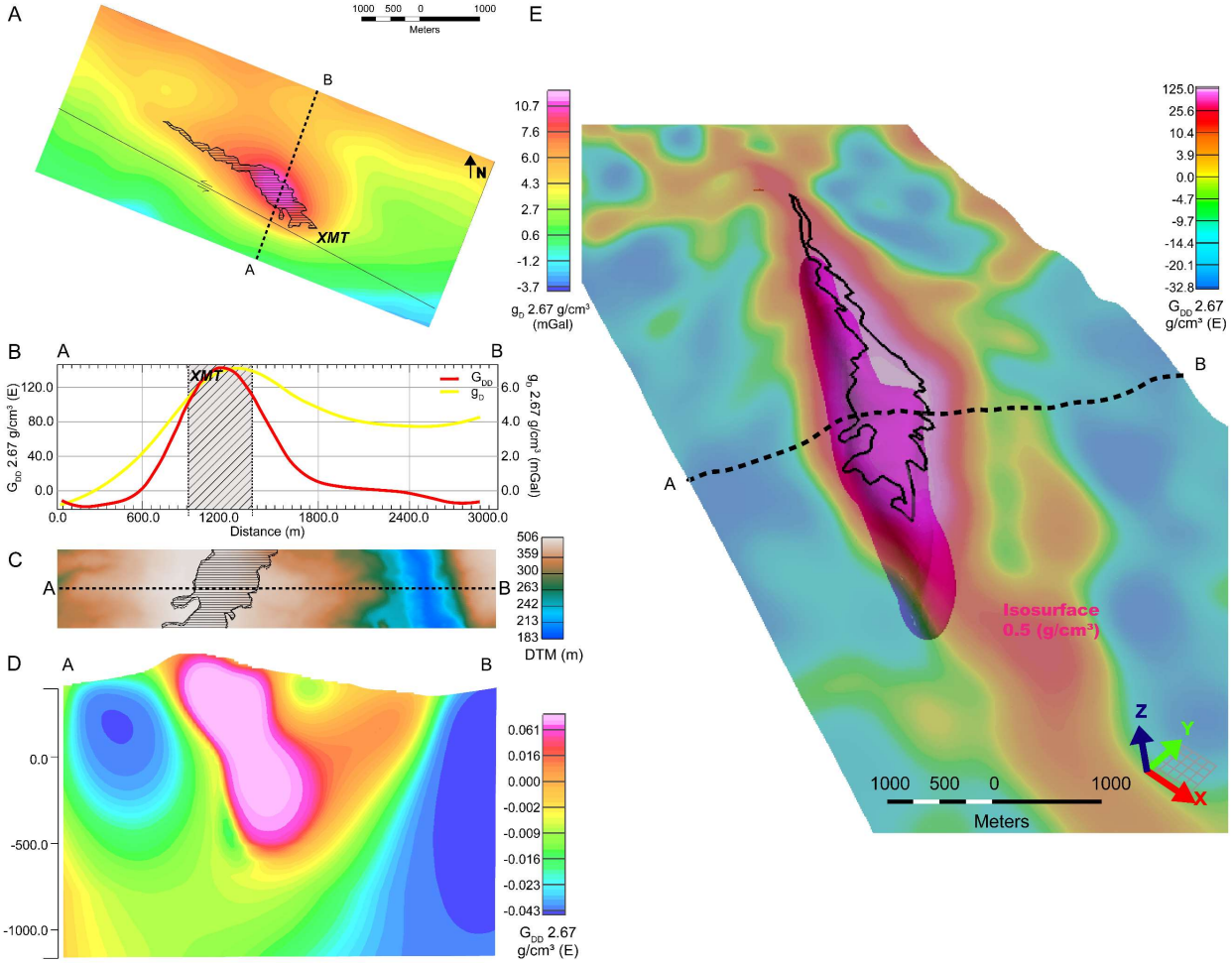


Figure 2. 6 - Gravity footprint at a district scale. A) Vertical gravity (g_D) map. B) Vertical gravity (g_D) and vertical gravity gradient (G_{DD}) along the AB profile. C) Topography along the AB profile. D) Section extracted from the gravity inversion model along the AB profile. E) 3D visualization of Salobo's G_{DD} signature, and a 3D isosurface from the inversion model (0.5 g/cm³). XMT - Magnetite Schist and DTM-Digital Terrain Model.

It is worth noting that Salobo lies within a very prominent topography high (Figure 2.6C) and there is a clear correlation between topography and AGG (Airborne Gravity Gradiometer) data (Figure 2.6). Several density values were tested in an effort to minimize this correlation. The terrain correction density applied in the final products presented in the figures was 2.67 g/cm³; however, this was not sufficient to fully eliminate the correlation. In this case, and many other areas in the Carajás Mineral Province, techniques to select ideal densities for terrain correction based on the correlation between gravity data and topography fail due to the natural correlation between high-density zones and topography highs.

Salobo was detected by the QUESTEM survey as an early-mid channel anomaly on both X and Z components. X component data exhibits anomalies on the borders of the deposit (Figures 2.7A and 2.7B). Z component data exhibits a broad, discrete, 550 ppm anomaly centered over the deposit (Figure 2.7C) and along the AB profile (Figure 2.7D). However, the anomaly is associated only with the thickest part of the deposit, where high-grade ore dominates. The along-strike extensions of the deposit, which are mostly lower-grade, chalcopyrite-rich zones, were not detected. No significant late-time signal was measured.

A Conductivity-Depth Image (CDI) along the AB profile shows a thin conductive cover and a steeply dipping conductive feature at about 300 meters depth (Figure 2.7E). The time constant (Tau) data shows increasing values upon entering the mineralized zone, reaching its highest value of 0.8 ms to the north of the deposit. The anomaly is uniform and centered, but it does not show lateral continuity (Figures 2.7F and 2.7G).

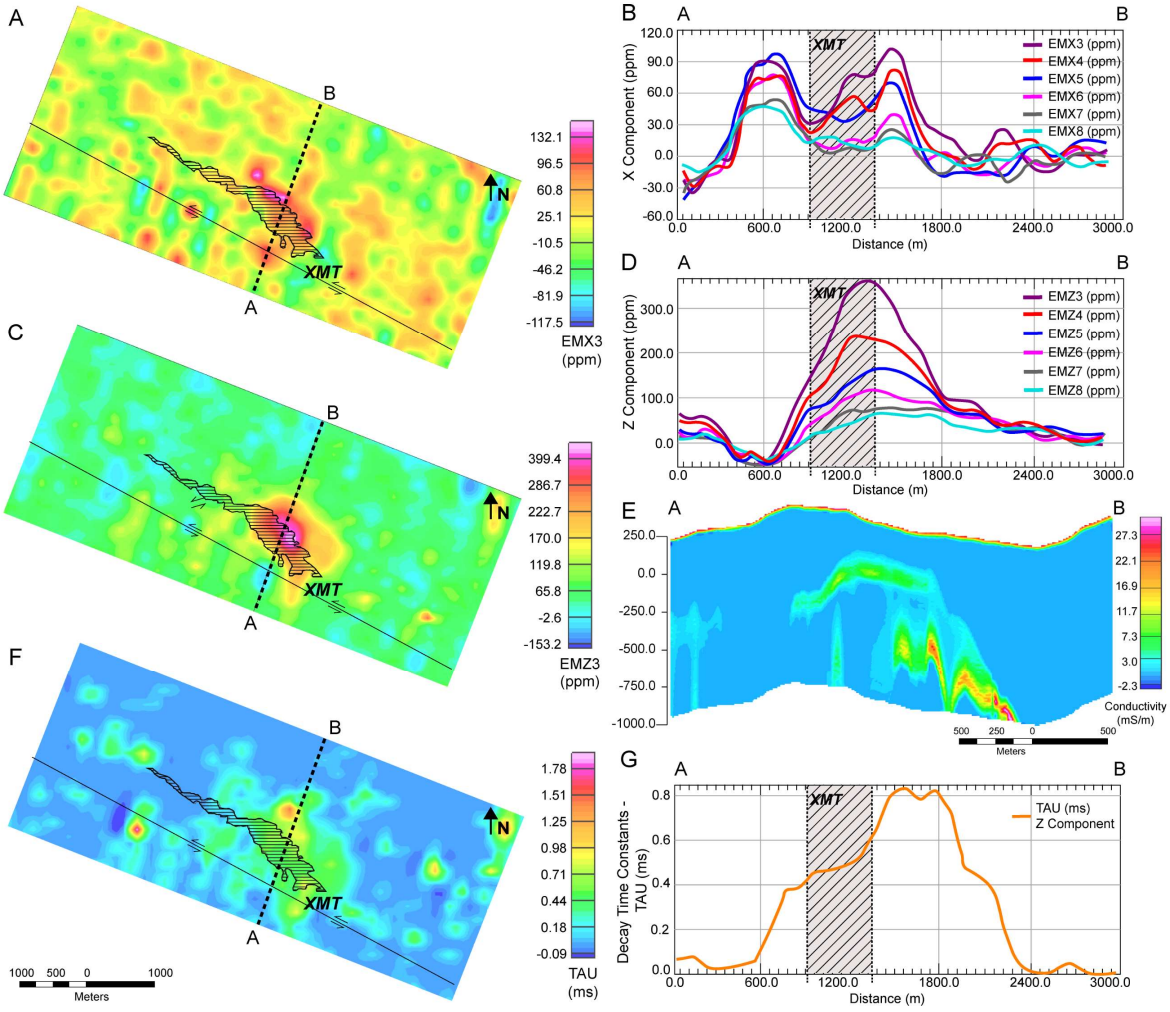


Figure 2. 7 – EM footprint at the district scale. The regional Cinzento shear zone is shown in the maps. A) X component of channel 3. B) Profiles of X component data for channels 3 – 8. C) Channel 3, Z component data. D) Profiles of the Z component for channels 3 – 8. E) EM CDI on the AB profile. F) Time constant (Z component). G) Time constant (Z component) profile. XMT - Magnetite Schist, EM – Electromagnetic, CDI – Conductivity-Depth Image and TAU – Decay Time Constants.

The district scale gamma spectrometric data shows U and Th highs around the deposit (Figures 2.8A and 2.8B). High concentrations of the three radioelements are associated with Old Salobo Granite. A K-rich area to the NE is associated with the Salobo-Pojuca geological domain (Figures 2.8A and 2.8B). Small-scale K anomalies over the deposit are interpreted to be associated with potassic alteration zones (Figure 2.1). U/Th ratio data shows anomalous values of up to 12 around the deposit and is the best proxy to mineralization (Figures 2.8C and 2.8D).

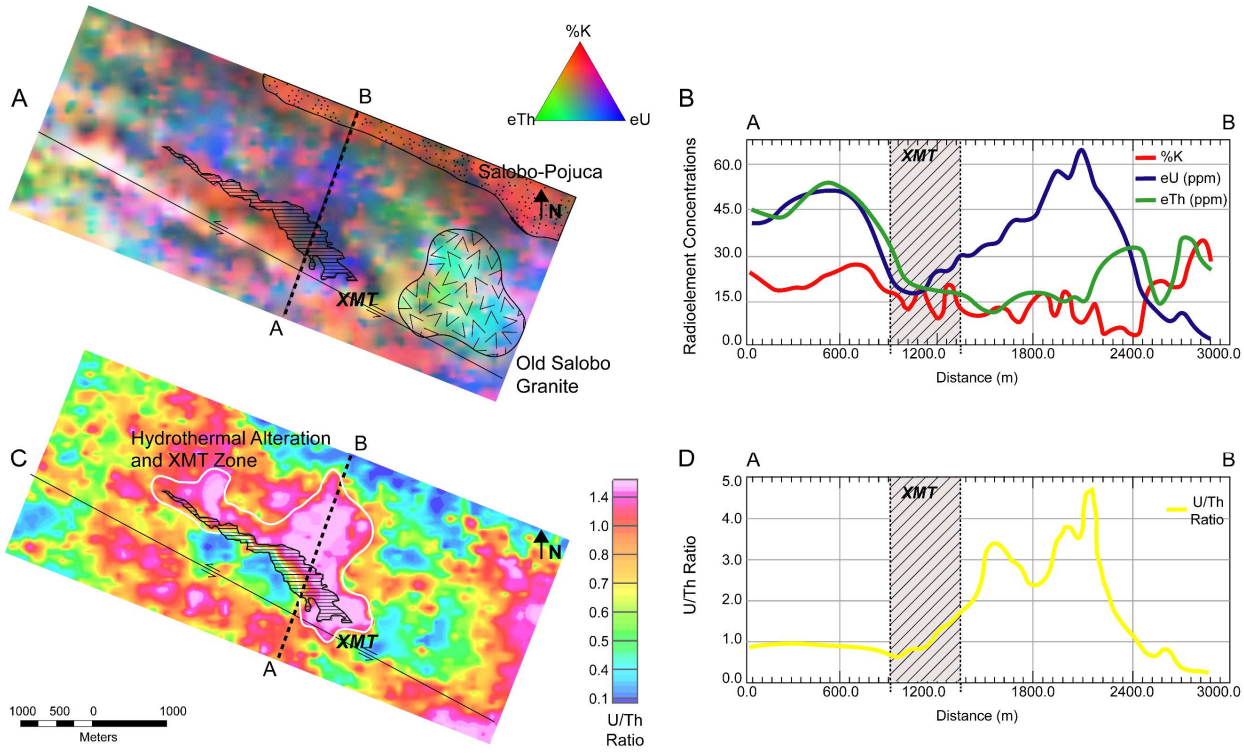


Figure 2. 8 – District scale gamma-ray spectrometric footprint. Cinzento Shear Zone, Old Salobo Granite, Salobo-Pojuca domain and XMT are shown in maps. A) RGB ternary composition image (K, eTh, eU). B) 1D profiles of K, eTh, and eU along the AB profile. C) U/Th ratio. D) U/Th ratio along the AB profile. XMT - Magnetite Schist.

2.4.3. Deposit Scale Footprint

Ground magnetic data adds significantly more information compared to the available airborne data. RTE data shows the same three-anomaly pattern seen in airborne data (Figure 2.9A) with amplitudes of up to 2700 nT (Figure 2.9C). On a deposit scale, anomalies are more limited in extension and width, and more compatible with the extension of the mineralization. TG data shows values of up to 10 nT/m and suggests a length of approximately 1600 meters (Figures 2.9B and 2.9C).

Figure 2.9D shows a section of the MVI model for the area. It indicates a large magnetic zone directly correlated with the deposit. Other alteration zones and host rocks are associated with low magnetization values.

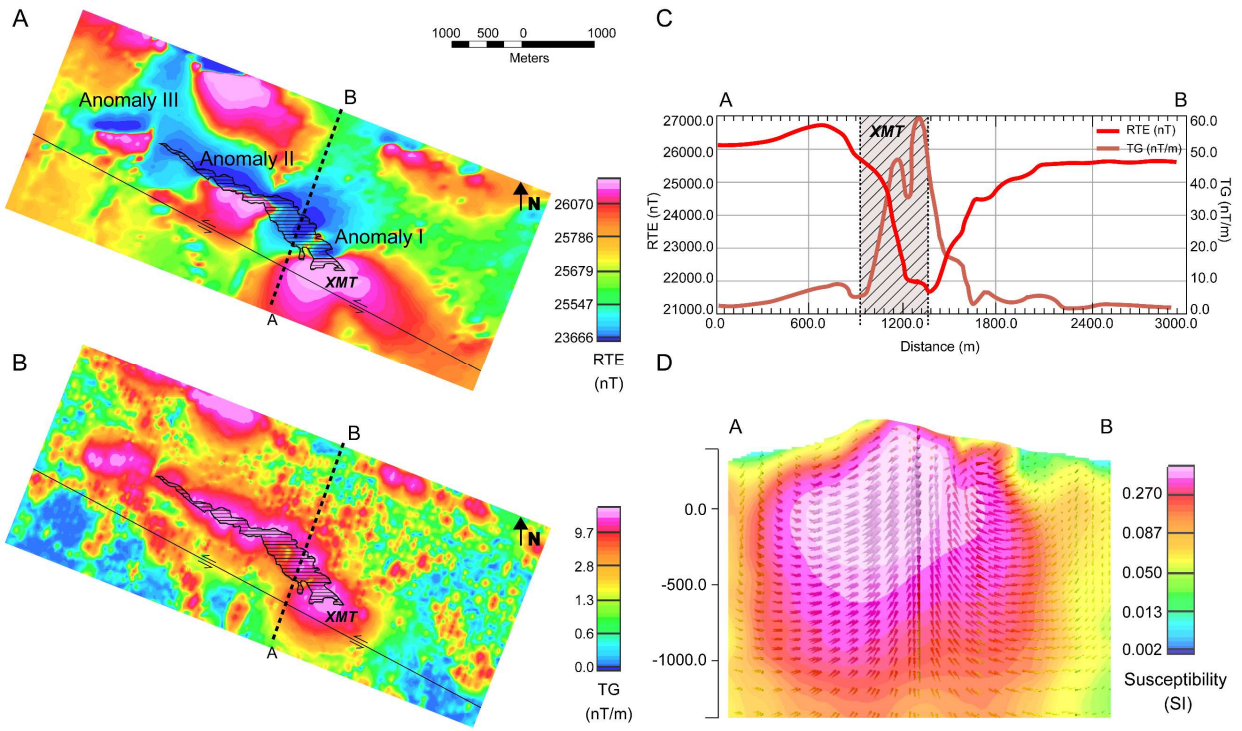


Figure 2. 9 - Magnetic footprint at the deposit scale. The regional Cinzento shear zone is shown in the maps. A) Reduce to Equator (RTE) data. B) Total Gradient (TG). C) RTE and TG signatures along the AB profile. D) Section extracted from the inversion along AB profile. MVI model magnetization shown as vector cones coloured by susceptibility. XMT - Magnetite Schist.

A Resistivity-Depth Image (RDI) slice from apparent resistivity transformations for each line of ground EM data collected over the deposit (Figure 2.10A) indicates three conductive zones (anomalies I, II and III). Anomalies I (15 Ωm) and II (200 Ωm) are directly associated with Salobo in a resistive background (3500 Ωm). An RDI section shows that the conductor correlates with the magnetic and dense zones from the potential field models and the mineralization (Figure 2.10B).

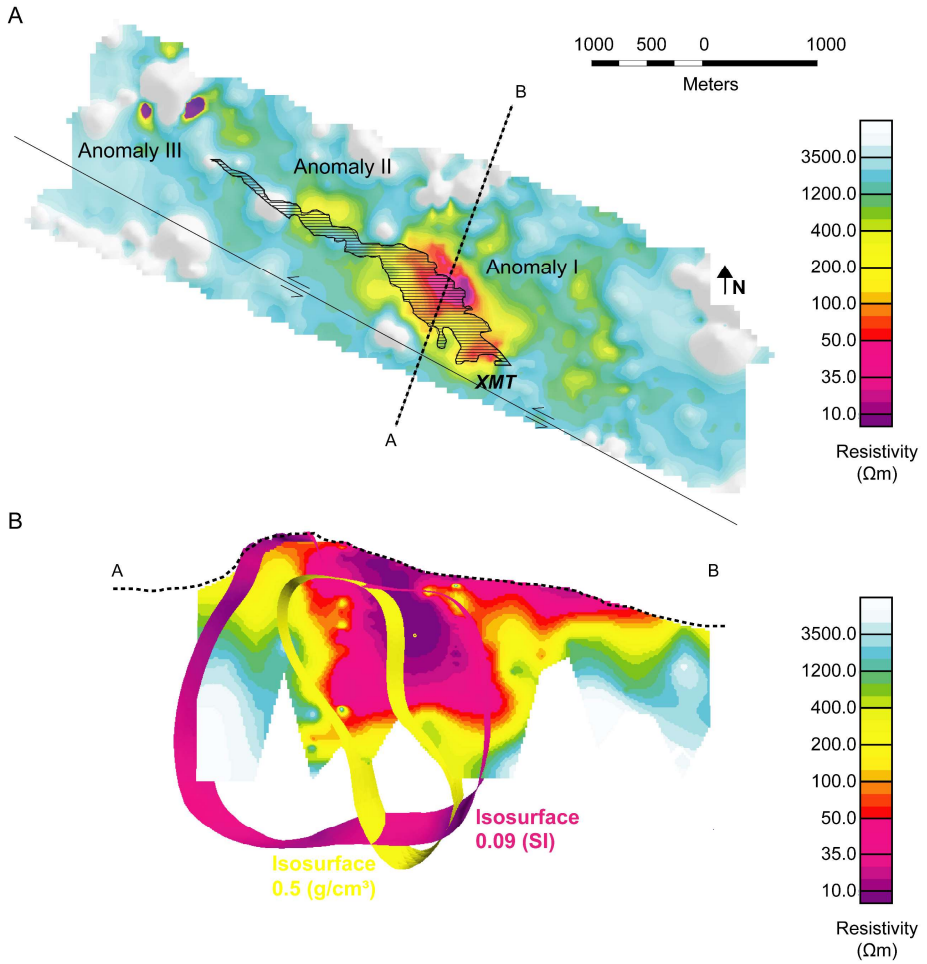


Figure 2. 10 – Deposit scale electromagnetic footprint. A) RDI slice of apparent resistivity from ground EM data at 300m depth and Cinzento shear zone. B) RDI section along the AB profile and isosurfaces of MVI susceptibility and density from inversions of magnetic and gravity data. RDI – Resistivity-Depth Image, EM – Electromagnetic, MVI - Magnetic Vector Inversion and XMT - Magnetite Schist.

Ground gamma spectrometric data shows the main geological units well (Figure 2.11A) despite significant weathering. The Salobo-Pojuca domain to the North and Old Salobo Granite to the East are clearly visible on most maps. The total count channel (TC) has some unusual readings of up to 4 cpm, with low values found towards the north and east (Figures 2.11B and 2.11D). Small K concentration anomalies (Figures 2.11C and 2.11D) are scattered throughout Salobo, with some readings as high as 1.13%, but most of the deposit is associated with low K concentrations. The eU channel (Figures 2.11E and 2.11H) also displays anomalous readings of up to 35.6 ppm. Th concentration data shows concentrations of up to 35.8 ppm (Figures 2.11F and 2.11H) and a good correlation with U concentration. The deposit is mostly associated with lower concentrations of radioelements compared to the adjacent units. The granitic host shows naturally higher U and Th concentrations, and mylonites along the Cinzento shear can be used to map the structure. The U/Th ratio eliminates the expected correlation and shows anomalies centered over Salobo (Figures 2.11G and 2.11H).

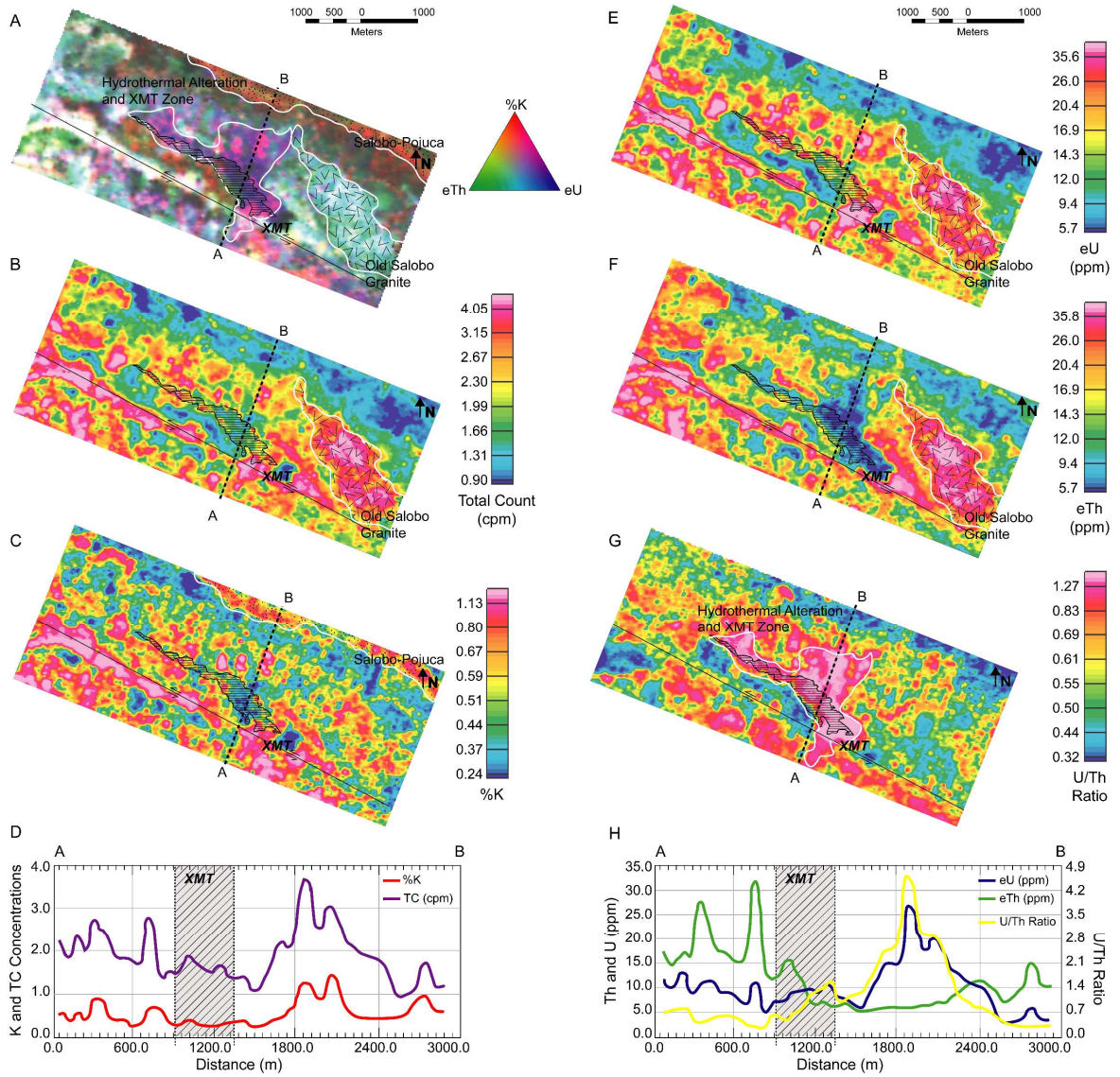


Figure 2. 11 - Deposit scale gamma spectrometric footprint. Cinzento Shear Zone, Old Salobo Granite, Salobo-Pojuca domain and XMT are shown in all maps. A) Gamma spectrometric ternary map (K = Red, eTh = Green, and eU = Blue). B) Total count C) K concentration, D) K concentration, and total count signatures along the AB profile. E) U concentration. F) Th concentration. G) U/Th ratio. H) Th concentration, U concentration, and U/Th ratio signatures along the AB profile XMT - Magnetite Schist and TC - Total count.

Historical DCIP (Direct Current resistivity and Induced Polarization) data was re-processed and modeled. Three anomalous trends (Figure 2.12A) are observed in the chargeability models: Trend I is the largest and correlates with the deposit. The highest amplitude chargeability anomalies (~40 mV/V) are associated with the Western part of the deposit, where low-grade, chalcopyrite-rich ore dominates. The central, high-grade zone is associated with intermediate to high values (~20 mV/V). The northern limit of the deposit is clear in the models, but the footwall appears as a chargeable zone with values that are often higher than those of the deposit itself. The other two trends, referred to as Trend II and Trend III, are located to the East of the deposit

and seem to be similar secondary structures associated with the main ~E-W Cinzento shear. An anomalous zone to the west of known mineralization was identified as a target (Figure 2.12A).

The resistivity models show a narrow conductive trend (~30Ωm) directly related to the deposit and chargeability trends II and III (Figure 2.12B). The lowest resistivity values are associated with the thickest and higher-grade portion of the deposit. The differences between resistivity and chargeability models are associated with the alteration zoning pattern of the deposit and can be used to map the proximal and distal alteration zones (Figure 2.12B).

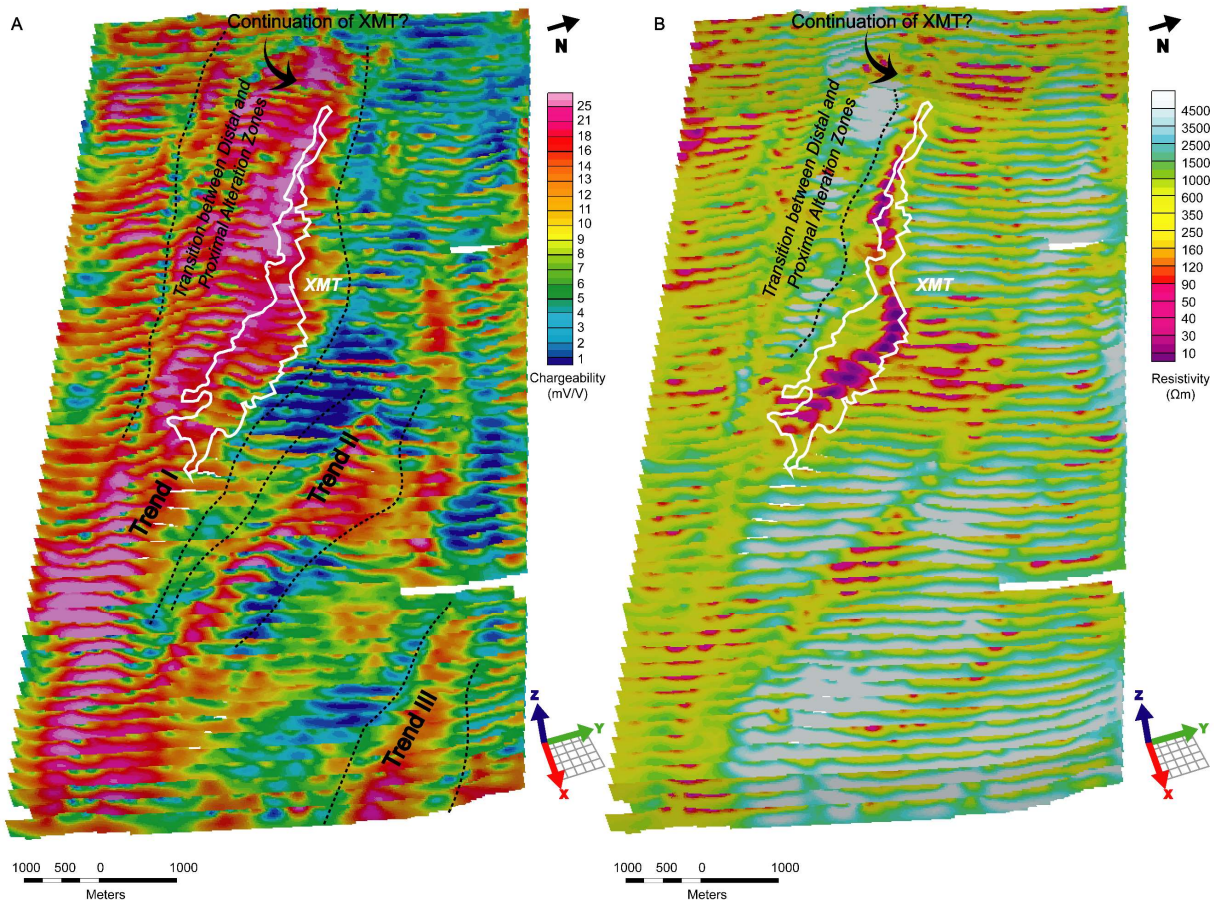


Figure 2. 12 - Deposit scale DCIP footprint. A) Chargeability 2D models showing three anomalous trends and a possible extension of the mineralization to the west. B) Resistivity 2D models showing a strong anomaly associated with XMT. XMT - Magnetite Schist.

2.5. Discussion

2.5.1. Magnetics

There is a direct correlation between the magnetic models and mineralization models (Figures 2.4, 2.5, and 2.9). The orebodies are very closely related to magnetite-alteration zones, which are clearly mapped in all scales of magnetic data. Magnetite is the only significantly magnetic mineral in the deposit. The Fe content in other alteration zones, such as biotite–garnet and garnet–grunerite (Figure 2.2) is in non-magnetic minerals, which significantly decrease their magnetic responses in comparison. Magnetite is also formed in K-Fe alteration zones (Figure

2.2), but ferric zones are significantly more magnetic. The richest zones, located in the central part of the deposit (Figures 2.1C and 2.2), correspond to the most Fe-altered areas associated with the highest magnetic anomalies.

The MVI susceptibility model and the vector cones for the deposit shows a small magnetic zone dipping to the South (Figures 2.4E, 2.5C, and 2.9D). This zone is considered an artifact of the MVI process due to the lack of magnetization direction information. This is a common side-effect in unconstrained MVI models in low magnetic latitudes which could be resolved with magnetization direction measurements or developing a comprehensive magnetic susceptibility database (Ellis et al., 2012).

Furnas, Cristalino, and Salobo share a similar geological context, but have significantly different signatures. Furnas is located along the same regional shear zone as Salobo in the northern part of Carajás (Cinzento shear zone), while Cristalino is located along the Canaã dos Carajás shear zone to the south. Leão-Santos (2015) shows that Furnas is associated with an intense magnetic anomaly attributed to a large grunerite-magnetite alteration zone which is directly related with Cu grades. Melo et al. (2016) showed that the apparent magnetic signature of Cristalino is mainly caused by an adjacent, barren iron formation. The mineralization at Cristalino is hosted in potassic alteration zones which are not magnetic. Salobo is more similar to Furnas in terms of magnetic signature, but some of its dense alteration zones are not magnetic which makes its signature complex, unlike Furnas.

2.5.2. Gravity Gradiometry

Gravity gradiometry data (Falcon) has been employed in mineral exploration for both the direct detection of a wide variety of deposit types and for geological mapping (Carlos, 2013). Ernest Henry, Prominent Hill, and King George IOCG deposits in Australia were discovered using gravity gradiometry as a primary or secondary approach (Mahanta et al., 2001; Dransfield, 2007; Braga et al., 2014).

The direct correlation between gravity data and topography showed by Falcon data over Salobo was created by the intense weathering these areas were exposed to, and dense rocks, such as BIF and Fe alteration zones, are more resistant to those processes. Therefore, the correlation between density and gravity data is to be expected and density correction values that minimize that correlation are not reasonable.

Gravity gradiometric data also shows a direct correlation between higher-density zones and copper content (Figure 2.6). Salobo's gravity anomaly is broad and encompasses several alteration zones which are denser than the granitic host rocks: biotite-garnet and garnet-grunerite (Figure 2.2). These K-Fe may be as dense as Fe alteration zones but are also significantly bigger. The XMT (magnetite schist) is often only a few meters thick, while the K-Fe alteration zones may be tens of meters thick.

2.5.3. Time Domain Electromagnetic – TDEM

The EM signature of the deposit is primarily controlled by sulphide type and content. The district scale showed a discrete anomaly with very limited strike length (Figure 2.7C). Ground data shows the second and third anomalies (Anomaly II and III)(Figure 2.10). The significant difference between the signatures of the low-grade area (NW) and high-grade area located in the center of the deposit (Figures 2.1C and 2.2) suggests that the higher content of bornite and chalcocite is the main control of conductivity. Magnetite may contribute to the conductivity of the deposit, but the absence of a consistent correlation between EM and magnetics in low-grade areas (chalcopyrite-rich) suggests that this is a secondary factor.

The absence of late time signal and the recovered conductivity models suggest that the deposit has low conductivity (0.4 ms time constant) (Figures 2.7F and 2.7G) compared to other massive sulphide deposits but is consistent with low conductivities observed in other IOCG deposits in the Carajás Mineral Province (Leão-Santos et al., 2015). CDI or RDI section/slice have been effective in delineating the Salobo Deposit, providing valuable insights for qualitative, and in some cases, semi-quantitative interpretation of subsurface features. This approach is particularly useful given that forward modeling remains a complex and computationally demanding process.

2.5.4. Gamma Spectrometry

Regional and district scale data shows K and U-enrichment zones (Figures 2.4 and 2.8) are mostly associated with the granitic host with smaller anomalies possibly associated with Na-K, Ca-K-Fe, and K-Fe alteration zones (Figures 2.1C and 2.2). In ground data, U anomalies due to alteration are more evident in the center of deposit compared to airborne data (Figure 2.11). While the regional-scale data showed only general information, ground data showed a detailed information in a very weathered terrain, including the extent of the main alteration envelope.

Most IOCG (Iron Oxide Copper-Gold) deposits are associated with significant Fe and U-Th enrichment. Consequently, they can be targeted by the presence of coincident magnetic and potassium±uranium-thorium radiometric signatures, such as the Olympic Dam (Mumin, 2002). However, the granitic host at Salobo requires the use of ratios to enhance the deposit's signature, such as U/Th. This ratio was able to remove the signature of the nearby Old Salobo granite and the granite host. Not only the survey was able to directly detect mineralization, it also provided structural information, as it detected the anomalous mylonite along the primary Cinzento shear.

2.5.5. Induced Polarization

Salobo appears as both chargeable and conductive in the models. The chargeability anomaly is much wider than resistivity (Figure 2.12). While chargeability data indicates that both the proximal and distal alteration zones are chargeable, resistivity only detected the proximal zones. The chargeable distal zones are associated with a late low-temperature hydrothermal

stage (chlorite, epidote, and hematite) that affects the footwall. Resistivity models show a narrow conductive trend and are directly associated with proximal alteration zones (Figure 2.12B). DCIP (Direct Current resistivity and Induced Polarization) models show a different pattern when compared to the EM (electromagnetic) models. While EM was able to detect mostly the highest-grade zone in the center, and only reasonably the lower grade zone to the NW (Figure 2.10), DCIP was able to image the whole alteration envelope with chargeability and resistivity providing different perspectives (Figure 2.12). Unlike EM, resistivity from DCIP shows the whole proximal alteration trend, which is dominated by lower conductivity, disseminated sulphides to the NW, and higher conductivity, massive sulphides to the SE. This is also thought to be the reason why chargeability is highest to the NW. Both the footwall and NW area show significant disseminated mineralization and/or alteration, which increases chargeability, but does not significantly change the resistivity.

2.5.6. Multiscale and multisource Geophysical footprint of the Salobo Deposit

Multisource and multiscale analyses are crucial when formulating exploration strategies. Drilling is often the most significant cost in mineral exploration and mining, and sometimes the only alternative to geophysics for subsurface investigation. While drilling provides accurate geological data from small areas, it is expensive and limited in coverage. The geophysical methods can cover larger areas and depending on the scale of the survey indicate a possible mineralization. However, well-designed geophysical surveys and data analysis can effectively target drilling locations, optimizing the use of resources. Thus, it is critical to understand the geophysical footprint of deposit signatures to properly design an efficient exploration model.

Figure 2.13 shows profiles of all the relevant and available geophysical data over Salobo. Magnetic data at all investigation scales shows a direct correlation between magnetic anomalies and, primarily, magnetite zones, but also K-Fe zones. These are proximal alteration zones and very closely related to sulphide zones, which makes magnetics the main geophysical for exploration. From a mineral exploration perspective, the regional and district scale of magnetic data already offers sufficient information for our analysis. While the deposit scale of magnetic data was beneficial, it not significantly enhances the dataset due to the size of the Salobo deposit. However, for smaller deposits, a deposit scale could provide additional insights and prove to be more advantageous. Gravity data and models show a direct correlation between density and copper content. This is due to the high-density K-Fe and Fe alteration zones hosted in a low-density granite.

Time-domain electromagnetic (TDEM) models effectively mapped Salobo at all investigation scales as a weak early/mid-time conductor. The electromagnetic signature of Salobo is consistent with other similar deposits in the Carajás, such as Furnas. The relative

content of bornite/chalcocite and chalcopyrite is the main control on the distribution of conductivity as the absence of significant signal outside of the high-grade, bornite-chalcocite-rich area shows. Salobo shows a clear gamma spectrometric signature. Its Na-K, Ca-K-Fe and K-Fe alteration zones, and elevated U (common in Iron Oxide Copper-Gold systems) content stand out from the granitic host. The U/Th ratio reduces the natural correlation between U and Th in granites and is one of the best proxies for exploration in this area.

DCIP (Direct Current resistivity and Induced Polarization) surveys showed that resistivity defines the deposit more effectively than chargeability. The chargeability anomaly covers an area much larger than the extent of the proximal alteration zones and suggests that other zones, such as late, low-temperature hydrothermal stages, common in the footwall, are also chargeable. Resistivity imaged the narrower proximal alteration envelope and is more effective in detecting and imaging the deposit. Salobo magnetic, gravimetric, Time-domain electromagnetic (TDEM), gamma spectrometric, and induced polarization anomalies are coincident, but controlled by different minerals and alteration zones (Figure 2.13).

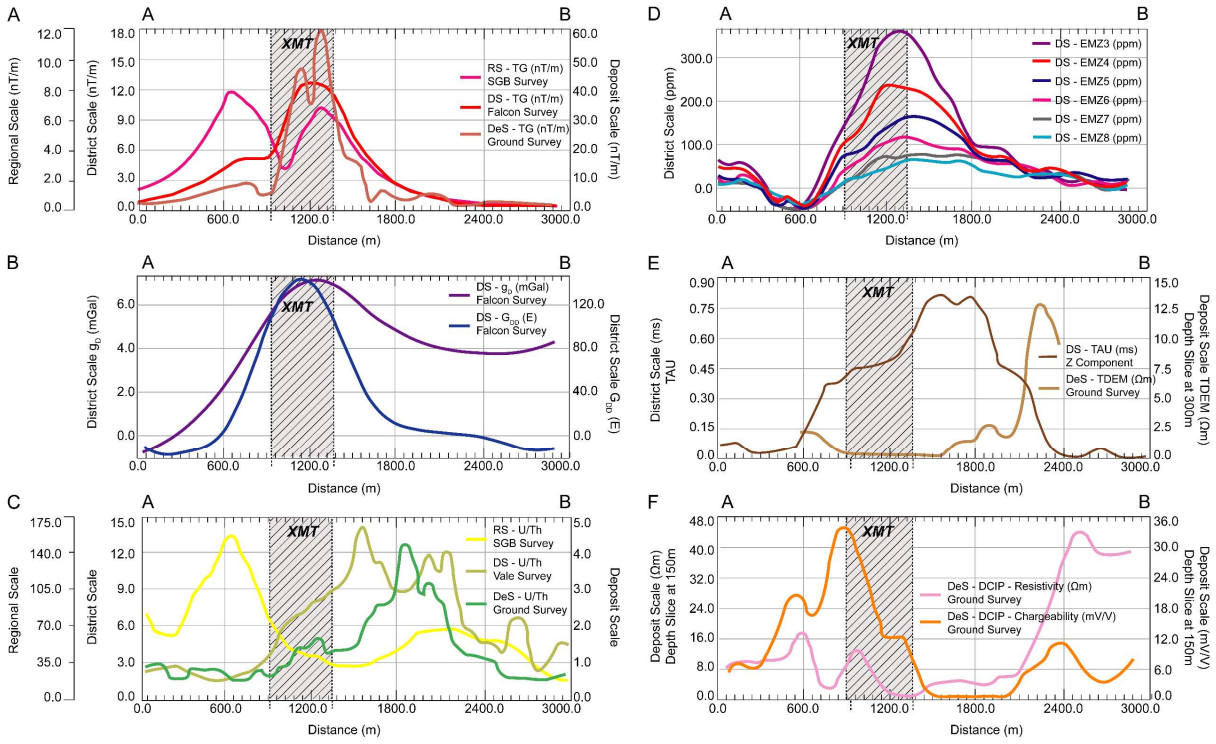


Figure 2. 13 – Multiscale and multisource geophysical footprint of Salobo. A) Multiscale magnetic data. B) Multiscale gravity data. C) Multiscale gamma spectrometric data. D) District-scale airborne TDEM data. E) Multiscale TDEM data. F) Profile of modelled resistivity and chargeability at 150m depth. XMT - Magnetite Schist, RS – Regional Scale, DS – District Scale, DeS – Deposit Scale, g_D and G_{DD} Falcon component, EM – Electromagnetic, TDEM - Time-Domain Electromagnetic, TAU - Time Constant, DCIP – Direct Current resistivity and Induced Polarization and SGB - Geological Survey of Brazil

Figure 2.14 shows a classification of the geophysical methods considered in this work based on their priority in exploration programs targeting Salobo-like deposits at different scales of investigation. Higher-priority methods would add the most value and should be applied first. Lower-priority methods may or may not add significant value and should be considered last. On a regional scale, magnetics and gamma spectrometry should be prioritized as they show clear anomalies associated with the deposit and are the cheapest among the airborne methods. Gravity gradiometry should be second priority given the coincident magnetic and gravity signatures. It would also help with deposits that are not significantly magnetic, such as Sossego and Cristalino (Melo et al 2014).

On a district scale, time-domain EM and gravity gradiometry are priorities as they may directly detect zones of proximal alteration or mineralization. In this scale, regional magnetic and gamma spectrometric data are often available and higher resolution data could be acquired during a gravity or EM survey, hence their reduced priority. On a deposit scale, DCIP is considered the top priority given the excellent resistivity signature of the deposit and lack of any other non-prospective conductors. Time domain EM is considered second on the priority list. Salobo and other IOCG (Iron Oxide Copper-Gold) deposits in the Carajás often have low conductivity and EM may only detect the high-grade areas. Lower-grade, chalcopyrite-rich ore was not detected by the ground surveys done over Salobo and other surveys may fail to identify them. However, the lack of non-prospective conductors makes any reasonable anomaly a potential target. Ground magnetic and gamma spectrometric data could be acquired at a lower cost, but are considered the least important sources of information at this stage. The data acquired in airborne surveys is enough given the size of economic systems.

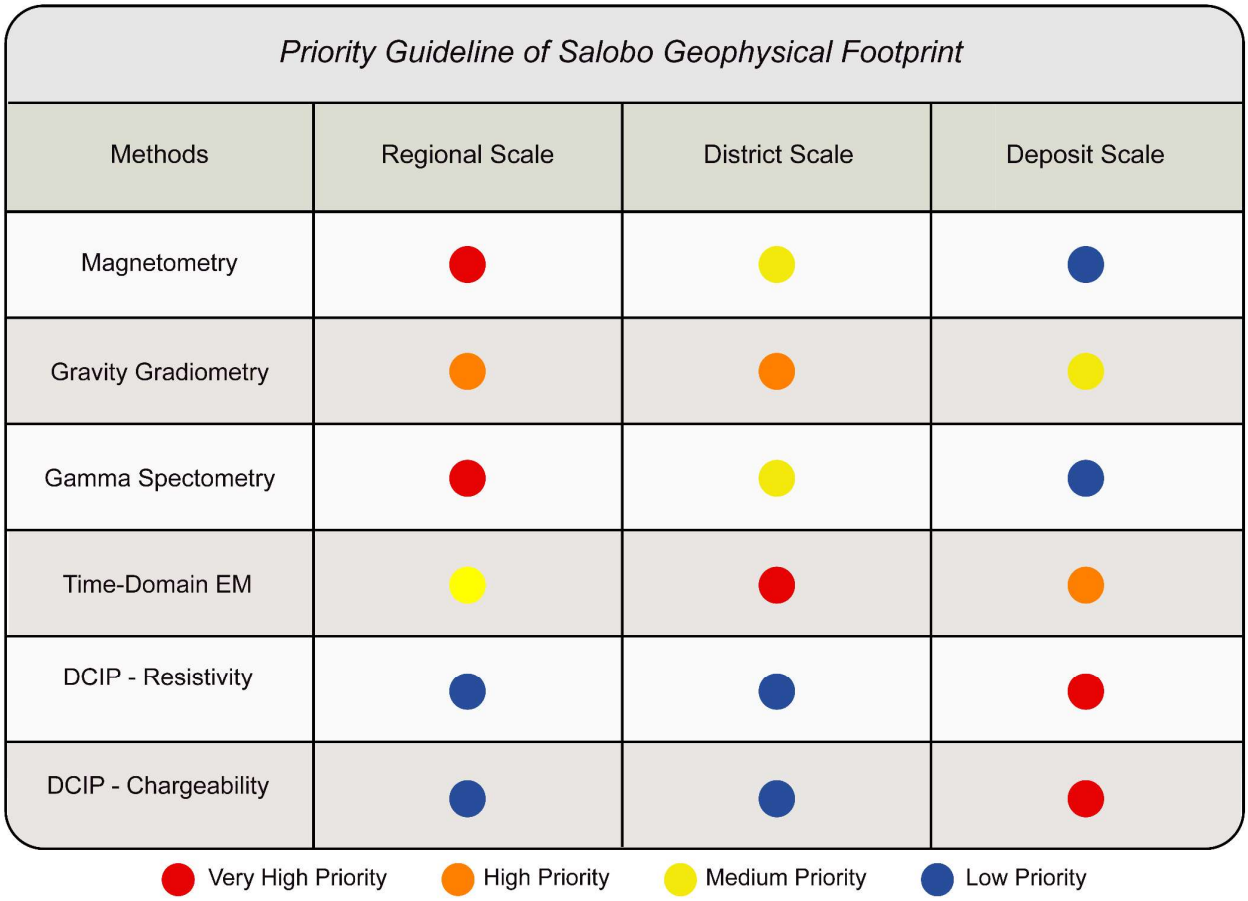


Figure 2. 14 - Priority guideline of the implemented geophysical methods at the Salobo Deposit. The low-priority methods are not related to its effectiveness in the mineral exploration of IOCG-type deposits. EM – Electromagnetic, DCIP – Direct Current resistivity and Induced Polarization and IOCG - Iron Oxide Copper-Gold.

2.6. Conclusion

Iron oxide copper-gold (IOCG) deposits are a challenging class of mineral deposits in terms of petrophysics and geophysical signatures. Although most of these deposits were initially discovered using simple exploration models, more complex models will be required for effective exploration in the future. The complexity of IOCG deposits in the Carajás Mineral Province poses a challenge in establishing a geophysics exploration model. Through this study, we have shown that Salobo's geophysical signature in multisource and multiscale are related to factors like mineralogy, texture, and structural controls.

Magnetic, gamma spectrometric, gravity gradiometry, Time-Domain Electromagnetic (TDEM) and, Direct Current resistivity and Induced Polarization (DCIP) data effectively map alteration zones and mineralization at Salobo. Magnetite/K-Fe and sulphide zones are magnetic and are easily mapped with magnetic data. Proximal alteration zones are significantly denser than the granitic host and produce a large gravity anomaly which is obvious despite high topographic relief and potential issues with terrain corrections. The deposit has a gamma

spectrometric signature, and its elevated U content is highlighted best by U/Th ratio. High-grade chalcocite-bornite zones are conductive and were detected by both airborne and ground EM surveys, but neither of these were able to identify low-grade chalcopyrite-rich zones. DCIP surveys show that resistivity better maps the deposit than chargeability. Unlike inductive resistivity (EM), galvanic resistivity shows both the high-grade and low-grade zones. Chargeability shows a much larger anomaly and seems to be affected by late and barren alteration events.

Each geophysical dataset provides complementary insights into the deposit. The various minerals and alteration zones create different petrophysical contrasts that must be properly understood in terms of geology. We established survey priority guidelines for IOCG exploration based on geophysical data collected at Salobo. The geophysical footprint provided here serves as a tool for identifying targets and to better evaluate exploration areas using an integrated approach. These guidelines may be used in similar geological contexts simplifying the identification of new exploration targets and should help optimize drilling campaigns. Understanding which factors or hydrothermal alteration phase can affect geophysical or petrophysical anomalies is crucial for efficient target generation. Given the complexity of IOCG deposits, their controlling factors, and the scale of investigation, detailed studies, such as geological, petrographic, and petrophysical analyses, are essential. These analyses could significantly enhance the prioritization process by providing a more refined and accurate characterization of the deposit, ultimately improving exploration outcomes.

Acknowledgments

This paper is part of the PhD research of the first author, funded in part by the Coordenação de Aperfeiçoamento de Pessoal de Nível Superior - Brasil (CAPES) Finance Code 001, and supported by the Brazilian National Council for Scientific and Technological Development (CNPq) and the CT-Universal Program (Project 408592/2021-4). The authors express their gratitude to the Vale-ADIMB-Brazilian Universities consortium for their support and permission to publish this work, as part of the Geodynamics and Metallogeny of the Carajás Mineral Province (PA) and Quadrilátero Ferrífero (QF) Project, funded by Vale S.A. Additionally, Adalene M. Silva and C. Toledo acknowledge their research grants from CNPq (Projects 309846/2023-4 and 313807/2021-3).

Appendix A

Regional scale survey parameters and other information of Brazil Geological Service Data

GEOLOGICAL SERVICE OF BRAZIL DATA (SGB)

Project Name and Number	***Rio Maria (1129)***	***Rio Maria (1129)***
Method	Magnetic	Gamma-Ray Spectrometric
Date	2015	2015
Line Direction	N-S	N-S
Spacing Line	500 m	500 m
Tie Line Direction	E-W	E-W
Tie Line Spacing	10 km	10 km
Sampling Rate	0.1 s	1 s
Nominal Terrain Clearance	100 m	100 m
Acquisition System	Aeromaster – VN2001	Aeromaster – VN2001
Equipment Model	Mobile: Scintrex CS-3 Base Station: GSM-19	Gamma: Pico Envirotec – GRS 410

Appendix B

District scale survey parameters and other information of airborne VALE S.A. data. AGG - Airborne Gravity Gradiometer and TDEM – Time-Domain Electromagnetic

AIRBORNE SURVEY VALE DATA

Project Name	***FALCON***	***QUESTEM***	***Salobo-Jaca***
Method	Magnetic and AGG	TDEM	Gamma-Ray Spectrometric

Date	2012/2018	1997	1996
Line Direction	N 30º E	N 20º E	N 17º E
Spacing Line	200 m	250 m	250 m
Tie Line Direction	N 60º E	N 70º E	N 73º E
Tie Line Spacing	5 km	5 km	5 km
Sampling Rate	0.1 s	0.2 s	1 s
Nominal Terrain Clearance	60 m	110 m	60 m
Acquisition System	FADAS	GPS Picodas/NovAtel	RMS DGR-33
Equipment Model	Mobile: Scintrex CS-3 Base Station: Scintrex CS-3 Grav: HeliFALCON	QUESTEM 450	Exploranium GR-820

Appendix C

Deposit scale survey parameters and other information of ground VALE S.A. data. DCIP – Direct Current resistivity and Induced Polarization, TDEM – Time-Domain Electromagnetic, and DP-DP – Dipole-Dipole

GROUND SURVEY VALE DATA

Method	Magnetic	Gamma-Ray Spectrometric	DCIP	TDEM
Date	2002	2002	2002	2003
Line Direction	N 23º E	N 23º E	N 23º E	N 23º E

Line Spacing	100 m	100 m	100 m	200 m
Station Spacing	20 m	20 m	80 m	100 m
Others Information	------	Integration Time: 60 s	Array DP-DP, n=6	Loops 200 x 200 m
Total Kilometres	212 km	214 km	180 km	750 Loops

References

Aisengart, T., J. L. Ando, L. Batista, and L. C. Ferreira, 2019, Automatic classification of density and magnetic domains from Carajás Mineral Province: Sixteenth International Congress of the Brazilian Geophysical Society.

Althoff, F., P. Barbey, and A.-M. Boullier, 2014, 2.8-3.0 Ga plutonism and deformation in the SE Amazonian craton: the Archaean granitoids of Marajoara (Carajás Mineral Province, Brazil): Precambrian Research, 104, 187–206.

Araújo Filho, R. C., A. C. R. Nogueira, and R. N. Araújo, 2020, New stratigraphic proposal of a Paleoproterozoic siliciclastic succession: Implications for the evolution of the Carajás Basin, Amazonian craton, Brazil: Journal of South American Earth Sciences, 102, 102665.

Asten, M. W. 1998.On the use of conductance and differential conductivity in TEM parasections (CDI). EM 1.8 -. Abstract from Society of Exploration Geophysics 68th Annual Meeting, Tulsa OK USA.

Austin, J., S. Geuna, D. Clark, and D. Hillan, 2014, Remanence, self-demagnetization and their ramifications for magnetic modelling of iron oxide copper-gold deposits: An example from Candelaria, Chile: Journal of Applied Geophysics, 109, 242–255.

Austin, J. R., Patterson, B. O., Le Gras, M., Birchall, R., and Walshe, J. L., 2017. Geophysical signatures of IOCG and Sedex style mineralization in the Mount Isa Eastern Succession, Queensland, Australia. *In:* Improving exploration with Petrophysics: the application of magnetic remanence and other rock physical properties to geophysical targeting. Exploration ’17. Toronto, Canada.

Braga, M. A., I. Endo, H. F. Galbiatti, and D. U. Carlos, 2014, 3D full tensor gradiometry and falcon systems data analysis for iron ore exploration: Baú mine, quadrilátero ferrífero, Minas Gerais, Brazil: Geophysics, 79, B213–B220.

Burns, N., P. Geo, C. Gauld, P. Geo, M. D. Alvim, P. Geo, F. Cp, M. Tagami, and P. Eng, 2019, Salobo Copper-Gold Mine Carajás, Pará State, Brazil Technical Report – Salobo III Expansion:

Carlos, D. U. 2013. Aplicação de Processamento e Inversão Geofísica 3D de Aerogradiometria da Gravidade na Estimação da Estrutura do Minério de Ferro no Sinclinal Gandarela - Quadrilátero Ferrífero - Minas Gerais. Tese de Doutorado. Observatório Nacional, Rio de Janeiro, RJ, Brasil.

Cordani U., 1981. Comentários sobre as determinações geocronológicas da região da Serra dos Carajás. Relatório Interno, Universidade de São Paulo, DOCEGEO.

Costa, U. A. P.; Paula, R. R.; Silva, D. P. B.; Barbosa, J. P. O.; Silva, C. M. G.; Tavares, F. M.; Oliveira, J. K. M.; Justo, A. P. Mapa geológico-geofísico ARIM Carajás. Belém: CPRM, 2016. 1 mapa color. Escala 1:250.000.

Dall'Agnol, R., D. C. de Oliveira, and C. N. Lamarao, 2013, Magmatismo granitoide arqueano e evolução geológica do Subdomínio de Transição da Província Carajás, sudeste do Cráton Amazônico, Brasil: Bol. Mus. Para. Emílio Goeldi. Cienc. Nat, 8, 251–256.

Dall'Agnol, R., M. A. Oliveira, J. A. C. Almeida, F. J. Althoff, A. A. S. Leita, D. C. Oliveira, and C. E. M. Barros, 2006, Archean and Paleoproterozoic granitoids of the Carajás Metallogenetic Province, eastern Amazonian craton: Abstracts of Symposium on Magmatism, Crustal Evolution, and Metallogenesis of the Amazonian Craton, 99–150.

Delinardo da Silva, M.A., 2014. Metatexitos e diatexitos do Complexo Xingu na região de Canaã dos Carajás: Implicações para a evolução mesoarqueana do Domínio Carajás, PA. Unpublished MSc. Thesis, Campinas, University of Campinas.

DOCEGEO, 1988, Revisão litoestratigráfica da Província Mineral de Carajás - Litoestratigrafia e principais depósitos minerais: 35th Congresso Brasileiro de Geologia, Belém.

Dransfield, M., 2007, Airborne Gravity Gradiometry in the Search for Mineral Deposits: Proceedings of Exploration 07: Fifth Decennial International Conference on Mineral Exploration, 341–354.

Duncan, R. J., H. J. Stein, K. A. Evans, M. W. Hitzman, E. P. Nelson, and D. J. Kirwin, 2010, A New Geochronological Framework for Mineralization and Alteration in the Selwyn-Mount Dore Corridor, Eastern Fold Belt, Mount Isa Inlier, Australia: Genetic Implications for Iron Oxide Copper-Gold Deposits: Economic Geology, 106, 169–192.

Ellis, R. G., B. de Wet, and I. N. Macleod, 2012, Inversion of Magnetic Data from Remanent and Induced Sources: ASEG Extended Abstracts, 2012, 1–4.Esdale, D., D. F. Pridmore, J. Coggon, P. Muir, P. Williams, and F. Fritz, 2003, The Olympic Dam copper-uranium-gold-silver-rare earth element deposit, South Australia: A geophysical case history: ASEG Extended Abstracts, 147–168.

Feio, G. R. L., R. Dall'Agnol, E. L. Dantas, M. J. B. Macambira, J. O. S. Santos, F. J. Althoff, and J. E. B. Soares, 2013, Archean granitoid magmatism in the Canaã dos Carajás area: Implications for crustal evolution of the Carajás province, Amazonian craton, Brazil: Precambrian Research, 227, 157–185.

Ferreira Filho, C. F., F. Cançado, C. Correa, E. M. B. Macambira, L. Siepierski, and T. C. J. Brod, 2007, Mineralizações estratiformes de EGP-Ni associadas a complexos acamadados em Carajás: os exemplos de Luanga e Serra da Onça. In: Publitec Gráfica & Editora, Contribuições à Geologia da Amazônia: 5, 1–14.

Freeman, H., and J. Hart, 2003, Geophysics of the Prominent Hill prospect, South Australia: ASEG Extended Abstracts, 2003, 93–100.

Gibbs, A. K., K. R. Wirth, Hirata W.K., and W. J. Olszewski Jr, 1986, Age and composition of the GrãoPará Group volcanics, Serra dos Carajás: Revista Brasileira de Geociencias, 201–2011.

Groves, D. I., F. P. Bierlein, L. D. Meinert, and M. W. Hitzman, 2009, Iron Oxide Copper-Gold (IOCG) Deposits through Earth History: Implications for Origin, Lithospheric Setting, and Distinction from Other Epigenetic Iron Oxide Deposits: Economic Geology, 105, 641–654.

Hitzman, M. W., 2000, Iron Oxide-Cu-Au Deposits: What, Where, When and Why, *In*: Porter, T.M., Ed., Hydrothermal Iron Oxide Copper-Gold and Related Deposits: A Global Perspective, 1st ed.Vol. 1. PGC Publishing, 9–25.

Lafon, J. M., M. J. B. Macambira, and R. T. Pidgeon, 2000, Zircon U-Pb SHRIMP dating of Neoarchean magmatism in the southwestern part of the Carjás Province (eastern Amazonian Craton, Brazil): International Geological Congress.

Leão-Santos, M., Y. Li, and R. Moraes, 2015, Application of 3D magnetic amplitude inversion to iron oxide-copper-gold deposits at low magnetic latitudes: A case study from Carajás Mineral Province, Brazil: Geophysics, 80, B13–B22.

Leão-Santos, M., Brake, D., Souza, J. P., Freitas, C., and Matos, F., 2015, Ground and borehole time domain electromagnetic response at disseminated iron oxide-copper-gold deposits, Carajás Mineral Province, Brazil: Near-Surface Asia Pacific Conference, 43-47.

Leão-Santos, M., R. Moraes, Y. Li, M. I. Raposo, and B. Zuo, 2022, Hydrothermal Alteration Zones' Magnetic Susceptibility Footprints and 3D Model of Iron Oxide-Copper-Gold (IOCG) Mineralization, Carajás Mineral Province, Brazil: Minerals, 12.

Lindenmayer, Z. G., 1990, Salobo sequence, Carajás, Brasil: Geology, Geochemistry and Metamorphism. University of Ontario, 1–407p.

Lindenmayer, Z. G., 2003, Depósito de Cu–Au do Salobo, Serra dos Carajás: Uma revisão, *in* L. H. Ronchu and F. J. Althoff, eds., Caracterização e Modelamento de Depósitos Minerais, Editora Unisinos, 69–98.

Lindenmayer, Z. G., and J. B. G. Teixeira, 1999, Ore genesis at the Salobo copper deposit, Serra dos Carajásds. in Silva, M.G., and Misi, A., eds., Base metal deposits of Brazil: MME/CPRM/DNPM: Base Metal Deposits of Brazil, 33–43.

Lindenmayer, Z. G., L. H. Ronchi, and J. H. LAUX, 1998, Geologia e Geoquímica da Mineralização de Cu-Au Primária da Mina de Au do Igarapé Bahia, Serra dos Carajás: Revista Brasileira de Geociências, 28, 257–268.

Lindenmayer, Z. G., J. H. Laux, and J. B. G. Teixeira, 2001, Considerações sobre a origem das Formações Ferriferas da formação Carajás, Serra dos Carajás: Revista Brasileira de Geociências, 21–28.

Macambira, J. B., 2003, O ambiente deposicional da Formação Carajás e uma proposta de modelo evolutivo para a Bacia Grão Pará. Universidade Estadual de Campinas, 1–200p.

Machado, N., Z. Lindenmayer, T. E. Krogh, and D. Lindenmayer, 1991, U-Pb Geochronology of Archean Magmatism and Basement Reactivation in the Carajás Area, Amazon Shield, Brazil:Macnae, J. et. al., (1998) Fast AEM data processing and inversion. Exploration Geophysics, Vol. 29, pp 163-169.

Macnae, J., King, A., Stolz, E., Osmakoff, A and Blaha, A., 1998, Fast AEM data processing and inversion, Exploration Geophysics 29, 163-169.

Mahanta, A. M., D. B. Boggs, M. H. Dransfield, M. Whittal, G. Liu, and R. Scott, 2001, KING GEORGE: Measured and modelled AGG response over an IOCG terrane: ASEG Extended Abstracts, 1–4.

Martins, P. L. G., C. L. B. Toledo, A. M. Silva, F. Chemale, J. O. S. Santos, and L. M. Assis, 2017, Neoarchean Magmatism in the Southeastern Amazonian Craton, Brazil: Petrography, Geochemistry and Tectonic Significance of Basalts from the Carajás Basin: Precambrian Research, 302, 340–357.

Melo, A. T., and Y. Li, 2019, Geology differentiation of geophysical inversions using machine learning: International Workshop on Gravity, Electrical & Magnetic Methods and Their Applications, 301–304

Melo, A. T., J. Sun, and Y. Li, 2015, Geophysical inversions applied to geological differentiation and deposit characterization: A case study at an IOCG deposit in Carajás Mineral Province, Brazil: SEG Technical Program Expanded Abstracts, 34, 2012–2016.

Melo, A. T., J. Sun, and Y. Li, 2017, Geophysical inversions applied to 3D geology characterization of an iron oxide copper-gold deposit in Brazil: Geophysics, 82, K1–K13.

Melo, A. T., M. G. H. Von, U. J. T. Filho, and R. Fuck, 2014, A comparison between 1D electromagnetic modeling programs: A case history for Cristalino iron Oxide Copper Gold Deposit, Carajás Mineral Province, Brazil: Revista Brasileira de Geofísica, 32, 433–443.

Melo, G. H. C. de, 2014, Evolução Temporal do Depósito de Óxido de Ferro-Cobre-Ouro do Salobo, Província Carajás. Dissertação de Mestrado. Universidade Estadual de Campinas, 1–99p.

Melo, G. H. C. de, 2018, Evolução Temporal e Fonte de Fluidos dos Depósitos IOCG Salobo e Igarapé Bahia, Província Carajás. Tese de Doutorado. Universidade Estadual de Campinas, 1–219p.

Melo, G. H. C. de, L. V. S. Monteiro, R. P. Xavier, C. P. N. Moreto, and E. Santiago, 2019, Tracing fluid sources for the Salobo and Igarapé Bahia deposits: Implications for the genesis of the iron oxide copper-gold deposits in the Carajás Province, Brazil: Economic Geology, 114, 697–718.

Moul, F., and K. Witherly, 2017, Geophysical Results at the Santo Domingo IOCG Deposit, Region III, Chile: Proceedings of Exploration 17: Sixth Decennial International Conference on Mineral Exploration, 17, 569–586.

Mumin, A.H. 2002: Scoping study for hydrothermal iron-oxide copper-gold deposits (Olympic Dam–type), Manitoba; in Report of Activities 2002, Manitoba Industry, Trade and Mines, Manitoba Geological Survey, p. 303308.

Pinheiro, R. V. L., and Holdsworth, R. E., 1997, Reactivation of Archean strike-slip fault systems, Amazon region, Brazil. Journal of the Geological Society, 154, 99–103

Quadros, M. L. do Espirito S., 2020, Geologia, geoquímica e geocronologia das rochas da Suíte Rio Branco, Cinturão Nova Brasilândia e implicações na evolução do orógeno Sunsás no sudoeste do Cráton Amazônico.Brasilia University, 1–132p.

Requia, K., H. Stein, L. Fontboté, and M. Chiaradia, 2003, Re – Os and Pb – Pb geochronology of the Archean Salobo iron oxide copper – gold deposit, Carajás mineral province, northern Brazil: Mineralium Deposita, 38, 727–738.

Richard S. Smith,R. N. Edwards,G. Buselli; An automatic technique for presentation of coincident-loop, impuise-response, transient, electromagnetic data. Geophysics 1994; 59 (10): 1542–1550. doi: https://doi.org/10.1190/1.1443543

Rossignol, C., E. Siciliano Rego, F. Narduzzi, L. Teixeira, J. N. Ávila, M. A. L. Silva, C. Lana, and P. Philippot, 2020, Stratigraphy and geochronological constraints of the Serra Sul Formation (Carajás Basin, Amazonian Craton, Brazil): Precambrian Research, 351, 105981.

Santos, J. O. S., L. A. Hartmann, H. E. Gaudette, D. I. Groves, N. J. Mcnaughton, and I. R. Fletcher, 2000, A New Understanding of the Provinces of the Amazon Craton Based on Integration of Field Mapping and U-Pb and Sm-Nd Geochronology: Gondwana Research, 3, 453–488.

Smith, R.S., and Buselli, G., 1991, Examples of data processed using a new technique for presentation of coincident and in-loop impulse-response transient electromagnetic data: Exploration Geophysics. 22, 363-368.

Tallarico, F. H. B., B. R. Figueiredo, D. I. Groves, N. Kositcin, N. J. McNaughton, I. R. Fletcher, and J. L. Rego, 2005, Geology and SHRIMP U-Pb geochronology of the Igarapé Bahia Deposit, Carajás Copper-Gold Belt, Brazil: an Archean (2.57 Ga) example of Iron-Oxide Cu-Au-(U-REE) Mineralization: Economic Geology, 100, 7–28.

Tavares, F. M.; Oliveira, J. M. O; De Paula, R. R; Costa, I. S. L; Prado, E. B. S. O Cinturão Norte do Cobre da Província Mineral de Carajás: Épocas Metalogenéticas e Controles Críticos das Mineralizações. In: Simpósio de Geologiada Amazônia, 15, SBG-NN, p. 272-275. 2017. [CD-ROM]

Tavares, F.M., Oliveira, J.K.M., Lima, R.B. (Orgs). 2021. Áreas de relevante interesse mineral Província Mineral de Carajá, PA: controles críticos das mineralizações de cobre e ouro do lineamento do Cinzento – Belém: CPRM, 2021. Informe de Recursos Minerais, Série Províncias Minerais do Brasil; n. 33. 154p.

Teixeira, W., M. A. Hamilton, V. A. V. Girardi, F. M. Faleiros, and R. E. Ernst, 2019, U-Pb baddeleyite ages of key dyke swarms in the Amazonian Craton (Carajás/Rio Maria and Rio Apa areas): tectonic implications for events at 1880, 1110 Ma, 535 Ma and 200 Ma: Precambrian Research, 329, 138–155.

Trendall, A. F., M. A. S. Basei, J. R. De Laeter, and D. R. Nelson, 1998, SHRIMP zircon U±Pb constraints on the age of the Carajás formation, Grão Pará Group, Amazon Craton: Journal of South American Earth Sciences, 11, 265–277.

VALE, 2023, Form 20-F. Annual report presented to the United States Securities and Exchange Commission pursuant to section 13 or 15 (d) of the securities exchange act of 1934 for the fiscal year ended: December 31, 2023.

Vasquez, M. L., and L. T. Rosa-Costa, 2008, Geologia e Recursos Minerais Do Estado Do Pará - Sistema de Informação SIG: Texto Explicativo Do Mapa Geológico e de Recursos Minerais Do Estado Do Pará: CPRM-Serviço Geológico do Brasil.

Vella, L., and M. Cawood, 2012, Geophysical Characteristics of the Carrapateena Iron-Oxide Copper-Gold Deposit: ASEG Extended Abstracts, 2012, 1–4.

Wirth, K.R., Gibbs, A.K., Olszewski, W.J., 1986. U-Pb ages of zircons from the Grão Pará Group and Serra dos Carajás Granite, Pará, Brazil: Revista Brasileira de Geociências 16, 195-200.

Xavier, R. P., L. V. S. Monteiro, C. R. Souza Filho, I. Torresi, E. R. Carvalho, A. M. Dreher, M. Wiedenbeck, R. B. Trumbull, A. L. S. Pestilho, and C. P. N. Moreto, 2010, The Iron Oxide Copper-Gold Deposits of the Carajas Mineral Province, Brazil: an Updated and Critical Review: In: Porter T.M. (Ed.), Hydrothermal Iron Oxide Copper-Gold and Related Deposits: A Global Perspective. Adelaide, PGC Publishing, 3, 285–306.

3. Petrophysical Signature of the Salobo IOCG Deposit: Insights into Lithology, Hydrothermal Alteration, and Mineralization

Moriá Caroline de Araújo[1], Adalene Moreira Silva[1], Catarina Labouré Bemfica Toledo[1], Daniel Shkromada de Oliveira[1], Victor Nogueira[2], Juliana Araújo[13], Edvaldo Gomes Farias[3], and Lucas Nunes Morais[1]

[1] University of Brasília, Institute of Geosciences, Brasília, DF, Brazil

[2] Axt and Automated Mineralogy Incubator

[3] Vale S.A. Estrada Raimundo Mascarenhas, s/n, Galpões de Testemunho de N5, 68516-000, Parauapebas PA, Brazil

moria_araujo@hotmail.com, adalene@unb.br, catarinatoledo@unb.br, daniel.oliveira@fundamentogeofisica.com.br, juliana.araujo@vale.com, victor.nogueira@axt.com.au, edvaldo.gomes.faria@vale.com, lucasnunesmorais612@gmail.com

ABSTRACT

The integration of petrophysical and mineralogical data is essential for understanding variations in the physical properties of hydrothermally altered rocks. In this study, petrophysical data were combined with mineralogical analyses obtained through TIMA (TESCAN Integrated Mineral Analyzer), QEMSCAN (Quantitative Evaluation of Minerals by Scanning Electron Microscopy), and LIBS (Laser-Induced Breakdown Spectroscopy core scanner) to characterize the petrophysical footprint of the Salobo IOCG (Iron Oxide Copper-Gold) deposit. The analysis and interpretation of rock physical properties and mineral mapping data reveal that the Salobo alteration zones exhibit distinct petrophysical signatures. Calcic-sodic alteration zone is characterized low density (~2.89 g/cm³), low magnetic susceptibility (~0.091 SI), and moderate resistivity (~2781 Ωm). A newly identified Ca-Fe-K subzone marks the transition from Ca-Na to Fe- and K-enriched systems presenting a slight increase in resistivity (~2958 Ωm). Iron enrichment zones display systematic transitions, progressing from grunerite-dominated assemblages to almandine-rich zones and magnetite precipitation. These zones are distinguished by high density (>3.30 g/cm³), elevated magnetic susceptibility (up to 7.516 SI), and increased chargeability (~62.2–89.7 mV/V). The K-Fe subzone and its advanced forms are characterized mainly by almandine and biotite, along with intense late chloritization that significantly affects petrophysical signatures. Potassic alteration presents a strong decrease in resistivity (~1658 Ωm), attributed to biotite and sulphides. This study highlights the importance of integrating multi-source data to enhance the understanding of mineral systems through mineralogical and petrophysical datasets. Petrophysical properties, controlled by mineral composition, provide insights into Salobo's geophysical signature and petrophysical footprint. Thus, a schematic model was developed to illustrate the petrophysical signature of each subzone hydrothermal alteration zone, linking variations in density, magnetic susceptibility, resistivity, and

chargeability to mineralogical data. The presented methodology provides a framework applicable to other IOCG deposits, similar systems, and potential targets, enhancing exploration efficiency, and providing valuable strategies for advancing mineral exploration on a broader scale.

3.1. Introduction

Understanding the petrophysical signature of mineral deposits and associated alteration zones at both surface and subsurface is crucial for mineral exploration. As exploration move deeper, reliance on geophysical data will increase, requiring appropriate interpretations through geological, petrophysical and, mineralogical analyses to inform prospecting strategies. Knowledge of how physical properties vary with rock types, hydrothermal alteration, and mineralization is therefore paramount as it improves exploration efficiency and increases the likelihood of new discoveries by improving exploration models.

Petrophysical data not only provides insights into the geophysical signature of deposits, it can also be used for many other applications. Petrophysical data analysis involves factors like rock type, alteration, weathering, metamorphism, deformation, porosity, and stratigraphy (Dentith & Mudge, 2014; Dentith et al., 2020; Araújo et al., 2022). Through the integration of petrophysical data with geological, petrological, and mineralogical information it is possible to investigate how these factors affect physical properties. These correlations can then be used to improve core logging, mapping and the overall geological understanding of mineral deposits.

Petrophysical databases in the mining industry are usually limited to magnetic susceptibility and density measurements due to their cost-effectiveness and easiness of acquisition (Williams, 2009; McGladrey et al., 2017). While these measurements are efficient, few studies have integrated petrophysical data with mineralogical and geochemical data (Sandrin et al., 2009; Aguilef et al., 2017; Bérubé et al., 2018; Austin et al., 2021). Although there are papers on combinations of geochemical and mineralogical data in the literature, the integrated analysis of multiple physical properties is still incipient.

Salobo, located in the Carajás Mineral Province, is the second biggest IOCG deposit in the world. It contains reserves of 1088.9 Mt at 0.62% Cu and 0.35 g/t Au (VALE, 2023), and it is one of the few known Archean IOCG deposits (Hitzman, 2000; Groves et al., 2009; Xavier et al., 2010). Its broad IOCG classification encompasses deposits with diverse deposits with varying petrophysical and geophysical signatures, influenced by variations in mineralogy, texture, and structural controls (Austin el al., 2018; Skirrow, 2022). Recognizing these signatures and underlying geological processes is critical for effective exploration. The deposit is associated with the Cinzento shear zone, a regional-scale structure formed around 2.55 Ga. It defines the contact between the Neoarchean volcanosedimentary rocks of the Itacaiúnas Supergroup, and the Igarapé Gelado metagranite. This structure focused intense deformation and hydrothermal alteration, which generated a corridor that hosts several IOCG deposits, district-scale alteration

and mylonitic rocks (Réquia et al., 2003; Melo et al., 2016). The ore is primarily composed of bornite, chalcocite, magnetite, and smaller amounts of chalcopyrite and gold, with significant contents of Co, Ni, As, Ag, Mo, and REE (Melo et al., 2019, Costa et al., 2016).

This paper aims to describe Salobo's alteration patterns and petrophysical signature through an integrated analysis of density, magnetic susceptibility, resistivity, conductivity, and chargeability data, combined with mineralogical information. By correlating petrophysical signatures with mineral assemblages and hydrothermal processes, this approach enhances IOCG exploration models and improves the detection of prospective targets in similar geological settings.

3.2. Geological Context

The Carajás Mineral Province is located in southeastern Amazonian Craton, a major Precambrian geotectonic unit in South America. The Amazonian Craton was formed through crustal accretion during the Paleoproterozoic and Mesoproterozoic (Vasquez & Rosa-Costa, 2008; Duncan et al., 2010). This craton is overlain by the Amazonas and Solimões sedimentary basins (Santos et al., 2000; Teixeira et al., 2019; Quadros, 2020) (Figure 3.1A). The Carajás Domain, located in the northern part of the Carajás Province, is prominent for hosting world-class Iron Oxide-Copper-Gold (IOCG) deposits along two main belts: Northern and Southern Copper Belts (Figure 3.1B) (Vasquez et al., 2008; Melo et al., 2021).

This domain features Neoarchean to Paleoproterozoic volcano-sedimentary sequences that overlie the Mesoarchean Xingu Complex (3066 ± 6 Ma), comprised of TTG gneisses and mafic granulites (Delinardo da Silva, 2014; Melo et al., 2021). The Neoarchean Itacaiúnas Supergroup (2.76–2.74 Ga) was likely formed in a rift or back-arc setting and comprises volcanic rocks, banded iron formations, and siliciclastic sequences (DOCEGEO, 1988; Tavares et al., 2018; Martins et al. 2017). Widespread felsic and A-type granite magmatism, including 1.88 Ga intrusions, is also present (Vasquez et al., 2008; Melo et al., 2021) (Figure 3.1B). Granitic magmatism events include: 1) Neoarchean (~2.76–2.73 Ga) marked by subalkaline type-A granites; 2) Younger intrusions (~2.56 Ga) peralkaline granites, such as Old Salobo; and 3) Paleoproterozoic anorogenic granitic plutons (~1.88 Ga), such as Young Salobo (Dall'Agnol et al., 2006).

The regional structural setting is characterized by NW-SE to WNW-ESE transtensional striking structures, primarily represented by the Carajás, Cinzento, and Canaã shear zones, which significantly influence the location of major Cu-Au deposits such as Paulo Afonso, Furnas, QT-02, and Salobo (Pinheiro et al., 2013; Melo et al., 2021) (Figure 3.1B). The northern belt comprises deposits hosted along the Carajás and Cinzento shears, while the southern belt comprises deposits hosted along the Canaã shear zone.

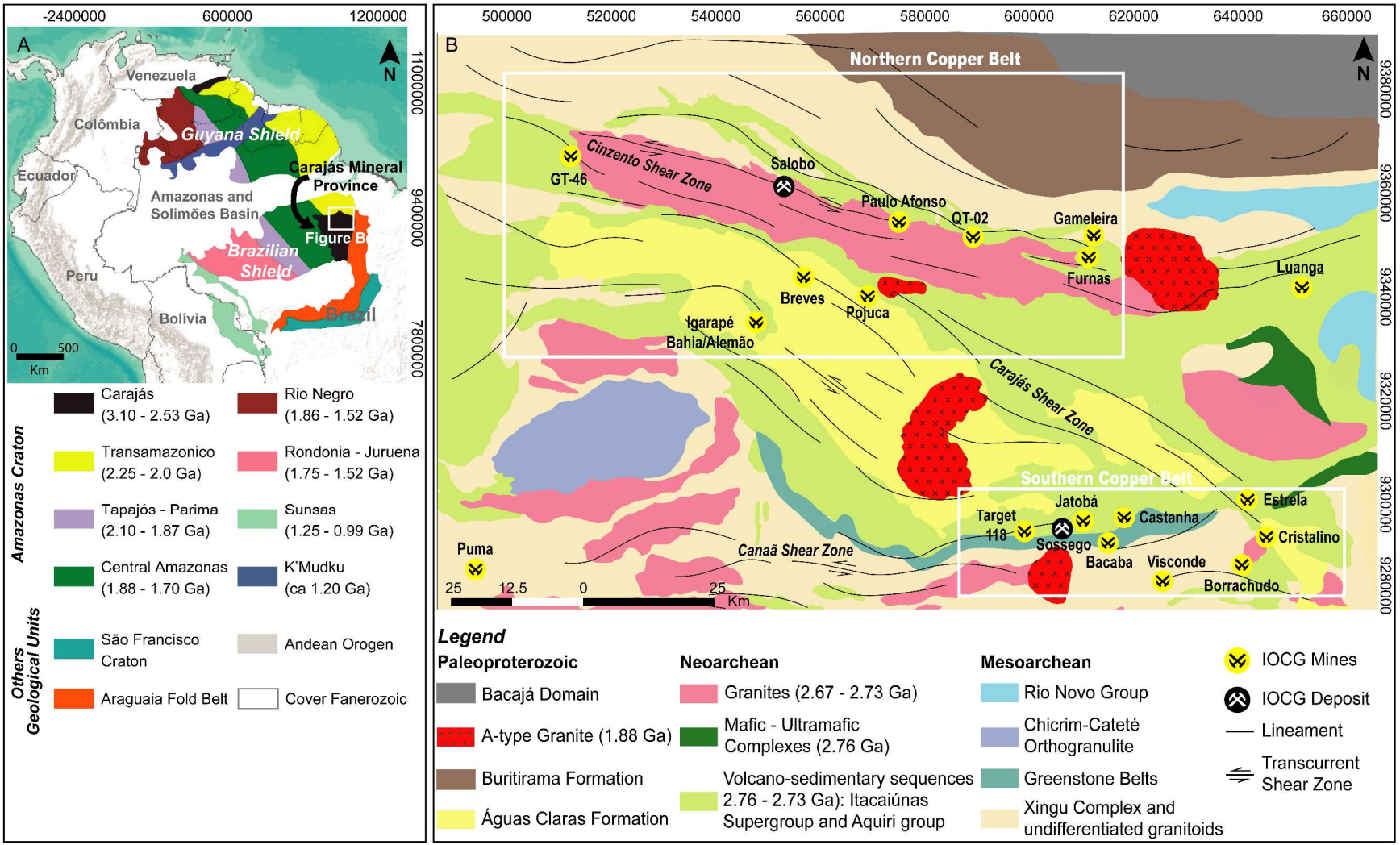


Figure 3. 1 – A) Tectonic division of the Amazonian Craton, showing the location of the Carajás Mineral Province (Modified from Santos et al., 2000). B) Geological map of the northern part of the Carajás Mineral Province, also known as the Northern and Southern Copper Belt, including the Cinzento Lineament. The location of the main Cu-Au deposits, including Salobo, is shown (modified from Vasquez & Rosa-Costa, 2008 and Tavares, 2015).

3.2.1. Salobo Deposit

Salobo is hosted within deformation zones that intersect the Neoarchean Igarapé Gelado Suite (2763 ± 4.4 Ma) and the orthogneisses of the Mesoarchean Xingu Complex (2950±25 and 2857 ± 6.7 Ma) (Melo, 2016). The mineralization appears as imbricated slices within the granites (Melo, 2014; Melo et al., 2019) (Figure 3.2A). The footwall features sheared quartzites (Figure 3.2A), and volcano-sedimentary sequences from the Itacaiúnas Supergroup (Melo et al, 2016). These highly deformed and hydrothermally altered rocks underwent through multiple episodes of fluid circulation and hydrothermal-mineralizing events (Moreto et al., 2015, Trunfull et al., 2020, Teixeira et al. 2021). The host rocks developed a sub-vertical mylonitic foliation associated with the Itacaiúnas shear zone (ca. 2.7 Ga) and the Cinzento Shear Zone (2.555 ± 4 Ma) (Machado et al., 1991).

Additionally, the host rocks are intruded by the A-type Old Salobo Granite (2573 ± 2 Ma) (Machado et al., 1991; Lindenmayer, 2003) (Figure 3.2A), and the Paleoproterozoic Young Salobo Granite (1.880 ± 80 Ma) (Cordani, 1981; Lindenmayer, 1990). These granitic intrusions are located on the northern and southern sides of the deposit, with Neoproterozoic diabase dikes cutting across both mineralization and host rocks, representing the last magmatic event in the region (Lindenmayer, 1990; Machado et al., 1991; Pinheiro and Holdsworth, 1997) (Figure 3.2A).

Intense ductile deformation due to shearing created NW-SE trending and steeply dipping mylonitic rocks which were strongly hydrothermally altered (Réquia et al., 2003; Melo et al., 2016; Burns et al., 2019). The orebodies are structurally controlled along the ductile-brittle shear zones (Réquia et al., 2003; Burns et al., 2019).

Salobo presents a complex history of hydrothermal alteration processes. The main sequence includes 1) extensive calcic-sodic alteration halos, dominated by hastingsite and actinolite (Figures 3.2B, 3.2C); 2) silicification, encompassing multiple phases of hydrothermal quartz formation (Figures 3.2B, 3.2C); 3) high-temperature Fe-K alteration halos characterized by almandine + grunerite + biotite + magnetite (Figures 3.2B, 3.2C); 4) proximal potassic-ferric alteration, with biotite and mineralized sulphides (Figures 3.2B, 3.2C) (Réquia et al., 2003; Melo, 2014, 2016); 5) an overprinting low-temperature hydrothermal assemblage mostly with stilpnomelane (Figures 3.2B, 3.C) (Melo et al, 2016); 6) late-zone potassic and propylitic hydrothermal alteration that overlays the typical IOCG hydrothermal assemblage marked by the presence of potassic feldspar (Melo et al, 2016) (Figures 3.2B, 3.2C). The ore at Salobo consists of abundant magnetite with disseminated or massive bornite and chalcocite, along with subordinate chalcopyrite (Réquia et al., 2003; Lindenmayer, 2003; Melo et al., 2016).

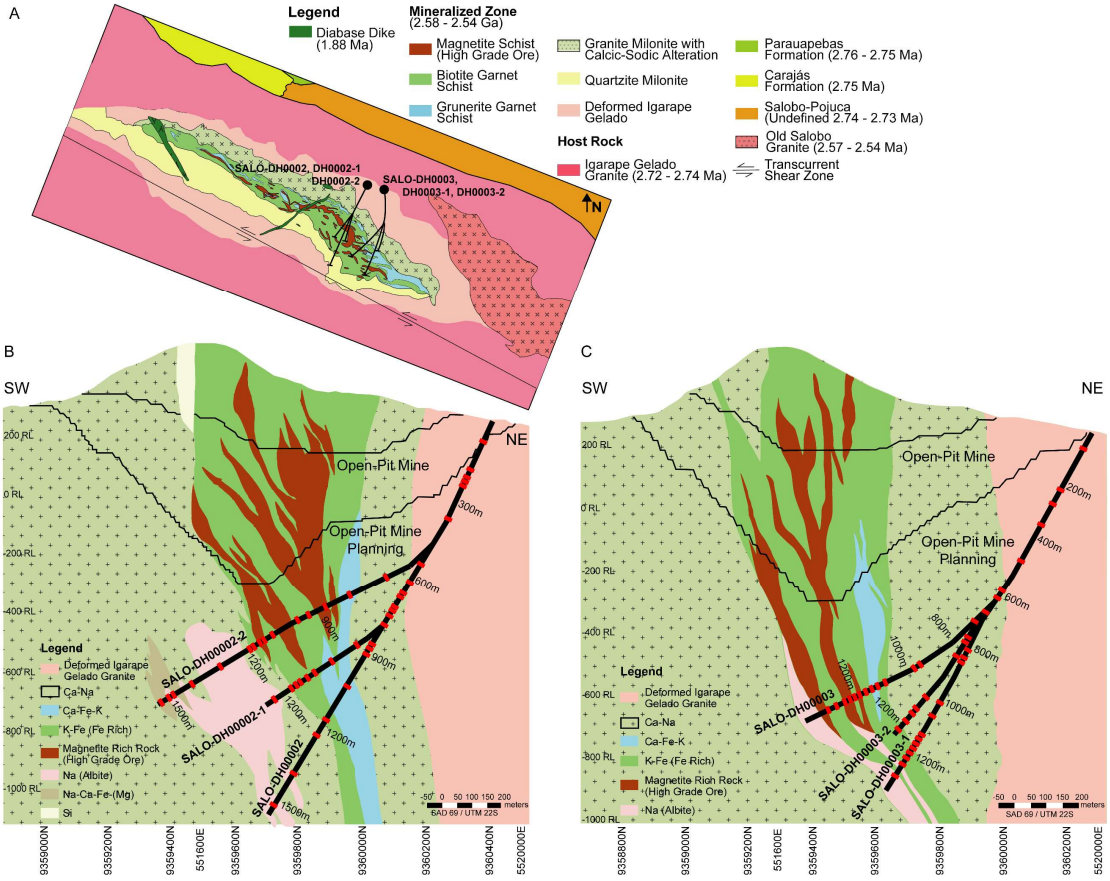


Figure 3. 2 – A) Geological map of the Salobo deposit illustrating the main geological units, alteration halos, and the mineralized zones. B) Geological cross-section depicts the alteration types of the Salobo deposit, highlighting the deep drilling holes SALO-DH00002, 2-1, and 2-2, along with the location of all samples (red points along the holes). C) Geological cross-section depicts the alteration types of the Salobo deposit, highlighting the deep drilling holes SALO-DH00003, 3-1, and 3-2, along with the location of all samples (red points along the holes) (Modified from Araújo et al., submitted).

3.3. Materials and Methods

This section presents the data and methods used in this study, focusing on a multidisciplinary approach that included established tools, and advanced analytics were adopted to investigate the petrophysical signature and mineralogical framework of Salobo. The methodology included petrophysics (multi-tool logging and core measurements), petrography, high-resolution Scanning Electron Microscopy (SEM), such as QEMSCAN and TIMA, as well as laser-induced breakdown spectroscopy (LIBS) data. Drill cores from six representative drill holes were provided by Vale S.A. for these measurements. Additional information for depths in the drill cores can be found in the supplementary material.

3.3.1. Sampling

The drill holes provided (DH00002, 2-1, 2-2, 3, 3-1, and 3-2) were analysed and sampled (Figures 3.2B, 3.2C). A total of 56 samples were collected (Figures 3.2B, 3.2C), encompassing

host granites from the Igarapé Gelado Suite, hydrothermal alteration sequences, and the mineralized zone.

3.3.2. Petrophysics

Magnetic susceptibility and inductive conductivity data were acquired on pulp samples. Density, chargeability and galvanic resistivity were acquired on core samples. Measurements were made at Vale's geophysics laboratory in Parauapebas, Brazil. Magnetic susceptibility and conductivity were measured with a KT-10 S/C portable meter from Terraplus Inc. To ensure representative results, physical properties (excluding density and chargeability) were measured four times for accuracy. The first measurement, used as a reference, was not recorded, while the subsequent three measurements were averaged. To ensure consistency, all readings were required to deviate by less than 10% from the initial reference value. If any measurement exceeded this variation or if the reference value fell outside the expected range, the process was restarted. Dry bulk density was determined using the water displacement method, as detailed in Burns et al. (2019), with core samples. Resistivity and chargeability were measured using a GDD SCIP tester from Instrumentation GDD. Sample preparation followed the GDD Sample Core Induced Polarization tester's guidelines. Detailed petrophysical data are available in Appendix A.

3.3.3. Petrography and Scanning Electron Microscope (SEM)

A total of 56 thin sections from quartered aliquots were analyzed and described. Of these, 34 were coated with a 15 nm carbon film for Scanning Electron Microscope (SEM) analysis. SEM-based automated mineralogical techniques, integrated with Energy Dispersive X-ray Spectroscopy (EDS), enabled precise mineral identification, elemental analysis, and quantitative evaluation of mineral content, grain size, and associations. Two SEM-based analyses were performed: QEMSCAN (Quantitative Evaluation of Minerals by Scanning Electron Microscopy) and TIMA (TESCAN Integrated Mineral Analyzer).

QEMSCAN analysis was conducted at the Institute of Geosciences, University of Brasília (IG-UnB), using a Quanta 650F field emission scanning electron microscope with a tungsten source, operating at 25 kV and 10 nA, and equipped with two Bruker XFlash 6–30 SDD energy-dispersive spectrometers. A total of 20 thin sections were scanned at 15-µm resolution. TIMA analysis was performed at AXT PTY LTD in Australia. This system integrates SEM with EDS, utilizing up to four EDAX Element silicon drift detectors to enhance sensitivity and accommodate high count rates. Fourteen thin sections were analyzed. Both provided detailed quantitative and qualitative mineral data, including concentrations, element distributions, and mineral texture properties. Image analysis generated mineral distribution maps with 47 identified minerals, accompanied by a table of percentages. The same color scale and regrouping method were applied in both analyses. Detailed mineral percentages are available in Appendix A.

3.3.4. Laser-induced breakdown spectroscopy (LIBS)

A total of 56 thin-section offcuts from samples were analyzed using LIBS to determine elemental composition. The analyses were conducted at AXT PTY LTD using the ECORE drill core analyzer (ELEMISSION Inc.), which employed a fully automated system integrating a laser source, spectrometer, 2-axis translation table, and ablation chamber. This setup features 3D laser profiling with 30 µm precision, a high-resolution optical camera, and advanced lighting for detailed imaging. The LIBS system, with a spectrometer range of 220–990 nm and a CMOS detector capturing 1000 frames per second, enabled multi-element assays, quantitative mineralogy, and rock quality assessments. Despite its lower resolution, the method identified 29 minerals, categorized using the same colour scale as QEMSCAN and TIMA analyses. Detailed mineral percentages are available in Appendix A.

3.3.5. Integration of petrophysical data and mineral mapping

Distinguishing the hydrothermal alteration zones within the complex Salobo system can be challenging. Previous studies on the parageneses and mineral associations identified six distinct zones (Melo et al., 2016 and Diniz et al., 2023). During sampling, while some of these zones were confirmed, new ones were identified and sampled in a deep portion known as Deep Salobo, below the current open pit of the deposit. In total, seven zones were identified and classified: host rocks, calcic-sodic, iron enrichment, potassic, mineralization (ore), later albitization, and post-ore.

To map the most well-preserved host rock and the progression of alteration, representative samples were categorized into six groups based on alteration intensity. These groups include: well-preserved host rock, initially altered host rock (Initial Alt.), moderately altered host rock (Mod. Alt.), advanced altered host rock (Adv. Alt.), chloritized host rock (Chl), and diabase (Dia). The remaining zones and subzones were classified based on specific mineral concentrations, resulting in fourteen subzones that will be described in detail later. The calcic-sodic alteration, for example, is identified in samples with significant content of actinolite and albite. Samples with high concentrations of minerals linked to various zones (e.g., biotite, which is linked to Fe enrichment and potassic alteration) were excluded to reduce misleading data distributions. While some overlap between zones may occur, this quantitative approach provided robust results.

Petrophysical data were integrated with mineral content for each zone and subzone, and analysed according to paragenetic sequences, highlighting overprinting relationships. Figure 3.3 is a general flowchart detailing all workflow steps, from sampling to the integration of petrophysical data, mineral mapping, and the development of an exploratory guide model. It also emphasizes the mineral mapping approach, highlighting the key minerals used to classify each zone and subzone. The results acquired allowed us to propose the petrophysical footprint and assess its implications for mineral exploration in the Northern Copper Belt.

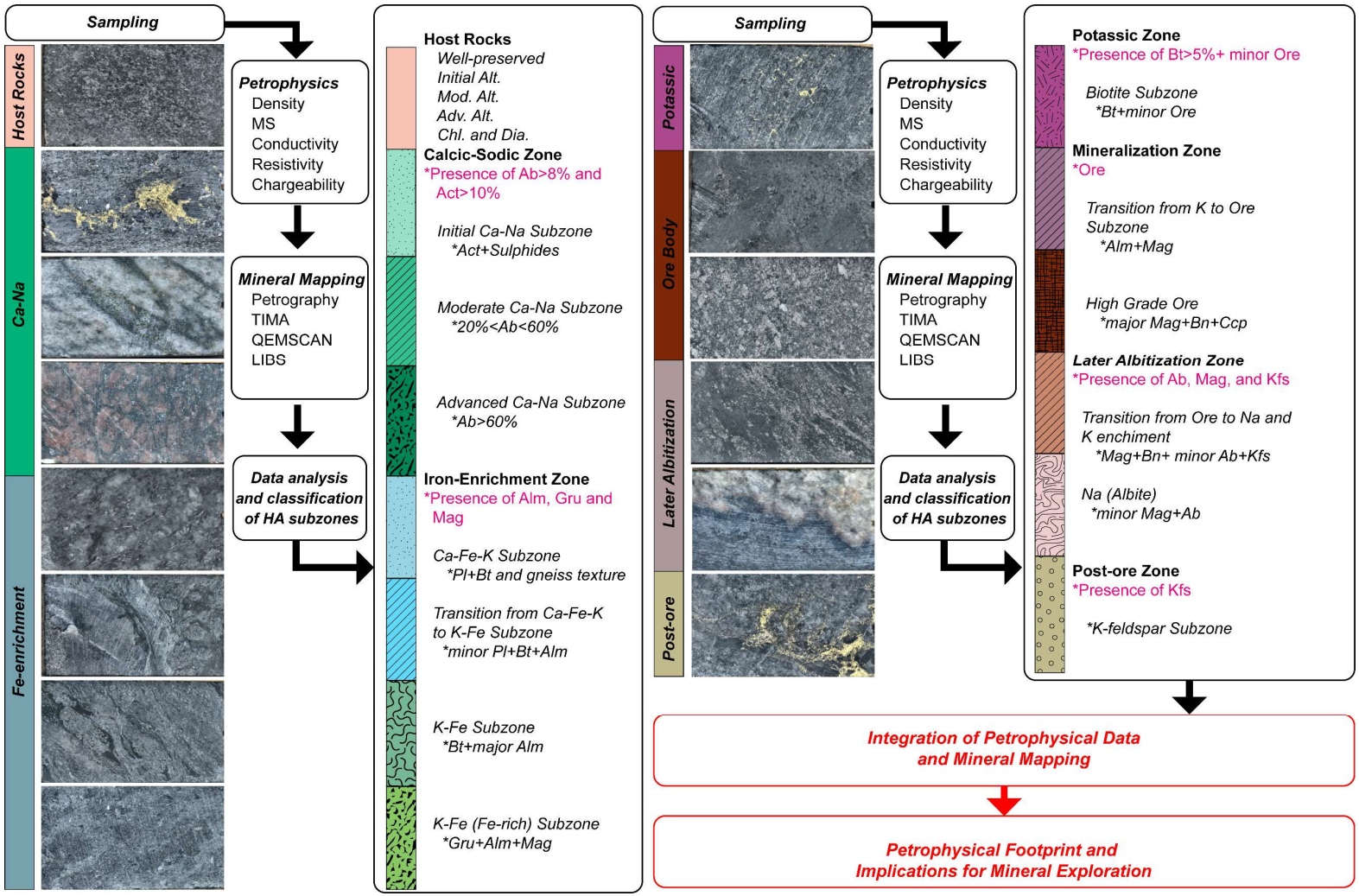


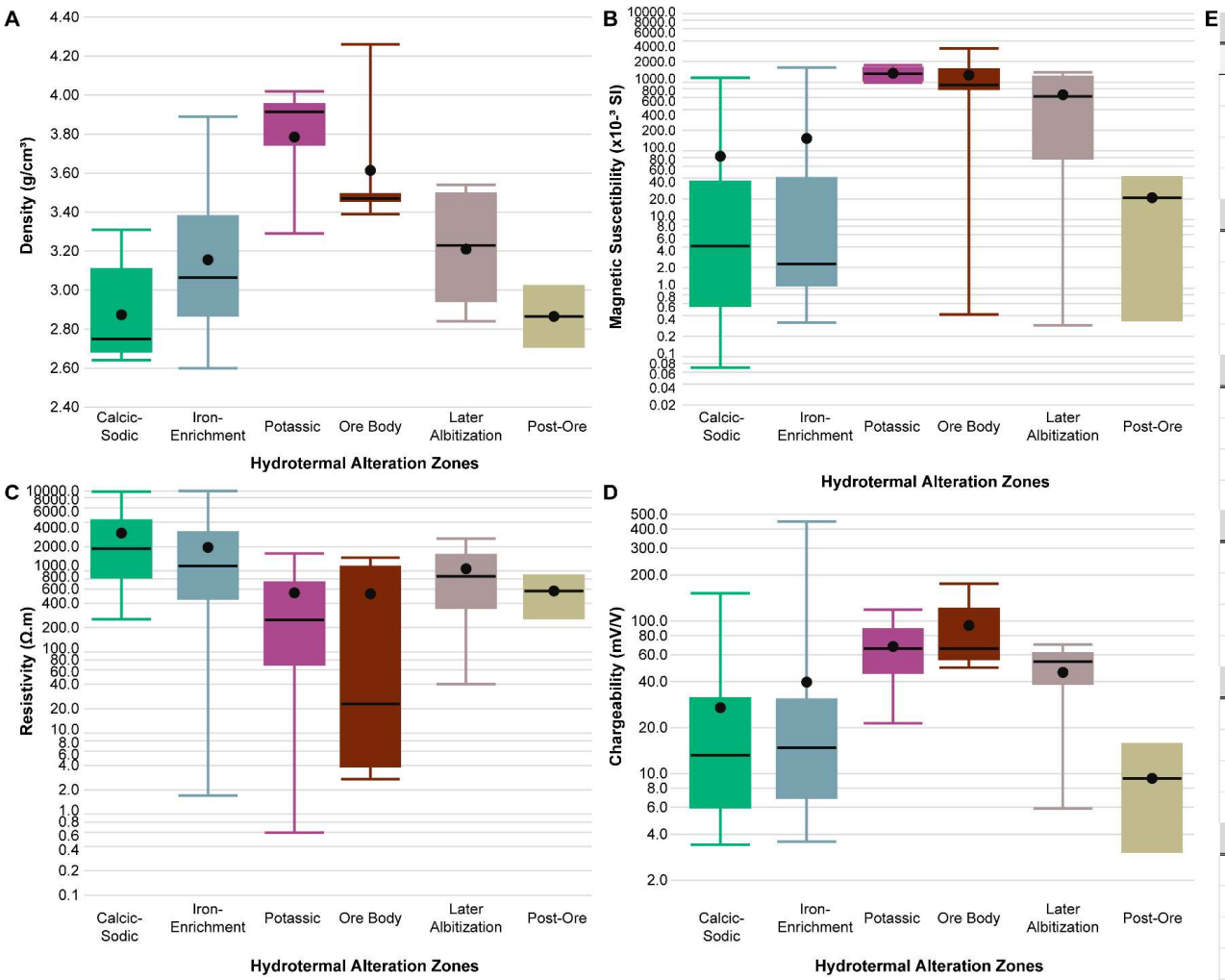
Figure 3. 3 - Flowchart detailing all workflow steps, from sampling to the integration of petrophysical data and, mineral mapping, for the characterization of the petrophysical footprint of the Salobo deposit. *Abbreviations: MS – Magnetic Susceptibility, HA – Hydrothermal Alteration, Initial Alt – initially altered rock, Mod Alt - moderately altered rock, Adv Alt - advanced altered rock, Chl – Chloritized, Dia - Diabase (Dia), Ab – Albite, Act – Actinolite, Alm – Almandine, Bt – Biotite, Bn – Bornite, Ccp – Chalcopyrite, Gru – Grunerite, Kfs – K-feldspar, Mag – Magnetite, Pl – Plagioclase, and Qz – Quart.*

3.4. Results and Discussion

Research on the petrophysical characteristics of mineralized systems remains relatively limited compared to the extensive geophysical interpretations of deposits and the abundance of geochemical studies (Sandrin et al., 2009; Williams, 2009; Aguilef et al., 2017; McGladrey et al., 2017; Bérubé et al., 2018; Austin et al., 2021). Nevertheless, numerous investigations over the years have contributed valuable qualitative and quantitative insights into the petrophysical properties and zonation of IOCG deposits.

Considering the six main zones identified in this study, as well as in the research by Melo et al. (2016) and Diniz et al. (2023), the qualitative petrophysical data exhibit significant variations when analysed using boxplots (Figure 3.4). These populations, evident in the broad range between minimum and maximum values and the interquartile range, underscore the need for further in-depth analysis and discussion. Among the average of hydrothermal alteration zones: 1) density is highest in the ore body (average value ~3.61 g/cm³) and lowest in the post-ore zone (average value ~2.87 g/cm³); 2) magnetic susceptibility reaches its highest value in the potassic zone (average value ~1347.49 x10^{-3} SI) and its lowest in the post-ore zone (average value ~0.34 x10^{-3} SI), which can be considered an outlier; 3) resistivity is highest in the calcic-sodic zone (average value ~2936.70 Ω.m) and lowest in the iron enrichment zone (average value ~1956.56 Ω.m); 4) chargeability is highest in the ore body (average value ~93.51 mV/V) and lowest in the post-ore zone (average value ~9.36 mV/V).

Given the substantial petrophysical variations across the six main alteration zones, along with the mineral compositions identified through mineral mapping, new subzones are proposed and discussed below.



E

Calcic-Sodic	No. of Samples	Min.	Average	Max.	Median	Std Dev
Density	18	2,64	2,85	3,31	2,73	0,22
MS		0,07	83,42	1168,22	4,13	264,75
Resistivity		254,66	2936,70	9833,03	1889,34	2687,43
Chargeability		3,42	27,03	151,71	13,17	35,78
Iron-Enrichment						
Density	23	2,60	3,14	3,89	3,05	0,36
MS		0,32	151,76	1625,78	2,25	379,70
Resistivity		1,70	1956,56	10022,78	1148,38	2306,54
Chargeability		3,58	39,78	449,24	14,78	89,67
Potassic						
Density	4	3,29	3,79	4,02	3,92	0,29
MS		978,78	1347,49	1770,07	1320,57	319,09
Resistivity		0,59	538,28	1651,98	250,28	660,30
Chargeability		21,34	68,09	118,89	66,07	35,55
Ore Body						
Density	5	3,39	3,61	4,26	3,47	0,32
MS		0,41	1266,02	3085,53	910,03	1031,34
Resistivity		2,71	523,71	1468,37	22,84	638,95
Chargeability		49,61	93,51	175,56	66,12	47,87
Later Albitization						
Density	4	2,84	3,21	3,54	3,23	0,30
MS		0,29	656,47	1388,58	618,51	612,08
Resistivity		40,38	1065,45	2509,29	856,07	940,77
Chargeability		5,89	46,05	70,02	54,14	24,27
Post-ore						
Density	2	2,71	2,87	3,02	2,87	0,16
MS		0,34	20,81	41,28	20,81	20,47
Resistivity		261,97	567,89	873,81	567,89	305,92
Chargeability		3,08	9,30	15,52	9,30	6,22

Figure 3. 4 - Petrophysical boxplots of hydrothermal alteration zones of Salobo Deposit and statistical summary table. A) Density boxplot; B) Magnetic Susceptibility boxplot; C) Resistivity boxplot; D) Chargeability boxplot; E) Statistical summary table of petrophysical data for hydrothermal alteration zones, including minimum, average, maximum, median, and standard deviation. *Abbreviations: MS – Magnetic Susceptibility*

3.4.1. Host rocks

The deep portion of the Salobo deposit is hosted in granitic rocks of the Gelado Suite and mafic rocks (Carvalho et al. - *submitted*). Although these rocks represent primary protoliths, they exhibit signs of incipient hydrothermal alteration, which becomes progressively more pronounced toward the core of the mineralized system.

This evolution is reflected in core samples, such as sample 3A, which represents a mafic protolith and is typically described as a metamorphic paragenesis composed of hornblende, plagioclase, and quartz, with minor sodic alteration minerals such as albite and chlorite (Figure 3.5A). The host rocks exhibit distinct petrophysical properties that differentiate them from altered and mineralized rocks. All supporting data are available in Appendix A.

Host rocks exhibit distinct petrophysical properties that set them apart from altered and mineralized rocks. The density of the host rocks (Figure 3.5B) is relatively low, ranging from 2.70 to 3.10 g/cm³, compared to altered rock (2.72 to 4.26 gcm^3). Magnetic susceptibility (Figure 3.5C) is very low, with values near 0.001 SI, contrasting with moderate (0.001 to 1.00 SI) and advanced (0.009 to 3.08 SI) alteration, where the higher magnetite content significantly increases magnetic susceptibility. Resistivity (Figure 3.5D) is high with a median value of 3,800 Ω.m and high value of 10,000 Ω.m, which provides a strong contrast compared to the sulphide-rich, conductive altered rocks (1 to 3,000 Ω.m). Additionally, chargeability (Figure 3.5E) is below 50 mV/V and significantly lower than altered rocks.

Samples classified as moderately altered (Mod Alt) exhibit a distinct signature, characterized by greater variability, larger quartiles, and the presence of outliers. This variation is associated to the other zones and subzones of Salobo hydrothermal alteration, which include a range of samples from the distal zone (Ca-Na alteration) to the proximal zone. This progression includes iron enrichment, the potassic alteration, and the beginning of the mineralisation, named as transition from K alteration to the ore body.

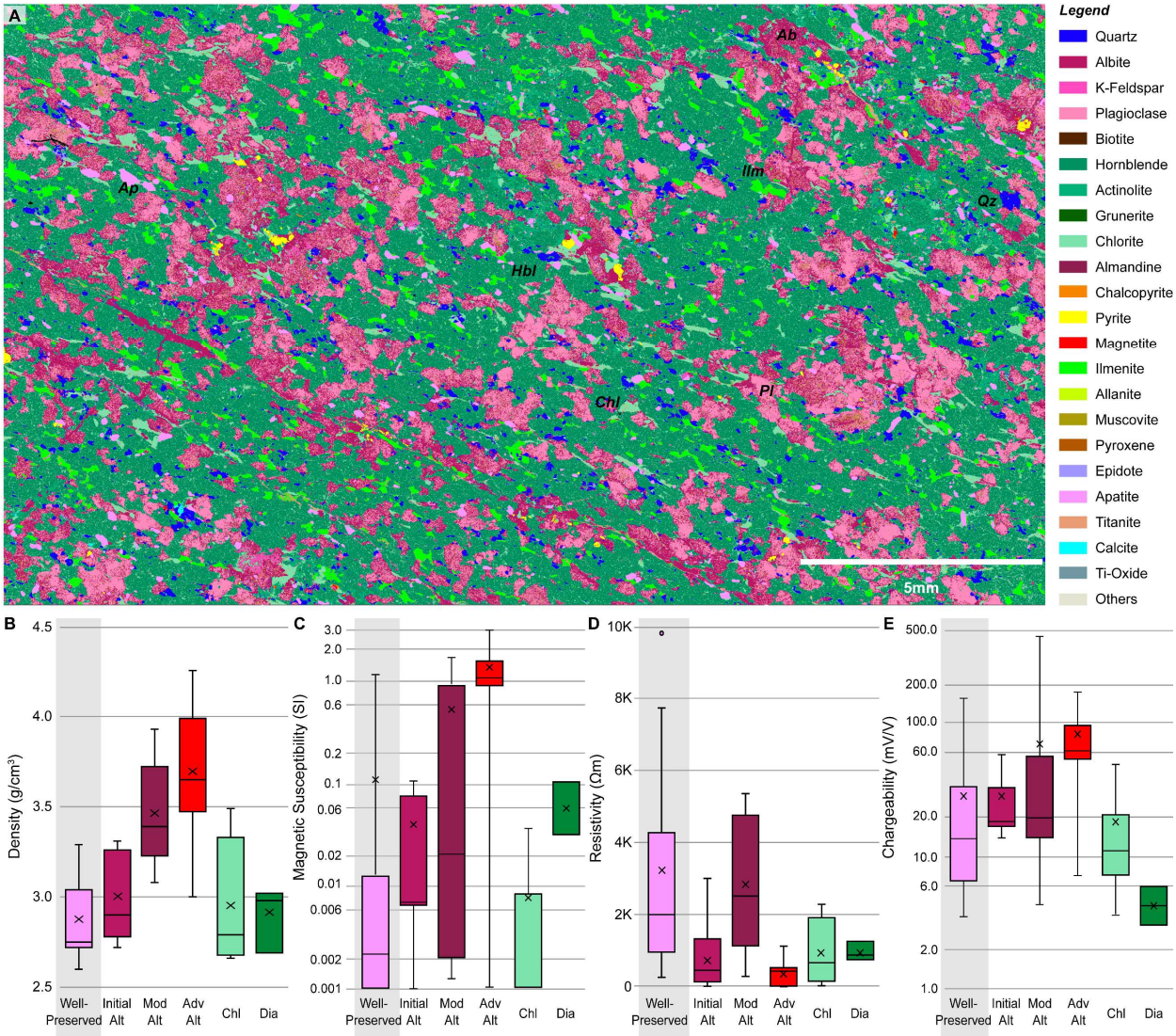


Figure 3. 5 - TIMA image of well-preserved host rock and petrophysical boxplots for the assigned classes. A) Sample 3A, representing the well-preserved host rock, is primarily composed of hornblende, plagioclase, quartz, and albite. B) Density boxplot. C) Magnetic susceptibility boxplot. D) Resistivity boxplot. E) Chargeability boxplot. *Abbreviations: Ab – Albite, Chl – Chlorite, Hbl - Hornblende, Ilm – Ilmenite, Pl – Plagioclase, Qz – Quartz, Initial Alt – initially altered rock, Mod Alt - moderately altered rock, Adv Alt - advanced altered rock, Chl – Chloritized and Dia - Diabase (Dia).*

3.4.2. Calcic-Sodic alteration

During sampling, three subzones of Ca-Na alteration were identified: 1) initial, 2) moderate, and 3) advanced (restricted to albitites). The initial zone, represented by sample 2C (Figure 3.6A), is characterized by the dominance of actinolite and biotite, chalcopyrite and pyrite, along with subordinate albite, aligning with Melo et al. (2016). The moderate zone, exemplified by sample 3-2A (Figure 3.6B), is characterized by quartz, albite, epidote, and titanite. The presence of epidote indicates a Ca enrichment in the alteration system. The advanced zone is represented by sample 2P (Figure 3.6C), described as albitite with minor magnetite. The observed mineralogy

in these three samples is consistent with the calcic-sodic (Ca-Na) alteration zone described by Melo et al. (2016).

Calcic-sodic alteration samples typically exhibit relatively low density (2.85 g/cm^3), low magnetic susceptibility (0.083 SI), and average resistivity values (2936 Ω.m), when compared to other IOCG deposits, such as Cristalino, Furnas and Ernest Henry (Austin el al., 2018; Melo et al., 2011; Leao et al., 2022). Figure 3.6D shows a plot of magnetic susceptibility versus density considering samples with albite>8% and actinolite>10%. Samples with ore minerals and biotite are considered outliers. They exhibit increased density (2.92 g/cm³) and magnetic susceptibility (0.174 SI), along with decreased resistivity (2752 Ω.m).

Albite-rich samples tend to have higher magnetic susceptibility (0.081 SI) than actinolite-rich samples (0.056 SI). This deviation could be attributed to either the difference in the amount of samples from each zone, 18 versus 4 respectively, or geological context. In some samples, albite-rich samples contain traces of magnetite, which increases the magnetic susceptibility values. Actinolite typically results in higher densities and resistivities (3.15 g/cm³ and 2970 Ω.m) (Figure 3.6D), compared to albite-rich samples (2.78 g/cm³ and 2759 Ω.m). The increased density in actinolite-rich samples (gray-shaded oval marks in Figure 3.6D) suggests a higher ferromagnesian content in the protolith. Albite-actinolite alteration is common in mafic to intermediate protoliths, such as gneisses, potentially replacing Na-Ca zones, as also reported by Melo et al., (2016).

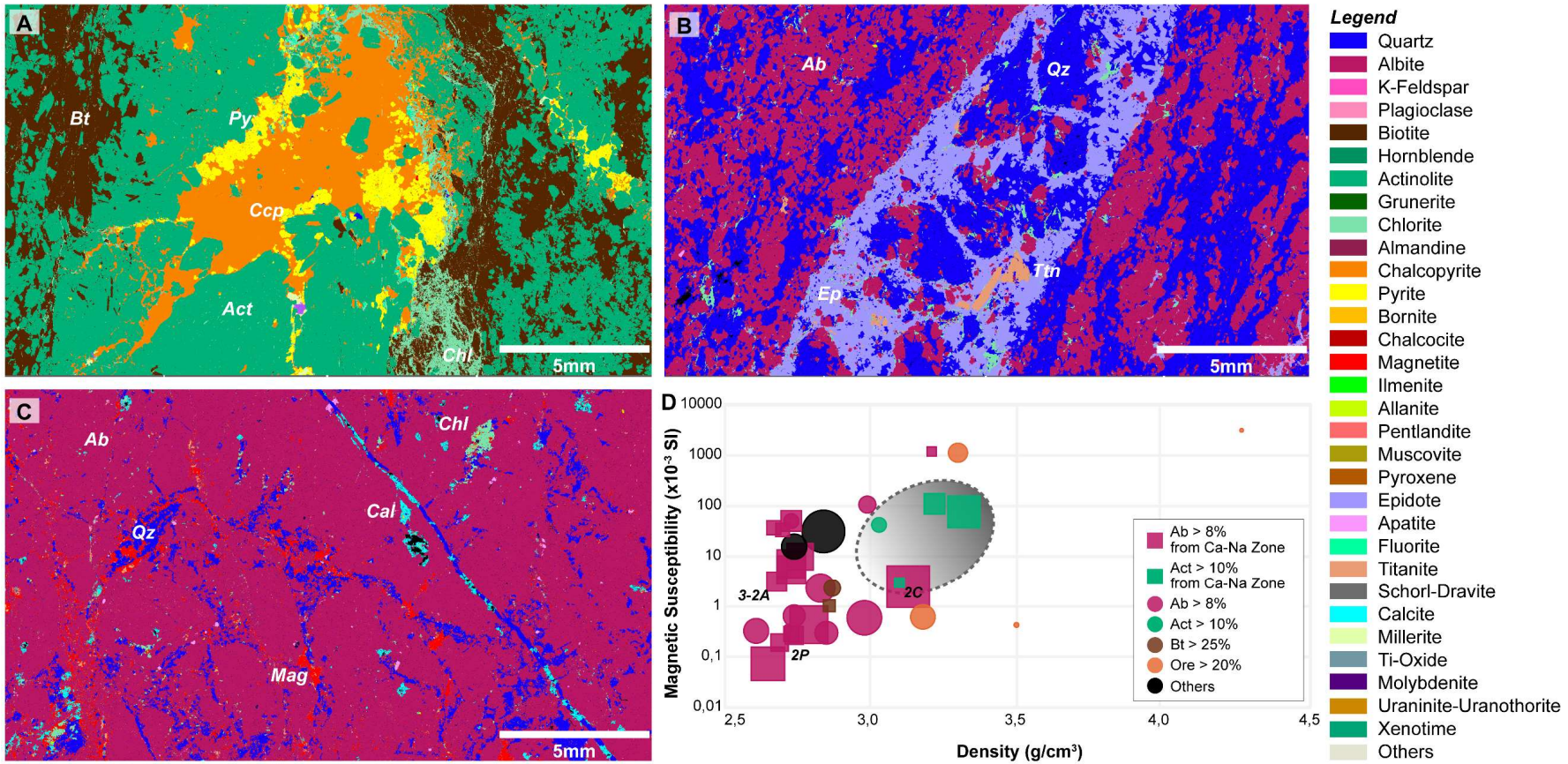


Figure 3. 6 - TIMA image and petrophysical scatter chart of calcic-sodic alteration zone Salobo Deposit. A) Sample 2C, illustrating the initial calcic-sodic alteration zone, is mainly composed of Act, Bt, Ccp, and Py, with minor Ab. B) Sample 3-2A, representing the moderate calcic-sodic alteration zone, is predominantly composed of Qz, Ab, Ep, and Ttn. C) Sample 2P, illustrating the advanced calcic-sodic alteration zone, is predominantly composed of Ab and Qz, with minor amounts of Mag. D) Scatter plot of density vs. magnetic susceptibility, highlighting samples with Ab, Act, Bt, and ore (Py, Ccp, Cct, Bn and Mag). The circle/square size represents resistivity values, with larger circles indicating higher resistivity. The gray-shaded oval marks highlight the high densities in samples with high Act content associated with a higher ferromagnesian content in the protolith. *Abbreviations: Ab – Albite, Act – Actinolite, Bt – Biotite, Bn – Bornite, Ccp -Chalcopyrite, Cct – Chalcocite, Ep – Epidote, Mag – Magnetite, Py – Pyrite, Qz – Quart and Ttn – Titanite.*

3.4.3. Iron enrichment

Iron enrichment is one of the most significant and complex phases in the deposit's evolution. It is characterized by the formation of grunerite, almandine, and magnetite. According to Melo et al., (2016) and Diniz et al., (2023) minor schorl-dravite is also an indication of this zone, and four transitional subzones are described: (1) the progression from actinolite (typical of calcic-sodic alteration) to grunerite with minor quartz, (2) the transition from grunerite to almandine assemblages, (3) peak hydrothermal almandine concentration, and (4) increased magnetite presence, still accompanied by almandine (Diniz et al., 2023; Skirrow, 2022). This study has confirmed these four transition subzones, although with some variations (Figures 3.7, 3.8, 3.9), which will be detailed below.

Ca-Fe-K Subzone

A newly identified Ca-Fe-K subzone representing a transition from calcic-sodic alteration to a system enriched in iron and potassium (Figure 3.7A). This subzone is exemplified by sample 2-2B, which is characterized by plagioclase, quartz, and biotite. Plagioclase remnants preserve gneissic textures and suggest initial deformation in certain areas, while biotite reflects Fe and K enrichment. To interpret the correlation between the Ca-Fe-K subzone and other subzones, as well as the relationship between plagioclase and biotite abundance, a scatter plot of magnetic susceptibility versus density (Figure 3.7B) was created. Symbol size was scaled according to plagioclase + biotite content, highlighting values above 20%.

Fig 7B shows that the iron enrichment zone (blue samples) presents the high content of plagioclase and biotite. The Ca-Fe-K subzone is characterized by relatively average density (2.82 g/cm³), low magnetic susceptibility (0.021 SI), high resistivity (3793 Ω.m), and low chargeability (11.2 mV/V). Samples with high plagioclase and biotite content (>20%, such as 2-2B) presented a small difference in petrophysical values (3.00 g/cm³, 0.018 SI,1981 Ω.m, and 18.6 mV/V). This change could be linked to the overprinting of plagioclase +biotite in other subzones such as Ca-Na, characterized by lower petrophysical average values, or mineralization subzones containing magnetite and sulphides, which are naturally denser, conductive, and magnetic (Figure 3.7B).

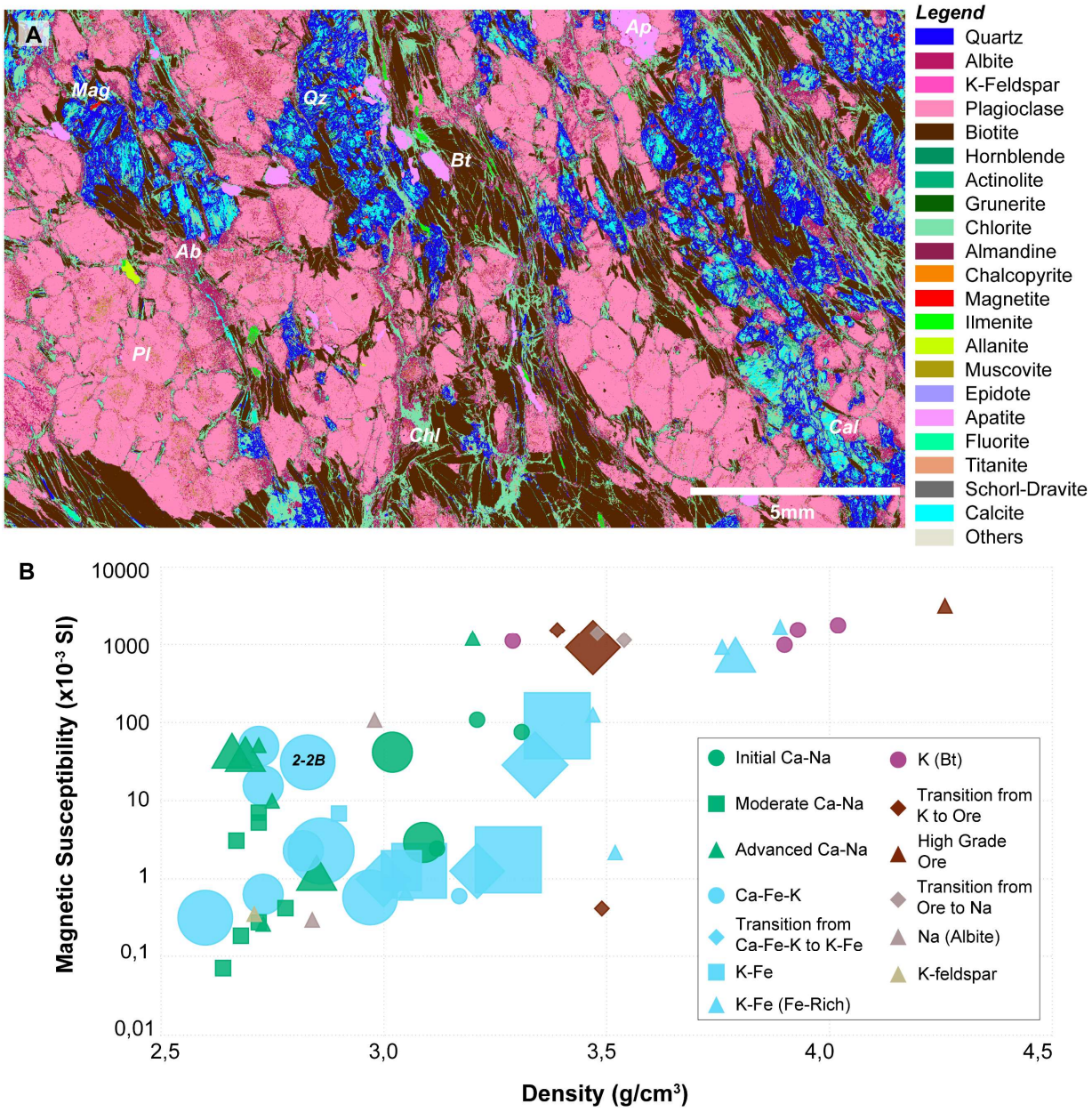


Figure 3. 7 - TIMA image and petrophysical scatter plots of Salobo Deposit samples and subzones hydrothermal alteration. A) Sample 2-2B composed of Pl, Qz, and Bt. B) Density vs. magnetic susceptibility scatter plot. Samples size represents Pl+Bt>20%, with larger sizes indicating higher mineral content. *Abbreviations: Ab – Albite, Ap – Apatite, Bt – Biotite, Cal – Calcite, Chl - Chlorite, Mag – Magnetite, Pl – Plagioclase, and Qz – Quartz.*

K-Fe Subzone

Sample 3-2G (Figure 3.8A) exemplifies the transition from the Ca-Fe-K subzone to the K-Fe subzone, containing quartz, minor plagioclase remnants, and biotite, almandine, and chlorite. The replacement of almandine and biotite by chlorite is related to the later albitization alteration that affected the deposit. Sample 3-1I (Figure 3.8C) represents a more advanced and deformed K-Fe subzone. It contains quartz, biotite, chlorite, and high hydrothermal almandine concentrations.

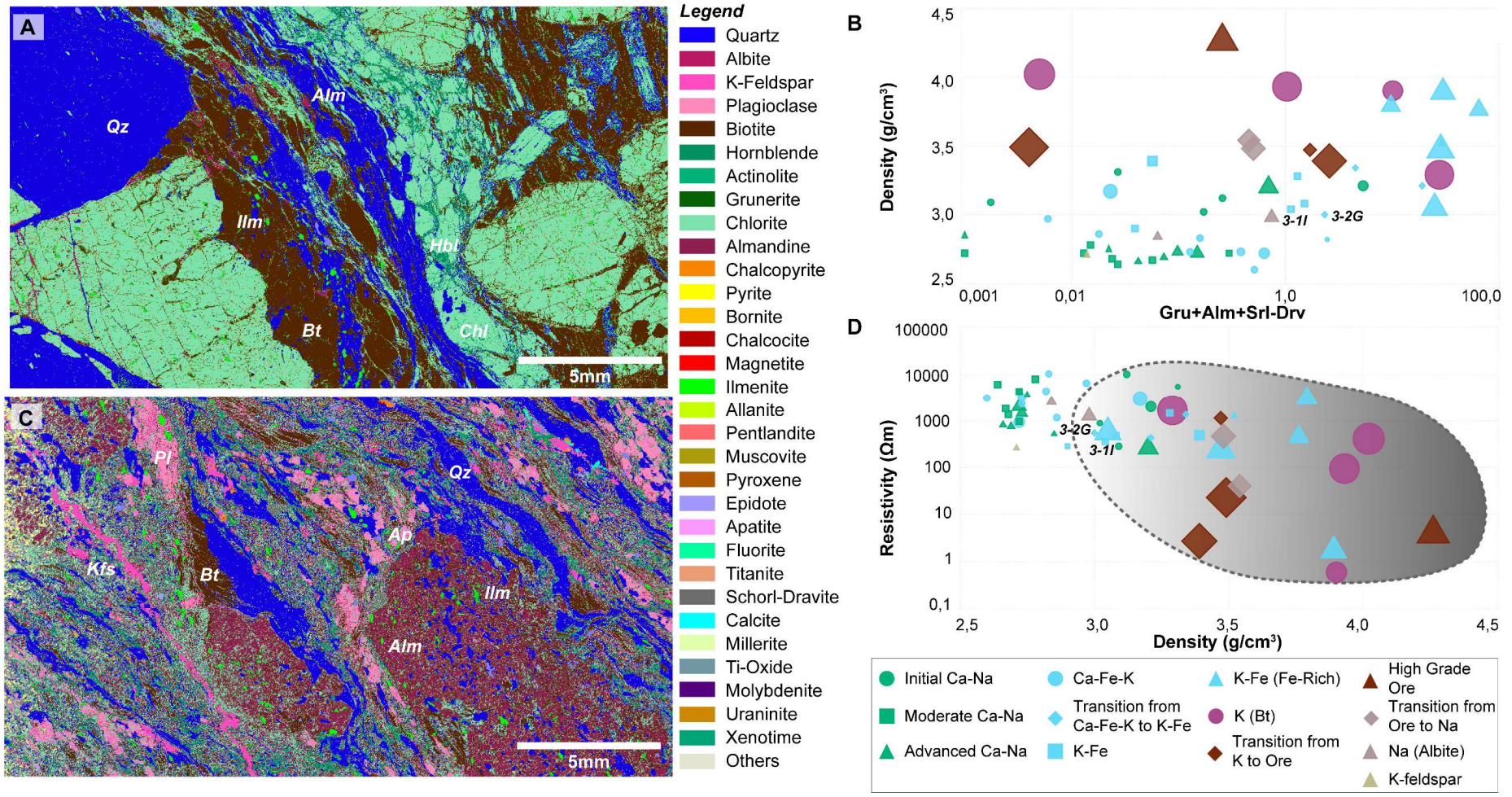


Figure 3. 8 - TIMA image and petrophysical scatter plots of K-Fe subzone of Salobo Deposit. A) Sample 3-2G (Ca-Fe-K to K-Fe subzone transition), predominantly composed of Alm, Bt, Chl, Pl, and minor Qz. B) Gru+Alm+Srl-Drv content vs. density scatter plot. Symbol size scaled by Mag. C) Sample 3-1I (K-Fe subzone), predominantly composed of deformed Alm, Bt, and Chl. D) Density vs. resistivity scatter plot. Symbol size represents Mag>20%. The gray-shaded oval marks the negative correlation between density and resistivity. *Abbreviations: Pl - Plagioclase, Bt - Biotite, Gru - Grunerite, Alm - Almandine, Chl - Chlorite, Qz - Quartz, Srl-Drv - Schorl-Dravite, and Mag – Magnetite.*

Grunerite, almandine, and schorl-dravite are key minerals that mark the transition from the Ca-Fe-K subzone to the advanced K-Fe subzone. However, as the system progresses into the iron-enriched zone, magnetite begins to appear. The key minerals in this zone show a strong correlation with magnetite, which dominates the physical properties. Consequently, magnetite will be incorporated into the petrophysical signature analysis of this zone. A scatter plot of grunerite+almandine+schorl-dravite content vs. density, with symbol size proportional to magnetite content (Figure 3.8B), demonstrates that samples with grunerite+almandine+schorl-dravite>1% exhibit density values higher than 3.1 g/cm³, with an average of 3.39 g/cm³. This increase is explained by the higher magnetite and sulphide contents in other zones, such as potassic and mineralization, as these denser minerals directly influence this physical property.

When considering only iron enrichment samples, the initial Ca-Fe-K subzone (represented by blue circles) has an average density of 2.82 g/cm³. In the more advanced subzones, the transition from Ca-Fe-K to K-Fe and K-Fe (represented by squares and diamonds, respectively), the average density increases to 3.15 g/cm³. This trend is attributed to the replacement of plagioclase and biotite by denser minerals such as grunerite, almandine, and predominantly magnetite. This also increases magnetic susceptibility (from 0.01 to 0.5 SI) and chargeability (from 21.2 to 58.7 mV/V). grunerite- and almandine-rich samples and magnetite-rich samples show similar density values (3.18 and 3.13 g/cm³, respectively).

On the other hand, a scatter plot of density versus resistivity (Figure 3.8D) shows that denser samples (>3.2 g/cm³) generally exhibit lower resistivity values (<1000 Ω.m). Samples with grunerite + almandine + schorl-dravite >1% have an average resistivity of 1034 Ω.m. Considering only iron enrichment samples, the initial Ca-Fe-K subzone (represented by blue circles) has an average resistivity of 3793 Ω.m, while in the more advanced subzones, the transition from Ca-Fe-K to K-Fe and K-Fe (represented by squares and diamonds, respectively), the average resistivity decreases to 762 Ω.m. This decline is correlated with the increasing presence of magnetite and minor sulphides. The clustering within the shaded zone highlights a linear relation between density and resistivity, suggesting that the strongly altered, denser samples tend to be more conductive. It is worth noting that the samples used for these calculations are not sulphide-rich. Additionally, it is important to note that the samples selected to represent the transition of Fe-enrichment subzones (3-2G and 3-1I) are located at the limit where a direct correlation between alteration, density, and resistivity begins to emerge. These samples effectively illustrate the transition between the zones of Fe enrichment.

K-Fe (Fe-rich) Subzone

The final K-Fe (Fe-rich) subzone is characterized by a significant increase in magnetite content, indicating proximity to mineralization. In this study, only substantial grunerite assemblages were observed, rather than the replacement of actinolite by grunerite described by

Melo et al. (2016). Samples 2K and 2L (Figures 3.9A, 3.9B) exemplify this subzone. Sample 2K (Figure 3.9A) is dominated by grunerite assemblages with well-preserved almandine, showing evidence of Fe enrichment. Discreet chlorite infills that crosscut the entire mineral assemblage, along with minor magnetite precipitation are also noted. In contrast, sample 2L (Figure 3.9B) has reduced grunerite, higher chlorite content and significantly more magnetite. Thus, it noted a strong correlation between grunerite, almandine, magnetite and chlorite.

The transition from the Ca-Fe-K to the K-Fe (Fe-rich) subzone in the iron enrichment process shows grunerite depletion and the precipitation of magnetite can be observed, alongside various ore minerals, including pyrite, chalcopyrite, chalcocite, bornite. This marks the onset of the mineralized body present in the central part of the Salobo Deposit. It is important to emphasize that we are analysing the petrophysical signature of iron enrichment zone and K-Fe (Fe-rich) subzone. Figure 3.9C presents iron enrichment subzones, main mineral content, and physical properties statistics.

As iron enrichment progresses from Ca-Fe-K to K-Fe (Fe-rich), magnetite (red) proportion increases significantly. The abundance of almandine, chlorite, and ore varies throughout the alteration zones. Chlorite is observed throughout the entire alteration zone, replacing the granodiorite in different proportions. Along with almandine, chlorite and ore minerals also show increased levels in the Ca-Fe-K zone. Magnetite exhibits distinct peaks, often coinciding with chlorite, while the occurrence of almandine and ore minerals decreases but remains present (Figure 3.9C). The inverse correlation between magnetite and copper minerals content is linked to redox variations within the hydrothermal system. Reducing conditions facilitate the precipitation of copper-bearing sulphide minerals, while oxidizing conditions facilitate the formation of magnetite (Figure 3.9C).

Magnetic susceptibility and density increase as the iron enrichment progresses, correlating with the increasing magnetite content. Magnetite content decreases in high-grade ore, which is not highly magnetic. However, its proximity to magnetite-rich zones ensures that it will most likely be associated with a magnetic anomaly, even though the sulphides are paramagnetic (Figure 3.9C). Chlorite and almandine are also paramagnetic and do not directly influence magnetic susceptibility. Minor increases in magnetic susceptibility observed in K-Fe and K-Fe (Fe-rich) zones are attributed to the presence of minor magnetite and ore minerals.

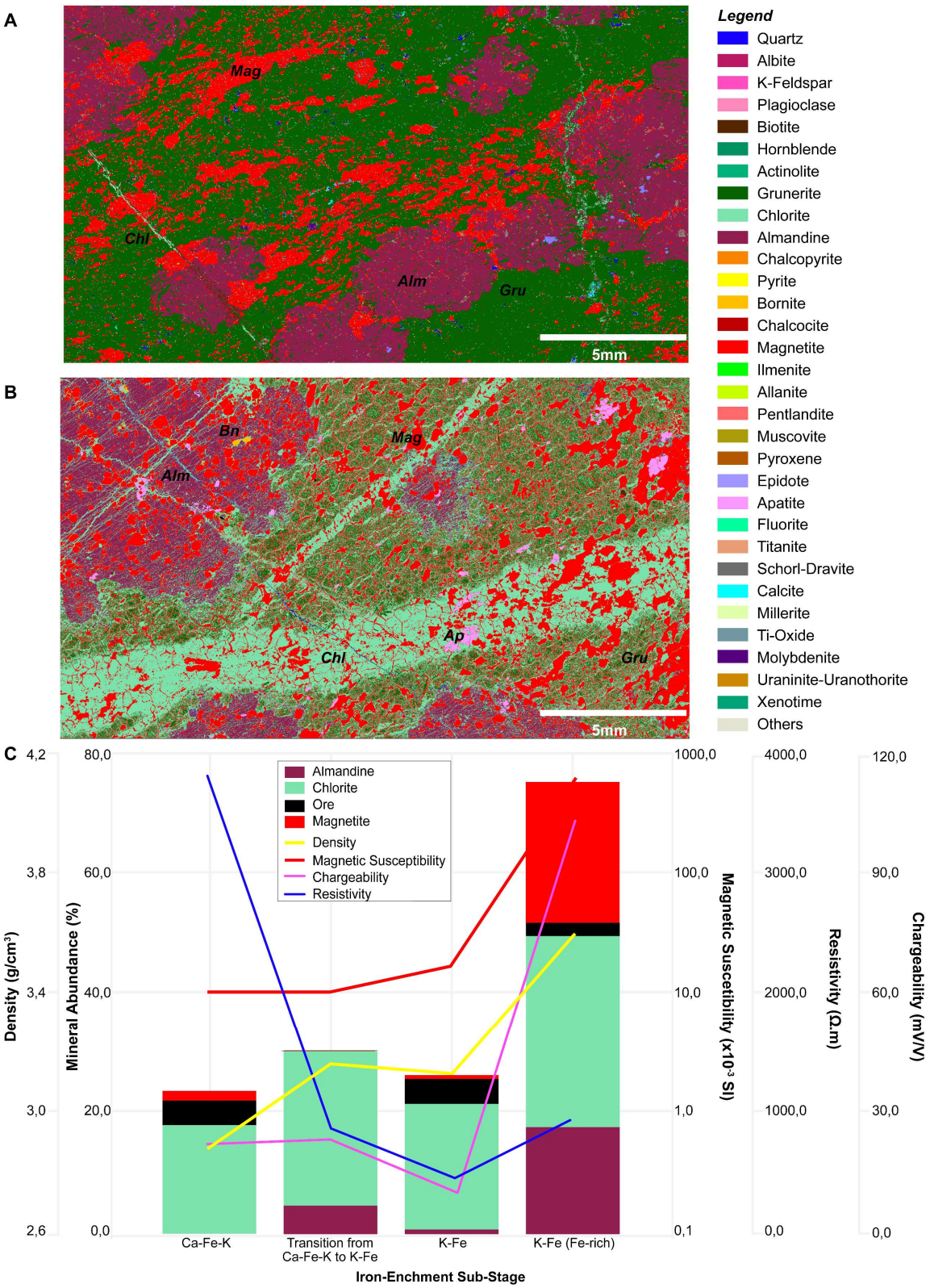


Figure 3. 9 - TIMA image and petrophysical plots of the iron enrichment of Salobo Deposit. A) Sample 2K is predominantly composed of Gru, Alm, Chl and Mag. B) Sample 2L is predominantly composed of minor Gru, Alm, Chl and major Mag. C) Iron enrichment zone vs. mineral content (volume %) and density (g/cm^3) vs. magnetic susceptibility (x10^{-3} SI), resistivity and chargeability (mV/V) plot of Salobo Deposit samples. *Abbreviations: Gru - Grunerite, Alm - Almandine, Chl - Chlorite, and Mag – Magnetite.*

The high density of almandine (~4.3 g/cm³; Dentith and Mudge, 2014) also has an impact on bulk density due to its abundance mainly in the Fe-enrichment zone. Magnetite and ore minerals (mainly pyrite and chalcopyrite) strongly influence density (average value greater than 3.5 g/cm³), even at low concentrations. This mineral correlation highlights the complexity of density variations within the proximal alteration zones of the deposit. If analyzed individually, chlorite tends to reduce the overall rock density.

Chargeability and resistivity are inversely correlated. Chargeability increases in the final zone, indicating the presence of metallic minerals, possibly ore and magnetite. In contrast, resistivity initially decreases, likely due to the presence of conductive phases, but rises in the final zone, reflecting mineralogical transitions that influence electrical conductivity. Chargeability remains below 50 mV/V in the host rock but increases to >80 mV/V in K-Fe (Fe-rich), correlating with sulphide-rich regions with pyrite, chalcopyrite, bornite, and magnetite (Figure 3.9C). Although magnetite is not inherently chargeable, it is closely associated with sulphides. Despite the higher ore content in the K-Fe subzone, chargeability exhibits an uneven decline, likely due to variations in the grain size and connectivity of metallic phases within the samples classified in this subzone. Oxidation reduces the concentration of chargeable sulphides, which decreases chargeability, even if total ore content increases.

Resistivity decreases from 4000 Ω.m to 1000 Ω.m upon entering iron enrichment zone (Figure 3.9C). Sulphides typically reduce resistivity, whereas magnetite increases it when compared to sulphides alone. Due to the dominance of magnetite in the K-Fe (Fe-rich) zone, resistivity rises sharply compared to the K-Fe subzone. Generally, the presence of metallic minerals reduces resistivity, but variations may also result from indirect factors such as porosity and mineral textures. Almandine has minimal impact.

3.4.4. Potassic alteration

Potassic alteration at Salobo is a proximal and pervasive process associated with mineralization, marked by the high biotite content, as observed by Melo et al., (2016), and Diniz et al., (2023), in the shallow portions of the deposit. Sample 2N (Figure 3.10A) exemplifies this zone, containing grunerite, almandine, chlorite, biotite, quartz, magnetite, chalcopyrite, and bornite. In this sample, biotite replaces grunerite and almandine and is intergrown with mineralization, as indicated by the occurrence of chalcopyrite, bornite, and minor magnetite. The association of biotite with sulphides, suggests that potassic alteration and ore were at least partially synchronous.

The scatter plot in figure 3.9B shows the relationship between sulphides content (pyrite, chalcocite, chalcopyrite, and bornite) and resistivity (Ω·m), revealing a negative correlation. High-grade ore and potassic subzones show low resistivity (<10 Ω·m) and high ore content (>10%), indicating a high concentration of conductive sulphide minerals. Ca-Na alteration subzones exhibit moderate to high resistivity (100 - 10,000 Ω·m) and lower ore content, suggesting a

predominance of silicate minerals such as quartz, K-feldspar, amphiboles and pyroxene. These comparisons reflect the influence of ore minerals (sulphides) rather than biotite alone. In summary, the potassic zone exhibits lower resistivity.

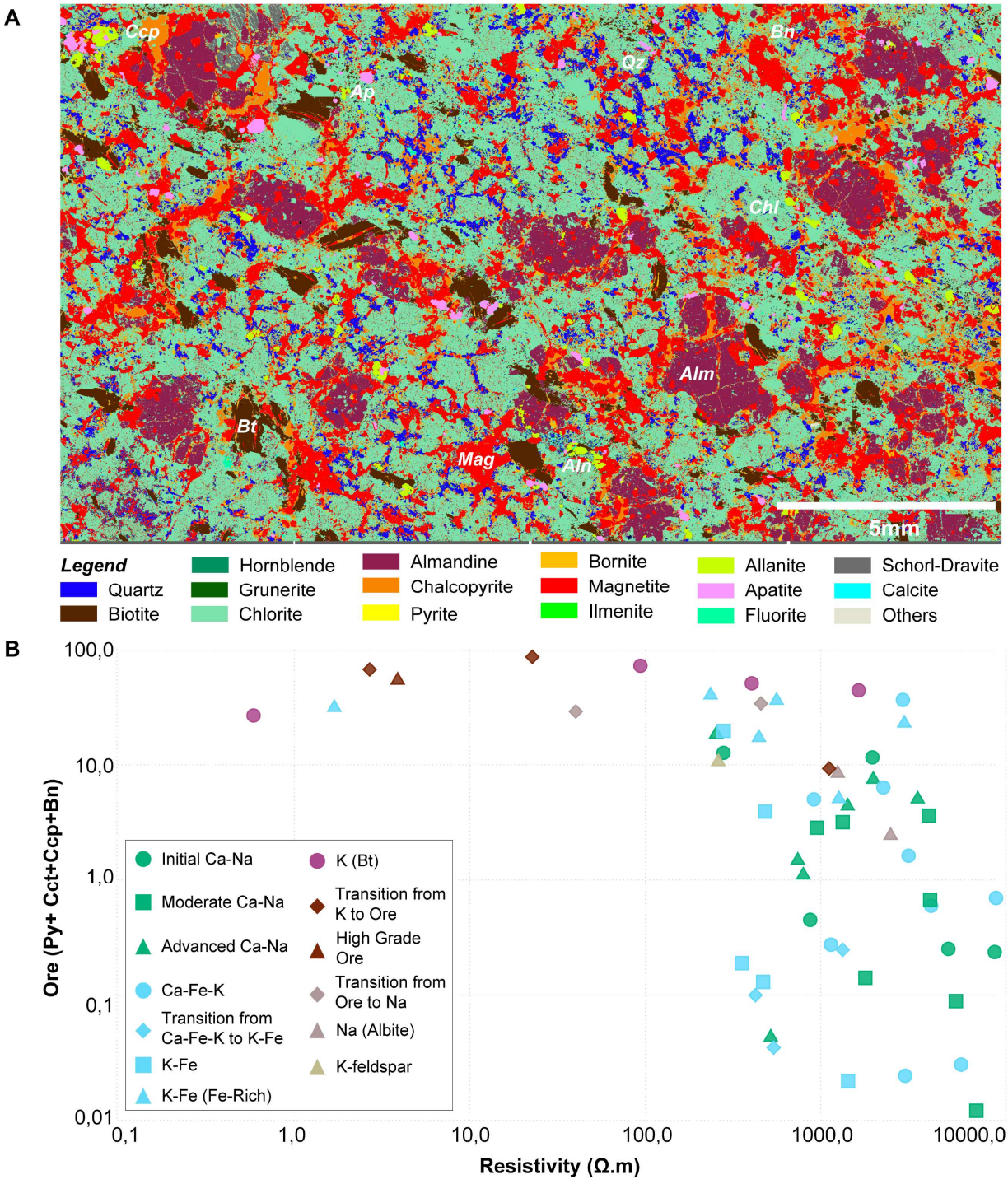


Figure 3. 10 - TIMA image, petrophysical plots of potassic alteration and matrix correlation of Salobo Deposit samples. A) Sample 2N composed of Gru, Alm, Chl, Bt, Qtz, Mag, Cpy and Bn. B) Scatter plot of sample resistivity (Ω.m) vs. ore content (% volume), with subzone alteration Salobo samples. *Abbreviations: Gru - Grunerite, Alm - Almandine, Chl - Chlorite, Qtz – Quartz, Mag – Magnetite, Cpy - Chalcopyrite, Bn – Bornite, Bt – Biotite, and Cct – Chalcocite.*

A Spearman correlation matrix (Table 1) was generated to analyze the relationships between key minerals and petrophysical properties in the potassic zone. The most notable correlations include 1) biotite and magnetite show a negative correlation (-0.331), supporting the suggestion that magnetite is depleted and biotite is introduced during the transition from iron enrichment to potassic alteration; 2) bornite with magnetite (0.301), chalcocite (0.742), and density (0.432) suggests that bornite, magnetite, and chalcocite frequently co-occur, reinforcing the high density of copper sulphides. The negative correlation with resistivity corroborates that bornite is a highly conductive mineral; 3) chalcocite and density shows a positive correlation further confirms the high copper sulphide density. Additional correlations include biotite, bornite, and chargeability, where biotite shows a positive correlation with bornite (0.299) and a negative correlation with chargeability (-0.248), suggesting that biotite is more abundant in areas where magnetite is depleted, and ore minerals are concentrated. Furthermore, the positive correlation between bornite and biotite (0.299) indicates that high-grade ore begins to appear in the potassic zone (Table 1).

Table 3.1 - Spearman correlation matrix showing the relationships between key minerals in the potassic alteration zone and their associated physical properties.

	Biotite	***Bornite***	***Chalcocite***
Biotite	**1**	**0,299**	**0,159**
Magnetite	**-0,331**	**0,301**	**0,147**
Bornite	**0,299**	**1**	**0,742**
Chalcocite	**0,159**	**0,742**	**1**
Density	**0,103**	**0,432**	**0,316**
Magnetic Suscetibility	**-0,077**	**0,167**	**-0,048**
Resistivity	**-0,115**	**-0,392**	**-0,081**
Chargeability	**-0,248**	**0,055**	**-0,091**

3.4.5. Mineralisation and ore body

Deep Salobo features ore bodies associated with iron enrichment and potassic alteration zones, with mineralization composed of disseminated bornite, chalcocite, chalcopyrite, and pyrite, occurring interstitially with magnetite. Without magnetite, the total ore mineral content ranges from 0% to 28%, a relatively low value compared to other deposits such as Furnas and Cristalino. According to Réquia et al., (2003); Costa et al., (2016); Melo et al., (2016); Diniz et al., (2023) these ore minerals frequently occur with fluorite, molybdenite, uraninite, ilmenite, apatite, monazite, and allanite.

Sample 3S (Figure 3.11A) demonstrates potassic alteration associated to mineralization, containing almandine, chlorite, biotite, quartz, magnetite, bornite, chalcopyrite, albite, epidote,

plagioclase, titanite, calcite, and apatite. Biotite often replaces earlier minerals such as almandine due to the percolation of hydrothermal fluid. Abundant magnetite and minor bornite and chalcopyrite highlight mineralization, while titanite, and apatite confirm its positioning in the mineralization zone, as noted by Melo et al., (2016) in shallow portions of the deposit. Although not depicted in the figure, sulphides are present in the zone and serve as key markers for its identification. Sample 2-2J (Figure 3.11B) shows advanced alteration and deformation, with Act, chlorite, and oriented foliation. Magnetite and apatite abundance positions it within the mineralization zone. The increase in magnetic susceptibility and density from the end of the iron enrichment zone (Fe-K and Fe-K Fe-rich) and potassium alteration to the mineralization is attributed to magnetite, sulphides and other dense minerals such as grunerite and almandine.

Figure 3.11C shows variations in density and magnetic susceptibility focusing on three primary mineral groups: quartz–feldspar–calcite (QFC), ferromagnesian silicates (FM), and magnetite. QFC (Quartz-Feldspar-Calcite) is positioned in the lower-left quadrant, reflecting its low magnetic susceptibility (diamagnetic or weakly paramagnetic) and moderate density. FM (e.g. iron, nickel, and cobalt) occupies the upper-right quadrant, marked by high magnetic susceptibility and high density. Magnetite is found in the upper-middle to upper-right quadrant, where it exhibits high magnetic susceptibility, though not as strong as ferromagnetic materials, and moderate-to-high density. This plot helps identify materials or phases, distinguish mineral types. Linear trends suggest systematic variation, clusters indicate multiple phases, and deviations may point to complex structures.

Salobo samples are distributed along both the magnetite and paramagnetic trends. This distribution is consistent with the composition of the Salobo protolith, which primarily consists of igneous rocks and gneisses. These samples are an example of magnetite-destructive redox processes which influences petrophysical properties. The classification indicates that samples from the Ca-Na and Fe-enrichment zones exhibit characteristics suggestive of both trends. The least altered samples, associated with paramagnetic minerals, such as actinolite, grunerite, and biotite are situated within the paramagnetic trend (QFC and FM minerals), which are indicative of the primary mineralogy of these alteration zones. In contrast, the more altered samples in proximal zone, associated to Fe-enrichment with ferromagnetic minerals, such as magnetite, are on the magnetite trend.

Samples from the potassic alteration zone, mineralized zone, and transitional zones between ore and Na-rich subzones, characterized by increased magnetite, sulphide, and oxide content, fall along the magnetite trend. These represent samples composed predominantly of quartz–feldspar–calcite and magnetite. Samples from later albitization and post-ore alteration are along the paramagnetic trend. These represent samples composed predominantly diamagnetic minerals, such as K-feldspar, Alb, and quartz, but present sulphides.

The Figure 3.11D shows a graph from Principal Component Analysis (PCA), used to highlight correlations between physical properties, main mineral abundances, and gangue minerals. Despite typically comprising less than 2%, gangue minerals are often undervalued but hold significant interpretative importance. Although they do not directly control the physical properties, accessory minerals are consistently associated with primary ore minerals. As a result, they can aid in identification, serve as vectors toward mineralized zones, and indicate proximity to ore-bearing areas. Additionally, it is important to emphasize that, for a more robust statistical analysis, samples from all zones were included. Detailed PCA data are available in Appendix B.

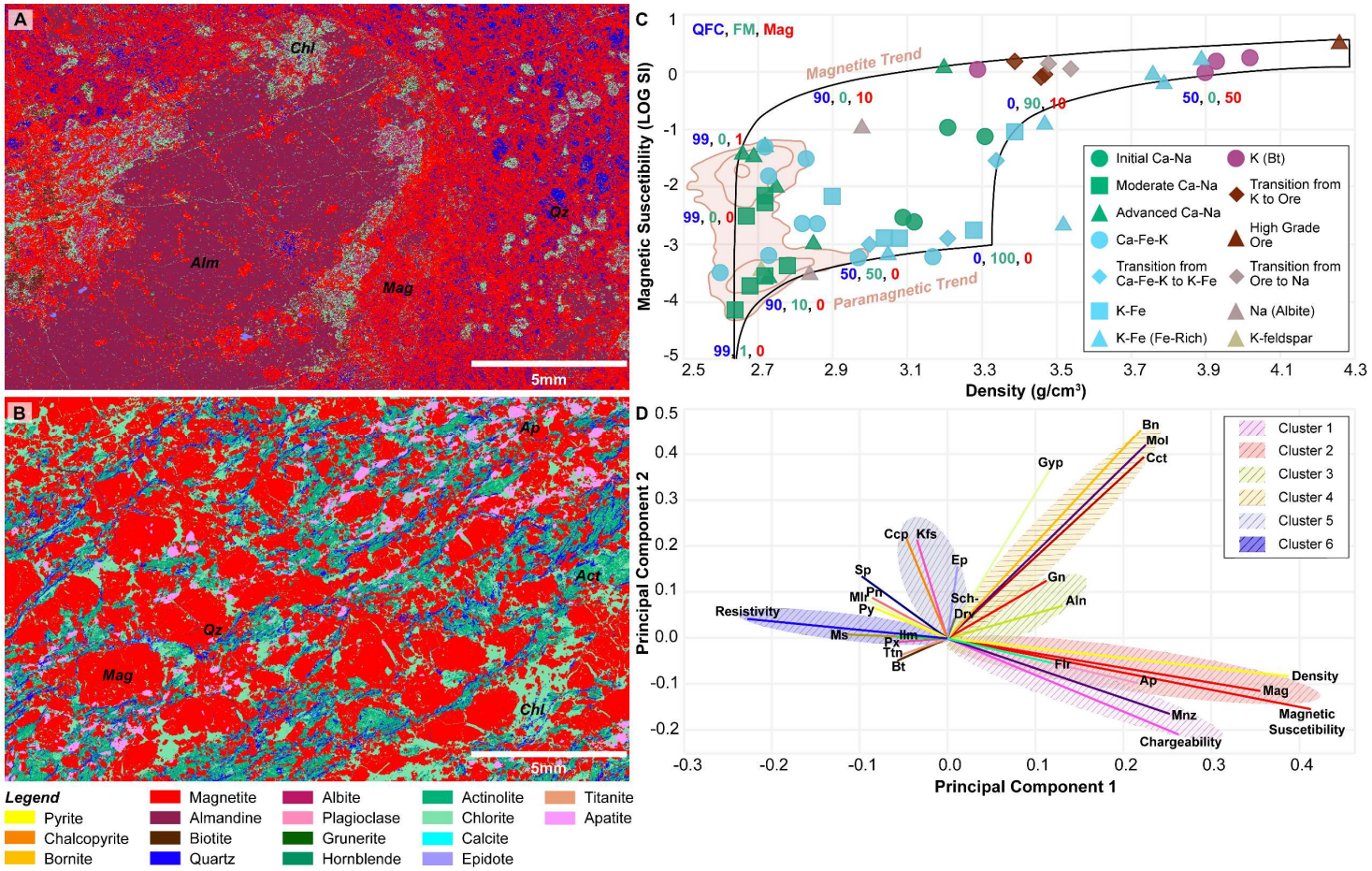


Figure 3. 11 - TIMA image and Principal Component Plots of the mineralization zone of Salobo Deposit. A) Sample 3S is predominantly composed of Mag, Alm, Chl, Bt, and minor Bn, Ccp, Ttn and Ap. B) Sample 2-2J is predominantly composed Mag, Act and Chl, and minor Ap. C) Density vs. Magnetic susceptibility of Salobo samples. D) Principal Component Analysis plot of among minerals and physical properties within the Salobo IOCG system. The hatched oval marks highlight the six main clusters identified. *Abbreviations: QFC – Qz-Ffs-Cal, FM - ferromagnesian silicates, Aln – Allanite, Ap – Apatite, Bn Bornite, Bt - Biotite, Cct - Chalcocite, Ccp - Chalcopyrite, Ep - Epidote, Flr - Fluorite, Gn - Galena, Gyp - Gypsum, Ilm - Ilmenite, Kfs - K-Feldspar, Mag - Magnetite, Mln - Millerite, Mol - Molybdenite, Mnz - Monazite, Ms - Muscovite, Pn - Pentlandite, Px - Pyroxene, Py - Pyrite, Sch-Drv - Schorl-Dravite, Sp - Sphalerite and Ttn - Titanite.*

The proportions of this PCA present a total of 25% of the database. However, it is important to note that key-forming minerals such as quartz, plagioclase, and amphiboles were not included in this analysis, which explains why the proportion accounts for only a quarter of the data. Despite this, significant associations were identified, providing valuable insights for interpretation. Six main clusters were noted in the first two principal components (Figure 3.11D): 1) monazite and chargeability; 2) Magnetite, magnetic susceptibility, and density; 3) allanite and galena (Gn); 4) bornite, molybdenite, and chalcocite; 5) epidote, K-feldspar, and chalcopyrite; 6) Resistivity, ilmenite, muscovite (Ms), and pyroxene. Negative correlations have opposing vectors, and uncorrelated variables form 90-degree angles.

Gangue minerals such as fluorite, molybdenite, ilmenite, apatite, monazite, and allanite are often underestimated at Salobo, unless associated with ore. PCA analysis (Figure 11D) reveals their correlations with ore and physical properties. Cluster 1, composed of monazite and chargeability, reflects a co-occurrence of monazite with sulphides in high-temperature hydrothermal halos enriched in REEs and trace elements with high chargeability. The main sulphides, such as pyrite, chalcopyrite, chalcocite and bornite, with monazite-rich zones, could be the explanation for the extensive anomaly in induced polarization survey appointed by Araujo et al. 2025.

Cluster 2, including magnetite, magnetic susceptibility, and density, corresponds to magnetite-rich zones identified by Melo et al., (2016) and Araujo et al., (2025), as expected. The presence of apatite and fluorite between cluster 1 and 2 (Figure 3.11D) with small angular separation confirms that apatite is commonly observed in the ore zone and the presence of fluorite as a fluorine-enriched during Ca-Na alteration, as noted by Melo et al., (2016).

Cluster 3 (allanite and Gn) (Figure 3.11D) reflects transitional hydrothermal zones. Allanite forms in REE-enriched fluids during early to intermediate alteration, while galena precipitates in late-zone, lead-enriched fluids precipitating in veins or fractures. Despite their differing formation conditions, these minerals overlap indicating interactions between REE- and base-metal-enriched fluids, linking distinct hydrothermal zones in mineralization. Cluster 4 (bornite, chalcocite, and molybdenite) (Figure 3.11D) reflects transitional hydrothermal alteration zones to high-grade ore zones. Bornite and chalcocite, associated with late-zone copper sulphides, overprint earlier assemblages, while molybdenite links to earlier zones according to Melo et al., (2016). Their overlapping deposition reflects decreasing temperature and pressure during mineralization and could be considered as a spatial link, explaining their co-occurrence.

Cluster 5 (chalcopyrite, epidote, and K-feldspar) (Figure 3.11D) is associated with alteration envelopes. Epidote crystallizes in distal Ca-Na zones, K-feldspar in proximal potassic zones, and chalcopyrite spans both environments, indicating its transitional area in mineralization. These findings, emphasizing the relationship between alteration and mineralization. Cluster 6 (resistivity, ilmenite, muscovite, and pyroxene) represents high-resistivity zones associated with

silicate- and oxide-rich alteration zones rather than sulphide mineralization (Araújo et al., submitted). Ilmenite, forms during early alteration and is linked to Salobo mineralization. Ms occurs in quartz mylonite host rocks and late-zone silicate-enriched zones, enhancing resistivity. Pyroxene, prevalent in mafic-ultramafic host rocks, marks early alteration zones.

The six clusters at Salobo reveal its mineralogical evolution through hydrothermal zones. Early-zone minerals (e.g., pyroxene, ilmenite) mark initial alteration, while transitional (e.g., allanite, molybdenite, epidote) and late-zone (e.g., muscovite, chalcopyrite) minerals reflect sequential fluid interactions.

An expected correlation between sulphides and conductivity was not clearly evidenced in the PCA results. This outcome may be influenced by the proportion of sulphide-bearing samples within the dataset - only 19 of 56 samples (approximately one-third). Additionally, texture is an important factor that controls conductivity. Given that sulphides in some samples are disseminated and often occur alongside high magnetite concentrations, these factors may have contributed to the lack in PCA results. However, this does not imply that the sulphides in the Salobo deposit are non-conductive, since previous analyses have demonstrated otherwise. Instead, this finding highlights the complexity of the dataset and the influence of multiple factors on PCA.

3.4.6. Later albitization alteration

The Fe-rich hydrated silicate alteration zone identified by Diniz et al. (2023) and Melo et al. (2016) was not observed in deep Salobo. Instead, a newly recognized alteration zone, characterized by the addition of sodium (Na) and potassium (K) to the system, has been identified and is named later albitization. Sample 3-1L (Figure 3.12A) represents the transition from mineralization to Na and K enrichment, containing quartz, chlorite, biotite, magnetite, bornite, albite, and K-Feldspar. Magnetite and bornite indicate a mineralized zone, while Alb and K-feldspar mark early Na and K enrichment. Sample 2T (Figure 3.12B) retains magnetite remnants from the mineralization within an iron-rich environment, as indicated by chlorite. The significant presence of Alb highlights the onset of Na enrichment.

Similar to the accessory minerals and gangue discussed in the previous section, principal component analysis (PCA) was applied to all samples, highlighting the main minerals and correlated gangue minerals of this zone. Detailed PCA data are available in Appendix C. The proportions of this PCA present a total of 30% of the database. Figure 3.12D shows four clusters 1) chlorite and Almandine; 2) ilmenite and biotite; 3) Conductivity, quartz, pyrite, K-feldspar, epidote, and chalcopyrite; 4) bornite and chalcocite. Cluster 1 (Figure 3.12D) highlights a relationship between chlorite and almandine, linking deformation and hydrothermal alteration and confirming two mineral phases: hydrothermal chlorite and chloritized almandine from a retrograde metamorphic process. Their association emphasizes structural control and fluid-rock interactions, consistent with studies describing the intense ductile deformation, steeply dipping

mylonitic rocks, and extensive hydrothermal alteration of Salobo (Réquia et al., 2003; Melo et al., 2016; Burns et al., 2019).

Cluster 2 (Figure 3.12D) combines ilmenite and biotite, indicating a magmatic-hydrothermal contribution to mineralization. Biotite occurs in potassic-altered zones near mineralization, while ilmenite is associated with magnetite-rich areas close to ore zones. This spatial overlap within alteration halos explains their statistical correlation. Although the PCA (Figure 3.12D) shows weaker or indirect relationships with chargeability and resistivity, biotite alteration can reduce resistivity if sulphides such as pyrite and chalcopyrite are introduced or if porosity and fluid saturation increase.

Cluster 3 (Figure 3.12D) groups conductivity with quartz, K-feldspar, pyrite, epidote, and chalcopyrite, showing the correlation between alteration and mineralization. High conductivity is associated with sulphides such as pyrite and chalcopyrite. Epidote, a Ca-enrichment marker, occurs in both distal calcic-sodic alteration zones and transitional phases from mineralization to later albitization alteration. K-feldspar indicates potassic alteration, while quartz, a resistive mineral, marks host rocks and transitional areas. Low conductivity in quartz-rich areas helps define the boundaries of alteration halos, providing insight into the spatial extent of mineralization.

Finally, Cluster 4 groups bornite and chalcopyrite (Figure 3.12D), both high-grade copper sulphides associated with advanced mineralization zones (Melo et al., 2016). While not directly correlated with physical properties in the PCA, these minerals have dominant physical properties that serve as important indicators of alteration or mineralization. Albite shows no significant correlation, likely due to its occurrence in both early and late-zone hydrothermal alteration. It forms over extensive areas and is not spatially confined to ore zones, such as magnetite, pyrite, chalcopyrite, or chalcocite, which are directly linked to conductivity or chargeability. Post-ore hydrothermal alterations can further mask the presence of albite, disrupting potential correlations (Figure 3.12D).

3.4.7. Post-ore alteration

Well-developed post-ore alteration assemblages are prominent in deeper sections, characterized by K-feldspar, followed by epidote, and chlorite. According to Diniz et al. (2023) and Melo et al. (2016), K-feldspar is associated with hematite. However, this was not confirmed in our sampling. They also describe this zone as a weaker propylitic alteration, featuring sericite and carbonate. Sample 3-1B (Figure 3.12C) reflects this zone, with albite, and abundant K-feldspar, alongside mineralization such as chalcopyrite and, pyrite. The presence of K-feldspar, albite, and chlorite confirms deformation overlap with multiple hydrothermal pulses. This subzone is characterized by relatively low density (2.69 g/cm³), low magnetic susceptibility (0.017 SI), low resistivity (689 Ω.m) and very low chargeability (8.6 mV/V).

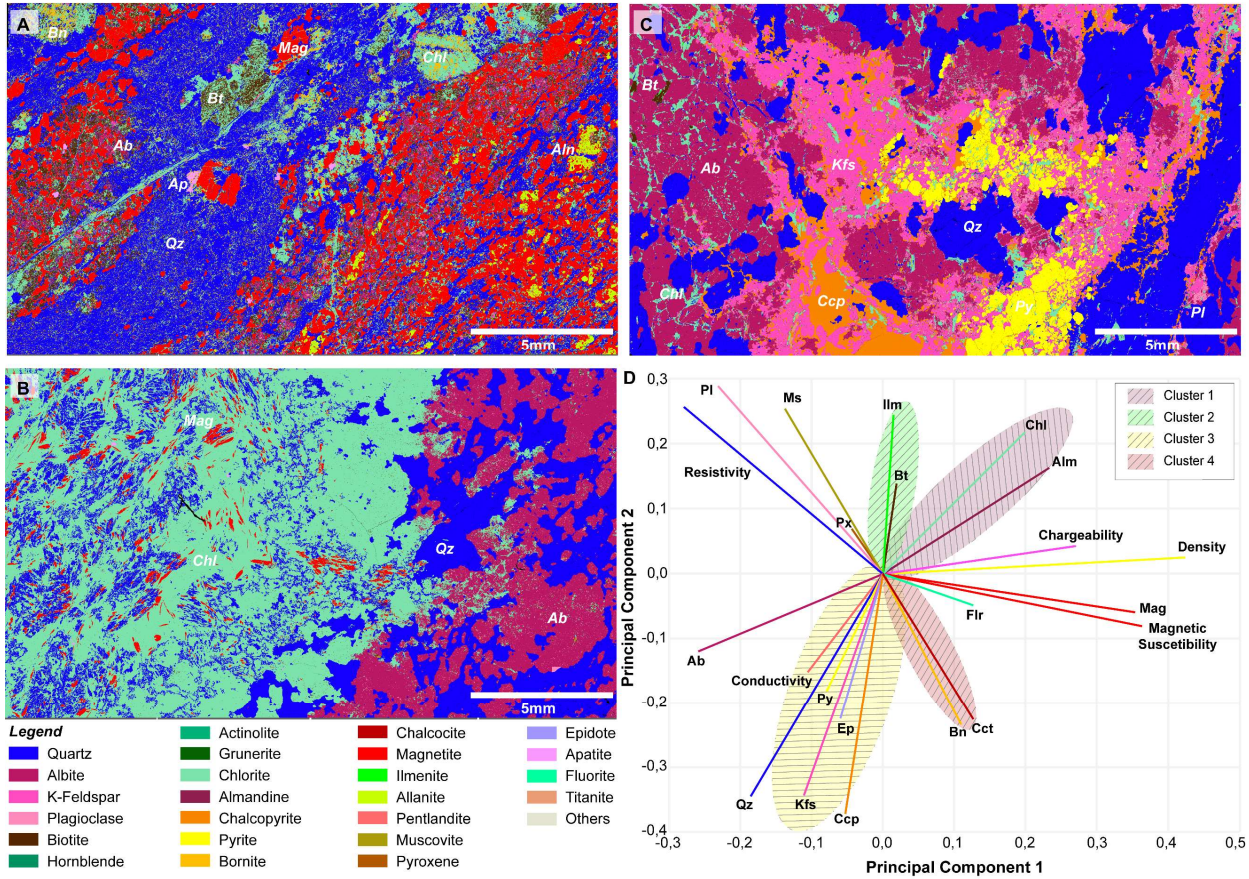


Figure 3. 12 - TIMA image and Principal Component Plots of the later albitization and post-ore alteration zone of Salobo Deposit. A) Sample 3-1L, representing the transition from high-grade mineralization to the later albitization alteration zone, includes Qz, Chl, Bt, Mag, Bn, Ab, and Kfs; B) Sample 2T, showing the transition from remnants of mineralization to the later albitization alteration zone, composed of remnant Mag, Chl, Qz, and Ab. C) Sample 3-1B, illustrating the post-ore alteration zone, is predominantly composed of Ab, Pl, Kfs, Ccp, and Py; D) Principal Component Analysis plot of among minerals and physical properties within the Salobo IOCG system. The gray-shaded oval marks highlight the four main clusters identified. *Abbreviations: Ab -Albite, Alm – Almandine, Bn Bornite, Bt - Biotite, Cct - Chalcocite, Ccp - Chalcopyrite, Chl – Chlorite, Ep - Epidote, Flr - Fluorite, Ilm - Ilmenite, Kfs - K-Feldspar, Mag - Magnetite, Ms – Muscovite, Pl – Plagioclase, Px - Pyroxene, Py – Pyrite and Qz -Quartz.*

3.5. Evaluating the Petrophysical Footprint of Salobo

The petrophysical footprint of Salobo provides insights into the correlations between host rock, hydrothermal alteration, and mineralization processes. The analysis of density, magnetic susceptibility, resistivity, and chargeability shows distinct signatures for each alteration zone. Host rocks present low density (2.70 - 3.10 g/cm³), very low magnetic susceptibility (~0.001 SI), high resistivity (4,000 - 5,000 Ωm), and low chargeability (<50 mV/V) (Figure 3.13). These rocks show significant contrast when compared to altered rocks.

Calcic-sodic alteration, an early zone, presents low density (~2.89 g/cm³), low magnetic susceptibility (0.081 - 0.091 SI), and moderate resistivity (~2,781 Ωm). Alb and actinolite dominate this zone, with minor magnetite. The low density and magnetic susceptibility reflect a mafic to intermediate protolith. This zone marks the distal zone and regional alteration halo (Figure 3.13). The iron enrichment zone, a key transition zone, exhibits high density (>3.30 g/cm³), high magnetic susceptibility (~0.414 - 7.516 SI in magnetite-rich samples), and increased chargeability (62.2 - 89.7 mV/V). Resistivity decreases with higher magnetite and sulphides (~95.1 - 942 Ω.m). Grunerite, almandine, and magnetite dominate this zone, transitioning from distal Na-Ca assemblages. These minerals strongly correlate with density, magnetic susceptibility, and conductivity, highlighting magnetite and ore mineralization (Figure 3.13).

Potassic alteration, a proximal mineralization zone, presents a moderate density increase (2.85 - 3.05 g/cm³), higher magnetic susceptibility (0.02 - 0.06 SI), and decreased resistivity (1,658 Ωm). Biotite dominates, replacing earlier minerals, and associates with bornite, chalcopyrite, and other sulphides, which makes it difficult to directly identify a petrophysical footprint for biotite. Biotite-associated sulphides decrease resistivity and increase chargeability. Ore minerals, including bornite, chalcopyrite, chalcocite, and pyrite, significantly increase magnetic susceptibility, density, and conductivity. (Figure 3.13).

Later albitization alteration, a transitional zone, presents moderate density (~3.0 g/cm³) and chargeability (~80 mV/V), with complex effects on magnetic susceptibility and resistivity. Chlorite dominates, with Ab and magnetite remnants marking the transition from mineralized systems to later-zone overprinting, indicating extended hydrothermal fluid activity. Post-ore alteration features low density from K-feldspar, Ab, and plagioclase assemblages (Figure 3.13). These minerals are gangue or accessories, so their impact on the physical properties would not be significant. Intense K-feldspar alteration defines this zone, with weaker epidote, sericite, and chlorite occurrence.

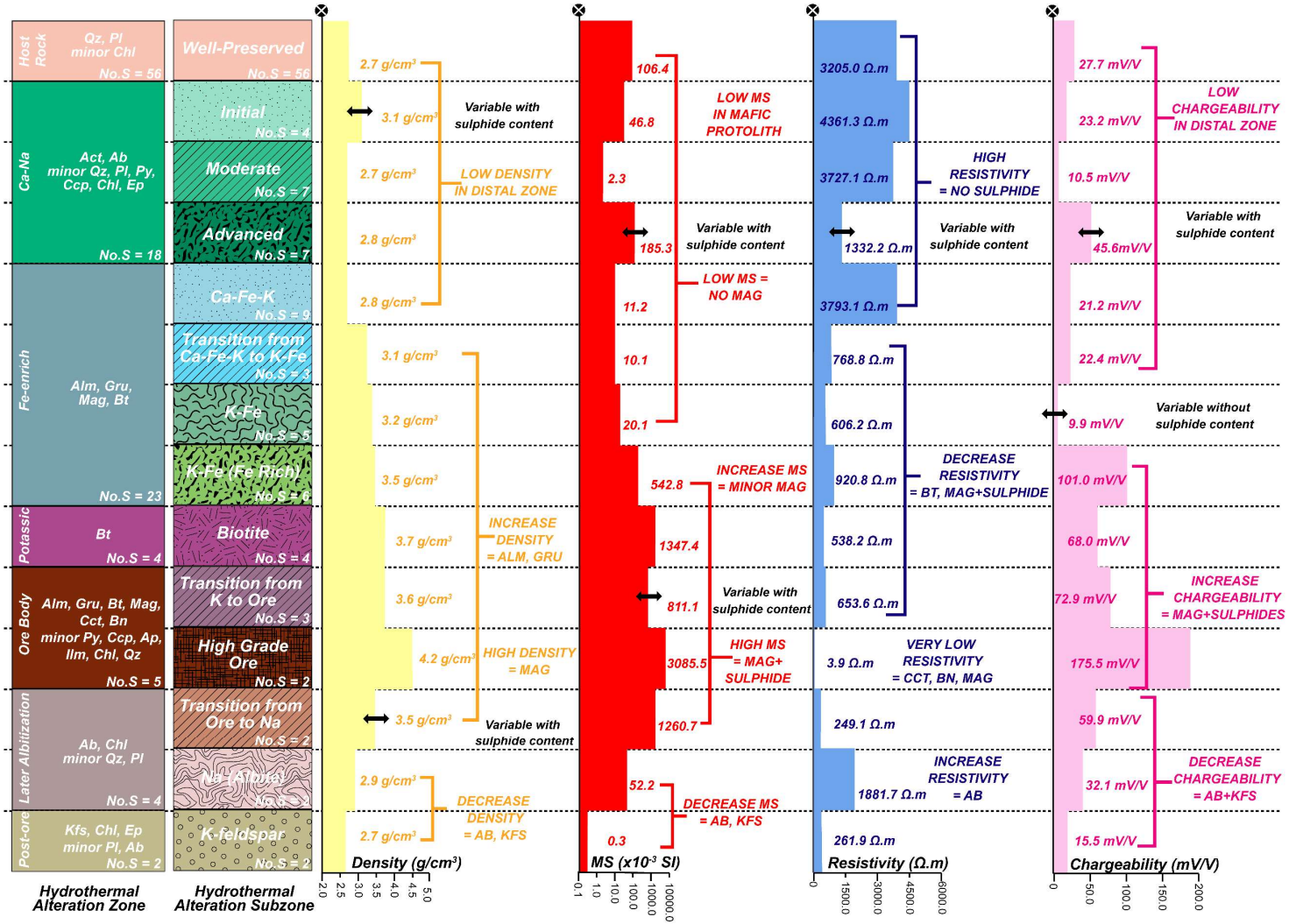


Figure 3. 13 - Petrophysical illustrative log of hydrothermal zone and subzone of Salobo deposit samples, main minerals, and physical properties average. *Abbreviations: Ab -Albite, Act – Actinolite, Alm – Almandine, Ap – Apatite, Bn Bornite, Bt - Biotite, Cct - Chalcocite, Ccp - Chalcopyrite, Chl – Chlorite, Ep – Epidote, Gru -Grunerite, Ilm - Ilmenite, Kfs - K-Feldspar, Mag - Magnetite, No.S - Number of Samples, Pl – Plagioclase, Py – Pyrite and Qz -Quartz.*

3.5.1. Geophysical Footprint

The analysis of petrophysical data from the Salobo deposit demonstrates its effectiveness to map the zonation of different alteration zones, enabling a clear distinction between host rocks, alteration zones, and mineralized areas. When compared to the geophysical footprint study (Araújo et al., submitted), these results highlight the importance of integrating petrophysical and geophysical data in identifying prospective zones.

Strong correlations between magnetite concentration and magnetic susceptibility are observed in iron enrichment zones, potassic alteration, and the mineralization zone. Host rocks and distal Na-Ca zones are mostly non-magnetic (Figure 3.14). Magnetic surveys effectively map these magnetite-rich zones, identifying transitions from distal halos to proximal areas (Figure 3.14). However, as noted by Araujo et al. (2025), magnetic methods are best for regional- or district-scale exploration. As magnetite is not necessarily associated with ore minerals, magnetic anomalies may point to barren alteration zones. These misinterpretations are widespread in the Carajás Mineral Province. This magnetite formation process is evident in the K-Fe and K-Fe (Fe-rich) zones, as well as in potassic alteration and post-ore zones of the Salobo deposit, which are not necessarily mineralized.

Density variations are a good indicator of alteration and mineralization since host rocks and distal alteration zones have lower densities (2.70–3.10 g/cm³), while proximal alteration and mineralized zones with bornite, chalcocite, chalcopyrite and magnetite show higher densities (>3.30 g/cm³). Gravity data and models show a direct correlation between density and copper content. This is due to the high-density K-Fe and Fe alteration zones hosted in a low-density granite. Other denser minerals, such as grunerite and almandine, associated with Fe-enrichment and potassic alteration zones, also increase density, creating contrasts compared to distal zones. This makes gravity surveys a good tool for regional-scale mapping and IOCG exploration (Figure 3.14) (Araújo et al., submitted).

Resistivity decreases in mineralized zones due to conductive minerals such as chalcopyrite, bornite, chalcocite, and pyrite, associated with potassic and late-zone alteration. Semi-conductive magnetite also lowers resistivity in these zones (Figure 3.14). High-resistivity zones correspond to silicate-dominated areas (e.g., Qtz, Alb) in host rocks or distal zones. Chlorite and Alb indirectly affect resistivity by altering porosity, fluid content, or sulphide distribution (Figure 3.14). Electrical surveys, such as direct current resistivity and induced polarization (DCIP) directly map mineralized areas as low resistivity zones. As discussed by (Araújo et al., submitted), Salobo's electromagnetic signature is detectable, similar to other deposits in Carajás, despite its association with others minerals, such as Paulo Afonso and Furnas. Paulo Afonso displays a stronger EM anomaly than Salobo due to its massive orebody, whereas Furnas, with a higher chalcopyrite content and less disseminated sulfide, presents a weaker anomaly. The conductivity distribution at Salobo is primarily controlled by the relative

abundance of bornite, chalcocite, chalcopyrite, and pyrite, as indicated by the absence of significant signals outside the high-grade, bornite-chalcocite-rich zone.

Chargeability peaks in iron enrichment and potassic alteration zones due to disseminated chalcopyrite, bornite, chalcocite, pyrite, and magnetite (Figure 3.14). High chargeability also occurs where chlorite and almandine co-occur. This approach supports the observations made by Araujo et al. (2025), emphasizing that resistivity is a more accurate indicator of mineralization compared to other physical properties. However, while chargeability may misinterpretations of a mineralized zone, chargeability anomalies should not be overlooked, even though the likelihood of them being associated with mineralization is less than in the case of a resistivity anomaly. Direct Current resistivity and Induced Polarization (DCIP) survey outcomes indicate that resistivity provides a clearer definition of the deposit compared to chargeability. The chargeability anomaly extends well beyond the proximal alteration zones, suggesting that additional zones, such as late-zone, low-temperature hydrothermal alterations commonly found in the footwall, also exhibit chargeable properties. While time-domain electromagnetic (TDEM), gamma spectrometry, and DCIP anomalies coincide spatially, they are influenced by distinct minerals and alteration zones.

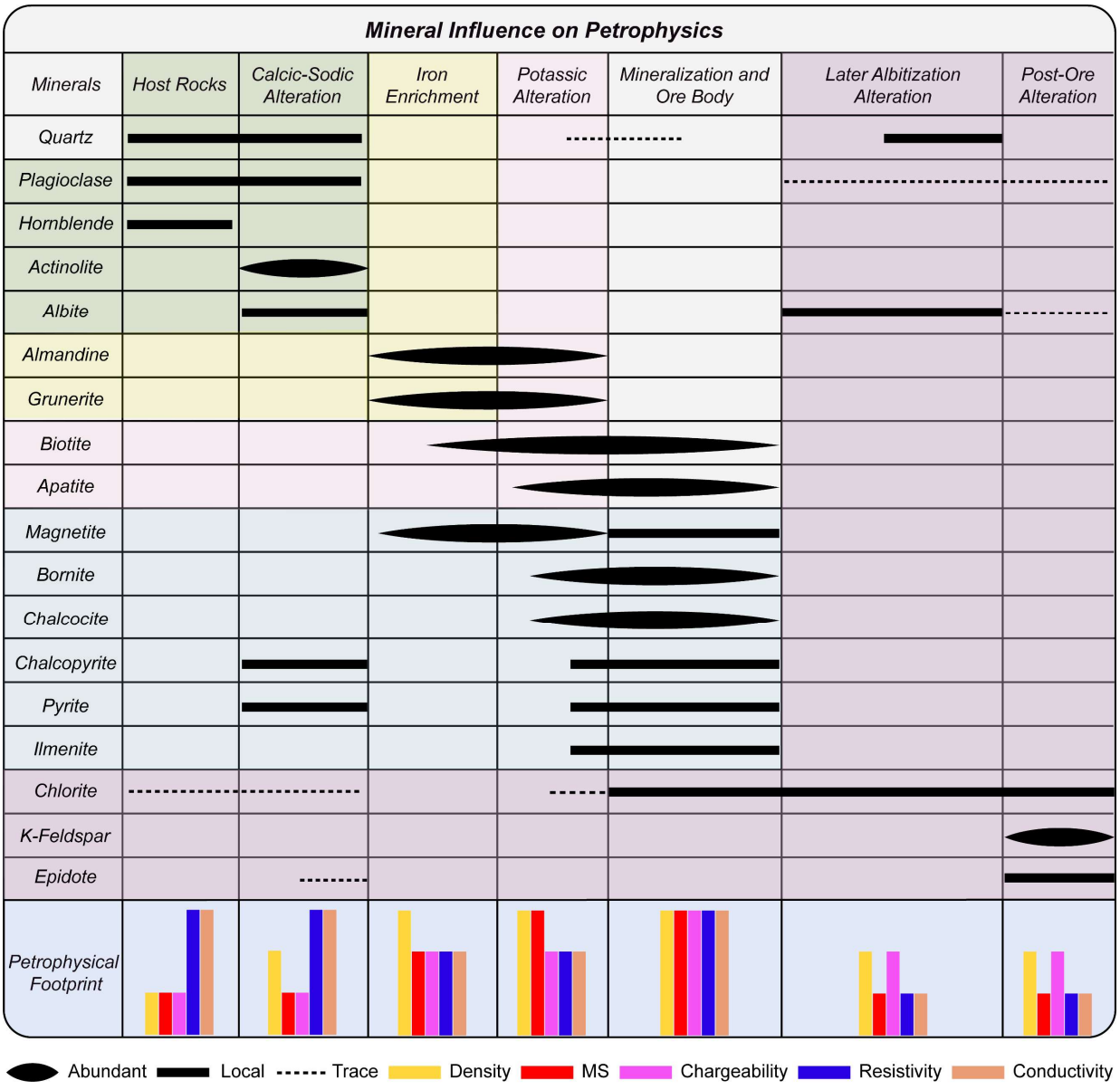


Figure 3. 14 - Influence of main minerals of Salobo IOCG Deposit and its impact on petrophysical and geophysical footprint. The size of columns in petrophysical footprint is correlated with mineral influence levels, where small columns are low influence, medium columns are moderate influence and large columns are high influence.

3.5.2. Implications for Mineral Exploration

Successful mineral exploration relies on integrating diverse datasets, including mineralogical, petrophysical, geophysical, and geological data, forming a robust framework for understanding ore-forming processes. Figure 3.15 illustrates the interconnections between these datasets, emphasizing their complementary roles in mineral exploration. Mineralogical and petrophysical data provide critical baseline information for interpreting regional geological, geophysical, and geochemical surveys, reinforcing the interdependence of these datasets. Multi-

source and multi-scale data integration is essential for characterizing mineral systems, as each dataset contributes to defining key alteration patterns and mineralization controls.

The petrophysical properties of rocks are primarily controlled by their dominant mineral constituents and relative abundances, making them valuable tools for differentiating deposit types. Geophysical anomalies are influenced both directly by ore minerals and indirectly by gangue minerals or structural overprinting. Furthermore, geological factors, such as the texture of the source body, impact geophysical signatures and must be carefully analyzed. Understanding these relationships allows geoscientists to enhance geophysical interpretations and refine exploration targeting (Airo, 2015; Austin et al., 2021). This integration enhances subsurface geological understanding and improves exploration accuracy.

However, data integration presents challenges, particularly due to scale mismatches among geological, geochemical, geophysical, petrophysical, and mineralogical datasets. Traditional map-based geological and geochemical approaches often differ in scale, resolution, and dimensionality from geophysical and petrophysical sampling methods. In this research, careful standardization, scaling, and cross-validation were applied to ensure data compatibility and enhance interpretability (Figure 3.15).

This study demonstrates how a multidisciplinary approach enhances the identification of mineralized zones, by correlating petrophysical properties with geophysical signatures and alteration patterns. Despite challenges related to data compatibility and scale differences, the systematic standardization and validation of datasets ensure more reliable interpretations. Ultimately, this methodology strengthens exploration strategies by refining target delineation, reducing uncertainty, and supporting more effective decision-making in IOCG deposit exploration.

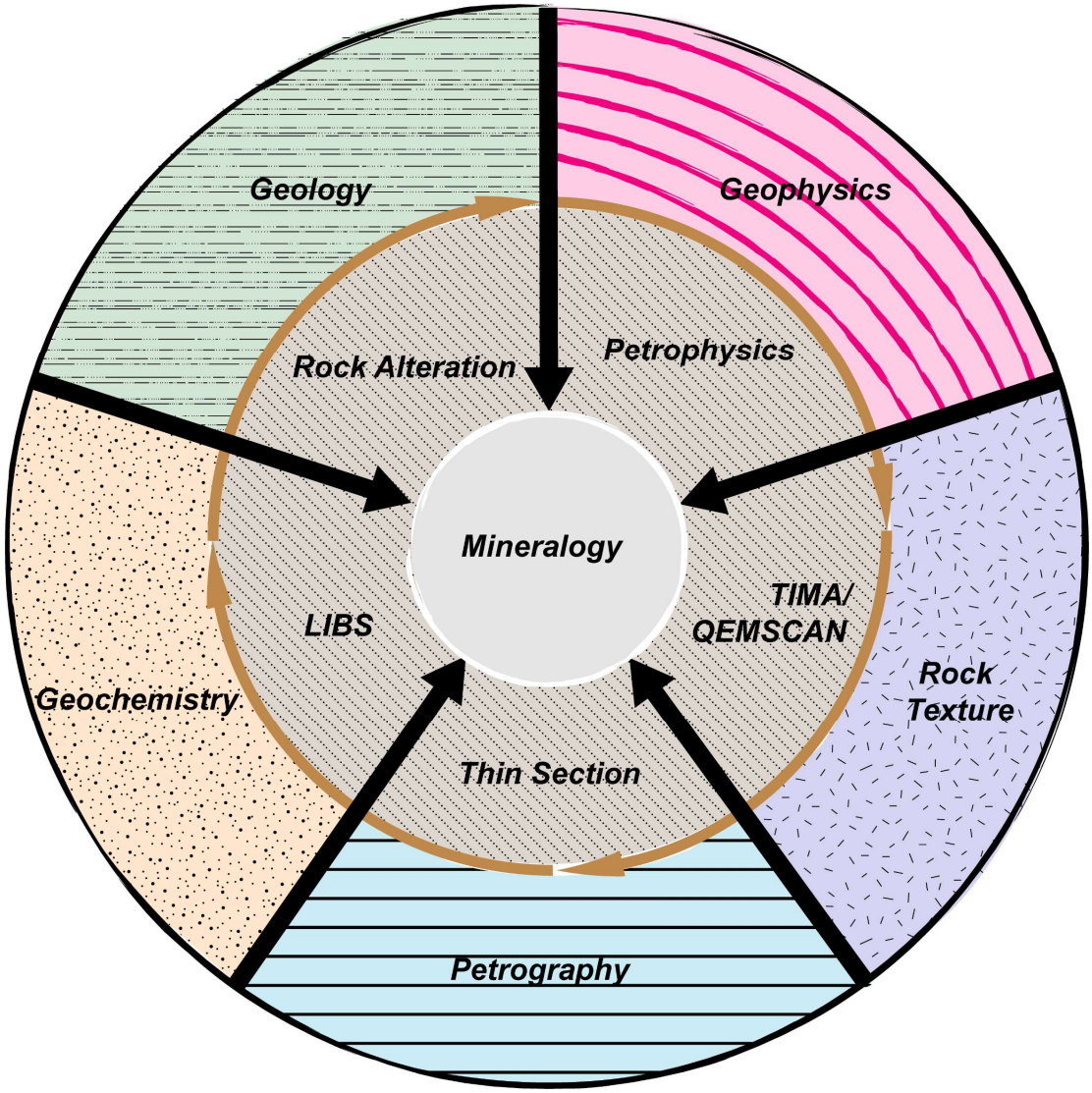


Figure 3. 15 - Conceptual framework illustrating the interconnections between mineralogical, petrophysical, geophysical, geological, and geochemical datasets used in this study. Mineralogy serves as the central axis, integrating analytical techniques such as LIBS, TIMA/QEMSCAN, and thin-section petrography to provide insights into mineral composition, texture, and alteration. Petrophysical and geophysical data contribute to characterizing ore-forming processes by defining variations in density, magnetic susceptibility, and chargeability. This integrated approach improves exploration targeting by refining the interpretation of alteration halos, mineralized zones, and structural controls.

3.6. Conclusion

The petrophysical footprint of the Salobo deposit provides valuable insights into the strong spatial and temporal correlation between hydrothermal alteration and mineralization processes. Multiple hydrothermal pulses and deformation events difficulty the boundaries between alteration zones, emphasizing the need for multivariate analysis to delineate the contrast of physical rock properties. Calcic-sodic alteration serves as an effective pathfinding and zoning indicator, whereas iron enrichment and potassic alteration define the economically mineralized zones.

Integrating petrophysical properties with mineral assemblages underscores the importance of combining mineralogical, petrophysical, and geophysical methods for precise ore body delineation. This approach enhances the understanding of deposit evolution and provides valuable indicators for exploration and modeling strategies.

A combined geophysical approach utilizing magnetic, gradiometric gravity, direct current resistivity and induced polarization (DCIP), and resistivity methods, is crucial for capturing the full range of petrophysical contrasts within the Salobo deposit. Magnetic surveys are particularly useful for mapping alteration in a regional scale. However, magnetic anomalies are often associated with barren, district-scale alteration, or barren intermediate, proximal alteration zones. Magnetic surveys in the Carajás Mineral Provinces often produces several misinterpretations. Gravity gradiometric surveys are an important tool for detecting and modelling denser proximal alteration and mineralized zones. Resistivity and chargeability anomalies, particularly in the iron enrichment and potassic alteration zones, serve as direct indicators of mineralization, with resistivity offering a more accurate means of identifying mineralized areas. Exploration can target anomalies characterized by high magnetic susceptibility, high density, low resistivity, and high chargeability. These anomalies will often not coincide, and the correlations shown in this paper may be used to help eliminating misinterpretations or prioritizing drill targets.

Important key signatures were identified in this study, including the correlation between magnetite and magnetic susceptibility anomalies, the relationship between almandine and grunerite with density, the association between sulphides and gangue minerals and its impact on chargeability, as well as resistivity serving as a direct indicator of mineralization. These insights were made possible by the extended dataset, which provided a powerful structure for exploration. This approach not only advances our understanding of the Salobo deposit but also offers a valuable framework that can be applied to other deposits, enhancing the precision and efficiency of future mineral exploration.

Acknowledgments

This paper is part of the PhD research of the first author, funded in part by the Coordenação de Aperfeiçoamento de Pessoal de Nível Superior - Brasil (CAPES) Finance Code 001, and supported by the Brazilian National Council for Scientific and Technological Development (CNPq) and the CT-Universal Program (Project 408592/2021-4). The authors express their gratitude to the Vale-ADIMB-Brazilian Universities consortium for their support and permission to publish this work, as part of the Geodynamics and Metallogeny of the Carajás Mineral Province (PA) and Quadrilátero Ferrífero (QF) Project, funded by Vale S.A. Additionally, Adalene M. Silva and C. Toledo acknowledge their research grants from CNPq (Projects 309846/2023-4 and 313807/2021-3). The authors also appreciate the technical support of geologist Érico Natal Pedro Zacchi

Appendix A

Detailed petrophysical, mineralogical and geological data

Sample ID	Drill Hole	Density (g/cm^3)	MS ($SI \times 10^{-3}$)	Resistivity (Ohm.m)	Chargeability (mV/V)	Zone	Subzone	Host Rocks
2B	DH00002	3,310	74,80	5354,67	14,09	Ca-Na	Initial Ca-Na	Initial Alt
2C	DH00002	3,090	2,90	280,55	49,05	Ca-Na	Initial Ca-Na	Mod Alt
2E	DH00002	2,720	5,21	4210,47	12,75	Ca-Na	Moderate Ca-Na	Unalteret
2G	DH00002	2,820	2,27	4270,00	6,97	Fe-Enrich	Ca-Fe-K	Unalteret
2I	DH00002	2,600	0,32	3039,09	6,35	Fe-Enrich	Ca-Fe-K	Unalteret
2J	DH00002	3,170	0,60	2948,58	24,69	Fe-Enrich	Ca-Fe-K	Unalteret
2K	DH00002	3,760	893,18	446,22	84,06	Fe-Enrich	K-Fe (Fe-rich)	Adv Alt
2L	DH00002	3,890	1625,78	1,70	449,24	Fe-Enrich	K-Fe (Fe-rich)	Mod Alt
2M	DH00002	3,520	2,10	1274,07	14,78	Fe-Enrich	K-Fe (Fe-rich)	Mod Alt
2N	DH00002	3,900	978,78	0,59	118,89	K	Bt	Adv Alt
2P	DH00002	2,730	0,26	1429,88	68,30	Ca-Na	Advanced Ca-Na	Unalteret
2T	DH00002	2,840	0,29	2509,29	58,47	Later Albitization	Na (Albite)	Initial Alt
2-1B	DH00002-1	3,210	107,47	1977,29	16,18	Ca-Na	Initial Ca-Na	Initial Alt
2-1C	DH00002-1	2,730	15,28	3177,01	57,31	Fe-Enrich	Ca-Fe-K	Unalteret
2-1D	DH00002-1	2,860	2,25	1148,38	46,39	Fe-Enrich	Ca-Fe-K	Unalteret
2-1F	DH00002-1	3,340	28,34	1338,73	55,62	Fe-Enrich	Transition from Ca-Fe-K to K-Fe	Mod Alt
2-1I	DH00002-1	3,930	1534,22	94,30	21,34	K	Bt	Mod Alt
2-1J	DH00002-1	3,290	1106,91	1651,98	77,91	K	Bt	Unalteret
2-1K	DH00002-1	2,720	49,51	1999,54	56,93	Ca-Na	Advanced Ca-Na	Unalteret
2-2A	DH00002-2	2,640	0,07	5905,48	4,85	Ca-Na	Moderate Ca-Na	Unalteret
2-2B	DH00002-2	2,830	30,62	10022,78	9,75	Fe-Enrich	Ca-Fe-K	Unalteret
2-2E	DH00002-2	3,210	1,25	426,37	4,40	Fe-Enrich	Transition from Ca-Fe-K to K-Fe	Mod Alt
2-2H	DH00002-2	3,470	121,15	236,59	36,38	Fe-Enrich	K-Fe (Fe-rich)	Mod Alt
2-2I	DH00002-2	3,490	0,41	22,84	49,61	Ore Body	Transition from K to Ore	Chl
2-2J	DH00002-2	4,260	3085,53	3,91	175,56	Ore Body	High Grade Ore	Adv Alt
2-2L	DH00002-2	2,980	104,16	1254,21	5,89	Later Albitization	Na (Albite)	Dia
2-2M	DH00002-2	3,020	41,28	873,81	3,08	DB	DB	Dia
3A	DH00003	3,120	2,41	9833,03	13,58	Ca-Na	Initial Ca-Na	Unalteret
3B	DH00003	2,780	0,42	7729,76	5,75	Ca-Na	Moderate Ca-Na	Unalteret
3C	DH00003	2,970	0,57	6333,95	14,95	Fe-Enrich	Ca-Fe-K	Unalteret
3D	DH00003	3,200	1168,22	254,66	151,71	Ca-Na	Advanced Ca-Na	Unalteret
3F	DH00003	2,750	9,62	3579,32	27,06	Ca-Na	Advanced Ca-Na	Unalteret
3G	DH00003	2,720	49,02	917,61	13,15	Fe-Enrich	Ca-Fe-K	Unalteret
3J	DH00003	2,900	6,78	281,03	17,00	Fe-Enrich	K-Fe	Initial Alt
3L	DH00003	3,080	1,25	471,18	6,94	Fe-Enrich	K-Fe	Mod Alt
3M	DH00003	3,790	614,49	3004,05	18,42	Fe-Enrich	K-Fe (Fe-rich)	Mod Alt
3N	DH00003	3,280	1,73	1437,61	6,97	Fe-Enrich	K-Fe	Mod Alt
3Q	DH00003	4,020	1770,07	406,26	54,24	K	Bt	Adv Alt
3R	DH00003	3,470	910,03	1120,71	56,59	Ore Body	Transition from K to Ore	Adv Alt
3S	DH00003	3,390	1527,33	2,71	119,66	Ore Body	Transition from K to Ore	Mod Alt
3-1A	DH00003-1	2,720	0,28	954,75	6,81	Ca-Na	Moderate Ca-Na	Unalteret
3-1B	DH00003-1	2,710	0,34	261,97	15,52	Post-ore	K-feldspar	Unalteret
3-1D	DH00003-1	2,680	0,19	1340,10	3,45	Ca-Na	Moderate Ca-Na	Unalteret
3-1F	DH00003-1	2,690	32,90	742,74	3,99	Ca-Na	Advanced Ca-Na	Dia
3-1H	DH00003-1	3,050	0,64	562,31	3,64	Fe-Enrich	K-Fe (Fe-rich)	Unalteret
3-1I	DH00003-1	3,040	1,26	356,76	3,58	Fe-Enrich	K-Fe	Unalteret
3-1K	DH00003-1	3,390	89,90	484,61	15,02	Fe-Enrich	K-Fe	Mod Alt
3-1L	DH00003-1	3,540	1132,86	40,38	49,81	Later Albitization	Transition from Ore to Na	Adv Alt
3-1M	DH00003-1	2,850	0,99	520,91	3,42	Ca-Na	Advanced Ca-Na	Chl
3-2A	DH00003-2	2,670	3,05	1801,39	7,85	Ca-Na	Moderate Ca-Na	Unalteret
3-2B	DH00003-2	2,730	0,63	2280,77	12,02	Fe-Enrich	Ca-Fe-K	Chl
3-2D	DH00003-2	2,720	6,95	4147,78	32,44	Ca-Na	Moderate Ca-Na	Initial Alt
3-2E	DH00003-2	2,660	36,29	798,37	8,42	Ca-Na	Advanced Ca-Na	Chl
3-2G	DH00003-2	3,000	0,98	541,41	7,32	Fe-Enrich	Transition from Ca-Fe-K to K-Fe	Adv Alt
3-2I	DH00003-2	3,480	1388,58	457,93	70,02	Later Albitization	Transition from Ore to Na	Adv Alt

Sample ID	Methods	Albite (Volume %)	Allanite (Volume %)	Grunerite (Volume %)	Hornblende (Volume %)	Actinolite (Volume %)	Apatite (Volume %)	Biotite (Volume %)	Bornite (Volume %)	Calcite (Volume %)
2B	TIMA	0,00	0,02	0,03	56,90	29,08	0,01	0,01	0,00	0,18
2C	TIMA	0,00	0,00	0,00	0,04	58,68	0,01	22,92	0,00	0,05
2E	QEMSCAN	53,26	1,26	0,08	13,48	0,25	0,03	1,46	0,00	0,10
2G	LIBS	8,37	0,07	2,38	10,70	11,81	0,13	2,84	0,11	0,15
2I	QEMSCAN	10,05	0,13	0,51	1,19	0,23	0,03	21,69	0,00	0,03
2J	TIMA	0,82	0,32	0,02	24,49	12,48	0,68	0,11	26,48	0,34
2K	QEMSCAN	0,00	0,08	51,39	0,02	0,07	0,01	0,12	0,05	0,00
2L	TIMA	0,00	0,00	11,95	0,01	0,01	0,79	0,06	0,07	0,00
2M	LIBS	1,33	0,37	8,60	0,06	0,10	0,30	6,62	4,12	0,02
2N	TIMA	0,00	0,80	2,25	0,23	0,00	0,80	6,06	2,40	0,31
2P	TIMA	82,53	0,04	0,10	0,00	0,00	0,27	0,00	0,00	0,96
2T	QEMSCAN	22,31	0,00	0,06	0,00	0,00	0,02	0,33	0,00	0,01
2-1B	QEMSCAN	0,21	0,06	3,57	50,38	24,78	0,10	0,03	0,02	0,02
2-1C	TIMA	5,21	0,00	0,37	0,07	2,45	0,00	3,09	0,00	1,19
2-1D	QEMSCAN	7,89	0,07	0,01	0,14	0,01	0,01	60,04	0,02	0,01
2-1F	LIBS	0,02	1,11	2,43	3,18	0,68	0,05	60,30	0,00	0,08
2-1I	LIBS	0,00	0,95	0,04	0,01	0,01	0,41	6,63	17,10	0,01
2-1J	QEMSCAN	0,00	0,02	18,16	0,29	6,59	0,20	0,08	0,00	0,01
2-1K	LIBS	74,02	0,03	0,07	0,03	0,07	0,20	0,00	0,00	0,02
2-2A	QEMSCAN	54,94	0,01	0,02	0,01	0,01	0,00	0,08	0,02	0,03
2-2B	TIMA	9,50	0,08	0,06	0,19	0,17	0,93	23,04	0,00	2,85
2-2E	LIBS	0,02	0,51	9,12	9,21	5,92	0,05	42,54	0,09	0,00
2-2H	LIBS	0,00	0,01	0,00	0,00	0,00	0,00	0,60	0,06	0,00
2-2I	QEMSCAN	9,73	0,02	0,00	0,00	0,00	0,10	0,00	0,02	0,02
2-2J	TIMA	0,00	0,00	0,25	0,49	15,41	3,63	0,01	0,00	0,22
2-2L	LIBS	28,94	0,01	0,35	0,94	1,38	0,06	0,00	0,00	0,04
2-2M	QEMSCAN	0,92	0,11	0,01	39,71	5,34	0,45	0,35	0,00	0,39
3A	TIMA	13,58	0,03	0,08	46,38	3,37	1,61	0,14	0,00	0,08
3B	LIBS	52,32	0,60	0,01	9,83	1,15	0,04	0,13	0,00	0,36
3C	LIBS	12,14	0,03	0,00	29,12	0,13	0,04	28,48	0,00	0,02
3D	QEMSCAN	55,73	0,01	0,03	0,14	0,16	0,09	0,11	0,00	1,00
3F	TIMA	39,88	0,05	0,01	0,01	0,01	2,83	0,99	0,00	0,00
3G	LIBS	27,13	0,84	0,05	2,77	1,58	1,83	2,93	0,02	0,02
3J	TIMA	1,18	0,03	0,01	0,01	0,00	0,20	0,89	0,01	0,05
3L	LIBS	0,13	0,13	0,00	0,39	0,34	0,13	57,38	0,12	0,01
3M	LIBS	0,03	0,06	3,49	0,04	0,20	0,13	21,90	3,98	0,00
3N	LIBS	0,15	0,06	0,00	0,05	0,03	0,12	75,19	0,01	0,00
3Q	QEMSCAN	0,27	0,95	0,00	0,33	0,00	0,98	12,36	0,41	0,01
3R	LIBS	1,07	4,21	0,04	4,11	0,11	0,91	44,73	2,35	2,43
3S	QEMSCAN	2,06	0,04	0,00	0,00	0,00	0,53	3,06	0,23	0,40
3-1A	QEMSCAN	31,25	0,29	0,00	0,01	0,00	0,12	7,62	0,48	0,02
3-1B	TIMA	36,72	0,05	0,00	0,00	0,00	0,12	0,60	0,01	0,01
3-1D	LIBS	32,69	0,22	0,00	0,01	0,03	0,03	0,30	0,15	0,05
3-1F	LIBS	58,73	0,37	0,01	0,23	0,03	0,25	19,19	0,01	0,04
3-1H	LIBS	0,66	0,30	2,34	0,00	0,31	0,14	7,67	0,32	0,00
3-1I	LIBS	0,15	0,41	0,00	6,60	2,29	0,10	33,48	0,13	0,00
3-1K	QEMSCAN	0,00	0,28	0,02	0,06	0,11	0,12	81,37	0,89	0,00
3-1L	TIMA	1,81	1,28	0,21	0,04	0,01	0,28	9,88	3,35	0,04
3-1M	LIBS	20,87	0,30	0,00	0,17	0,06	0,07	28,61	0,01	0,35
3-2A	TIMA	44,02	0,02	0,00	0,00	0,00	0,05	0,00	0,00	0,01
3-2B	LIBS	8,31	0,02	0,01	0,01	0,01	0,01	28,04	0,18	0,00
3-2D	QEMSCAN	35,66	0,10	0,00	0,11	0,03	0,05	0,05	0,03	0,01
3-2E	LIBS	65,83	0,25	0,00	0,74	0,02	0,31	9,76	0,00	0,22
3-2G	QEMSCAN	0,27	0,14	0,12	0,95	0,92	0,96	47,18	0,00	0,00
3-2I	TIMA	0,00	1,09	0,38	2,43	0,19	0,91	14,86	4,32	1,22

Sample ID	Chalcocite (Volume %)	Chalcopyrite (Volume %)	Chlorite (Volume %)	Dolomite (Volume %)	Epidote (Volume %)	Fluorite (Volume %)	Galena (Volume %)	Almandine (Volume %)
2B	0,00	0,00	0,11	0,01	0,10	0,01	0,00	0,00
2C	0,00	9,75	4,02	0,00	0,00	0,24	0,00	0,00
2E	0,00	0,00	4,01	0,00	0,68	0,01	0,00	0,21
2G	0,01	0,34	27,09	0,00	1,56	0,04	0,00	0,08
2I	0,00	0,02	15,68	0,00	0,23	0,01	0,00	0,00
2J	2,06	0,31	0,77	0,00	4,44	0,02	0,00	0,01
2K	0,02	0,01	17,78	0,00	0,01	0,00	0,00	13,11
2L	0,00	0,03	37,56	0,00	0,00	0,00	0,00	17,83
2M	0,68	0,19	40,85	0,00	0,26	0,00	0,00	18,57
2N	0,00	5,27	48,46	0,00	0,00	0,15	0,00	7,75
2P	0,00	0,00	1,53	0,00	0,00	0,00	0,00	0,00
2T	0,00	0,00	43,83	0,00	0,00	0,00	0,00	0,00
2-1B	0,01	1,56	5,75	0,00	0,07	0,05	0,00	1,74
2-1C	0,00	0,00	31,08	0,13	0,02	0,00	0,00	0,01
2-1D	0,00	0,21	12,68	0,00	0,16	0,00	0,00	0,00
2-1F	0,00	0,00	28,37	0,00	0,14	0,00	0,00	2,09
2-1I	6,06	4,03	8,70	0,00	0,16	0,14	0,00	0,96
2-1J	0,00	0,02	18,15	0,00	0,07	0,00	0,00	9,43
2-1K	0,00	0,00	0,16	0,00	0,20	0,00	0,00	0,05
2-2A	0,04	0,01	1,61	0,00	0,06	0,00	0,00	0,01
2-2B	0,00	0,01	17,03	0,02	0,01	0,03	0,00	0,10
2-2E	0,01	0,00	18,37	0,00	0,14	0,00	0,00	9,90
2-2H	0,01	0,10	28,63	0,00	0,01	0,00	0,00	28,27
2-2I	0,02	0,02	0,02	0,00	0,03	0,00	0,00	0,00
2-2J	0,00	0,00	19,30	0,01	0,00	0,00	0,00	0,00
2-2L	0,00	0,01	46,81	0,00	0,14	0,00	0,00	0,31
2-2M	0,00	0,00	1,03	0,00	0,33	0,00	0,00	0,13
3A	0,00	0,04	10,74	0,00	0,16	0,00	0,00	0,18
3B	0,00	0,00	2,40	0,00	0,64	0,06	0,00	0,01
3C	0,00	0,01	7,22	0,00	0,02	0,03	0,00	0,00
3D	0,00	0,02	3,71	0,00	0,15	0,00	0,00	0,40
3F	0,00	1,79	9,87	0,00	0,01	0,00	0,00	0,01
3G	0,00	1,06	11,52	0,00	1,36	0,03	0,00	0,53
3J	0,00	19,28	13,41	0,00	0,19	0,01	0,00	0,03
3L	0,01	0,00	26,26	0,00	0,21	0,02	0,00	1,51
3M	0,02	1,44	38,79	0,00	0,14	0,01	0,00	6,07
3N	0,01	0,00	18,30	0,00	0,06	0,01	0,00	1,28
3Q	0,01	0,05	22,62	0,00	0,08	3,32	0,00	0,01
3R	0,05	0,04	12,70	0,00	8,02	0,02	0,00	1,57
3S	0,00	0,31	19,05	0,00	1,96	0,00	0,00	2,58
3-1A	0,00	2,29	4,37	0,00	0,22	0,02	0,00	0,00
3-1B	0,00	7,90	5,98	0,00	0,00	0,00	0,00	0,01
3-1D	0,00	2,78	11,22	0,00	1,38	0,00	0,00	0,02
3-1F	0,00	0,04	6,39	0,00	0,41	0,10	0,00	0,04
3-1H	0,01	1,50	26,75	0,00	0,45	0,00	0,00	22,48
3-1I	0,01	0,01	40,75	0,00	0,43	0,07	0,00	1,13
3-1K	0,00	0,07	5,05	0,00	0,04	0,05	0,00	0,04
3-1L	0,00	0,48	17,44	0,00	0,03	0,02	0,00	0,15
3-1M	0,00	0,03	24,04	0,00	1,51	0,01	0,00	0,00
3-2A	0,00	0,00	2,06	0,00	10,20	0,00	0,00	0,06
3-2B	0,01	3,29	38,47	0,00	0,01	0,01	0,00	0,10
3-2D	0,00	3,31	13,67	0,00	0,20	0,01	0,00	0,01
3-2E	0,00	0,00	4,89	0,00	0,51	0,77	0,00	0,03
3-2G	0,00	0,00	29,92	0,00	0,43	0,01	0,00	2,21
3-2I	0,40	0,35	16,68	0,00	0,11	0,46	0,00	0,12

Sample ID	Andradite (Volume %)	Gold (Volume %)	Gypsum (Volume %)	Ilmenite (Volume %)	K-Feldspa (Volume %)r	Linnaeite-Carrollite Group (Volume %)	Magnetite (Volume %)	Millerite (Volume %)
2B	0,02	0,00	0,00	0,00	0,01	0,00	0,24	0,00
2C	0,00	0,00	0,01	0,00	0,00	0,07	0,02	0,17
2E	0,02	0,00	0,03	0,00	1,14	0,00	0,65	0,00
2G	0,09	0,00	0,33	0,02	1,76	0,01	0,13	0,00
2I	0,00	0,00	0,00	0,00	0,21	0,02	0,00	0,02
2J	3,06	0,00	8,31	0,00	2,85	0,00	7,67	0,00
2K	0,00	0,00	0,00	0,00	0,00	0,00	17,08	0,02
2L	0,00	0,00	0,00	0,00	0,00	0,00	31,24	0,00
2M	0,01	0,00	0,03	9,31	1,36	0,01	0,05	0,06
2N	0,00	0,00	0,00	0,13	0,00	0,00	19,06	0,00
2P	0,00	0,00	0,00	0,00	0,00	0,00	4,35	0,00
2T	0,00	0,00	0,00	0,00	0,00	0,00	2,42	0,00
2-1B	0,06	0,00	0,03	0,07	0,06	0,00	3,30	0,00
2-1C	0,00	0,00	0,00	0,27	0,28	0,00	1,61	0,00
2-1D	0,00	0,00	0,00	1,41	0,18	0,00	0,02	0,00
2-1F	0,00	0,00	0,00	0,00	0,18	0,00	0,22	0,00
2-1I	0,01	0,00	0,48	0,01	0,79	0,01	45,20	0,00
2-1J	0,03	0,00	0,13	0,00	0,01	0,00	44,23	0,00
2-1K	0,09	0,00	0,29	0,13	0,00	0,00	7,44	0,00
2-2A	0,00	0,00	0,00	0,01	0,15	0,00	0,02	0,00
2-2B	0,00	0,00	0,00	0,43	0,45	0,00	0,67	0,00
2-2E	0,00	0,00	0,00	0,46	0,39	0,01	0,00	0,00
2-2H	0,00	0,00	0,00	1,15	0,01	0,00	40,06	0,00
2-2I	0,04	0,00	1,25	0,32	0,00	0,00	86,36	0,00
2-2J	0,00	0,00	0,00	0,03	0,00	0,00	54,16	0,00
2-2L	0,03	0,00	0,04	0,07	0,00	0,00	8,37	0,00
2-2M	0,04	0,00	0,01	5,07	0,05	0,00	0,42	0,00
3A	0,01	0,00	0,00	3,29	0,48	0,00	0,04	0,00
3B	0,00	0,00	0,00	0,01	0,03	0,00	0,01	0,00
3C	0,00	0,00	0,00	0,22	0,12	0,00	0,00	0,00
3D	0,04	0,00	0,15	1,18	0,03	0,00	18,36	0,02
3F	0,00	0,00	0,00	0,00	0,89	0,00	0,01	0,00
3G	0,06	0,00	0,30	0,64	0,21	0,00	3,79	0,02
3J	0,00	0,00	0,00	0,15	5,40	0,02	0,22	0,00
3L	0,00	0,00	0,00	0,56	0,83	0,00	0,00	0,03
3M	0,01	0,00	0,01	0,58	0,11	0,00	17,44	0,00
3N	0,00	0,00	0,00	1,37	0,48	0,00	0,00	0,00
3Q	0,00	0,00	0,10	0,07	0,14	0,00	50,46	0,00
3R	0,01	0,00	0,28	0,28	2,08	0,00	6,81	0,00
3S	0,19	0,00	0,13	0,13	0,03	0,00	66,44	0,00
3-1A	0,00	0,00	0,00	0,08	2,70	0,00	0,02	0,00
3-1B	0,00	0,00	0,00	0,10	13,56	0,00	0,01	0,00
3-1D	0,00	0,00	0,21	0,04	0,01	0,00	0,20	0,00
3-1F	0,00	0,00	0,02	0,47	3,39	0,00	1,30	0,00
3-1H	0,01	0,00	0,01	0,43	0,02	0,00	33,77	0,00
3-1I	0,00	0,00	0,00	2,00	1,00	0,00	0,00	0,00
3-1K	0,00	0,00	0,00	0,30	0,22	0,00	2,93	0,00
3-1L	0,00	0,00	0,00	0,12	0,68	0,00	25,15	0,00
3-1M	0,00	0,00	0,00	0,21	1,23	0,00	0,00	0,00
3-2A	0,00	0,00	0,00	0,00	0,02	0,00	0,00	0,00
3-2B	0,00	0,00	0,00	0,01	0,07	0,00	0,57	0,00
3-2D	0,00	0,00	0,00	0,21	0,02	0,00	0,23	0,00
3-2E	0,00	0,00	0,02	0,23	2,50	0,00	1,05	0,00
3-2G	0,00	0,00	0,00	1,25	0,49	0,00	0,03	0,00
3-2I	0,02	0,00	0,00	0,08	0,00	0,00	28,93	0,00

Sample ID	Molybdenite (Volume %)	Monazite (Volume %)	Muscovite (Volume %)	Other Sulphides (Volume %)	Others (Volume %)	Pentlandite (Volume %)	Plagioclase (Volume %)	Pyrite (Volume %)
2B	0,00	0,00	0,00	0,00	0,08	0,00	0,00	0,00
2C	0,00	0,00	0,00	0,00	0,86	0,02	0,00	2,88
2E	0,01	0,00	0,00	0,00	0,00	0,00	6,79	0,00
2G	0,00	0,00	0,00	0,00	0,00	0,00	27,82	0,00
2I	0,00	0,00	0,00	0,00	0,00	0,00	32,25	0,00
2J	0,06	0,00	0,11	0,00	0,00	0,00	0,59	0,02
2K	0,00	0,00	0,00	0,00	0,00	0,00	0,01	0,00
2L	0,00	0,00	0,00	0,00	0,10	0,00	0,00	0,00
2M	0,01	0,00	0,00	0,00	0,00	0,00	0,55	0,00
2N	0,00	0,00	0,00	0,00	0,06	0,00	0,00	0,01
2P	0,00	0,00	0,01	0,00	0,03	0,00	0,21	0,00
2T	0,00	0,00	0,25	0,00	0,04	0,00	0,89	0,00
2-1B	0,00	0,00	0,00	0,00	0,00	0,00	0,38	6,66
2-1C	0,00	0,00	1,11	0,00	0,19	0,00	22,60	0,00
2-1D	0,00	0,00	0,00	0,00	0,00	0,00	14,50	0,02
2-1F	0,00	0,00	0,00	0,00	0,00	0,00	0,96	0,02
2-1I	0,13	0,00	0,00	0,00	0,00	0,00	0,00	0,05
2-1J	0,00	0,00	0,00	0,00	0,00	0,00	0,02	0,01
2-1K	0,00	0,00	0,00	0,00	0,00	0,00	16,57	0,00
2-2A	0,00	0,00	0,00	0,00	0,00	0,00	14,21	0,00
2-2B	0,00	0,00	1,27	0,00	0,24	0,00	30,90	0,00
2-2E	0,00	0,00	0,00	0,00	0,00	0,00	0,02	0,00
2-2H	0,00	0,00	0,00	0,00	0,00	0,00	0,00	0,02
2-2I	0,00	0,00	0,00	0,00	0,00	0,00	1,58	0,12
2-2J	0,00	0,01	0,00	0,00	0,02	0,00	0,00	0,00
2-2L	0,00	0,00	0,00	0,00	0,00	0,00	11,67	0,01
2-2M	0,00	0,00	0,00	0,00	0,00	0,00	35,97	0,02
3A	0,00	0,00	0,87	0,00	0,09	0,00	13,87	0,16
3B	0,00	0,00	0,00	0,00	0,00	0,00	9,53	0,00
3C	0,00	0,00	0,00	0,00	0,00	0,00	22,33	0,01
3D	0,00	0,00	0,00	0,00	0,00	0,00	18,01	0,01
3F	0,02	0,00	0,05	0,00	0,01	0,00	0,87	3,21
3G	0,00	0,00	0,00	0,00	0,00	0,00	26,26	0,11
3J	0,02	0,00	0,08	0,00	0,50	0,00	1,06	0,12
3L	0,01	0,00	0,00	0,00	0,00	0,00	2,53	0,00
3M	0,00	0,00	0,00	0,00	0,00	0,00	0,03	0,03
3N	0,00	0,00	0,00	0,00	0,00	0,00	0,66	0,00
3Q	0,00	0,00	0,00	0,00	0,00	0,00	0,05	0,04
3R	0,01	0,00	0,00	0,00	0,00	0,00	1,42	0,01
3S	0,00	0,00	0,00	0,00	0,00	0,00	0,40	0,23
3-1A	0,00	0,00	0,00	0,00	0,00	0,00	2,77	0,03
3-1B	0,00	0,00	0,04	0,00	0,01	0,00	2,50	2,66
3-1D	0,00	0,00	0,00	0,00	0,00	0,00	2,79	0,03
3-1F	0,00	0,00	0,00	0,00	0,00	0,00	5,12	0,12
3-1H	0,01	0,00	0,00	0,00	0,00	0,00	0,44	0,56
3-1I	0,00	0,00	0,00	0,00	0,00	0,00	4,83	0,03
3-1K	0,01	0,00	0,00	0,00	0,00	0,00	0,03	0,02
3-1L	0,00	0,00	0,05	0,00	0,39	0,00	0,36	0,00
3-1M	0,00	0,00	0,00	0,00	0,00	0,00	6,67	0,00
3-2A	0,00	0,00	0,00	0,00	0,01	0,00	0,68	0,14
3-2B	0,00	0,00	0,00	0,00	0,00	0,00	8,14	2,29
3-2D	0,00	0,00	0,00	0,00	0,00	0,00	7,83	0,03
3-2E	0,00	0,00	0,00	0,00	0,00	0,00	12,13	0,04
3-2G	0,00	0,00	0,00	0,00	0,00	0,00	0,30	0,01
3-2I	0,01	0,00	0,01	0,00	0,37	0,00	0,00	0,01

Sample ID	Pyroxene (Volume %)	Pyrrhotite (Volume %)	Quartz (Volume %)	Schorl-Dravite (Volume %)	Silver (Volume %)	Sphalerite (Volume %)	Thorite (Volume %)	Ti-Oxide (Volume %)
2B	12,60	0,00	0,38	0,00	0,00	0,00	0,00	0,00
2C	0,00	0,05	0,09	0,00	0,00	0,00	0,00	0,00
2E	0,01	0,00	16,52	0,01	0,00	0,00	0,00	0,00
2G	0,14	0,00	3,98	0,01	0,00	0,00	0,00	0,00
2I	0,00	0,00	17,69	0,00	0,00	0,00	0,00	0,00
2J	0,03	0,03	3,79	0,00	0,00	0,00	0,00	0,00
2K	0,00	0,00	0,18	0,05	0,00	0,00	0,00	0,00
2L	0,00	0,00	0,28	0,00	0,00	0,00	0,00	0,00
2M	0,00	0,00	4,58	1,78	0,00	0,00	0,00	0,00
2N	0,00	0,00	6,11	0,13	0,00	0,00	0,00	0,00
2P	0,00	0,00	9,37	0,00	0,00	0,00	0,00	0,10
2T	0,00	0,00	29,63	0,00	0,00	0,00	0,01	0,17
2-1B	0,13	0,00	0,88	0,03	0,00	0,00	0,00	0,00
2-1C	0,05	0,00	17,46	0,00	0,00	0,00	0,00	0,01
2-1D	0,00	0,00	2,54	0,00	0,00	0,00	0,00	0,00
2-1F	0,02	0,00	0,13	0,00	0,00	0,00	0,00	0,00
2-1I	0,00	0,00	8,06	0,04	0,00	0,00	0,00	0,00
2-1J	0,17	0,00	2,40	0,00	0,00	0,00	0,00	0,00
2-1K	0,01	0,00	0,18	0,03	0,00	0,00	0,00	0,00
2-2A	0,00	0,00	28,75	0,00	0,00	0,00	0,00	0,00
2-2B	0,01	0,00	11,29	0,00	0,00	0,00	0,00	0,04
2-2E	0,01	0,00	3,20	0,00	0,00	0,00	0,00	0,00
2-2H	0,00	0,00	0,96	0,11	0,00	0,00	0,00	0,00
2-2I	0,00	0,00	0,14	0,00	0,00	0,00	0,00	0,00
2-2J	0,01	0,00	6,35	0,00	0,00	0,00	0,00	0,07
2-2L	0,02	0,00	0,22	0,09	0,00	0,00	0,00	0,00
2-2M	0,06	0,00	0,03	0,03	0,00	0,00	0,00	0,00
3A	0,04	0,01	3,73	0,00	0,00	0,00	0,00	0,03
3B	0,01	0,00	22,85	0,00	0,00	0,00	0,00	0,00
3C	0,00	0,00	0,04	0,00	0,00	0,00	0,00	0,00
3D	0,00	0,00	0,10	0,27	0,00	0,00	0,00	0,00
3F	0,00	0,08	39,18	0,00	0,00	0,00	0,00	0,00
3G	0,03	0,00	16,49	0,06	0,00	0,00	0,00	0,00
3J	0,00	0,01	56,72	0,00	0,00	0,00	0,00	0,00
3L	0,00	0,00	9,17	0,00	0,00	0,00	0,00	0,00
3M	0,01	0,00	5,32	0,15	0,00	0,00	0,00	0,00
3N	0,00	0,00	2,07	0,02	0,00	0,00	0,00	0,00
3Q	0,00	0,00	7,74	0,00	0,00	0,00	0,00	0,00
3R	0,01	0,00	6,02	0,10	0,00	0,00	0,00	0,00
3S	0,00	0,00	1,96	0,00	0,00	0,00	0,00	0,00
3-1A	0,00	0,00	47,71	0,00	0,00	0,00	0,00	0,00
3-1B	0,00	0,07	29,42	0,00	0,00	0,00	0,00	0,03
3-1D	0,00	0,00	47,81	0,01	0,00	0,00	0,00	0,00
3-1F	0,00	0,00	2,99	0,03	0,00	0,00	0,00	0,00
3-1H	0,00	0,00	1,15	0,09	0,00	0,00	0,00	0,00
3-1I	0,00	0,00	6,24	0,00	0,00	0,00	0,00	0,00
3-1K	0,01	0,00	8,36	0,01	0,00	0,00	0,00	0,00
3-1L	0,00	0,00	38,11	0,09	0,00	0,00	0,00	0,00
3-1M	0,00	0,00	15,64	0,00	0,00	0,00	0,00	0,00
3-2A	0,00	0,00	42,13	0,00	0,00	0,00	0,00	0,00
3-2B	0,00	0,00	10,44	0,02	0,00	0,00	0,00	0,00
3-2D	0,00	0,00	38,24	0,01	0,00	0,00	0,00	0,00
3-2E	0,00	0,00	0,22	0,01	0,00	0,00	0,00	0,00
3-2G	0,00	0,00	14,60	0,00	0,00	0,00	0,00	0,00
3-2I	0,01	0,00	27,01	0,00	0,00	0,00	0,00	0,00

Sample ID	Titanite (Volume %)	Uraninite (Volume %)	Violarite (Volume %)	Xenotime (Volume %)	Zircon (Volume %)
2B	0,21	0,00	0,00	0,00	0,00
2C	0,12	0,00	0,00	0,00	0,00
2E	0,01	0,00	0,00	0,00	0,00
2G	0,07	0,00	0,00	0,00	0,00
2I	0,01	0,00	0,00	0,00	0,00
2J	0,09	0,00	0,00	0,00	0,01
2K	0,00	0,00	0,00	0,00	0,00
2L	0,00	0,00	0,00	0,00	0,00
2M	0,18	0,00	0,00	0,00	0,00
2N	0,00	0,00	0,00	0,00	0,01
2P	0,43	0,00	0,00	0,00	0,05
2T	0,01	0,00	0,00	0,00	0,01
2-1B	0,06	0,00	0,00	0,00	0,00
2-1C	0,03	0,00	0,00	0,00	0,01
2-1D	0,08	0,00	0,00	0,00	0,00
2-1F	0,01	0,00	0,00	0,00	0,00
2-1I	0,02	0,00	0,00	0,00	0,00
2-1J	0,00	0,00	0,00	0,00	0,00
2-1K	0,43	0,00	0,00	0,00	0,00
2-2A	0,01	0,00	0,00	0,00	0,00
2-2B	0,67	0,00	0,00	0,00	0,01
2-2E	0,03	0,00	0,00	0,00	0,00
2-2H	0,01	0,00	0,00	0,00	0,00
2-2I	0,21	0,00	0,00	0,00	0,00
2-2J	0,01	0,00	0,00	0,00	0,00
2-2L	0,49	0,00	0,00	0,00	0,00
2-2M	9,54	0,00	0,00	0,00	0,00
3A	0,97	0,00	0,00	0,00	0,03
3B	0,01	0,00	0,00	0,00	0,00
3C	0,04	0,00	0,00	0,00	0,00
3D	0,30	0,00	0,00	0,00	0,00
3F	0,17	0,00	0,00	0,00	0,01
3G	0,36	0,00	0,00	0,00	0,00
3J	0,41	0,00	0,00	0,00	0,00
3L	0,23	0,00	0,00	0,00	0,00
3M	0,03	0,00	0,00	0,00	0,00
3N	0,14	0,00	0,00	0,00	0,00
3Q	0,00	0,00	0,00	0,00	0,00
3R	0,65	0,00	0,00	0,00	0,00
3S	0,28	0,00	0,00	0,00	0,00
3-1A	0,01	0,00	0,00	0,00	0,00
3-1B	0,15	0,00	0,00	0,00	0,02
3-1D	0,04	0,00	0,00	0,00	0,00
3-1F	0,72	0,00	0,00	0,00	0,00
3-1H	0,57	0,00	0,00	0,00	0,00
3-1I	0,34	0,00	0,00	0,00	0,00
3-1K	0,02	0,00	0,00	0,00	0,00
3-1L	0,01	0,00	0,00	0,00	0,01
3-1M	0,23	0,00	0,00	0,00	0,00
3-2A	0,58	0,00	0,00	0,00	0,01
3-2B	0,01	0,00	0,00	0,00	0,00
3-2D	0,22	0,00	0,00	0,00	0,00
3-2E	0,48	0,00	0,00	0,00	0,00
3-2G	0,21	0,00	0,00	0,00	0,00
3-2I	0,00	0,00	0,00	0,00	0,00

Appendix B

Principal component analysis eigenvectors of the mineralized zone in the Salobo Deposit

Variable	*CP1*	*CP2*	*CP3*	*CP4*	*CP5*	*CP6*
Density	0,385	-0,082	-0,071	-0,123	0,144	-0,051
SM	0,411	-0,155	-0,074	0,073	0,102	-0,067
Resistivity	-0,229	0,042	0,168	0,294	0,357	-0,084
Chargeability	0,261	-0,209	-0,129	0,095	0,110	-0,077
Conductivity	-0,088	0,031	0,102	0,052	-0,139	-0,081
Allanite	0,131	0,071	0,170	-0,010	-0,030	0,044
Apatite	0,215	-0,097	-0,072	0,242	0,244	0,120
Biotite	-0,062	-0,045	0,107	-0,200	-0,162	-0,061
Bornite	0,219	0,454	0,122	-0,024	0,069	-0,030
Calcite	0,013	-0,009	0,204	0,227	0,269	0,075
Chalcocite	0,224	0,395	0,079	-0,095	0,078	-0,098
Chalcopyrite	-0,047	0,215	-0,428	0,082	-0,089	0,099
Epidote	0,011	0,153	0,222	0,078	-0,108	-0,026
Fluorite	0,129	-0,071	-0,026	-0,051	-0,017	-0,125
Galena	0,104	0,142	-0,187	0,225	-0,163	0,325
Gypsum	0,115	0,364	0,119	0,072	0,018	-0,030
Ilmenite	-0,058	0,002	0,034	-0,380	0,340	0,418
K-Feldspar	-0,035	0,213	-0,200	0,184	-0,225	0,397
Magnetite	0,354	-0,115	-0,034	-0,027	0,007	-0,127
Millerite	-0,092	0,083	-0,343	-0,292	0,235	-0,194
Molybdenite	0,225	0,421	0,059	-0,048	0,043	-0,093
Monazite	0,252	-0,164	-0,212	0,236	0,057	0,172
Muscovite	-0,114	0,015	0,106	0,301	0,394	0,062
Pentlandite	-0,088	0,084	-0,368	-0,155	0,139	-0,305
Pyrite	-0,085	0,070	-0,283	0,072	-0,054	-0,056
Pyroxene	-0,056	-0,010	0,027	0,068	0,097	-0,157
Schorl-Dravite	0,009	0,038	-0,018	-0,377	0,297	0,311
Sphalerite	-0,098	0,133	-0,296	0,124	0,124	0,082
Titanite	-0,048	-0,033	0,079	-0,125	0,090	0,312

Eigenvectors and eigenvalues of the correlation matrix from the principal component analysis of the mineralized zone in the Salobo Deposit

Autovalor	4,4016	3,1442	2,8990	2,3298	2,1067	1,8787	1,7972	1,5495	1,3393	1,1428
Proportion	0,147	0,105	0,097	0,078	0,070	0,063	0,060	0,052	0,045	0,038
Accumulated	0,147	0,252	0,348	0,426	0,496	0,559	0,619	0,670	0,715	0,753
Autovalor	1,0449	0,9986	0,9790	0,8530	0,7133	0,5751	0,5341	0,4225	0,3271	0,2426
Proportion	0,035	0,033	0,033	0,028	0,024	0,019	0,018	0,014	0,011	0,008
Accumulated	0,788	0,821	0,854	0,882	0,906	0,925	0,943	0,957	0,968	0,976
Autovalor	0,1963	0,1376	0,1206	0,0845	0,0620	0,0541	0,0329	0,0172	0,0084	0,0077
Proportion	0,007	0,005	0,004	0,003	0,002	0,002	0,001	0,001	0,000	0,000
Accumulated	0,983	0,987	0,991	0,994	0,996	0,998	0,999	0,999	1,000	1,000

Appendix C

Principal component analysis eigenvectors of the later albitization and post-ore alteration zone of Salobo Deposit

Variable	*CP1*	*CP2*	*CP3*	*CP4*	*CP5*	*CP6*
Density	0,425	0,026	-0,121	0,008	0,078	-0,123
SM	0,362	-0,078	-0,209	-0,218	-0,110	0,057
Resistivity	-0,278	0,260	-0,336	-0,040	0,082	-0,102
Chargeability	0,270	0,043	-0,072	-0,327	-0,113	-0,136
Conductivity	-0,103	-0,151	0,009	0,221	-0,467	-0,340
Albite	-0,257	-0,116	-0,066	-0,250	-0,252	0,237
Biotite	0,019	0,138	0,286	0,351	-0,017	0,086
Bornite	0,113	-0,229	-0,383	0,409	0,193	0,086
Chalcocite	0,127	-0,224	-0,383	0,339	0,229	0,137
Chalcopyrite	-0,050	-0,374	0,183	-0,110	0,366	-0,082
Chlorite	0,200	0,221	0,307	0,115	0,041	-0,039
Epidote	-0,060	-0,220	-0,120	0,321	-0,456	-0,211
Fluorite	0,128	-0,047	-0,075	-0,153	-0,072	0,214
Almandine	0,232	0,164	0,177	0,050	0,078	-0,296
Ilmenite	0,016	0,248	0,103	0,282	0,170	-0,037
K-Feldspar	-0,110	-0,343	0,152	-0,019	0,288	0,094
Magnetite	0,356	-0,059	-0,175	-0,188	-0,087	0,069
Muscovite	-0,137	0,257	-0,214	-0,002	0,142	0,057
Plagioclase	-0,237	0,304	-0,152	-0,038	0,009	0,291
Pyrite	-0,077	-0,180	0,115	-0,158	0,243	-0,326
Pyroxene	-0,039	0,066	-0,197	-0,080	0,095	-0,413
Quartz	-0,185	-0,345	0,104	-0,085	-0,069	0,066

Eigenvectors and eigenvalues of the correlation matrix from the principal component analysis of the later albitization and post-ore alteration zone in the Salobo Deposit

Autovalor	4,5026	2,4243	1,9692	1,7877	1,7471	1,4217	1,3586	1,2183	0,9622	0,9379
Proportion	0,196	0,105	0,086	0,078	0,076	0,062	0,059	0,053	0,042	0,041
Accumulated	0,196	0,301	0,387	0,465	0,540	0,602	0,661	0,714	0,756	0,797
Autovalor	0,7662	0,6275	0,6154	0,5339	0,5112	0,3990	0,3104	0,2707	0,2200	0,1616
Proportion	0,033	0,027	0,027	0,023	0,022	0,017	0,013	0,012	0,010	0,007
Accumulated	0,830	0,858	0,884	0,908	0,930	0,947	0,961	0,972	0,982	0,989
Autovalor	0,1365	0,0680	0,0497							
Proportion	0,006	0,003	0,002							
Accumulated	0,995	0,998	1,000							

References

Airo, M. (2015). Geophysical signatures of mineral deposit types – synopsis. In: Airo, M. (Ed.). *Geophysical signatures of mineral deposit types*. Espoo, Geological Survey of Finland, Special Paper, 58, 9–70. Available at: http://tupa.gtk.fi/julkaisu/specialpaper/sp_058.pdf

Araújo, M. C., Silva, A. M., Barbosa, P. F., Boniatti, J. H., Früchting, A., Bouças do Lago, S., & Betancourt, R. H. S. (2022). Petrophysics applied in mineralizations, hydrothermal alterations and lithology mapping: A case study from the Zn–Pb (Cu–Ag) epithermal deposit of Santa Maria, Brazil. *Geophysical Prospecting, 70*, 765–789. https://doi.org/10.1111/1365-2478.13180

Austin, J. R., Patterson, B., Birchall, R., Björk, A., Walshe, J., Schlegel, T., Stromberg, J., McFarlane, H., Shelton, T. D., & Pearce, M. (2021). Metasomatic controls on petrophysical zonation in IOCG mineral systems: An example from Ernest Henry, Cloncurry District: Part III: Cloncurry METAL Final Report 2018/21. *CSIRO, Australia.*

Austin, J. R., Patterson, B. O., Le Gras, M., Birchall, R., & Walshe, J. L. (2017). Geophysical signatures of IOCG and Sedex style mineralization in the Mount Isa Eastern Succession, Queensland, Australia. In: *Improving exploration with Petrophysics: The application of magnetic remanence and other rock physical properties to geophysical targeting*. Exploration ’17. Toronto, Canada.

Burns, N., P. Geo, C. Gauld, P. Geo, M. D. Alvim, P. Geo, F. Cp, M. Tagami, & P. Eng (2019). Salobo Copper-Gold Mine Carajás, Pará State, Brazil: Technical Report – Salobo III Expansion.

Cordani, U. (1981). Comentários sobre as determinações geocronológicas da região da Serra dos Carajás. *University of São Paulo, Rio Doce Geologia e Mineração (DOCEGEO)*, Internal Report (in Portuguese).

Costa, U. A. P., Paula, R. R., Silva, D. P. B., Barbosa, J. P. O., Silva, C. M. G., Tavares, F. M., Oliveira, J. K. M., & Justo, A. P. (2016). *Mapa geológico-geofísico ARIM Carajás*. Belém: CPRM. 1 mapa color. Escala 1:250.000.

Dall’Agnol, R., Oliveira, D. C., & Lamarao, C. N. (2013). Magmatismo granitoide arqueano e evolução geológica do Subdomínio de Transição da Província Carajás, sudeste do Cráton Amazônico, Brasil. *Bol. Mus. Para. Emílio Goeldi. Cienc. Nat, 8*, 251–256.

Delinardo da Silva, M. A. (2014). Metatexitos e diatexitos do Complexo Xingu na região de Canaã dos Carajás: Implicações para a evolução mesoarqueana do Domínio Carajás, PA (Unpublished MSc Thesis). *University of Campinas*.

Dentith, M., & Clark, R. (2020). *Petrophysics and Mineral Exploration: A Workflow for Data Analysis and a New Interpretation Framework.*

Dentith, M., & Mudge, S. T. (2014). *Geophysics for the Mineral Exploration Geoscientist.* Cambridge University Press.

Diniz, A. C., de Melo, G. H., de Carvalho Lana, C., Queiroga, G. N., de Castro, M. P., & Reis, H. L. (2022). Unravelling magmatic-hydrothermal processes at Salobo and GT-46 IOCG deposits, Carajás mineral province, Brazil: Constraints from whole-rock geochemistry and trace elements in apatite. *Journal of South American Earth Sciences.*

Duncan, R. J., Stein, H. J., Evans, K. A., Hitzman, M. W., Nelson, E. P., & Kirwin, D. J. (2010). A New Geochronological Framework for Mineralization and Alteration in the Selwyn-Mount Dore Corridor,

Eastern Fold Belt, Mount Isa Inlier, Australia: Genetic Implications for Iron Oxide Copper-Gold Deposits. *Economic Geology, 106*, 169–192.

Groves, D. I., Bierlein, F. P., Meinert, L. D., & Hitzman, M. W. (2009). Iron Oxide Copper-Gold (IOCG) Deposits through Earth History: Implications for Origin, Lithospheric Setting, and Distinction from Other Epigenetic Iron Oxide Deposits. *Economic Geology, 105*, 641–654.

Hitzman, M. W. (2000). Iron Oxide-Cu-Au Deposits: What, Where, When and Why. In T. M. Porter (Ed.), *Hydrothermal Iron Oxide Copper-Gold and Related Deposits: A Global Perspective* (1st ed., Vol. 1, pp. 9–25). PGC Publishing.

Leão-Santos, M., Moraes, R., Li, Y., Raposo, M. I., & Zuo, B. (2022). Hydrothermal Alteration Zones' Magnetic Susceptibility Footprints and 3D Model of Iron Oxide-Copper-Gold (IOCG) Mineralization, Carajás Mineral Province, Brazil. *Minerals, 12.*

Lindenmayer, Z. G. (1990). Salobo Sequence, Carajás, Brasil: Geology, Geochemistry and Metamorphism. *Ph.D. Thesis*. University of Ontario, Ontario, Canada.

Lindenmayer, Z. G. (2003). O depósito de Cu-Au do Salobo, Serra dos Carajás: Uma revisão. In Ronchi, L. H., & Althoff, F. J. (Eds.), *Caracterização e modelamento de depósitos minerais* (1st ed., Vol. 1, pp. 63–91). São Leopoldo: Unisinos (in Portuguese).

Machado, N., Lindenmayer, D. H., Krogh, T. E., & Lindenmayer, Z. G. (1991). U-Pb geochronology of Archean magmatism and basement reactivation in the Carajás area, Amazon Shield, Brazil. *Precambrian Research, 49*, 1–26.

McGladrey, A. J., Olivo, G. R., Silva, A. M., Oliveira, G. D., Botura Neto, B., & Perrouty, S. (2017). The integration of physical rock properties, mineralogy, and geochemistry for the exploration of large zinc silicate deposits: A case study of the Vazante zinc deposits, Minas Gerais, Brazil. *Journal of Applied Geophysics, 136*, 400–416. https://doi.org/10.1016/j.jappgeo.2016.11.013

Melo, A. T., and Li, Y. (2019). Geology differentiation of geophysical inversions using machine learning. *International Workshop on Gravity, Electrical & Magnetic Methods and Their Applications,* 301–304.

Melo, A. T., Sun, J., and Li, Y. (2015). Geophysical inversions applied to geological differentiation and deposit characterization: A case study at an IOCG deposit in Carajás Mineral Province, Brazil. *SEG Technical Program Expanded Abstracts, 34,* 2012–2016.

Melo, A. T., Sun, J., and Li, Y. (2017). Geophysical inversions applied to 3D geology characterization of an iron oxide copper-gold deposit in Brazil. *Geophysics, 82,* K1–K13.

Melo, A. T., Von, M. G. H., Filho, U. J. T., and Fuck, R. (2014). A comparison between 1D electromagnetic modeling programs: A case history for Cristalino iron oxide copper gold deposit, Carajás Mineral Province, Brazil. *Revista Brasileira de Geofísica, 32,* 433–443.

Melo, G. H. C. de. (2014). Evolução Temporal do Depósito de Óxido de Ferro-Cobre-Ouro do Salobo, Província Carajás. *Dissertação de Mestrado.* Universidade Estadual de Campinas, 1–99p.

Melo, G. H. C., Monteiro, L. V. S., Hunger, R. B., Toledo, P. I. F., Xavier, R. P., Zhao, X.-F., Su, Z.-K., Moreto, C. P. N., & Jesus, S. S. G. P. (2021). Magmatic-hydrothermal fluids leaching older seafloor exhalative rocks to form the IOCG deposits of the Carajás Province, Brazil: Evidence from boron isotopes. *Precambrian Research, 365,* 106412.

Melo, G. H. C., Monteiro, L. V. S., Xavier, R. P., Moreto, C. P. N., Santiago, E. B. S., Dufrane, S. A., Aires, B., & Santos, A. F. F. (2016). Temporal evolution of the giant Salobo IOCG deposit, Carajás Province (Brazil): Constraints from paragenesis of hydrothermal alteration and U-Pb geochronology. *Mineralium Deposita, 52,* 709–732. https://doi.org/10.1007/s00126-016-0693-5

Melo, G. H. C., Monteiro, L. V. S., Xavier, R. P., Moreto, C. P. N., & Santiago, E. B. S. (2019). Tracing fluid sources for the Salobo and Igarapé Bahia deposits: Implications for the genesis of the iron oxide copper-gold deposits in the Carajás Province, Brazil. *Economic Geology, 114,* 697–718.

Moreto, C. P. N., Monteiro, L. V. S., Xavier, R. P., Creaser, R. A., Dufrane, S. A., Melo, G. H. C., Delinardo da Silva, M. A., Tassinari, C. C. G., & Sato, K. (2015). Timing of multiple hydrothermal events in the iron oxide-copper-gold deposits of the Southern copper belt, Carajás Province, Brazil. *Mineralium Deposita, 50,* 517–546.

Requia, K., Stein, H., Fontboté, L., & Chiaradia, M. (2003). Re – Os and Pb – Pb geochronology of the Archean Salobo iron oxide copper–gold deposit, Carajás mineral province, northern Brazil. *Mineralium Deposita, 38,* 727–738.

Skirrow, R. G. (2022). Iron oxide copper-gold (IOCG) deposits – A review (part 1): Settings, mineralogy, ore geochemistry and classification. *Ore Geology Reviews, 140,* 104569. https://doi.org/10.1016/j.oregeorev.2021.104569

Teixeira, N. A., Campos, L. D., Paula, R. R. D., Lacasse, C. M., Ganade, C. E., Monteiro, C. F., Lopes, L. B. L., & Oliveira, C. G. (2021). Carajás Mineral Province - Example of metallogeny of a rift above a cratonic lithospheric keel. *Journal of South American Earth Sciences, 108,* 103091.

Teixeira, W., Hamilton, M. A., Girardi, V. A. V., Faleiros, F. M., & Ernst, R. E. (2019). U-Pb baddeleyite ages of key dyke swarms in the Amazonian Craton (Carajás/Rio Maria and Rio Apa areas): Tectonic implications for events at 1880, 1110 Ma, 535 Ma, and 200 Ma. *Precambrian Research, 329,* 138–155.

Trunfull, E. F., Hagemann, S. G., Xavier, R. P., & Moreto, C. P. N. (2020). Critical assessment of geochronological data from the Carajás Mineral Province, Brazil: Implications for metallogeny and tectonic evolution. *Ore Geology Reviews, 121,* 103556.

VALE. (2023). Salobo Project: Mineral Reserves and Resources. *Internal Report.*

Xavier, R. P., Monteiro, L. V. S., Souza Filho, C. R., Torresi, I., Carvalho, E. R., Dreher, A. M., Wiedenbeck, M., Trumbull, R. B., Pestilho, A. L. S., & Moreto, C. P. N. (2010). The iron oxide copper-gold deposits of the Carajás Mineral Province, Brazil: An updated and critical review. In T. M. Porter (Ed.), *Hydrothermal Iron Oxide Copper-Gold and Related Deposits: A Global Perspective* (pp. 285–306). PGC Publishing.

Williams, N. C. (2009). Mass and magnetic properties for 3D geological and geophysical modelling of the southern Agnew–Wiluna Greenstone Belt and Leinster nickel deposits, Western Australia. *Australian Journal of Earth Sciences*, *56*(8), 1111–1142. https://doi.org/10.1080/08120090903246220

4. Integração de Dados Multifontes

Esta tese de doutorado utilizou dados geofísicos multifonte e multiescala para mapear a assinatura do maior depósito de cobre de um sistema mineral do tipo IOCG na Província Mineral de Carajás. Esses dados foram integrados com informações petrofísicas e geológicas, permitindo a identificação de vetores exploratórios e a compreensão de fatores críticos por meio da análise de múltiplas assinaturas. A caracterização integrada do footprint possibilita o mapeamento de novos alvos, incluindo aqueles com afloramento parcial ou sem expressão em superfície.

A caracterização do *footprint* geofísico do depósito Salobo mostra assinaturas e anomalias distintas associadas à mineralização. Foram utilizados dados aeromagnéticos e gamaespectrométricos regionais (500 m de espaçamento), aerogeofísicos de alta resolução (gravimetria gradiométrica, eletromagnético, magnético e gamaespectrométrico) para escala de distrito e geofísicos terrestres (magnetometria, gamaespectrometria, TDEM e DCIP) para escala de depósito. O depósito exibe forte contraste em dados magnéticos, gravimétricos e eletromagnéticos, refletindo a alta suscetibilidade da magnetita disseminada no granito hospedeiro e zonas de alteração ricas em magnetita. Modelos de TDEM mapearam concentrações de calcocita-bornita, enquanto dados gamaespectrométricos indicaram anomalias proeminentes de urânio e U/Th. Levantamentos de DCIP mostraram que a resistividade é mais eficaz do que a cargabilidade para delimitar a mineralização, sendo esta última influenciada por eventos tardios de alteração estéril associada ao evento de 1,88 Ga.

A caracterização petrofísica e geofísica de depósitos do tipo IOCG (Iron Oxide Copper-Gold) é essencial para aprimorar modelos exploratórios e otimizar a detecção de novos alvos mineralizados, especialmente em terrenos tropicais com intensa cobertura, como na Província Mineral de Carajás. Esses depósitos apresentam assinaturas geofísicas complexas, resultantes da interação entre processos hidrotermais, composição mineralógica e controles estruturais. A integração de dados geoquímicos, petrofísicos e geofísicos permite uma melhor definição das zonas de alteração, diferenciação entre anomalias e maior eficácia dos modelos exploratórios. A identificação de diferentes assinaturas da mineralização e o desenvolvimento de um sistema de vetorização são ferramentas essenciais para a seleção de novos alvos, sobretudo em subsuperfície. Para isso, é crucial correlacionar assinaturas mineralógicas, petrofísicas e geoquímicas com dados geológicos existentes na literatura.

Nesta pesquisa, dados litogeoquímicos foram integrados em *strip logs* conceituais, combinados com dados de mapeamento mineral e petrofísicos, visando aprimorar a vetorização do depósito do tipo Salobo. De a cordo com Dentith et al. (2018), a petrofísica, geofísica e geoquímica desempenham um papel crucial na exploração mineral ao fornecer dados quantitativos para o refinamento de modelos exploratórios e distinção de zonas mineralizadas

de rochas hospedeiras e estruturas geológicas adjacentes. Dentith et al. (2020) enfatizam que um fluxo de trabalho integrado possibilita o mapeamento da extensão espacial das zonas mineralizadas e priorização de alvos exploratórios. Adams & Dentith (2018) argumentam que a incorporação de dados geoquímicos e petrofísicos em um modelo geofísico pode reduzir ambiguidades na interpretação de anomalias. Kitzig et al. (2017) destacam que a análise simultânea das propriedades químicas e físicas das rochas em perfis verticais (*Strip Log Plot*) permite identificar zonas de alteração, mineralização e variações litológicas, que em muitos casos a geologia tradicional generaliza.

Os resultados obtidos neste trabalho mostram, em consonância com os estudos de Melo et al. (2016) e Diniz et al. (2022), que as seis principais zonas de alteração hidrotermal identificadas no Depósito Salobo, juntamente com as subzonas detalhadas por meio da caracterização mineralógica, fornecem um arcabouço robusto para a compreensão do sistema. Com base nisso, foi realizada uma análise integrada de geoquímica e petrofísica em perfis verticais ilustrativos de furos do depósito. A análise integrada de dados geoquímicos e petrofísicos confirmou a existência das subzonas de alteração hidrotermal previamente identificados e classificados na caracterização mineralógica (TIMA e QEMSCAN), os quais, na abordagem geológica convencional, foram simplificados em zonas amplas. As propriedades densidade e resistividade e os elementos químicos Cu, Au, Ag, Bi, U e Mo evidenciam contrastes significativos entre a zona distal (rocha hospedeira e zona Ca-Na) e o início do enriquecimento em ferro (Figura 4.1). A susceptibilidade magnética (MS), cargabilidade e teor de Fe também evidenciam a zona Ca-Na de forma mais ampla, com valores mais altos e consideráveis, mas ainda contrastantes com a zona de enriquecimento em ferro (Figura 4.1). No entanto, uma análise mais detalhada revela que essa região de valores petrofísico um pouco maiores corresponde a subzonas avançadas de alteração Ca-Na, com a presença de magnetita. Se interpretados apenas com base nas zonas definidos pela descrição geológica convencional, esses valores seriam considerados sem significado geológico claro.

Na porção de enriquecimento em ferro, os valores petrofísicos e dos elementos passam a apresentar valores maiores e contrastantes com a zonas de alteração vizinhas. A partir da zona de alteração potássica, todas as propriedades físicas e elementos químicos indicam a transição entre as zonas distal e proximal do depósito. Se avaliado de forma detalhada, esse contraste passa a ser observado desde a zona avançada do enriquecimento em ferro (K-Fe e K-Fe rico em Fe), passando pela zona potássica, até a zona mineralizada propriamente dita (Figura 4.1). Essa região é caracterizada pela presença de minerais como magnetita, bornita, calcopirita, monazita e molibdenita, que apresentam a assinatura esperada das propriedades físicas e dos elementos químicos. A susceptibilidade magnética especificamente apresenta uma sensibilidade maior as subzonas devido a presença de magnetita (alta susceptibilidade).

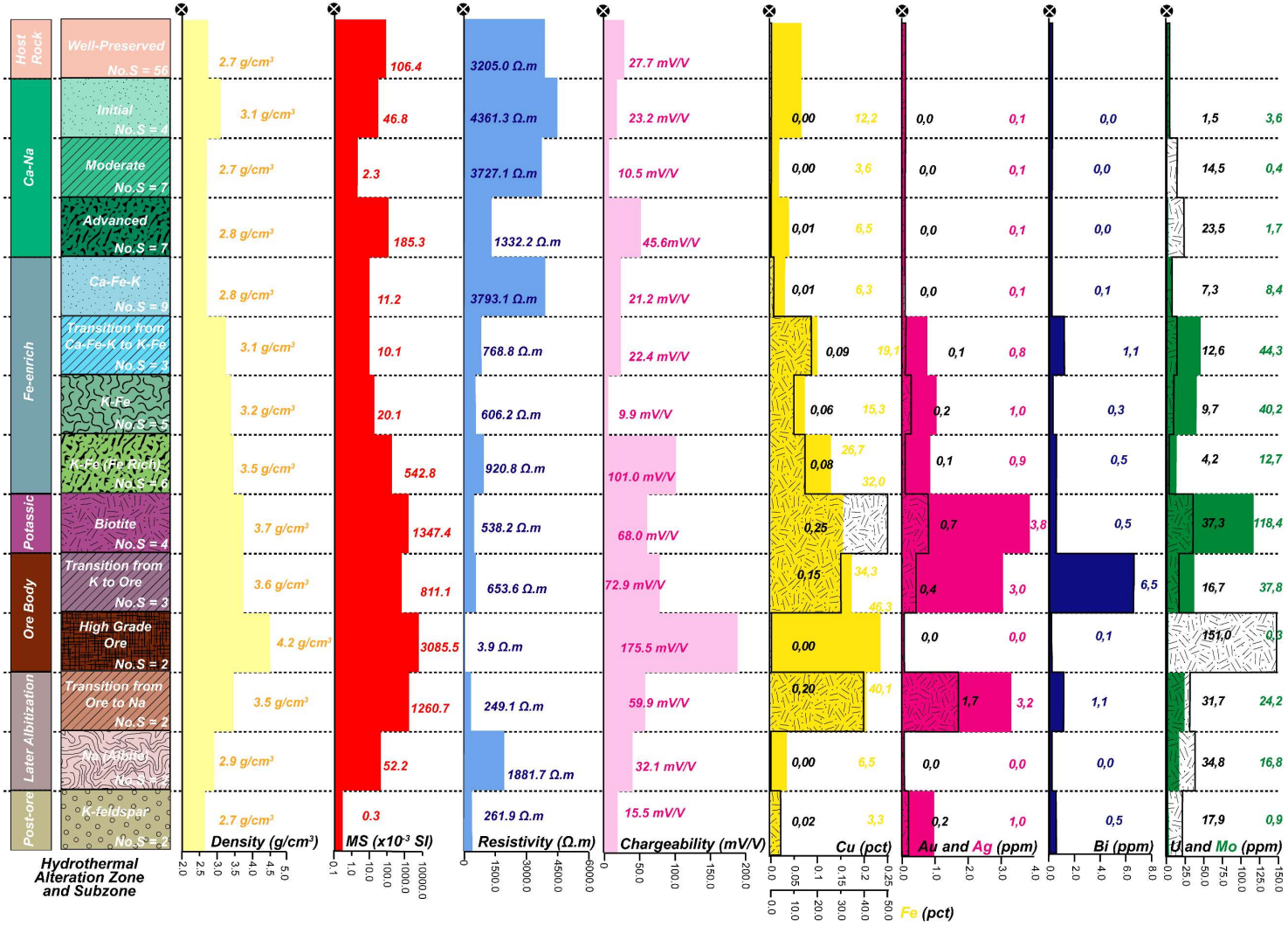


Figura 4. 1 – *Strip Log* ilustrativo das principais zonas e subzonas de alteração do Depósito Salobo, valores petrofísicos médios e valores litogeoquímicos médios dos principais elementos indicadores de mineralização. Abreviações: Au – Ouro, Ag – Prata, Bi – Bismuto, Cu – Cobre, Fe – Ferro, Mo – Molibdênio, No.S – Número de amostras e U – Urânio.

A porção final do Depósito Salobo (Na e K-feldspato subzonas) evidencia os contrastes entre a zona mineralizada e a zona pós-mineralização (Figura 4.1). A densidade, suscetibilidade magnética e a cargabilidade destacam com clareza esse contraste, refletindo o decaimento nos teores de magnetita e sulfetos, além do enriquecimento em sódio associado à albita. A resistividade apresenta pico na subzona de albitização, pois as zonas adjacentes ainda apresentam resquícios de sulfetos disseminados, como calcopirita, pirita, calcocita e bornita. De forma geral, todas as propriedades físicas delineiam o limite entre a zona mineralizada e a zona pós-mineralização, marcada por um enriquecimento em sódio associado à albita.

Por outro lado, a distribuição dos elementos químicos analisados evidencia o contraste entre o fim da zona enriquecida em ferro, da zona mineralizada e da zona pós-mineralização. Nota-se que, à medida que avançamos da zona transicional para a zona mineralizada, os teores de Fe, C, Au e Mo caem drasticamente, marcando o término da zona de transição. Esse contraste abrupto pode estar relacionado ao número de amostras que efetivamente contêm sulfetos, como calcocita ou bornita, ou a sua textura, uma vez que sulfetos disseminados podem ser mascarados. Além disso, as amostras categorizadas como "*High Grade Ore*" são predominantemente compostas por magnetita, o que é evidenciado pelo pico nos valores de Fe e queda nos valores de Cu. Outro contraste abrupto ocorre na subzona de albitização, possivelmente associado ao baixo número de amostras coletadas nessa zona.

Como os principais elementos geoquímicos indicadores da mineralização do Deposito Salobo foram inicialmente considerados na análise, os elementos indicadores de alteração como Ca, Na e K também foram considerados para validação do processo de alteração hidrotermal. Além desses, os *High-Field-Strenght-Elements* (HFSE – Ti, P, Y, Zr, Hf, Nb, Ta) também foram considerados, dada sua ampla aplicação no estudo de alterações hidrotermais, petrogênese e associações tectônicas em rochas ígneas (Pearce & Cann, 1973; Winchester & Floyd, 1977). Estudos como os de Finlow-Bates & Stumpfl (1981) indicam que, em zonas intensamente alteradas, sulfuretos circundantes podem influenciar a mobilidade de elementos como Nb e Y, enquanto Ti e Zr tendem a permanecer imóveis, reforçando seu papel como marcadores confiáveis no contexto de alterações hidrotermais. Ao final Ca, Na, K, Hf e Zr foram incorporados à análise (Figura 4.2).

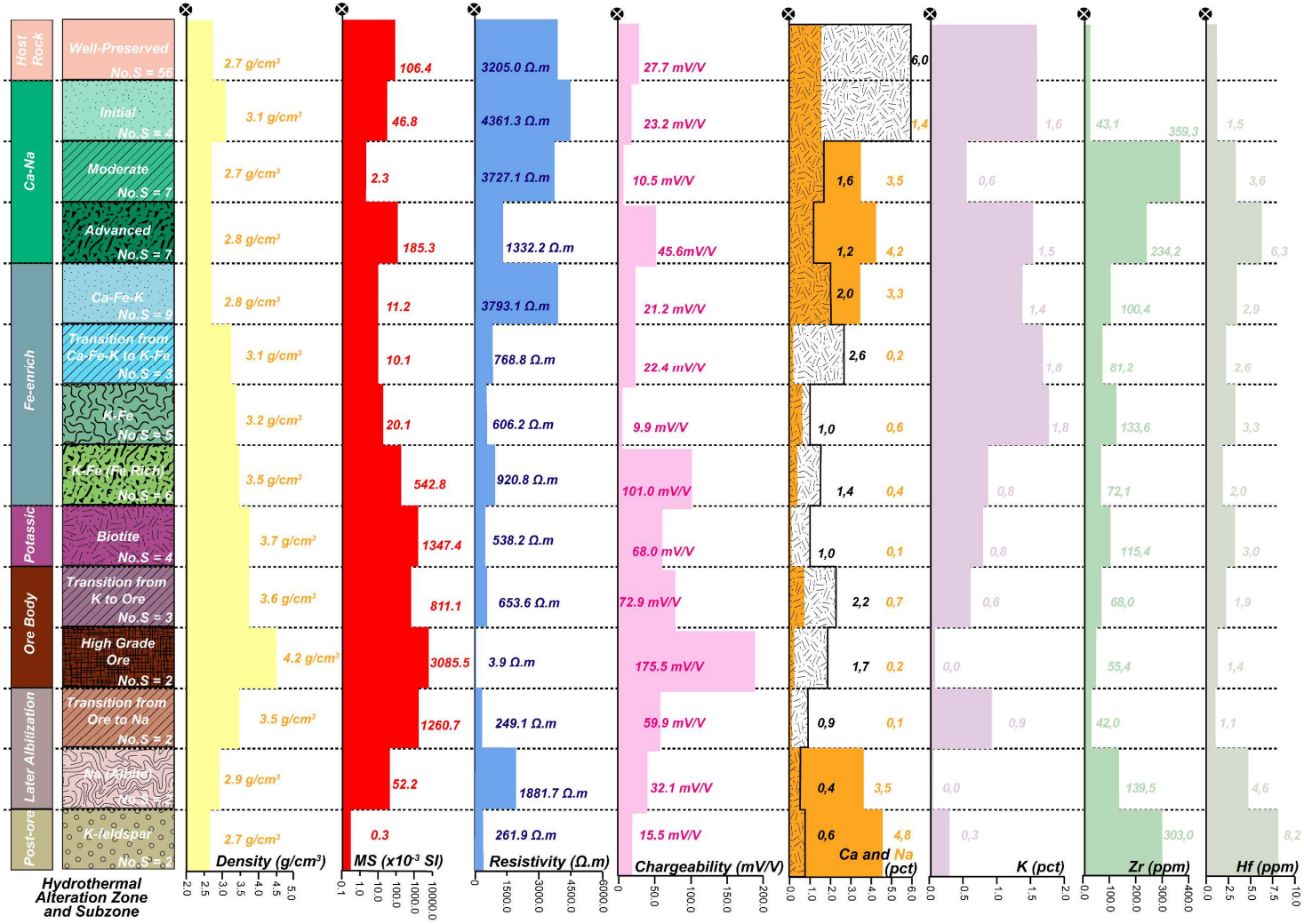


Figura 4. 2 - - *Strip Log* ilustrativo das principais zonas e subzonas de alteração do Depósito Salobo, valores petrofísicos médios e valores litogeoquímicos médios dos principais elementos indicadores de alteração. Abreviações: Ca - Cálcio, Hf – Háfnio, K – Potássio, Na – Sódio, No.S – Número de amostras e Zr - Zircônioi.

Os valores médios desses elementos demonstram, conforme esperado, predominância de Ca e Na na zona de alteração distal do Depósito Salobo. É interessante observar que no topo do perfil integrado predomina Ca, o qual é atribuído à mineralogia original do protólito ígneo, enquanto que em profundidade o elemento sódio passa a prevalecer. Na descrição geológica, esta transição é caracterizada por albititos, originados a partir de fluidos hidrotermais que delimitam a zona de alteração Ca-Na avançada (Figura 4.2). Em termos de propriedades físicas, este intervalo inicial apresenta alta resistividade e baixa suscetibilidade magnética e cargabilidade, sem contrastes petrofísicos significativos. Este fato corrobora que, a depender dos objetivos do estudo, a conjugação de ferramentas geofísicas e geoquímicas é fundamental.

O potássio marcou de forma assertiva a transição da zona potássica para a mineralização, ao que anteriormente já era caracterizado na descrição de furos de sondagem como mineralização (Figura 4.2). Contrastes físicos são observados para as propriedades cargabilidade e suscetibilidade magnética. O háfnio e o zircônio podem estar associados ao enriquecimento de sódio (Albita), mas não se limitam a esta zona de alteração. Ao longo da zona de enriquecimento em Fe, por exemplo, picos no teor destes HFSE podem estar associados a minerais traços (titanita e zircão), cuja relevância para a definição de contrastes físicos é pequena.

Como os campos das unidades sódicas não foi bem definido no *Strip Log* da figura 4.2, optou-se por criar um gráfico de dispersão Fe x (Ca+Mg) com os sub estágios de alteração hidrotermal (Figura 4.3A). As amostras mais enriquecidas em ferro (K-Fe e K-Fe rico em Fe), amostras da zona potássica e da zona de mineralização estão localizadas a partir de 10 % (parte inferior direta do gráfico) e apresentam respostas significativas de todos as propriedades físicas devido a presença de magnetita e sulfetos no geral. Já as amostras Ca-Fe-K (estágio inicial de enriquecimento em Fe), Ca-Na e da zona pós-alteração, que representam um processo de enriquecimento em Na, situam-se à esquerda, sob a elipse listrada (Figura 4.3A). As amostras com maiores teores de Ca encontram-se na parte superior da elipse. Com o aumento do teor de sódio e o consequente declínio de Fe, Ca, Mg e K, as amostras migram para a parte inferior da elipse (Figura 4.3A). Esse padrão sugere um *trend* de decaimento, onde o Na diminui à medida que aumenta o Ca. Amostras localizadas dentro deste *trend* devem apresentar contraste significativo de resistividade e suscetibilidade magnética, devido à ausência de magnetita e sulfetos, e um contraste moderado em densidade devido ainda à presença de almandina e grunerita.

Foi elaborado um gráfico de dispersão Zr x Hf (Figura 4.3B) com as subzonas de alteração do Salobo para facilitar a visualização e permitir consolidar as interpretações obtidas. O objetivo foi avaliar se esses elementos poderiam estar associados a outros minerais presentes em diferentes tipos de alteração, além do enriquecimento em Na observado nos *Strip Logs* (Figura

4.3). No gráfico, identificam-se três domínios distintos. Na parte superior direita, encontram-se as amostras com altos teores de sódio, associadas principalmente a albititos e que apresentam baixos valores em todas as propriedades físicas. Na parte inferior esquerda, estão as amostras com elevados teores de Fe, pertencentes à zona de mineralização e que apresentam altos valores de densidade, suscetibilidade magnética, condutividade e cargabilidade. De forma mais dispersa, observa-se um terceiro domínio, composto por amostras das zonas de alteração Ca-Na e de enriquecimento em ferro, onde ainda há pequenas quantidades de Na. A análise sugere que os teores de Zr e Hf aumentam com a albitização. Com a evolução para as fases hidrotermais férricas e o início da mineralização, ocorre uma diminuição gradual dos teores desses elementos. Esses minerais podem apresentar correlação direta a minerais que controlam as propriedades físicas, e serem auxiliares na interpretação da assinatura petrofisica e geofisica.

O gráfico de dispersão Fe x Na (Figura 4.3C) evidencia a separação de dois principais domínios: um correspondente à zona distal, associada à alteração Ca-Na rica em Na onde esperam-se ótimos contrastes de resistividade e densidade, e outro relacionado à zona potássica e à zona de mineralização, rica em Fe, onde esperam-se ótimos contrastes em todas as propriedades físicas, sendo dependente de minerais chaves como almandina, grunerita, biotita, magnetita, bornita, calcocita e calcopirita. Além disso, observa-se a classificação de quatro subestágios da zona de enriquecimento em Fe:1) Ca-Fe-K e a transição de Ca-Fe-K para K-Fe – apresentam teores relativamente elevados de Na e menores de Fe, caracterizando uma zona de transição entre a alteração cálcico-sódica e o início do enriquecimento em ferro; 2) K-Fe e K-Fe (rico em Fe) – não apresentam mais Na e possuem teores mais elevados de Fe, embora ainda não suficientemente altos para serem classificados como pertencentes à zona de mineralização.

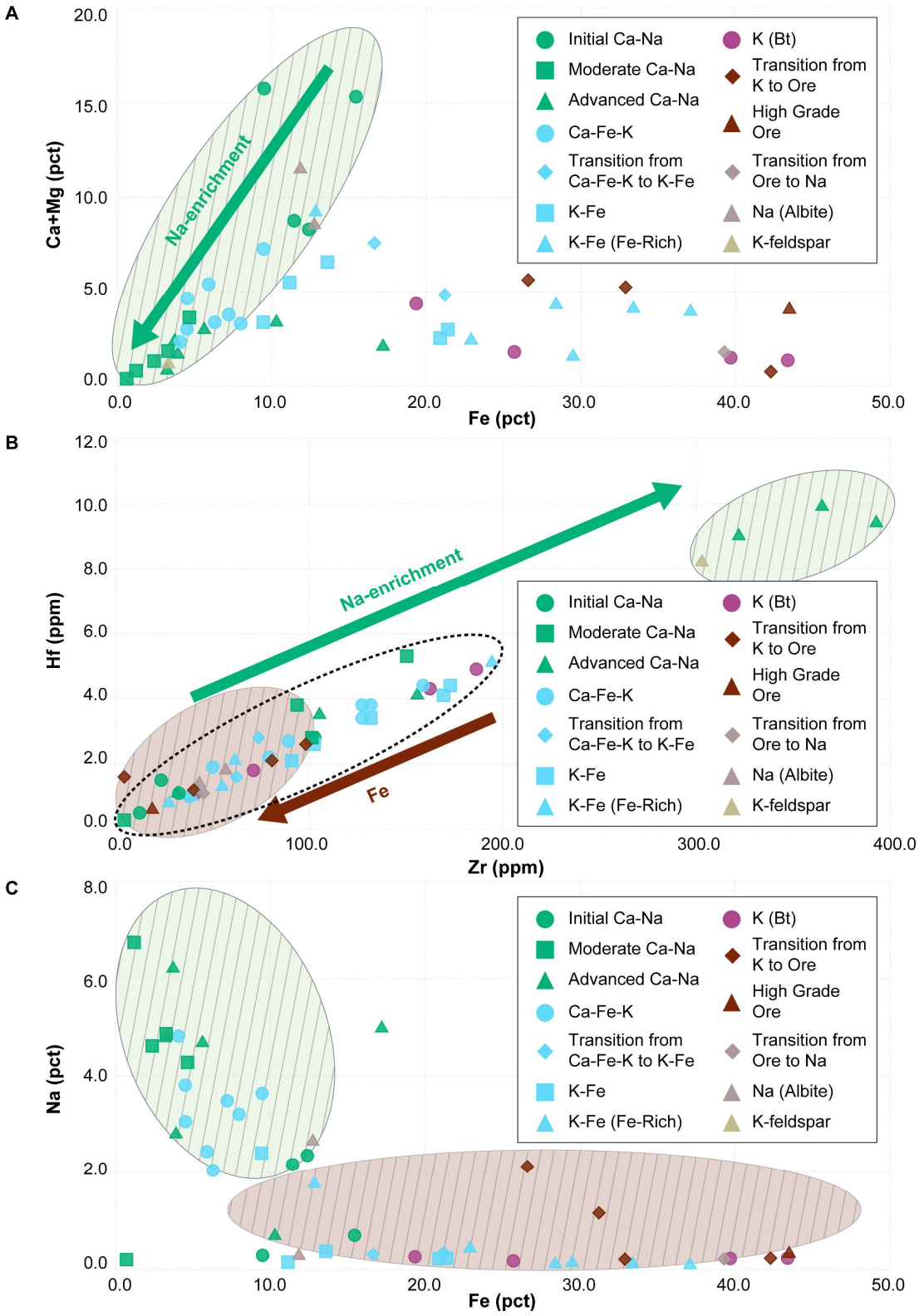


Figura 4. 3 – Gráfico de dispersão das amostras das principais subzonas de alteração hidrotermais do Salobo. A) Diagrama bivariante de Fe x (Ca + Mg) para amostras das principais subzonas de alteração hidrotermais do Salobo com indicação do enriquecimento de sódio no sistema) Diagrama bivariante de Zr x Hf para amostras das principais subzonas de alteração hidrotermais do Salobo com indicação do enriquecimento de sódio e decaimento de Fe, Ca, Mg e K no sistema. C) Diagrama bivariante Fe x Na para amostras das principais subzonas de alteração hidrotermais do Salobo.

Pode-se concluir que a análise integrada de dados geoquímicos e petrofísicos foi essencial para consolidar a caracterização das subzonas de alteração hidrotermal no Depósito Salobo. Apesar das propriedades físicas e químicas apresentarem as respostas esperadas em diferentes zonas, a confirmação dessas interpretações só foi possível devido ao banco de dados expressivo e disponível para esta pesquisa. A densidade, susceptibilidade magnética, resistividade e cargabilidade foram determinantes para identificar com maior precisão as transições entre as zonas de alteração, especialmente a zona mineralizada e a zona pós-alteração, evidenciando um papel confirmatório e detalhado.

Se não houvesse um banco de dados geoquímico e mineralógico tão robusto, as interpretações baseadas apenas na petrofísica teriam caráter assertivo, devido à sua capacidade de delinear as variações e transições entre as zonas de alteração, especialmente em regiões como a zona mineralizada e a zona enriquecida em sódio, onde os elementos químicos apresentaram limitações para diferenciar as transições, mas ainda assim existiram lacunas informativas e anomalias a serem explicadas. Assim, o estudo ressalta a importância de abordagens integradas para um entendimento mais completo, mas também destaca a confiabilidade das propriedades físicas como ferramenta interpretativa em cenários com menor disponibilidade de dados.

5. Conclusões

A presente pesquisa teve como objetivo central caracterizar o *footprint* geofísico e petrofísico das mineralizações e alterações hidrotermais do depósito Salobo, integrando dados geofísicos multifonte e em multiescala com propriedades físicas. A investigação baseou-se em um banco de dados amplo e diversificado, que permitiu a análise aprofundada de diferentes aspectos e contribuiu significativamente para a compreensão da assinatura do Salobo na Província Mineral de Carajás. Além disso, a tese apresenta como resultado guias exploratórios aplicáveis à prospecção de novos alvos ou depósitos do tipo IOCG. A identificação de padrões de resposta geofísica e petrofísica permitiu o aprimoramento de metodologias para reduzir incertezas e otimizar campanhas de exploração mineral.

A pesquisa adotou uma abordagem sistemática para caracterizar a assinatura geofísica do depósito Salobo. Os métodos de magnetometria, gravimetria gradiométrica, gamaespectrometria, eletromagnetometria no domínio do tempo (TDEM) e, eletroresistividade e polarização induzida (DCIP) demonstraram eficácia no mapeamento de alterações hidrotermais e mineralizações. O processamento, análise e interpretação mostram que o depósito Salobo mostra contraste em todos os métodos aplicados. O Salobo mostra fortes correlações entre anomalias magnéticas e zonas de magnetita e alteração K-Fe, consolidando a magnetometria como um método-chave na exploração mineral IOCG em escala regional, apesar de mostrar resposta em todas as escalas. Os dados gravimétricos gradiométrico evidenciaram uma relação direta entre densidade e identificam bem a zona mineralizada, enquanto os modelos derivados de dados eletromagnéticos (TDEM) indicam uma anomalia de condutividade no Salobo, similar a de outros depósitos da Província Mineral de Carajás como o Furnas. A assinatura gamaespectrométrica destacou zonas de alteração e um elevado teor de urânio, sendo a razão U/Th um indicador eficaz para exploração. Os levantamentos de eletroresistividade e polarização induzida (DCIP) demonstraram que a resistividade mapeia melhor o depósito do que a cargabilidade, pois a cargabilidade pode indicar zonas não mineralizadas. Apesar da coincidência entre as diversas anomalias geofísicas, elas refletem minerais e processos de alteração distintos, reforçando a importância da integração de múltiplos métodos na exploração mineral.

A combinação dessas técnicas resultou na criação de um guia exploratório aplicável à identificação de alvos potenciais. Esse guia enfatiza a relevância da integração de dados geofísicos na delimitação de áreas prospectivas, que proporcionam uma eficiência maior das campanhas exploratórias e redução de custos com sondagens diretas.

A análise petrofísica baseou-se em dados de densidade, susceptibilidade magnética, resistividade e cargabilidade, que indicaram assinaturas distintas para cada zona de alteração, refletindo a complexidade do sistema IOCG do Salobo. Os resultados evidenciaram padrões sistemáticos nas propriedades físicas de cada fase de alteração. As rochas hospedeiras

apresentam valores baixos e homogêneos em comparação com outros depósitos IOCG na Província Mineral de Carajás, como Furnas e Cristalino. A alteração cálcico-sódica, interpretada como zona distal, caracterizou-se pela presença de albita e actinolita, associadas a baixa densidade e susceptibilidade magnética. A zona de enriquecimento em ferro, dominada por magnetita, grunerita e almandina, apresenta alta densidade, maior susceptibilidade magnética e aumento na condutividade, indicando transição para áreas mineralizadas. A alteração potássica, rica em biotita e associada a bornita, calcopirita e calcocita, reduziu a resistividade e aumentou a cargabilidade. As fases de alteração tardia marcaram a transição para as zonas finais do sistema mineralizado, com variações na susceptibilidade magnética e resistividade, associadas a minerais ganga com valores petrofísicos reduzidos. A alteração pós-mineralização, caracterizada por feldspato potássico, albita, plagioclásio e clorita, apresenta baixa densidade e alta resistividade.

A assinatura petrofísica de Salobo destacou fortes correlações entre magnetita e susceptibilidade magnética nas zonas mineralizadas, facilitando o mapeamento de alterações hidrotermais. No entanto, anomalias magnéticas também podem indicar zonas estéreis, tornando esses levantamentos mais eficazes em escala regional. A densidade revelou-se um indicador confiável de alteração e mineralização, permitindo diferenciar rochas hospedeiras de zonas mineralizadas devido à presença de minerais como bornita, calcocita, calcopirita e magnetita. Além disso, diferenciou zonas de alteração proximal pela presença de minerais como granada e almandina. Assim, levantamentos gravimétricos gradiométricos foram fundamentais para identificar zonas de alteração proximal e mineralização em Salobo. A resistividade, reduzida em áreas ricas em sulfetos como calcopirita, bornita, calcocita e pirita, mostrou-se um indicador mais preciso de mineralização. Por outro lado, a cargabilidade, embora útil, gerou interpretações errôneas devido à influência de minerais como clorita, almandina e monazita, mas ainda auxiliou na interpretação geofísica.

A integração dos dados geoquímicos e petrofísicos permitiu a distinção detalhada das zonas de alteração hidrotermal, evidenciando a importância da abordagem multidisciplinar. A geoquímica demonstrou que o depósito Salobo apresenta padrões geoquímicos característicos, como altas concentrações de elementos traço associado ao sistema mineralizante. Além disso, revelou assinaturas elementares distintas associadas às zonas de alteração hidrotermal e mineralização. As concentrações de cobre, ferro, urânio e elementos terras raras (ETR) apresentaram padrões específicos em diferentes fases de alteração. A alteração potássica, por exemplo, destacou-se pelo enriquecimento em K, Fe e U, enquanto zonas com alto sódio apresentaram altos teores de Na e Ca. Essa abordagem possibilitou uma correlação robusta entre as propriedades petrofísicas e geoquímicas, reforçando a confiabilidade da modelagem exploratória.

No entanto, a pesquisa apresenta algumas limitações como o tamanho da área de estudo e o número de amostras, pois restringiram na extrapolação dos resultados para áreas adjacentes. Além disso, a complexidade dos processos hidrotermais e tectônicos envolvidos nos depósitos IOCG requer abordagens complementares para validação de modelos exploratórios. A continuidade da pesquisa em escalas mais detalhadas, poderá fornecer *insights* ainda mais precisos sobre os processos de formação e evolução desses sistemas mineralizantes. O aumento no número de amostras também contribuirá para validar as correlações geoquímicas observadas. A variabilidade nos teores de elementos traço e a presença de múltiplos pulsos hidrotermais introduziram incertezas adicionais na interpretação geoquímica. Os avanços proporcionados por este estudo evidenciam o potencial de expansão da metodologia empregada para outros contextos geológicos. Os resultados obtidos possuem implicações diretas para para prospecção de depósitos IOCG na própria Província Carajás. Depósitos como Furnas, Cristalino e Gameleira poderiam implementar a metodologia desenvolvida no Salobo, otimizando os métodos de exploração e reduzindo riscos associados a furos de sondagem locados em áreas com pouco conhecimento geológico e o que os torna , em alguns casos, imprecisos. Além disso, a integração da petrofísica com os dados geofísicos permitiu uma calibração mais refinada das respostas dos diferentes métodos, o que permitiu a diferenciação entre mineralizações economicamente viáveis e zonas estéreis referentes a alterações hidrotermais distal.

Em um contexto global, os resultados obtidos possuem implicações diretas para depósitos IOCG em outras regiões, como Ernest Henry e Olympic Dam. Esses depósitos compartilham diversas características com Salobo, incluindo a presença de magnetita em fases dominantes, fortes anomalias magnéticas e gravimétricas, e um sistema hidrotermal complexo com diferentes pulsos e associação a zona de cisalhamento e deformação. O depósito Ernest Henry, por exemplo, apresenta uma assinatura geofísica marcada por alta magnetização residual e forte resposta de gravimetria, características também observadas em Salobo. Da mesma forma, Olympic Dam exibe uma associação entre mineralização de cobre-ouro e um extenso halo de alteração hidrotermal, que pode ser modelado e utilizar os mesmos princípios adotados no Salobo.

A metodologia desenvolvida nesta pesquisa permitiu uma melhor interpretação das anomalias geofísicas e uma exploração mais eficiente, além de aprimorar o modelo exploratório do deposito. A adaptação da abordagem para diferentes ambientes geológicos pode fornecer novas perspectivas sobre a aplicabilidade de métodos geofísicos e petrofísicos na identificação de sistemas mineralizantes ainda pouco compreendidos. A integração de geofísica, petrofísica e geoquímica demonstrou ser um caminho eficiente para a caracterização de depósitos minerais, reduzir custos e aumentar a precisão na seleção de alvos.

REFERÊNCIAS BIBLIOGRÁFICAS

Adams C., Dentith M., 2018, Defining Petrophysical Propertiesof Ultramafic and Mafic Rocks In Terms of Alteration, ASEG Extended Abstracts, 2018:1, 1-8

Aisengart, T., J. L. Ando, L. Batista, and L. C. Ferreira, 2019, Automatic classification of density and magnetic domains from Carajás Mineral Province: Sixteenth International Congress of the Brazilian Geophysical Society.

Barton, M. D., and D. A. Johnson, 2004, Footprints of Fe-oxide(-Cu-Au) systems: SEG 2004: Predictive Mineral Discovery Under Cover. Centre for Global Metallogeny, Spec. Pub. 33 The University of Western Australia, 112–116.

Carlos, D. U. 2013. Aplicação de Processamento e Inversão Geofísica 3D de Aerogradiometria da Gravidade na Estimação da Estrutura do Minério de Ferro no Sinclinal Gandarela - Quadrilátero Ferrífero - Minas Gerais. Tese de Doutorado. Observatório Nacional, Rio de Janeiro, RJ, Brasil.

Craveiro G.S., Villas R.N.N, Xavier R.P. 2019. Mineral chemistry and geothermometry of alteration zones in the IOCG Cristalino deposit, Carajás Mineral Province, Brazil. Journal of South American Earth Sciences, v. 92, p. 481-505.

Dentith, M., Yuan, H., Johnson, S., Murdie, R., & Piña-Varas, P. (2018). Application of deep-penetrating geophysical methods to mineral exploration: Examples from Western Australia. *Geophysics*, *83*(3), WC29-WC41.

Dentith, M., & Clark, R. (2020). *Petrophysics and Mineral Exploration: A Workflow for Data Analysis and a New Interpretation Framework.*

Diniz, A. C., de Melo, G. H., de Carvalho Lana, C., Queiroga, G. N., de Castro, M. P., & Reis, H. L. (2024). Unravelling magmatic-hydrothermal processes at Salobo and GT-46 IOCG deposits, Carajás mineral province, Brazil: Constraints from whole-rock geochemistry and trace elements in apatite. *Journal of South American Earth Sciences.*

Dransfield, M., 2010, Conforming Falcon gravity and the global gravity anomaly: Geophysical Prospecting, 58, 469–483.

Esdale, D., D. F. Pridmore, J. Coggon, P. Muir, P. Williams, and F. Fritz, 2003, The Olympic Dam copper-uranium-gold-silver-rare earth element deposit, South Australia: A geophysical case history: ASEG Extended Abstracts, 147–168.

Finlow-Bates, T., and Stumpfi, E.F., 1981, The behavior of so-called immobile elements in hydrothermally altered rocks associated with volcanogenie submarine-exhalative ore deposits: Mineralium Deposita, v.16, p.319-328.

Groves, D. I., F. P. Bierlein, L. D. Meinert, and M. W. Hitzman, 2009, Iron Oxide Copper-Gold (IOCG) Deposits through Earth History: Implications for Origin, Lithospheric Setting, and Distinction from Other Epigenetic Iron Oxide Deposits: Economic Geology, 105, 641–654.

Henrique, E. F., P. J. M. B. de Andrade, and J. G. X. P. Valle, 2013, Geophysics over the Boa Esperança Copper-Cobalt Deposit, Carajás Province, Pará State, Brazil:

Hitzman, M. W., 2000, Iron Oxide-Cu-Au Deposits: What, Where, When and Why, *in* In: Porter, T.M., Ed., Hydrothermal Iron Oxide Copper-Gold and Related Deposits: A Global Perspective, 1st ed.Vol. 1. PGC Publishing, 9–25.

Hitzman, M. W., N. Oreskes, and M. T. Einaudi, 1992, Geological Characteristics and Tectonic Setting of Proterozoic Iron Oxide (Cu-U-Au-REE) Deposits: Precambrian Research, 58, 241–287.

Hunger R.B., Xavier R.P., Moreto C.P.N., Gao J.F. 2018. Hydrothermal alteration, fluid evolution, and Re-Os geochronology of the Grota Funda iron oxide copper-gold deposit, Carajas Province (Para State), Brazil. Economic Geology, 113(8), 1769-1794.

Kitzig MC, Kepic A, Kieu DT. Testing cluster analysis on combined petrophysical and geochemical data for rock mass classification. Explor Geophys. 2017;48(3):344-352

Leão-Santos, M., 2014, Interpretação, Inversão 3D de Dados Magnéticos e Modelagem 3D da Susceptibilidade Magnética Medida, Aplicadas à Prospecção Geofísica de Depósitos de Óxidos de Ferro - Cobre - Ouro (IOCG Iron Oxide-Copper-Gold) – Província Mineral de Carajás, Brasil: 128.

Leão-Santos, M., Y. Li, and R. Moraes, 2015, Application of 3D magnetic amplitude inversion to iron oxide-copper-gold deposits at low magnetic latitudes: A case study from Carajás Mineral Province, Brazil: Geophysics, 80, B13–B22.

Leão-Santos, M., R. Moraes, Y. Li, M. I. Raposo, and B. Zuo, 2022, Hydrothermal Alteration Zones' Magnetic Susceptibility Footprints and 3D Model of Iron Oxide-Copper-Gold (IOCG) Mineralization, Carajás Mineral Province, Brazil: Minerals, 12.

Lindenmayer, Z. G., 2003, Depósito de Cu–Au do Salobo, Serra dos Carajás: Uma revisão, *in* L. H. Ronchu and F. J. Althoff, eds., Caracterização e Modelamento de Depósitos Minerais, Editora Unisinos, 69–98.

Melo, A. T., J. Sun, and Y. Li, 2015, Geophysical inversions applied to geological differentiation and deposit characterization: A case study at an IOCG deposit in Carajás. Mineral Province, Brazil: SEG Technical Program Expanded Abstracts, 34, 2012–2016.

Melo, A. T., J. Sun, and Y. Li, 2017, Geophysical inversions applied to 3D geology characterization of an iron oxide copper-gold deposit in Brazil: Geophysics, 82, K1–K13.

Melo, G. H. C. de, 2014, Evolução Temporal do Depósito de Óxido de Ferro-Cobre-Ouro do Salobo, Província Carajás. Dissertação de Mestrado. Universidade Estadual de Campinas, 1–99p.

Melo, G. H. C., Monteiro, L. V. S., Xavier, R. P., Moreto, C. P. N., Santiago, E. B. S., Dufrane, S. A., Aires, B., & Santos, A. F. F. (2016). Temporal evolution of the giant Salobo IOCG deposit, Carajás Province (Brazil): Constraints from paragenesis of hydrothermal alteration and U-Pb geochronology. *Mineralium Deposita, 52,* 709–732. https://doi.org/10.1007/s00126-016-0693-5

Melo, G. H. C. de, 2018, Evolução Temporal e Fonte de Fluidos dos Depósitos IOCG Salobo e Igarapé Bahia, Província Carajás. Tese de Doutorado. Universidade Estadual de Campinas, 1–219p.

Melo, G. H. C. de, L. V. S. Monteiro, R. P. Xavier, C. P. N. Moreto, and E. Santiago, 2019, Tracing fluid sources for the Salobo and Igarapé Bahia deposits: Implications for the genesis of the iron oxide copper-gold deposits: In Carajás Province, Brazil: Economic Geology, 114, 697–718.

Pearce, J.A., Cann, J.R., 1973. Tectonic setting of basic volcanic rocks determined using trace element analyses Earth Planet. Sci. Lett. 19(2),290–300.

Pollard, P. J., 2000, Evidence of a magmatic fluid and metal source for Fe-oxide Cu-Au mineralisation, *in* In: Porter T.M. (ed.) Hydrothermal iron oxide copper-gold and related deposits: A global perspective, 1st ed.Vol. 1. PGC Publishing, 27–41.

Pollard, P. J., 2006, An intrusion-related origin for Cu-Au mineralization in iron oxide-copper-gold (IOCG) provinces: Mineralium Deposita, 41, 179–187.

Requia, K., H. Stein, L. Fontboté, and M. Chiaradia, 2003, Re – Os and Pb – Pb geochronology of the Archean Salobo iron oxide copper – gold deposit, Carajás mineral province, northern Brazil: Mineralium Deposita, 38, 727–738.

Santos, J. O. S., L. A. Hartmann, H. E. Gaudette, D. I. Groves, N. J. Mcnaughton, and I. R. Fletcher, 2000, A New Understanding of the Provinces of the Amazon Craton Based on Integration of Field Mapping and U-Pb and Sm-Nd Geochronology: Gondwana Research, 3, 453–488.

Silva, A. T. M. C., 2012, Resposta Eletromagnética e Magnética do Depósito IOCG (Iron Oxide Copper Gold) Cristalino, Província Mineral Carajás, Pará, Brasil. Tese de Doutorado. Universidade de Brasília, 65p.

Skirrow, R. G., 2022, Iron Oxide Copper-Gold (IOCG) deposits – A review (part 1): Settings, mineralogy, ore geochemistry and classification: Ore Geology Reviews, 140.

Tavares, F. M., 2015, Evolução Geotectônica do Nordeste Da Província Carajás. Tese de Doutorado. Universidade Federal do rio de Janeiro, 1–131p.

VALE, 2020, Formulário 20-F. Relatório Anual, de Acordo Com a Seção 13 Ou 15(d) Da Lei de Mercado de Capitais de 1934:

Vasquez, M. L., and L. T. Rosa-Costa, 2008, Geologia e Recursos Minerais Do Estado Do Pará - Sistema de Informação SIG: Texto Explicativo Do Mapa Geológico e de Recursos Minerais Do Estado Do Pará: CPRM-Serviço Geológico do Brasil.

Williams, P. J., M. D. Barton, D. A. Johnson, L. Fontboté, A. de Haller, G. Mark, N. H. S. Oliver, and R. Marschik, 2005, Iron oxide-copper-gold deposits: Geology, spacetime distribution, and possible modes of origin, *in* J. W. Hedenquist, J. F. H. Thompson, R. J. Goldfarb, and J. P. Richards, eds., Economic Geology, 100th Anniversary Volume. SEG, 371–405.

Winchester, J.A. and Floyd, P.A. (1977) Geochemical Discrimination of Different Magma Series and Their Differentiation Product Using Immobile Elements. Chemical Geology, 20, 325-343.

Xavier, R. P., L. V. S. Monteiro, C. R. Souza Filho, I. Torresi, E. R. Carvalho, A. M. Dreher, M. Wiedenbeck, R. B. Trumbull, A. L. S. Pestilho, and C. P. N. Moreto, 2010, The Iron Oxide Copper-Gold Deposits of the Carajás Mineral Province, Brazil: an Updated and Critical Review: In: Porter T.M. (Ed.), Hydrothermal Iron Oxide Copper-Gold and Related Deposits: A Global Perspective. Adelaide, PGC Publishing, 3, 285–306.

APPENDIX A

Banco de dados litogeoquimicos das amostras do Deposito Salobo

Sample ID	Ag_ME-MS61_ppm	Au_Au-AA23_ppm	Bi_ME-MS61_ppm	Ca_ME-MS61_pct	Cu Sol_Cu-AA04_pct	Fe_ME-MS61_pct	Hf_ME-MS61_ppm	K_ME-MS61_pct	Mo_ME-MS61_ppm	Na_ME-MS61_pct	U_ME-MS61_ppm	Zr_ME-MS61_ppm
2B	0.02	<0,005	0.01	10.35	N/A	15.45	1.5	0.37	0.15	0.7	1.1	23.7
2C	0.19	0.04	0.05	4.68	N/A	9.51	0.5	3.28	0.3	0.29	2.6	12.6
2E	<0,01	<0,005	<0,01	1.36	N/A	3.29	18.7	0.74	0.29	4.86	16.7	>500
2G	0.03	0.01	0.02	2.51	N/A	4.53	1	1.82	0.18	3.05	0.7	38.3
2I	<0,01	0.01	0.02	0.74	<0,01	6.31	2.2	2.19	12.6	2.04	4.3	79.5
2J	0.84	0.14	0.63	3.24	0.07	5.92	3.8	1.71	41.2	2.43	32.3	127.5
2K	0.83	0.19	0.26	0.69	0.08	33.4	1.3	0.88	22.6	0.11	5.1	55.2
2L	1.01	0.14	0.28	0.45	0.06	22.9	5.1	1.83	22.3	0.43	8.4	194.5
2M	0.16	0.05	0.04	0.46	0.02	37.1	0.8	0.26	18.4	0.09	2.2	27.7
2N	5.68	1.57	0.63	0.83	0.35	43.4	1.1	0.22	240	0.03	96.4	41.2
2P	0.18	<0,005	0.05	0.43	0.01	3.23	9	0.76	0.35	4.77	35.6	322
2T	<0,01	0.01	0.04	0.17	N/A	11.85	1.8	0.04	33.4	0.28	4.1	57
2-1B	0.11	0.02	0.01	4.05	N/A	11.45	1.1	1.77	12.3	2.16	1.7	32.9
2-1C	0.1	0.03	0.04	1.01	N/A	4.08	3.4	0.68	0.89	4.81	7.9	127.5
2-1D	0.05	0.01	0.02	0.68	N/A	7.99	2.7	1.51	2.51	3.2	5	89.4
2-1F	0.2	0.07	0.12	1.73	0.03	21.2	2.8	1.76	12.3	0.17	14.3	73.9
2-1I	4.05	0.5	0.89	0.73	0.22	25.7	4.9	1.38	141.5	0.06	17.9	186.5
2-1J	0.09	<0,005	0.02	1.59	<0,01	19.35	4.3	1.07	4.39	0.26	2.7	162.5
2-1K	<0,01	<0,005	0.04	1.91	<0,01	3.73	9.9	1.67	0.22	6.2	69.1	365
2-2A	0.22	0.01	0.04	0.53	N/A	2.38	3.8	0.45	0.42	4.61	19.9	93.9
2-2B	0.02	0.02	0.04	1.79	<0,01	7.22	3.8	1.07	0.74	3.48	3.4	132
2-2E	0.45	0.03	0.3	2.93	0.04	16.65	1.6	2.04	12	0.31	4.4	62.6
2-2H	0.53	0.12	0.12	0.17	0.07	29.5	1.2	0.13	1.15	0.02	3.6	42.1
2-2I	0.08	0.01	0.74	3.55	0.01	26.6	2.6	0.91	0.97	2.12	28.5	98.4
2-2J	<0,01	<0,005	0.01	1.13	N/A	43.5	0.6	0.05	0.34	0.12	1.7	19.1
2-2L	0.01	<0,005	0.02	2.82	N/A	12.75	1.4	0.12	0.13	2.64	5.9	43.4
2-2M	0.01	<0,005	0.02	4.52	N/A	11.9	4.3	1.32	0.8	1.91	0.8	136.5
3A	0.08	<0,005	0.05	5.38	N/A	12.4	2.8	0.98	1.77	2.35	0.6	103
3B	0.05	<0,005	<0,01	2.36	N/A	4.67	5.3	0.27	0.61	4.27	46	150.5
3C	0.04	<0,005	0.01	3.98	N/A	9.48	1.9	1.3	8.38	3.63	2	50.3
3D	0.01	0.01	0.01	1.23	N/A	17.2	1.1	0.6	3.2	4.97	0.8	32.2
3F	0.11	0.02	0.01	1.47	N/A	5.63	3.5	0.21	0.75	4.67	11.4	105.5
3G	0.04	0.01	0.02	1.77	N/A	4.52	4.4	0.98	0.7	3.8	2.4	159
3J	0.76	0.73	0.07	1.11	0.04	9.45	3.4	1.31	46.3	2.4	14	132
3L	0.13	0.03	0.04	1.15	0.01	11.15	4.1	2.66	13.8	0.15	2.6	169.5
3M	2.53	7.31	0.74	0.63	0.23	28.4	1	0.73	9.61	0.11	3.1	39.6
3N	0.58	0.06	0.06	0.34	0.06	21.4	2.6	1.51	76.7	0.06	3.6	102.5
3Q	5.41	0.91	0.64	1.02	0.4	39.7	1.8	0.54	87.9	0.11	32	71.4
3R	8.4	0.53	18.55	4.67	0.33	32.9	2.1	0.55	105	0.21	22.4	80.9
3S	1.69	0.73	2.19	0.45	0.15	42.3	1.2	0.28	17	0.23	5.1	40.5
3-1A	N/A	N/A	N/A	N/A	N/A	N/A	N/A	N/A	N/A	N/A	N/A	N/A
3-1B	0.98	0.2	0.53	0.55	0.02	3.31	8.2	0.29	0.87	4.82	17.9	303
3-1D	0.21	<0,005	0.06	0.64	0.01	1.22	2.8	0.29	0.56	6.74	0.8	101.5
3-1F	0.05	<0,005	0.07	1.2	<0,01	3.92	9.4	3.9	1.8	2.79	11.8	393
3-1H	0.07	0.02	0.02	6.24	<0,01	12.85	2.1	0.88	0.53	1.76	0.7	61.8
3-1I	0.42	0.04	0.1	2.2	0.03	13.6	4.4	1.46	9.78	0.37	3.6	173
3-1K	3.03	0.37	1.32	0.4	0.15	20.9	2.1	1.99	54.2	0.05	24.7	91.1
3-1L	3.2	2.5	1.43	1.28	0.19	39.3	1.1	0.95	24.7	0.1	34.1	45.5
3-1M	0.05	0.01	0.09	1.12	<0,01	10.3	4.1	2.43	4.16	0.69	7.6	156
3-2A	N/A	N/A	N/A	N/A	N/A	N/A	N/A	N/A	N/A	N/A	N/A	N/A
3-2B	N/A	N/A	N/A	N/A	N/A	N/A	N/A	N/A	N/A	N/A	N/A	N/A
3-2D	N/A	N/A	N/A	N/A	N/A	N/A	N/A	N/A	N/A	N/A	N/A	N/A
3-2E	N/A	N/A	N/A	N/A	N/A	N/A	N/A	N/A	N/A	N/A	N/A	N/A
3-2G	N/A	N/A	N/A	N/A	N/A	N/A	N/A	N/A	N/A	N/A	N/A	N/A
3-2I	N/A	N/A	N/A	N/A	N/A	N/A	N/A	N/A	N/A	N/A	N/A	N/A